

M. Suda

# Quantum Interferometry in Phase Space

Theory and Applications



Springer

# Quantum Interferometry in Phase Space

M. Suda

---

# Quantum Interferometry in Phase Space

Theory and Applications

With 87 Figures



Martin Suda

ARC Seibersdorf research GmbH  
Tech Gate Tower  
Donau-City-Str. 1, 5. OG  
1200 Wien, Austria  
e-mail: Martin.Suda@arcs.ac.at  
www.smart-systems.at  
www.quantenkryptographie.at

Library of Congress Control Number: 2005930381

ISBN-10 3-540-26070-6 Springer Berlin Heidelberg New York  
ISBN-13 978-3-540-26070-7 Springer Berlin Heidelberg New York

This work is subject to copyright. All rights are reserved, whether the whole or part of the material is concerned, specifically the rights of translation, reprinting, reuse of illustrations, recitation, broadcasting, reproduction on microfilm or in any other way, and storage in data banks. Duplication of this publication or parts thereof is permitted only under the provisions of the German Copyright Law of September 9, 1965, in its current version, and permission for use must always be obtained from Springer. Violations are liable for prosecution under the German Copyright Law.

Springer is a part of Springer Science+Business Media  
[springeronline.com](http://springeronline.com)  
© Springer-Verlag Berlin Heidelberg 2006  
Printed in The Netherlands

The use of general descriptive names, registered names, trademarks, etc. in this publication does not imply, even in the absence of a specific statement, that such names are exempt from the relevant protective laws and regulations and therefore free for general use.

Typesetting: by the authors and SPI Publisher Services using a Springer L<sup>A</sup>T<sub>E</sub>X macro package

Cover design: *design & production* GmbH, Heidelberg

Printed on acid-free paper SPIN: 11344025 57/SPI 5 4 3 2 1 0

Dedicated to Helmut Rauch

# Preface

This book is a monograph of a text that originated from lectures given by the author at the Technical University of Vienna. The aim of this work is to give a concise overview concerning the phase-space description of interference phenomena of both interferometry using photons and neutron interferometry. The material presented in the book originates to some extent from a number of publications written during the last 10 years by the author and his colleagues, but contains new work as well.

Since the beginning of the 1990s a lot of effort has been undertaken to transfer the well-known quantum-optical phase-space formalism to matter wave optics. In particular, neutron interferometry has been described using the above-mentioned formalism, taking into account quantum-mechanical distribution functions like Wigner functions, Q-functions and P-functions. Thereby the investigation of the interrelations between quantum optics using photons and neutron optics leads to interesting and novel results. The present book attempts to combine both fields of research.

Coherence properties play an important role in any kind of interferometry. In this book we intend, in some sense, to summarize known results and add some new ones obtained with photons and neutrons, and analyze them in terms of general quantum optics, which can be applied to photon and matter waves as well.

The aim of this book was to write a monograph on the essentials of quantum optical light and matter wave interferometry for first- or second-year graduate students interested in eventually pursuing research in this area and for people interested in this field of research. A precondition is solely some basic knowledge of quantum mechanics and some knowledge of solid state physics.

Part I is devoted to the theory of quantum mechanical distribution functions, which are currently used to describe and graphically display wave functions in phase-space. After some basics about expectation values formulated in quantum mechanics, the Wigner function, the P-function and the Q-function are defined and their properties are worked out in detail. A systematic approach to these quasi-distribution functions is elaborated by using coherent states.

## VIII Preface

In Part II optical interferometry in quantum networks is investigated. Based on the wave packet formalism, the intensity as well as the momentum and the position distribution functions in various network structures are considered. Thereby network elements such as the fiber glass, beam splitter, the absorber and the phase shifter play a central role. The Mach–Zehnder interferometer, a combination of three Mach–Zehnder interferometers, double-loop systems and Mach–Zehnder interferometers with two inputs are examined in detail.

Part III is devoted to neutron interferometry. First the dynamical theory of diffraction in a perfect crystal is worked out rather precisely. Using these results the so-called Laue interferometer can be described comprehensively. Subsequently, the phase-space formalism is applied to three and four plate neutron interferometry, including the graphical presentation of the quantum mechanical distribution functions mentioned above. Thereby a special squeezing effect is identified. Further issues are decoherence in neutron interferometry, correlations and novel aspects about the intensity and the visibility in double-loop systems.

Finally, in Part IV spin interferometry is considered. The spin-echo system is formulated and the Wigner function description of spin interference of neutrons in magnetic fields is executed. The influence of inhomogeneities of magnetic fields on the fragile interference pattern is discussed. The zero-field spin-echo system is a further topic of Part IV. Starting from the description of the interaction of neutrons with a rotating magnetic field, the wave functions in a dynamical spin flipper can be investigated. The procedure of a spin flip in a time-dependent magnetic field yields interesting energy characteristics in a spin flipper and a particular quantum state in the subsequent field-free region as well.

I wish to express my sincere gratitude to my revered teacher and friend Helmut Rauch, who inspired me with most of the ideas presented in this book. Without his encouragement and promotion this work would not have been accomplished. I would like to thank him for constant discussions and interchange of ideas. I wish to lay emphasis on the fact that, for me, he is representative of scientific thinking and acting.

Over the years I collaborated with colleagues who directly or indirectly contributed to this work. I would like to thank them cordially for their valuable cooperation and for giving to me many tips, suggestions and encouragement. In particular: Gerald Badurek, Matthias Baron, Winfried Boxleitner, Paolo Facchi, Norman Finger, Matthias Jakob, Thomas Länger, Othmar Lasser, Thomas Lorünser, Michael Nölle, Christoph Pacher, Saverio Pascazio, Momtchil Peev, Bernhard Ömer, Dieter Petrascheck, Andreas Poppe and Johann Summhammer.

Last, but not least, I would like to thank my wife Ingrid for her understanding and endurance. Certainly it was not always easy to get along with me during all this time of book-writing and forgetting everyday life.

I would like to thank ARC Seibersdorf research GmbH, the company I have been with for many years, for the assistance and promotion of my work as well as for creating a productive scientific climate. I would especially like to thank Christian Monyk for his help and support while I was writing this book.

I am also indebted to the Atomic Institute of the Austrian Universities, Vienna, of which I am a member, for aid and assistance writing this book.

I am grateful to Birgitt Ortner and Ian Glendinning who carefully examined the manuscript and considerably improved linguistic phrases and expressions.

This work was supported by the EC/IST Integrated Project SECOQC (Contract No. 506813) and by the Austrian Fonds zur Förderung der wissenschaftlichen Forschung (FWF), Vienna, project No. SFB F-1513.

Vienna, August 2005

*Martin Suda*

# Contents

---

## Part I Theory of Quantum Mechanical Distribution Functions

---

<b>1 Some Basics</b> . . . . .	3
1.1 Classical Mean Value . . . . .	3
1.1.1 One Variable $q$ . . . . .	3
1.1.2 Two Variables $q_1$ and $q_2$ . . . . .	4
1.2 Expectation Value . . . . .	4
1.2.1 Quantum Mechanical Harmonic Oscillator . . . . .	4
1.2.2 Density Operator and Expectation Value . . . . .	5
<b>2 Quantum Mechanical Distribution Functions</b> . . . . .	9
2.1 Wigner Function . . . . .	9
2.1.1 Wigner Function of a Wave Packet . . . . .	10
2.1.2 Properties of the Wigner Function . . . . .	11
2.1.3 Derivation of the Wigner Function . . . . .	13
2.1.4 Wigner Function of the Harmonic Oscillator . . . . .	14
2.2 Q-Function . . . . .	16
2.3 A Systematic Approach of Quasi-Distribution Functions . . . . .	17
2.3.1 Coherent States . . . . .	18
2.3.2 Normal Ordering of Operators (P-Function) . . . . .	22
2.3.3 Symmetric Ordering of Operators (Wigner Function) .	23
2.3.4 Anti-Normal Ordering of Operators (Q-Function) . . .	24
2.3.5 Quasi-Distribution Functions of Coherent States . . .	25
2.3.6 Q-Function of the Harmonic Oscillator . . . . .	25
2.3.7 Distribution Functions of a Radiation Field . . . . .	27
2.4 Uncertainty Relations and Squeezed States . . . . .	31
2.4.1 Uncertainty of the Coherent States . . . . .	31
2.4.2 Uncertainty of Squeezed States . . . . .	33

---

## Part II Optical Interferometry

---

<b>3 Interferometry Using Wave Packets</b> . . . . .	37
3.1 Beam Splitter . . . . .	38
3.1.1 Wave Packet . . . . .	38
3.1.2 Action of a Beam Splitter . . . . .	40

3.2	Mach–Zehnder Interferometer (MZ) . . . . .	41
3.2.1	Wave Functions of the MZ . . . . .	42
3.2.2	Spectra, Intensities and Visibility of the MZ . . . . .	43
3.3	Three Mach–Zehnder Interferometers . . . . .	47
3.3.1	Wave Functions of Three MZs . . . . .	47
3.3.2	Spectra, Intensities and Visibility of Three MZs . . . . .	48
3.4	Double-Loop . . . . .	56
3.4.1	Wave Functions in a Double-Loop . . . . .	57
3.4.2	Spectra and Intensities in a Double-Loop . . . . .	57
3.4.3	Simple Example of Visibility in a Double-Loop . . . . .	60
3.5	Mach–Zehnder with Two Inputs . . . . .	61
3.5.1	Wave Functions, Spectra and Intensities . . . . .	62
3.5.2	Discussion of MZ with Two Inputs . . . . .	65
3.6	Comment on Two-Photon Interference . . . . .	67

**Part III Neutron Interferometry**

4	<b>Introductory Remarks</b> . . . . .	71
4.1	Coherence Length . . . . .	72
4.2	Wigner Function, Wave Packets and Shannon Entropy . . . . .	72
5	<b>The Dynamical Theory of Diffraction</b> . . . . .	75
5.1	Interaction Potential . . . . .	76
5.1.1	Lattice Factor LF . . . . .	76
5.1.2	Structure Factor SF . . . . .	78
5.2	Basic Equations . . . . .	79
5.3	One-Beam Approximation . . . . .	80
5.4	Two-Beam Approximation . . . . .	81
5.5	Solutions for Plane Plate in Laue Position . . . . .	84
5.5.1	Intensities of Laue Position . . . . .	85
5.5.2	Wave Functions for Different Incident Directions . . . . .	87
6	<b>Laue Interferometer</b> . . . . .	91
6.1	Wave Functions and Focusing Condition . . . . .	91
6.2	Intensities and Phase Shift . . . . .	94
7	<b>Three Plate Interferometry in Phase-Space</b> . . . . .	97
7.1	Superposition of Wave Packets . . . . .	97
7.2	Wigner Function of Superposition . . . . .	98
7.3	Momentum and Position Spectra . . . . .	102
7.4	Squeezing of Momentum Spectrum . . . . .	104
7.5	Q-Function . . . . .	108
7.5.1	Q-Function of a Wave Packet . . . . .	108

7.5.2	Q-Function of Superposition . . . . .	109
7.6	Dephasing in Wigner Formalism . . . . .	111
7.6.1	Influence of Inhomogeneities of the Phase Shifter . . . . .	112
7.6.2	Fluctuations of the Beam Parameter . . . . .	115
7.6.3	Decoherence in Neutron Interferometry . . . . .	115
<b>8</b>	<b>Four-Plate Interferometry in Phase-Space . . . . .</b>	<b>119</b>
8.1	Double-Loop System . . . . .	119
8.1.1	Superposition of Three Waves . . . . .	120
8.1.2	Wigner Function of the Double-Loop System . . . . .	121
8.1.3	Momentum Distribution and Squeezing . . . . .	121
8.2	Correlations in a Double-Loop Interferometer . . . . .	125
8.2.1	First Loop . . . . .	125
8.2.2	Second Loop . . . . .	126
8.3	Intensity and Visibility in a Double-Loop System . . . . .	128
8.3.1	Intensity Aspects . . . . .	129
8.3.2	Visibility Aspects of Single and Double-Loops . . . . .	131

## Part IV Spin Interferometry

<b>9</b>	<b>Spin-Echo System . . . . .</b>	<b>141</b>
9.1	Basic Description and Formulation . . . . .	142
9.1.1	Wave Functions and Polarization . . . . .	143
9.1.2	Mean Intensity of the Wave Packet . . . . .	144
9.1.3	Wigner Function and Spectra . . . . .	146
9.1.4	Squeezing of Spectra . . . . .	148
9.2	Dephasing and Spin-Echo After Two Magnetic Fields . . . . .	149
9.3	Influence of Space-Dependent Inhomogeneities of Magnetic Fields . . . . .	153
9.4	Experimental Verification . . . . .	155
<b>10</b>	<b>Zero-Field Spin-Echo . . . . .</b>	<b>157</b>
10.1	Dynamical Spin-Flip . . . . .	157
10.1.1	Interaction of Neutrons with a Rotating Magnetic Field . . . . .	158
10.1.2	Time-Dependent Polarization . . . . .	163
10.1.3	Probability for $\pi$ -Flip . . . . .	163
10.1.4	Energy States of the System for Spin-Flip . . . . .	164
10.1.5	Energy Characteristics of a Dynamical Spin-Flipper . . . . .	166
10.2	Wave Functions in the Case of Zero-Field Spin-Echo . . . . .	168
10.3	Polarization and the Wigner Function . . . . .	171
10.4	Spectra of Zero-Field Spin-Echo . . . . .	172

XIV    Contents

<b>11   Summary .....</b>	175
<b>References .....</b>	177
<b>Index .....</b>	181

Part I

**Theory  
of Quantum Mechanical Distribution Functions**

# 1 Some Basics

In this chapter we review some basics that are of importance in the rest of the book. On the one hand, we consider the construction of classical mean values, and on the other, the quantum mechanical concept of expectation values.

In particular, the difference between the approach of the classical mean value and of the classical probability density function in comparison with the quantum mechanical concept of formation of a “mean”, called expectation value, and quantum mechanical distribution functions defined in Chap. 2 should be clearly recognized. To this end, a glimpse is thrown on the quantum mechanical harmonic oscillator and on the concept of the density operator.

## 1.1 Classical Mean Value

### 1.1.1 One Variable $q$

The classical mean value  $\langle A \rangle_{cl}$  of a quantity  $A(q)$  can be expressed as

$$\langle A \rangle_{cl} = \int_a^b A(q) P_{cl}(q) dq, \quad (1.1)$$

where  $P_{cl}(q)$  is a probability density function.

A first simple example is given by the rectangular probability density function  $P_{cl}^r(q) = 1/(b-a)$ .  $P_{cl}^r(q)$  is constant ( $\neq 0$ ) between  $a$  and  $b$  ( $b > a$ ) and outside this interval the function is zero.  $P_{cl}^r(q)$  is normalized to 1. If  $A(q) = q$  we get the arithmetic mean value  $\langle q \rangle = (a+b)/2$ . The mean square deviation (or variance) is  $\Delta q = \sqrt{\langle q^2 \rangle - \langle q \rangle^2} = (b-a)/\sqrt{12}$ .

A second, very important example is the normalized Gaussian distribution function

$$P_{cl}^G(q) = \frac{1}{\sqrt{2\pi}(\Delta q)} \exp \left[ -\frac{(q-q_0)^2}{2(\Delta q)^2} \right], \quad (1.2)$$

where  $\langle q \rangle = q_0$  and  $\langle q^2 \rangle = q_0^2 + (\Delta q)^2$ . The full width at half maximum (FWHM) is  $(\Delta q)\sqrt{8 \ln 2}$ .

### 1.1.2 Two Variables $q_1$ and $q_2$

The corresponding two-dimensional classical distribution function  $P_{cl}(q_1, q_2)$  is defined by the mean value

$$\langle A \rangle_{cl} = \iint A(q_1, q_2) P_{cl}(q_1, q_2) dq_1 dq_2. \quad (1.3)$$

**Example 1:** In the case when the variables  $q_1$  and  $q_2$  are independent, a product of two Gaussian distribution functions can be used instead of  $P_{cl}(q_1, q_2)$ . The total mean square deviation  $\Delta q$  is in this case  $\Delta q = \sqrt{(\Delta q_1)^2 + (\Delta q_2)^2}$ , where  $\Delta q_1$  and  $\Delta q_2$  are the mean square deviations of the single Gaussian functions, respectively.

**Example 2:** If the two values  $q_1$  and  $q_2$  are not independent of each other, a two-dimensional Gaussian distribution function  $P_{cl}^{G2}(q_1, q_2)$  is frequently used:

$$P_{cl}^{G2}(q_1, q_2) = \frac{\exp\left\{-\frac{1}{2(1-\rho^2)}\left[\left(\frac{q_1-q_{01}}{\Delta q_1}\right)^2 - 2\rho\left(\frac{q_1-q_{01}}{\Delta q_1}\right)\left(\frac{q_2-q_{02}}{\Delta q_2}\right) + \left(\frac{q_2-q_{02}}{\Delta q_2}\right)^2\right]\right\}}{2\pi(\Delta q_1)(\Delta q_2)\sqrt{1-\rho^2}}. \quad (1.4)$$

In this formula  $q_{01}$  and  $q_{02}$  are mean values and  $\rho$  is called the correlation coefficient ( $-1 \leq \rho \leq 1$ ). Using this distribution function, the expressions  $\langle q_1 \rangle$ ,  $\langle q_2 \rangle$  and  $\langle q_1 q_2 \rangle$  can be determined. The quantity  $\sigma_{12} = \langle q_1 q_2 \rangle - \langle q_1 \rangle \langle q_2 \rangle$  is called covariance. It turns out that  $\sigma_{12} = \rho(\Delta q_1)(\Delta q_2)$ . The total variance  $\Delta q = \sqrt{(\Delta q_1)^2 + (\Delta q_2)^2 + 2\sigma_{12}}$ . If  $\sigma_{12} = 0$ , the result is the same as in the first example. Two-dimensional Gaussian probability density functions are used in Part IV to describe the influence of space-dependent inhomogeneities of magnetic fields on the coherent superposition of wave functions in spin interferometry.

## 1.2 Expectation Value

Some important results in quantum mechanics are briefly summarized in this section. Because of the importance of the quantum mechanical harmonic oscillator in quantum optics, its basics are introduced, and a formula for expectation values is developed, which represents an analogue to that of the classical mean value of a quantity. In the process, the concept of the density operator is introduced.

### 1.2.1 Quantum Mechanical Harmonic Oscillator

The Schrödinger equation

$$i\hbar \frac{d}{dt} |\psi\rangle = \hat{H} |\psi\rangle \quad (1.5)$$

characterizes the time-dependent evolution of the wave function  $|\psi\rangle$  under the action of the Hamilton operator  $\hat{H}$ . For the one-dimensional quantum mechanical oscillator the Hamiltonian reads as follows

$$\hat{H} = \hat{p}^2/(2M) + U(\hat{x}), \quad (1.6)$$

where the potential

$$U(\hat{x}) = M\Omega^2\hat{x}^2/2 \quad (1.7)$$

is proportional to the square of the position operator  $\hat{x}$ . Here  $\Omega$  is the frequency of a particle of mass  $M$ .  $\hat{p}$  is the momentum operator. Eigenstates of the Hamiltonian are the energy eigenstates  $|m\rangle$ , which belong to the eigenvalues  $E_m$ :

$$\hat{H}|m\rangle = E_m|m\rangle. \quad (1.8)$$

If  $u_m(x) \equiv \langle x|m\rangle$  are the energy eigenfunctions in position representation, this equation can be written as

$$\frac{d^2 u_m(x)}{dx^2} + \frac{2M}{\hbar^2} \left( E_m - \frac{1}{2} M \Omega^2 x^2 \right) u_m(x) = 0. \quad (1.9)$$

The solutions of this equation are known (see, e.g., [1]) as

$$u_m(x) = N_m H_m(\alpha' x) \exp\{-(\alpha' x)^2/2\}, \quad (1.10)$$

where  $N_m = (\alpha'^2/\pi)^{1/4}/\sqrt{2^m m!}$  and  $\alpha' = \sqrt{M\Omega/\hbar}$ .  $H_m(z)$  are Hermite polynomials:  $H_0 = 1$ ,  $H_1 = 2z$ ,  $H_2 = 4z^2 - 2$ , ... . The energy eigenvalues are  $E_m = \hbar\Omega(m + 1/2)$ .

### 1.2.2 Density Operator and Expectation Value

In this section, we introduce the concept of the density operator and use it to construct the expectation value.

The state vector contains the entire information about a quantum system. However, in many cases we do not know every detail of the system because it has too many degrees of freedom. For example, if it is coupled to a reservoir, one cannot predict exactly the movement of the components of the system. An atom that is subjected to spontaneous emission is another example. In these cases, the system cannot be specified entirely by a single state vector. The concept of the density operator is required (see, e.g., [1] or [2]).

$|\langle x|m\rangle|^2 = |u_m(x)|^2$ , the probability density of an energy eigenstate in position representation, describes the probability of a quantum mechanical pure state. However, we want to specify mixed states where a superposition of  $|m\rangle$ -states, namely  $|\psi\rangle = \sum_{m=0}^{\infty} c_m|m\rangle$ , has to be considered.  $c_m$  are complex coefficients depending on the properties of the reservoir, for example.  $P_m = |c_m|^2$  is the probability of the single energy state  $|m\rangle$ . Alternatively,  $c_m$  can

be expressed by  $P_m$  and an arbitrary phase  $\Phi_m$ :  $c_m = \sqrt{P_m} \exp\{\imath\Phi_m\}$ . In this case, the wave function

$$\psi(x) \equiv \langle x|\psi\rangle = \sum_{m=0}^{\infty} c_m u_m(x) \quad (1.11)$$

is a superposition of energy eigenfunctions with probability density

$$|\psi(x)|^2 = \sum_{m,n=0}^{\infty} c_m^* c_n u_m^*(x) u_n(x) = \sum_{m=0}^{\infty} P_m |u_m(x)|^2 + \sum_{m \neq n} c_m^* c_n u_m^*(x) u_n(x). \quad (1.12)$$

The first term specifies the probability of finding a particle that is in the  $m$ -th-energy eigenstate at position  $x$ . In addition, a second term gives rise to interactions between the different wave functions. The major difference between classical and quantum mechanics becomes apparent here and is caused by this second term.

In order to arrive at the concept of the density operator  $\hat{\rho}$ , we rewrite  $|\psi(x)|^2$  as follows:

$$|\psi(x)|^2 = \langle x|\psi\rangle\langle\psi|x\rangle = \langle x|\hat{\rho}|x\rangle, \quad (1.13)$$

where

$$\hat{\rho} = |\psi\rangle\langle\psi| = \sum_{m=0}^{\infty} P_m |m\rangle\langle m| + \sum_{m \neq n} \sqrt{P_m P_n} \exp\{\imath(\Phi_m - \Phi_n)\} |m\rangle\langle n|. \quad (1.14)$$

Since the phases are completely unknown we have to average. Because of  $\int_{-\pi}^{\pi} \exp\{\imath\Phi\} d\Phi = 0$  the density operator finally reads

$$\hat{\rho} = |\psi\rangle\langle\psi| = \sum_{m=0}^{\infty} P_{|\psi_m\rangle} |\psi_m\rangle\langle\psi_m|, \quad (1.15)$$

where we have generalized to an orthogonal and normalized system of wave vectors  $|\psi_m\rangle$  instead of  $|m\rangle$ . The trace of  $\hat{\rho}$  is 1:

$$Tr(\hat{\rho}) = \sum_{m=0}^{\infty} \langle\psi_m|\hat{\rho}|\psi_m\rangle = \sum_{m=0}^{\infty} P_{|\psi_m\rangle} = 1. \quad (1.16)$$

The expectation value  $\langle\hat{O}\rangle$  of an operator  $\hat{O}$  can now be written as  $Tr(\hat{O}\hat{\rho})$ :

$$Tr(\hat{O}\hat{\rho}) = \sum_{l,m=0}^{\infty} \langle\psi_l|\hat{O}|\psi_m\rangle P_{|\psi_m\rangle} \langle\psi_m|\psi_l\rangle = \sum_{m=0}^{\infty} P_{|\psi_m\rangle} \langle\psi_m|\hat{O}|\psi_m\rangle = \langle\hat{O}\rangle. \quad (1.17)$$

We shall see afterwards that the density operator is a very useful concept for phase-space representations of the wave function. Two examples of expectation values are given subsequently.

**Example 1:** The expectation value of  $\hat{\rho}$  is  $\leq 1$ :

$$\langle \hat{\rho} \rangle = Tr(\hat{\rho}^2) = \sum_{l=0}^{\infty} \langle \psi_l | \hat{\rho}^2 | \psi_l \rangle = \sum_{l=0}^{\infty} P_{|\psi_l\rangle}^2 \leq \sum_{l=0}^{\infty} P_{|\psi_l\rangle} = 1. \quad (1.18)$$

**Example 2:** The thermal state (see, e.g., [2, 3])

We denote by  $|\psi_n\rangle \equiv |n\rangle$  the energy eigenstates of the quantum harmonic oscillator (e.g., number states or photons). In a thermal state the probability  $P_n$  of finding a quantum system (e.g., an electromagnetic radiation field) in its  $n$ -th energy state is given by Boltzmann's law  $P_n = N \exp\{-n\beta\}$ , where  $\beta = \hbar\Omega/(k_B T)$ .  $k_B$  is Boltzmann's constant,  $\Omega$  is the frequency of the oscillators,  $T$  is the temperature of the ensemble, and  $N$  is a normalization constant. According to (1.15) the density operator of a thermal state is given by

$$\hat{\rho}_{th} = N \sum_{n=0}^{\infty} \exp\{-n\beta\} |n\rangle \langle n|. \quad (1.19)$$

It can be seen that  $\langle n | \hat{\rho}_{th} | n \rangle = P_n$ .  $N$  can be determined from  $Tr(\hat{\rho}_{th}) = 1$  and is shown to be  $N = 1 - \exp\{-\beta\}$ . The temperature  $T$  is defined via the mean energy  $\langle \hat{H} \rangle$ , where  $\hat{H}$  is the Hamiltonian of the quantum mechanical oscillator. We get

$$\langle \hat{H} \rangle = Tr(\hat{H} \hat{\rho}_{th}) = \hbar\Omega \sum_{n=0}^{\infty} \langle n | (n + 1/2) \hat{\rho}_{th} | n \rangle = \hbar\Omega(n_{th} + 1/2), \quad (1.20)$$

where  $n_{th} = \sum_{n=0}^{\infty} n P_n \equiv \langle n \rangle$  is the mean number of photons in the thermal state. Moreover,

$$\langle n \rangle = N \sum_{n=0}^{\infty} n \exp\{-n\beta\} = -N \frac{\partial}{\partial \beta} \sum_{n=0}^{\infty} \exp\{-n\beta\} = \frac{1}{\exp\{\beta\} - 1}. \quad (1.21)$$

Immediately we have  $\exp\{\beta\} = (\langle n \rangle + 1)/\langle n \rangle$ . The density operator for the thermal state now reads

$$\hat{\rho}_{th} = \frac{1}{\langle n \rangle + 1} \sum_{n=0}^{\infty} \left( \frac{\langle n \rangle}{\langle n \rangle + 1} \right)^n |n\rangle \langle n|. \quad (1.22)$$

Likewise, the energy distribution  $P_n$  can be expressed as a function of  $\langle n \rangle$ :  $P_n = \frac{1}{\langle n \rangle + 1} \left( \frac{\langle n \rangle}{\langle n \rangle + 1} \right)^n$ . Moreover, Planck's law for the black-body spectrum at temperature  $T$  can be expressed as a function of  $\beta$  by the formula

$$\langle W_T(\Omega) \rangle \frac{(\pi\hbar)^2 c^3}{(k_B T)^3} = \beta^3 \langle n \rangle, \quad (1.23)$$

where the radiative energy density  $\langle W_T(\Omega) \rangle$  is the energy per unit volume per unit angular frequency range in the black-body spectrum and its units are  $Jsm^{-3}$ .

## 2 Quantum Mechanical Distribution Functions

It is well-known that quantum states of the electromagnetic field lead to an interesting representation, which is also particularly useful for the treatment of optical coherence. This coherent-state representation leads to a close correspondence between the quantum and classical correlation functions. Coherent states turn out to be particularly appropriate for the description of electromagnetic fields generated by coherent sources like lasers. Coherent states were first discovered in connection with the quantum harmonic oscillator by E. Schrödinger (1926), who referred to them as states of minimum uncertainty product. Their properties were further investigated by J.R. Klauder (1960), who introduced a functional representation of quantum states. Shortly afterwards, R.J. Glauber [4] pointed out that coherent states are particularly important and appropriate for the quantum treatment of optical coherence and their adoption in quantum optics. In the course of the following chapters, it will become apparent that coherence and interference properties are closely connected in the phase-space formulation of quantum mechanics, which has its roots in the classical work of E.P. Wigner (1932). The main tool of that formalism is the introduction of phase-space “quasi-probability” distribution functions, from which the Wigner distribution function is the best known one. Various kinds of phase-space distribution functions (the Wigner function, the P-function, the Q-function) can provide useful physical insights providing practical advantages. A general review, including dynamical features of quantum distribution functions, demonstrates this advantage [5].

In this chapter we shall treat some important quantum mechanical distribution functions. Among them the Wigner function, the Q-function and the P-function are the most relevant. Of particular interest in interferometry is the Wigner function. Due to this fact we, therefore, attach special importance to the Wigner formalism in the following sections.

### 2.1 Wigner Function

As we have seen in (1.13) the probability  $\rho(x)$  of finding a particle at position  $x$  is expressed by the density operator  $\hat{\rho}$  as follows:  $\rho(x) = |\psi(x)|^2 = \langle x|\psi\rangle\langle\psi|x\rangle = \langle x|\hat{\rho}|x\rangle$ . The density matrix  $\rho(x, x') = \langle x|\hat{\rho}|x'\rangle$  of two distinct

positions  $x$  and  $x'$  is the starting point for the definition of the Wigner function. That is to say, the Fourier transformation of  $\rho(x - y/2, x + y/2)$  for displaced position coordinates provides the Wigner function  $W(x, p)$  [5]:

$$W(x, p) = \frac{1}{2\pi\hbar} \int_{-\infty}^{\infty} \left\langle x - \frac{y}{2} | \hat{\rho} | x + \frac{y}{2} \right\rangle \exp\{iyp/\hbar\} dy, \quad (2.1)$$

where  $p = \hbar k$  and  $k$  are the momentum coordinate and the wave number, respectively. The derivation of the Wigner function is carried out below.

### 2.1.1 Wigner Function of a Wave Packet

First of all we write the Wigner function for a pure state  $\hat{\rho} = |\psi\rangle\langle\psi|$ :

$$W(x, p) = \frac{1}{2\pi\hbar} \int_{-\infty}^{\infty} \psi^* \left( x + \frac{y}{2} \right) \psi \left( x - \frac{y}{2} \right) \exp\{iyp/\hbar\} dy. \quad (2.2)$$

As a next step the concept of the wave packet is presented. A Gaussian wave packet

$$\alpha(k) = [2\pi(\delta k)^2]^{-1/4} \exp \left\{ -\frac{(k - k_0)^2}{4(\delta k)^2} \right\} \quad (2.3)$$

describes a wave number distribution with mean wave number  $k_0$  and mean square deviation  $(\delta k)^2$ , where the normalization condition  $\int_{-\infty}^{\infty} \alpha^2(k) dk = 1$  holds. The time-dependent wave function  $\psi(x, t)$  is defined via the Fourier transformation

$$\psi(x, t) = \frac{1}{\sqrt{2\pi}} \int_{-\infty}^{\infty} \alpha(k) \exp\{i(kx - \Omega t)\} dk, \quad (2.4)$$

where the dispersion relation for massive particles of mass  $M$  reads  $\Omega = \hbar k^2/(2M)$ . The calculation yields [1]

$$\psi(x, t) = [2(\delta k)^2/\pi]^{1/4} \frac{1}{\sqrt{1 + i\gamma t}} \exp \left\{ -\frac{[x(\delta k)]^2 - ik_0(x - v_0 t/2)}{1 + i\gamma t} \right\}, \quad (2.5)$$

where  $\gamma = 2\hbar(\delta k)^2/M$  and the mean particle velocity  $v_0 = \hbar k_0/M$ . The squared absolute value specifies the position distribution

$$|\psi(x, t)|^2 = \frac{1}{\sqrt{2\pi}[\Delta x(t)]} \exp \left\{ -\frac{(x - v_0 t)^2}{2[\Delta x(t)]^2} \right\}. \quad (2.6)$$

Because  $\Delta x(t) = \sqrt{1 + (\gamma t)^2}/[2(\delta k)]$  this formula describes the time-broadening of the wave packet in time. In the case of  $t = 0$ , we get the minimum Heisenberg uncertainty relation  $\Delta x(0) \equiv \delta x = 1/[2(\delta k)]$ . In addition we have  $\int_{-\infty}^{\infty} |\psi(x, t)|^2 dx = 1$ .

$\psi(x, t)$  of (2.5) is inserted into (2.2) and we get the Wigner function of a wave packet

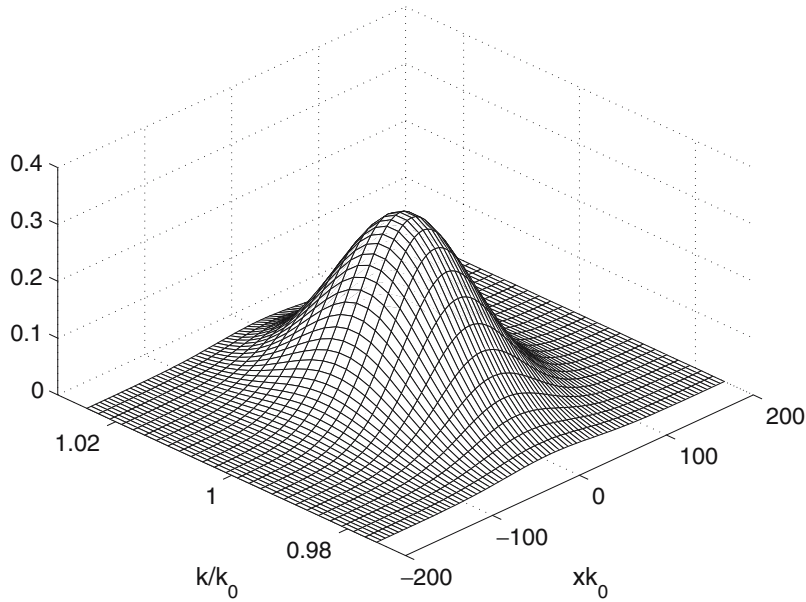


**Fig. 2.1.** Wigner function of a wave packet (2.7),  $\delta k/k_0 = 1\%$

$$W_{WP}(x, k, t) = \frac{1}{\pi} \exp \left\{ -\frac{(k - k_0)^2}{2(\delta k)^2} - 2(\delta k)^2(x - vt)^2 \right\}, \quad (2.7)$$

where  $v = \hbar k/M$  is the particle velocity. This is the two-fold Gaussian function drawn in Fig. 2.1 for  $t = 0$ , where  $\delta k/k_0 = 1\%$ .

### 2.1.2 Properties of the Wigner Function

Some important properties of Wigner functions are derived in order to understand the features of their graphical representations shown throughout the book. In the following, the time-dependence is omitted and the boundaries of the integrals are  $-\infty$  to  $+\infty$ . Likewise, we derive these properties using the pure quantum state for the density operator  $\hat{\rho}$ . In the case of mixed states, only a summation over the corresponding probability has to be carried out. It is anticipated that the Wigner function is a real function.

$$1. \quad \int W(x, p) dp = |\psi(x)|^2 \quad (2.8)$$

*Proof:*  $\int W(x, p) dp = [1/(\pi\hbar)] \iint \langle x-y|\hat{\rho}|x+y \rangle \exp\{2ipy/\hbar\} dy dp = \int \langle x-y|\hat{\rho}|x+y \rangle \delta(y) dy = \langle x|\hat{\rho}|x \rangle = |\psi(x)|^2 \square$

$$2. \quad \int W(x, p) dx = |\varphi(p)|^2 \quad (2.9)$$

*Proof:*  $\int W(x, p)dx = [1/(\pi\hbar)] \int \exp\{2ipy/\hbar\} [\int \langle x - y | \hat{\rho} | x + y \rangle dx] dy$

$$= [1/(\pi\hbar)] \int \exp\{2ipy/\hbar\} [\int \langle x' | \hat{\rho} | x' + 2y \rangle dx'] dy$$

$$= [1/(2\pi\hbar)] \int \int \exp\{\imath p(x'' - x')/\hbar\} [\langle x' | \hat{\rho} | x'' \rangle dx'] dx''$$

$$= [1/\sqrt{2\pi\hbar}] \int \exp\{-\imath px'/\hbar\} \langle x' | dx' \hat{\rho} [1/\sqrt{2\pi\hbar}] \int \exp\{\imath px''/\hbar\} |x''\rangle dx''$$

$$= \langle p | \hat{\rho} | p \rangle = |\varphi(p)|^2, \text{ where we have used the Fourier transform}$$

$$[1/\sqrt{2\pi\hbar}] \int \exp\{\imath px/\hbar\} |x\rangle dx = |p\rangle \text{ and } \varphi(p) = \langle p | \psi \rangle \quad \square$$

$$3. \quad \int \int W(x, p) dx dp = 1 \quad (2.10)$$

$$4. \quad W(x, p) = \frac{1}{2\pi\hbar} \int \varphi^*(p + p'/2) \varphi(p - p'/2) \exp\{-\imath xp'/\hbar\} dp' \quad (2.11)$$

*Proof:* In the following derivation the Fourier transforms

$$\varphi(p) = [1/\sqrt{2\pi\hbar}] \int \psi(x) \exp\{-\imath px/\hbar\} dx \text{ and}$$

$$\psi(x) = [1/\sqrt{2\pi\hbar}] \int \varphi(p) \exp\{\imath px/\hbar\} dp \text{ are applied:}$$

$$\begin{aligned} W(x, p) &= [1/(\pi\hbar)] \int \exp\{2ipy/\hbar\} dy [1/(2\pi\hbar)] \\ &\times \int \varphi^*(p') \exp\{-\imath p'(x + y)/\hbar\} dp' \int \varphi(p'') \exp\{\imath p''(x - y)/\hbar\} dp'' \\ &= [1/(\pi\hbar 2\pi\hbar)] \int \varphi^*(p') \exp\{-\imath p'x/\hbar\} dp' \\ &\times \int \varphi(p'') \exp\{\imath p''x/\hbar\} dp'' 2\pi\hbar \delta(2p - p' - p'') \\ &= [1/(\pi\hbar)] \int \varphi^*(p') \exp\{-\imath p'x/\hbar\} dp' \varphi(2p - p') \exp\{\imath x(2p - p')/\hbar\} \\ &= [1/(\pi\hbar)] \int \varphi^*(p + p') \varphi(p - p') \exp\{-2\imath xp'/\hbar\} dp' \quad \square \end{aligned}$$

Equation (2.11) is very valuable, because it is often much easier to calculate the Wigner function using  $\varphi(p)$  instead of (2.2) applying  $\psi(x)$ .

$$5. \quad 2\pi\hbar \int \int W_{\psi_1}(x, p) W_{\psi_2}(x, p) dx dp = \left| \int \psi_1^*(q) \psi_2(q) dq \right|^2 \geq 0 \quad (2.12)$$

$$\begin{aligned} \text{Proof: } &2\pi\hbar \int \int \{ [1/(\pi\hbar)] \int dy \psi_1^*(x + y) \psi_1(x - y) \exp\{2ipy/\hbar\} \} \\ &\times \{ [1/(\pi\hbar)] \int dz \psi_2^*(x + z) \psi_2(x - z) \exp\{2ipz/\hbar\} \} dx dp \\ &= 2\pi\hbar \int [1/(\pi\hbar)^2] \int dy \psi_1^*(x + y) \psi_1(x - y) \int dz \psi_2^*(x + z) \psi_2(x - z) \pi\hbar \delta(y + z) dx \\ &= -2 \int \int \psi_1^*(x + y) \psi_1(x - y) \psi_2^*(x - y) \psi_2(x + y) dx dy \\ &= \int \psi_1^*(u) \psi_2(u) du \int \psi_1(v) \psi_2^*(v) dv = \left| \int \psi_1^*(u) \psi_2(u) du \right|^2 \quad \square \end{aligned}$$

For  $\psi_1(q) = \psi_2(q)$  the right-hand side of (2.12) is 1.

One important implication can be drawn from (2.12): the right-hand side is  $\geq 0$ . However, the two functions  $\psi_1(q)$  and  $\psi_2(q)$  can be orthogonal. This means that the equal sign is valid, which implies that the Wigner function cannot be positive everywhere. This is an important distinction to classical distribution functions, which are  $\geq 0$  everywhere.

### 2.1.3 Derivation of the Wigner Function

If the Wigner function is the desired quantum mechanical distribution function, the expectation value of an operator  $\hat{A}$  can be expressed with it:

$$\langle \hat{A} \rangle = \langle \psi | \hat{A} | \psi \rangle = \text{Tr}[\hat{\rho} \hat{A}] = \iint A(x, p) W(x, p) dx dp, \quad (2.13)$$

which is the quantum mechanical equivalent to the classical expression (1.3) in two dimensions.

*Proof:* It is assumed that a Fourier transform  $\alpha(\sigma, \tau)$  of  $A(x, p)$ , namely  $A(x, p) = \iint \alpha(\sigma, \tau) \exp\{\imath(\sigma x + \tau p)/\hbar\} d\sigma d\tau$ , exists. Moreover, an operator  $\hat{A}(\hat{x}, \hat{p})$  is associated to the Fourier transform via the expression  $\hat{A}(\hat{x}, \hat{p}) = \iint \alpha(\sigma, \tau) \exp\{\imath(\sigma \hat{x} + \tau \hat{p})/\hbar\} d\sigma d\tau$ . The expectation value of  $\hat{A}$  is thus

$$\langle \hat{A} \rangle = \langle \psi | \hat{A} | \psi \rangle = \iint \alpha(\sigma, \tau) \langle \psi | \exp\{\imath(\sigma \hat{x} + \tau \hat{p})/\hbar\} | \psi \rangle d\sigma d\tau. \quad (2.14)$$

If the matrix element

$$\langle \psi | \exp\{\imath(\sigma \hat{x} + \tau \hat{p})/\hbar\} | \psi \rangle = \iint W(x, p) \exp\{\imath(\sigma x + \tau p)/\hbar\} dx dp = C(\sigma, \tau) \quad (2.15)$$

is the Fourier transform of the Wigner function, where  $C(\sigma, \tau)$  is the characteristic function (or Weyl function), then  $\langle \hat{A} \rangle$  is exactly (2.13). So (2.15) has to be proved. Consider the following: the right-hand side gives

$$\begin{aligned} & C(\sigma, \tau) \\ &= \frac{1}{2\pi\hbar} \iiint \psi^* \left( x + \frac{y}{2} \right) \psi \left( x - \frac{y}{2} \right) \exp\{\imath p(y + \tau)/\hbar\} \exp\{\imath \sigma x/\hbar\} dy dx dp \\ &= \iint \psi^* \left( x + \frac{y}{2} \right) \psi \left( x - \frac{y}{2} \right) \exp\{\imath \sigma x/\hbar\} \delta(y + \tau) dy dx \\ &= \int \psi^* \left( x - \frac{\tau}{2} \right) \psi \left( x + \frac{\tau}{2} \right) \exp\{\imath \sigma x/\hbar\} dx. \end{aligned}$$

In order to calculate the left-hand side of (2.15), the matrix has to be determined using the Baker–Campbell–Hausdorff theorem (see, e.g., [2]):

$\exp\{\hat{A} + \hat{B}\} = \exp\{\hat{A}\} \exp\{\hat{B}\} \exp\{-[\hat{A}, \hat{B}]/2\}$ . Due to Heisenberg's uncertainty relation  $[\hat{x}, \hat{p}] = i\hbar$ , the matrix element reads

$$\begin{aligned} \langle \psi | \exp\{i(\sigma\hat{x} + \tau\hat{p})/\hbar\} | \psi \rangle &= \exp\{i\sigma\tau/(2\hbar)\} \langle \psi | \exp\{i\sigma\hat{x}/\hbar\} \exp\{i\tau\hat{p}/\hbar\} | \psi \rangle \\ &= \int dx \exp\{i\sigma\tau/(2\hbar)\} \langle \psi | \exp\{i\sigma\hat{x}/\hbar\} | x \rangle \langle x | \exp\{i\tau\hat{p}/\hbar\} | \psi \rangle \\ &= \int dx \exp\{i\sigma\tau/(2\hbar)\} \langle \psi | \exp\{i\sigma x/\hbar\} | x \rangle \langle x + \tau | | \psi \rangle \\ &= \int dx \exp\{i(\sigma x + \sigma\tau/2)/\hbar\} \psi^*(x) \psi(x + \tau) \\ &= \int dx' \exp\{i\sigma x'/\hbar\} \psi^*(x' - \tau/2) \psi(x' + \tau/2) = C(\sigma, \tau), \end{aligned}$$

where the translation operation  $\exp\{-i\tau\hat{p}/\hbar\}|x\rangle = |x + \tau\rangle$  has been used. The matrix element is exactly the characteristic function. Thus (2.15) has been proved. Inserting (2.15) into (2.14), we get

$$\begin{aligned} \langle \hat{A} \rangle &= \iint \alpha(\sigma, \tau) \iint W(x, p) \exp\{i(\sigma x + \tau p)/\hbar\} dx dp d\sigma d\tau \\ &= \iint W(x, p) \iint \alpha(\sigma, \tau) \exp\{i(\sigma x + \tau p)/\hbar\} d\sigma d\tau dx dp \\ &= \iint A(x, p) W(x, p) dx dp \quad \square \end{aligned}$$

#### 2.1.4 Wigner Function of the Harmonic Oscillator

The wave functions  $u_n(x)$  of (1.10) for the quantum mechanical harmonic oscillator (QMHO) are inserted according to (2.2) in order to construct the Wigner distribution  $W_{HO}(x, p, n)$ . We obtain (see, e.g., [2, p.105])

$$\begin{aligned} W_{HO}(x, p, n) &= \frac{1}{\pi\hbar} \int u_n^*(x + y) u_n(x - y) \exp\{2ipy/\hbar\} dy \\ &= \frac{1}{\pi\hbar} \frac{\alpha'}{2^n n! \sqrt{n}} \exp\{-(\alpha' x)^2\} \int e^{2ipy/\hbar - (\alpha' y)^2} \\ &\quad \times H_n[\alpha'(x + y)] H_n[\alpha'(x - y)] dy. \end{aligned}$$

We introduce a new quantity  $z = \alpha'y - \beta'$ , where  $\alpha' = \sqrt{M\Omega/\hbar}$  and  $\beta' = ip/(\alpha'\hbar)$ . The associated integral becomes  $\int \exp\{-z^2\} H_n(z + \beta' + \alpha'x) H_n(z + \beta' - \alpha'x) dz = 2^n n! \sqrt{n} L_n[2(\alpha'^2 x^2 - \beta'^2)]$ .  $L_n(x)$  are Laguerre polynomials. Finally, we get

$$\pi W_{HO}(x, k, n) = (-1)^n \exp\{-2h(x, k)\} L_n[4h(x, k)], \quad (2.16)$$

where the Hamiltonian

$$h(x, k) = \frac{1}{\hbar\Omega} \left[ \frac{p^2}{2M} + \frac{1}{2} M\Omega^2 x^2 \right] = \frac{1}{2} \left( \frac{k^2}{\alpha'^2} + x^2 \alpha'^2 \right) \quad (2.17)$$

is defined and the wave number  $k = p/\hbar$  is introduced. The Laguerre polynomials are:  $L_0(x) = 1$ ,  $L_1(x) = 1 - x$ ,  $L_2(x) = 1 - 2x + x^2/2$ ,  $L_3(x) = 1 - 3x + 3x^2/2 - x^3/6$ ,.... The Wigner functions of (2.16) for  $n = 0, 1, 2, 3$  and  $\alpha' = 1$  are shown in Figs. 2.2 to 2.5. The related states are called Fock states. For higher orders, the negative parts of the Wigner function are clearly seen.

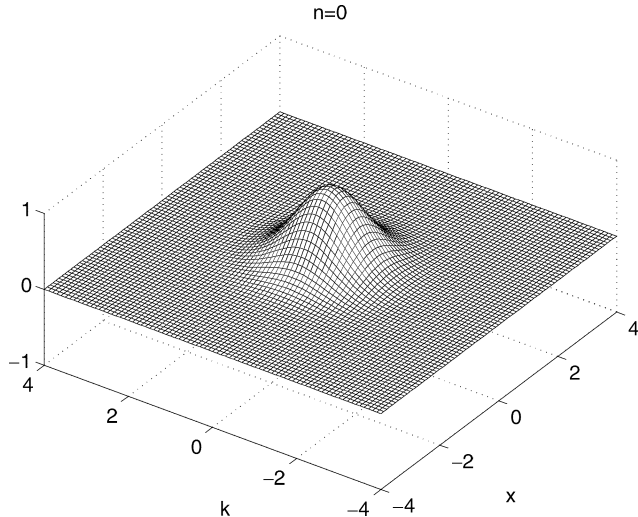


**Fig. 2.2.** Wigner function of QMHO (2.16): ground state  $n = 0$  ( $\alpha' = 1$ )

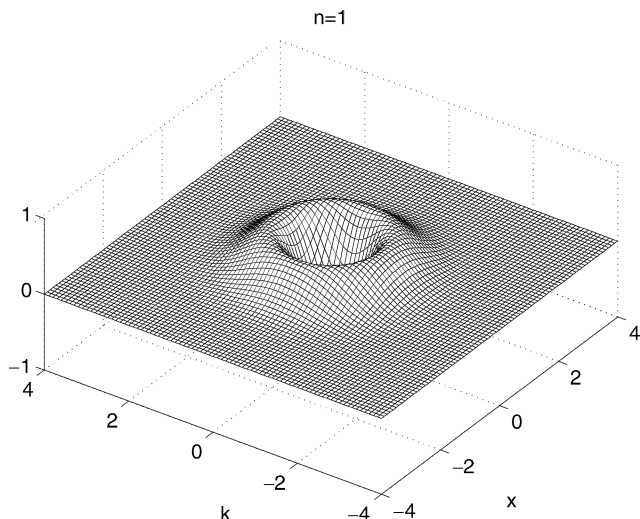


**Fig. 2.3.** Wigner function of QMHO: first state  $n = 1$

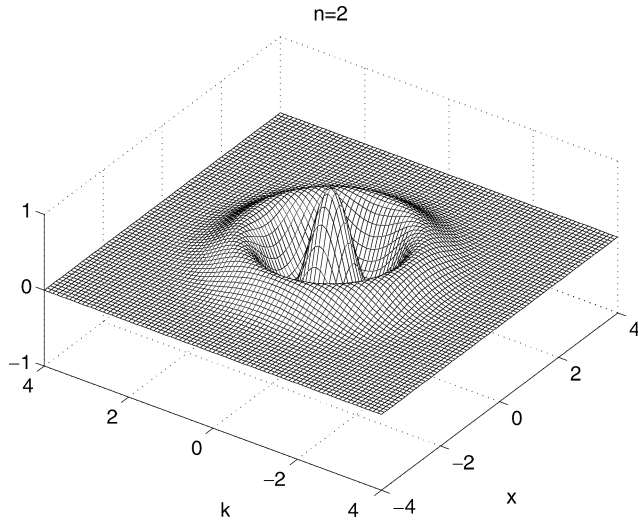


**Fig. 2.4.** Wigner function of QMHO: second state  $n = 2$

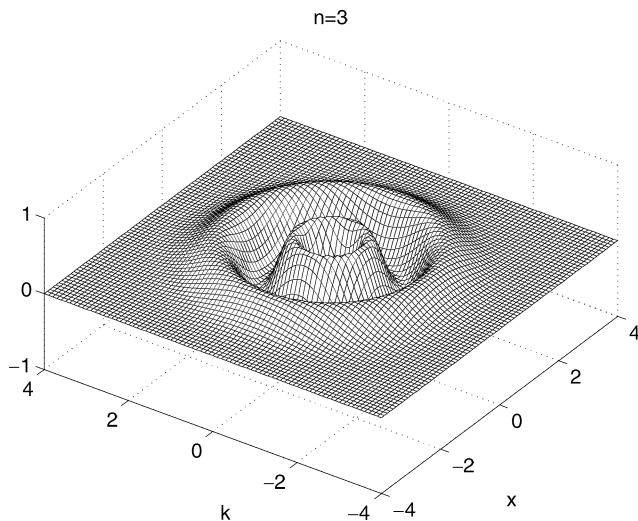


**Fig. 2.5.** Wigner function of QMHO: third state  $n = 3$

## 2.2 Q-Function

A general distribution function  $P_g(x, p)$  evolves from smearing (by convolution) the Wigner function using a function  $g(x - x', p - p')$ :  $P_g(x, p) = \iint g(x - x', p - p')W(x', p')dx'dp'$ . The Q-function  $Q(x, p)$  (or Husimi

function) applies a Gaussian distribution

$$G(x - x', p - p', \gamma) = \frac{1}{\pi \hbar} \exp \left\{ -\frac{(x - x')^2}{\gamma} - \frac{\gamma(p - p')^2}{\hbar^2} \right\}, \quad (2.18)$$

such that

$$Q(x, p) = \iint G(x - x', p - p', \gamma) W(x', p') dx' dp'. \quad (2.19)$$

According to property 5 of Sect. 2.1.2, the Q-function is always positive because the Gaussian distribution function of two variables can be considered as a special Wigner function. For example, the Wigner function of the ground state of the QMHO (see (2.16)), that is to say  $\pi W_{HO}(x, k, n = 0) = \exp\{-2h(x, k)\}$ , is a double Gaussian function in  $x$  and  $k$ . If we put  $\alpha'^2 = 1/\gamma$ , the relation  $W_{HO}(x - x', k - k', n = 0) = G(x - x', k - k', \gamma)$  is valid. We shall see below that the mean square deviation of the QMHO-Q-function of the ground state is twice as large as for the Wigner distribution. So  $\pi Q_{HO}(x, k, n = 0) = \exp\{-h(x, k)\}$ . This can also be directly verified by insertion in (2.19).

## 2.3 A Systematic Approach of Quasi-Distribution Functions

In the following, we shall introduce two new operators: the creation operator  $\hat{a}^+$  and the annihilation operator  $\hat{a}$ . The application of these operators has been a very successful concept in the quantum theory of the electromagnetic field. Thereby the QMHO is described by  $\hat{a}^+$  and  $\hat{a}$  (see, e.g., [1]). On the other hand, the formalism of creation and annihilation operators provides the possibility for a systematic approach in order to develop the theory of quantum mechanical distribution functions (also called quasi-distribution functions). The Wigner function and the Q-function are examples of the quasi-distributions discussed above. Hence, we make use of these two operators in the following.

We start with the Hamiltonian of the QMHO (1.6):

$$\hat{H} = \frac{\hat{p}^2}{2M} + \frac{M\Omega^2 \hat{x}^2}{2} = \hbar\Omega \left[ \frac{\hat{p}^2}{2\hbar\lambda^2} + \frac{\lambda^2 \hat{x}^2}{2\hbar} \right], \quad (2.20)$$

where  $\lambda = \sqrt{M\Omega}$  ( $= \sqrt{\hbar}\alpha'$  as before). If we define  $\hat{a}^+$  and  $\hat{a}$  as

$$\hat{a}^+ = \frac{1}{\sqrt{2\hbar}} \left( \lambda \hat{x} - \frac{i}{\lambda} \hat{p} \right), \quad \hat{a} = \frac{1}{\sqrt{2\hbar}} \left( \lambda \hat{x} + \frac{i}{\lambda} \hat{p} \right), \quad (2.21)$$

the Hamiltonian can be written as

$$\hat{H} = \frac{\hbar\Omega}{2} (\hat{a}\hat{a}^+ + \hat{a}^+\hat{a}) = \hbar\Omega \left( \hat{N} + \frac{1}{2}\hat{I} \right), \quad (2.22)$$

where  $\hat{N} = \hat{a}^\dagger \hat{a}$  is called the number operator. In (2.22) Heisenberg's uncertainty relation  $[\hat{x}, \hat{p}] = i\hbar \hat{I}$  or  $[\hat{a}, \hat{a}^\dagger] = \hat{I}$  has been used. Now the energy eigenvalues of  $\hat{H}$  are  $E_n = \hbar\Omega(n + 1/2)$ . Hence  $\hat{N}$  has eigenvalues  $n = 0, 1, 2, \dots$ . The corresponding eigenvalue equation reads as follows:

$$\hat{N}|n\rangle = n|n\rangle, \quad (2.23)$$

where  $|n\rangle$  are the normalized basis vectors (likewise called Fock states, or number states or energy states of the QMHO). The following properties of Fock states are very important:

$$\hat{a}^+|n\rangle = \sqrt{n+1}|n+1\rangle, \quad \hat{a}|n\rangle = \sqrt{n}|n-1\rangle, \quad \langle n|m\rangle = \delta_{nm}. \quad (2.24)$$

Some other relations are frequently used below:

$$\hat{a}|0\rangle = 0, \quad \sum_n |n\rangle \langle n| = \hat{I}, \quad [\hat{a}, (\hat{a}^\dagger)^n] = n(\hat{a}^\dagger)^{n-1}, \quad (2.25)$$

where  $|0\rangle$  is called vacuum state of the QMHO where no photons exist. There are no fluctuations for any single photon state  $|n\rangle$ , because  $\langle n|(\Delta \hat{N})^2|n\rangle = \langle n|(\hat{N})^2|n\rangle - (\langle n|\hat{N}|n\rangle)^2 = n^2 - n^2 = 0$ . This is not the case with the coherent states discussed subsequently.

### 2.3.1 Coherent States

In this context the characteristic operator

$$\hat{C}(\sigma, \tau) = \exp\{\imath(\sigma \hat{x} + \tau \hat{p})/\hbar\} \quad (2.26)$$

in (2.15) plays an important role. The quantities  $\sigma$  and  $\tau$  are real. We define a complex value  $\alpha$  in such a way that  $\sigma = -\imath\lambda\sqrt{\hbar/2}(\alpha - \alpha^*)$  and  $\tau = -(1/\lambda)\sqrt{\hbar/2}(\alpha + \alpha^*)$ . Using (2.21) the characteristic operator  $\hat{C}(\sigma, \tau)$  can then be transformed to the displacement operator  $\hat{D}(\alpha)$  and we get the result:

$$\hat{C}(\sigma, \tau) \equiv \exp\{\alpha \hat{a}^\dagger - \alpha^* \hat{a}\} = \hat{D}(\alpha). \quad (2.27)$$

The properties of  $\hat{D}(\alpha)$  are described in the following lines. Using the Baker–Campbell–Hausdorff theorem we get the relations below: [4–10]

$$\begin{aligned} \hat{D}(\alpha) &= e^{-|\alpha|^2/2} e^{\alpha \hat{a}^\dagger} e^{-\alpha^* \hat{a}} = e^{|\alpha|^2/2} e^{-\alpha^* \hat{a}} e^{\alpha \hat{a}^\dagger}, \\ \hat{D}(\alpha) &= \hat{D}(-\alpha)^{-1}, \quad \hat{D}(\alpha)^+ = \hat{D}(-\alpha) = \hat{D}(\alpha)^{-1}, \quad \hat{D}(\alpha)^+ \hat{D}(\alpha) = \hat{I}. \end{aligned} \quad (2.28)$$

It is interesting to note that  $\hat{D}(\alpha) \neq \hat{D}(\alpha)^+$ .  $\hat{D}(\alpha)$  is not Hermitian. After some algebra we get

$$\frac{\partial}{\partial \alpha^*} \hat{D}(\alpha) = \hat{D}(\alpha) \left[ -\frac{\alpha}{2} - \hat{a} \right], \quad \hat{D}(\alpha) \left[ \frac{\alpha}{2} + \hat{a} \right] = \left[ \hat{a} - \frac{\alpha}{2} \right] \hat{D}(\alpha)$$

and the following operator equations:

$$\hat{D}(\alpha)^{-1}\hat{a}\hat{D}(\alpha) = \hat{a} + \alpha, \quad \hat{D}(\alpha)^{-1}\hat{a}^+\hat{D}(\alpha) = \hat{a}^+ + \alpha^*. \quad (2.29)$$

Because of these two transformation properties  $\hat{D}(\alpha)$  is called a displacement operator. The eigenstates of  $\hat{a}$  are called coherent states  $|\alpha\rangle$ . In order to identify these states we apply  $\hat{D}(\alpha)$  on the vacuum state  $|0\rangle$ :

$$\begin{aligned} |\alpha\rangle &= \hat{D}(\alpha)|0\rangle = e^{-|\alpha|^2/2}e^{\alpha\hat{a}^+}|0\rangle = e^{-|\alpha|^2/2}\sum_{n=0}^{\infty}\frac{\alpha^n}{n!}(\hat{a}^+)^n|0\rangle \\ &= e^{-|\alpha|^2/2}\sum_{n=0}^{\infty}\frac{\alpha^n}{\sqrt{n!}}|n\rangle, \end{aligned} \quad (2.30)$$

where (2.25) has been used. Furthermore, it is easy to show that the equations  $\hat{a}|\alpha\rangle = \alpha|\alpha\rangle$  and  $\langle\alpha|\hat{a}^+ = \langle\alpha|\alpha^*$  are satisfied. The normalization of the coherent states yields

$$\langle\alpha|\alpha\rangle = \sum_{n=0}^{\infty}|\langle n|\alpha\rangle|^2 = \sum_{n=0}^{\infty}e^{-|\alpha|^2}\frac{|\alpha|^{2n}}{n!} = \sum_{n=0}^{\infty}P_n = 1. \quad (2.31)$$

The photons in a coherent state are distributed according to a Poissonian distribution  $P_n = \exp\{-|\alpha|^2\}|\alpha|^{2n}/(n!)$ . The expectation value of photons (the mean photon number) in a coherent state is

$$\begin{aligned} \langle n \rangle &= \langle\alpha|n|\alpha\rangle = \sum_{n=0}^{\infty}nP_n = \sum_{n=1}^{\infty}e^{-|\alpha|^2}\frac{|\alpha|^{2n}}{(n-1)!} \\ &= \sum_{n=0}^{\infty}e^{-|\alpha|^2}\frac{|\alpha|^{2(n+1)}}{(n)!} = |\alpha|^2. \end{aligned} \quad (2.32)$$

In an analogous manner we can calculate  $\langle n^2 \rangle = |\alpha|^4 + |\alpha|^2$ . The mean square deviation  $\sigma_n = \langle n^2 \rangle - \langle n \rangle^2 = |\alpha|^2 = \langle n \rangle$ . This is characteristic for a Poissonian distribution. In Fig. 2.6  $P_n$  is drawn for  $\langle n \rangle = 3$ . For  $\alpha = 0 \rightarrow P_0 = 1$ . In the limit of large  $\alpha$ , the Poissonian distribution passes into a Gaussian distribution:

$$\lim_{\alpha \rightarrow \infty} P_n = \frac{1}{\sqrt{2\pi}\alpha} \exp\left\{-\frac{n+1/2-\alpha^2}{2\alpha^2}\right\}. \quad (2.33)$$

Using the definition of the coherent states (2.30) it can easily be shown that two different coherent states  $|\alpha\rangle$  and  $|\beta\rangle$  are not orthogonal:  $\langle\beta|\alpha\rangle = \exp\{-|\alpha|^2/2 - |\beta|^2/2 + \alpha\beta^*\}$ . Moreover,  $|\langle\beta|\alpha\rangle|^2 = \exp\{-|\alpha - \beta|^2\}$ . Only for highly distinguishable states, that is to say if  $|\alpha - \beta| \gg 1$ , is the product nearly orthogonal:  $\langle\beta|\alpha\rangle \simeq 0$ . One important property of coherent states should be mentioned yet:

$$\hat{I} = \frac{1}{\pi} \int |\alpha\rangle\langle\alpha|d^2\alpha, \quad (2.34)$$

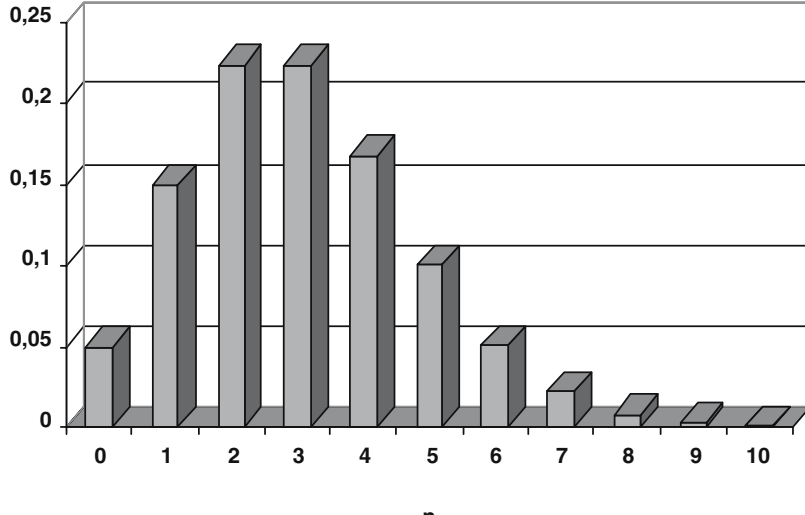


Fig. 2.6. Poissonian distribution  $P_n = e^{-|\alpha|^2} \frac{|\alpha|^{2n}}{n!}$  for  $\langle n \rangle = |\alpha|^2 = 3$

where  $d^2\alpha = d(\Re\alpha)d(\Im\alpha) = |\alpha|d|\alpha|d\theta$ . Coherent states are complete. That means that a trace of an operator can be written as the trace over coherent states:  $Tr(\hat{A}) = (1/\pi) \int \langle \alpha | \hat{A} | \alpha \rangle d^2\alpha$ . In the following two examples, the position wave functions of coherent states are determined.

**Example 1:** We would like to calculate the position wave function of the coherent state for  $\alpha = 0$ . Equations (2.25) and (2.21) yield

$$\langle x | \hat{a} | 0 \rangle = 0 = \langle x | \frac{1}{\sqrt{2\pi}} \left[ \lambda \hat{x} + \frac{i}{\lambda} \hat{p} \right] | 0 \rangle = \frac{1}{\sqrt{2\pi}} \left[ \lambda x + \frac{\hbar}{\lambda} \frac{\partial}{\partial x} \right] \psi_0(x), \quad (2.35)$$

where the wave function  $\psi_0(x) = \langle x | 0 \rangle$  has been defined. We get the differential equation and the appropriate solution:

$$\frac{1}{\psi_0(x)} \frac{\partial}{\partial x} \psi_0(x) = -\frac{\lambda^2}{\hbar} x \longrightarrow \psi_0(x) = \left[ \frac{\lambda^2}{\pi \hbar} \right]^{1/4} \exp \left\{ - \left[ \frac{\lambda x}{\sqrt{2\hbar}} \right]^2 \right\}. \quad (2.36)$$

The position distribution reads

$$\psi_0^2(x) = \frac{1}{\sqrt{2\pi}(\delta x)} \exp \left\{ -\frac{x^2}{2(\delta x)^2} \right\}, \quad (2.37)$$

where  $(\delta x)^2 = \hbar/(2\lambda^2)$  is the mean square deviation of the Gaussian distribution. Because  $\lambda = \sqrt{\hbar}\alpha' = \sqrt{M\Omega}$ , this equation is in agreement with the eigenfunctions in position representation  $u_0^2(x)$  of the QMHO of the ground

state (see (1.10)). The related Wigner function has been discussed in Fig. 2.2. Because of Heisenberg's minimum uncertainty relation  $(\delta p)(\delta x) = \hbar/2$ , we achieve  $(\delta p) = \lambda^2(\delta x)$ .

We can calculate the Wigner function  $W_{\alpha=0}(x, k)$  using the wave function  $\psi_0(x)$  (2.36):

$$W_{\alpha=0}(x, k) = \frac{1}{2\pi} \int \psi_0 \left( x - \frac{y}{2} \right) \psi_0^* \left( x + \frac{y}{2} \right) e^{iky} dy = \frac{1}{\pi} e^{-\alpha'^2 x^2 - k^2/\alpha'^2}.$$

If this result is compared to (2.16), the following relation can be written instantaneously:

$$W_{\alpha=0}(x, k) = W_{HO}(x, k, n = 0).$$

In other words, the Wigner function of the coherent state for  $\alpha = 0$  is identical to the Wigner function of the ground state of the quantum mechanical harmonic oscillator. A coherent state  $|\alpha\rangle$  is the closest analogue to a classical light field and exhibits a Poisson photon number distribution with an average photon number  $|\alpha|^2$ . Coherent states have minimal fluctuations permitted by the Heisenberg uncertainty principle. On the contrary, a Fock state  $|n\rangle$  is strictly quantum mechanical and contains a precisely defined number  $n$  of quanta of field excitation. Coherent states and Fock states meet exactly at  $\alpha = 0$  and  $n = 0$ , respectively. The transition from quantum to classical states has been studied using single-photon-added coherent states of light [11].

**Example 2:** The position wave function of the coherent state for  $\alpha \neq 0$  is determined from the eigenvalue equation  $\hat{a}|\alpha\rangle = \alpha|\alpha\rangle$ :

$$\langle x|\hat{a}|\alpha\rangle = \left\langle x \left| \frac{1}{\sqrt{2\hbar}} \left[ \lambda \hat{x} + \frac{i}{\lambda} \hat{p} \right] \right| \alpha \right\rangle = \alpha \langle x|\alpha\rangle. \quad (2.38)$$

The wave function is denoted by  $\psi_\alpha(x) = \langle x|\alpha\rangle$ . The result is:

$$\psi_\alpha(x) = \left[ \frac{\lambda^2}{\pi\hbar} \right]^{1/4} \exp \left\{ - \left[ \frac{\lambda x}{\sqrt{2\hbar}} - \alpha \right]^2 \right\}. \quad (2.39)$$

This is a similar Gaussian function to that in (2.36) but displaced by  $\alpha$ . The position distribution reads

$$\psi_\alpha^2(x) = \frac{1}{\sqrt{2\pi}(\delta x)} \exp \left\{ - \frac{[x - 2(\delta x)\alpha]^2}{2(\delta x)^2} \right\}. \quad (2.40)$$

Because of the constant displacement of  $x$  by  $2(\delta x)\alpha$  and the same mean square deviation  $(\delta x)^2$ , the coherent states  $\psi_\alpha(x)$  are only shifted Gaussian functions of the distribution function  $\psi_0(x)$  of the QMHO ground state. The Wigner function of  $\psi_\alpha(x)$  looks like that in Fig. 2.2, only the coordinate

system has been shifted by a corresponding  $\alpha$ -value. Furthermore, the Poissonian distribution  $P_n$  can be expressed by  $\psi_\alpha(x)$ :

$$P_n = |\langle n|\alpha \rangle|^2 = \left| \left\langle n \left| \left( \int |x\rangle dx \langle x| \right) |\alpha \right\rangle \right|^2 = \left| \int u_n(x) \psi_\alpha(x) dx \right|^2. \quad (2.41)$$

In the following sections we shall concentrate on three important arrangements of the operators  $\hat{a}$  and  $\hat{a}^+$ :

1. The normal ordering  $(\hat{a}^+)^m \hat{a}^n$ , which entails the P-function.
2. The symmetric ordering  $\{\hat{a}^+ \hat{a}\} \equiv (\hat{a}^+ \hat{a} + \hat{a} \hat{a}^+)/2$  or  $\{\hat{a}^+ \hat{a}^2\} \equiv (\hat{a}^+ \hat{a}^2 + \hat{a} \hat{a}^+ \hat{a} + \hat{a}^2 \hat{a}^+)/3$ , etc., which gives the Wigner function.
3. The anti-normal ordering  $\hat{a}^m (\hat{a}^+)^n$ , which gives rise to the Q-function.

### 2.3.2 Normal Ordering of Operators (P-Function)

When we are dealing with the normal operator ordering, the creation operator  $\hat{a}^+$  has to be arranged to left of the annihilation operator  $\hat{a}$  in an operator product. Therefore, we write for an operator  $\hat{A}$ :

$$\hat{A} = \sum_{m,n=0}^{\infty} c_{m,n} (\hat{a}^+)^m \hat{a}^n. \quad (2.42)$$

Now the P-function  $P(\alpha)$  is introduced according to the density operator concept in (1.15) using the completeness of the coherent states  $|\alpha\rangle$ :

$$\hat{\rho} = \int P(\alpha) |\alpha\rangle \langle \alpha| d^2\alpha, \quad (2.43)$$

where the normalization condition  $Tr(\hat{\rho}) = \int P(\alpha) d^2\alpha = 1$  is fulfilled. Interestingly, besides a Gaussian function, a Delta-function is also able to meet this condition.

As a special case for normal operator ordering  $\hat{A}_N$ , we now consider the expression

$$\hat{A}_N = \exp\{\xi \hat{a}^+\} \exp\{-\xi^* \hat{a}\}. \quad (2.44)$$

The expectation value  $\langle \hat{A}_N \rangle$  can be written as a Fourier integral

$$\langle \hat{A}_N \rangle = Tr[\hat{\rho} \hat{A}_N] = \int P(\alpha) \langle \alpha | \hat{A}_N | \alpha \rangle d^2\alpha = \int P(\alpha) e^{\xi \alpha^* - \xi^* \alpha} d^2\alpha = \chi_N(\xi), \quad (2.45)$$

where  $\chi_N(\xi)$  is the characteristic function of normal ordered operators  $\hat{A}_N$ . The P-function can be expressed by the inverse Fourier transformation (note that  $\xi \alpha^* - \xi^* \alpha$  is purely imaginary):

$$P(\alpha) = \frac{1}{\pi^2} \int \chi_N(\xi) e^{\xi^* \alpha - \xi \alpha^*} d^2\xi. \quad (2.46)$$

We can evaluate  $|\chi_N(\xi)|$  using the Baker–Campbell–Hausdorff theorem:

$$|\chi_N(\xi)| = e^{|\xi|^2/2} |Tr[\hat{\rho}e^{\xi\hat{a}^+ - \xi^*\hat{a}}]| \leq e^{|\xi|^2/2}. \quad (2.47)$$

If  $|\xi| \rightarrow \infty$ , the P-function is singular.

A simple example is the number operator  $\hat{N} = \hat{a}^+\hat{a}$ . The expectation value yields the mean photon number according to (2.32) and the result is  $\langle \hat{N} \rangle = Tr[\hat{\rho}\hat{N}] = \int P(\alpha')|\alpha'|^2 d^2\alpha' = |\alpha|^2 \equiv \langle n \rangle$ , where we conclude that the P-function has to be  $P(\alpha) = \delta^2(\alpha - \alpha')$ . We shall see later that the thermal state of a radiation field (see Sect. 1.2.2) yields a Gaussian distribution for the P-function.

### 2.3.3 Symmetric Ordering of Operators (Wigner Function)

If the operator ordering is symmetric, we consider the following operator polynomial:

$$\hat{A} = \sum_{m,n=0}^{\infty} b_{m,n} \{(\hat{a}^+)^m \hat{a}^n\}, \quad (2.48)$$

where the curly braces mean “symmetrically ordered” as defined before (e.g.,  $\{\hat{a}^+ \hat{a}\} \equiv (\hat{a}^+ \hat{a} + \hat{a} \hat{a}^+)/2$ ). Let us examine the displacement operator  $\hat{D}(\xi)$  defined in (2.27):

$$\hat{D}(\xi) = \exp\{\xi\hat{a}^+ - \xi^*\hat{a}\}. \quad (2.49)$$

Because

$$\begin{aligned} \hat{D}(\xi) &= \sum_{m=0}^{\infty} (\xi\hat{a}^+ - \xi^*\hat{a})^m / (m!), \\ (\xi\hat{a}^+ - \xi^*\hat{a})^m &= \sum_{l=0}^m (-1)^l \xi^{m-l} (\xi^*)^l \frac{m!}{l!(m-l)!} \{(\hat{a}^+)^{m-l} \hat{a}^l\}, \end{aligned}$$

the displacement operator is symmetric. Using the Baker–Campbell–Hausdorff theorem (see (2.28)) and (2.45), the expectation value of  $\hat{D}$  reads as

$$\langle \hat{D} \rangle = Tr[\hat{\rho}\hat{D}(\xi)] = \int P(\alpha)\langle \alpha | \hat{D}(\xi) | \alpha \rangle d^2\alpha = e^{-|\xi|^2/2} \chi_N(\xi) = \chi_S(\xi), \quad (2.50)$$

where  $\langle \alpha | \hat{D}(\xi) | \alpha \rangle = e^{\xi\alpha^* - \xi^*\alpha - |\xi|^2/2}$  has been used.  $\chi_S(\xi)$  is the characteristic function of symmetric ordered operators. Comparing to (2.27) and (2.15), we recognize that the Wigner function is the Fourier transform of  $\chi_S(\xi)$ :

$$W(\alpha) = \frac{1}{\pi^2} \int \chi_S(\xi) e^{\alpha\xi^* - \alpha^*\xi} d^2\xi. \quad (2.51)$$

If  $\chi_S(\xi)$  of (2.50) is inserted into (2.51), after some algebra we achieve the following relation:

$$W(\alpha) = \frac{2}{\pi} \int P(\beta) e^{-2|\alpha-\beta|^2} d^2\beta. \quad (2.52)$$

Considering (2.50) and (2.47), we draw the following conclusion:

$$|\chi_S(\xi)| = e^{-|\xi|^2/2} |\chi_N(\xi)| \leq 1, \quad (2.53)$$

which means that symmetric characteristic functions are bounded contrary to  $\chi_N(\xi)$ . For example, if  $\hat{\rho} = |\alpha\rangle\langle\alpha|$  is the density operator of coherent states,  $P(\alpha)$  becomes a Delta-function  $\delta^2(\alpha - \alpha')$  (because of (2.43)). According to (2.45) we then have the relation  $|\chi_S(\xi)| = e^{-|\xi|^2/2} |e^{\xi\alpha'^* - \xi^*\alpha'}| = e^{-|\xi|^2/2} \leq 1$  for all  $\xi$ .

### 2.3.4 Anti-Normal Ordering of Operators (Q-Function)

Anti-normal ordered operators look like

$$\hat{A} = \sum_{m,n=0}^{\infty} d_{m,n} \hat{a}^m (\hat{a}^+)^n. \quad (2.54)$$

We consider the particular operator

$$\hat{A}_A = \exp\{-\xi^* \hat{a}\} \exp\{\xi \hat{a}^+\}. \quad (2.55)$$

The expectation value is calculated according to

$$\langle \hat{A}_A \rangle = Tr[\hat{\rho} \hat{A}_A] = \int P(\alpha) \langle \alpha | \hat{A}_A | \alpha \rangle d^2\alpha = \chi_A(\xi). \quad (2.56)$$

Characteristic functions are expectation values of the corresponding operators under consideration. We determine directly  $\chi_A(\xi)$  using the completeness of coherent states (2.34):

$$\begin{aligned} \chi_A(\xi) &= Tr[\hat{\rho} e^{-\xi^* \hat{a}} \hat{I} e^{\xi \hat{a}^+}] = Tr \left[ \hat{\rho} e^{-\xi^* \hat{a}} \left( \frac{1}{\pi} \int |\alpha\rangle\langle\alpha| d^2\alpha \right) e^{\xi \hat{a}^+} \right] \\ &= \frac{1}{\pi} \int e^{\xi\alpha^* - \xi^*\alpha} \langle \alpha | \hat{\rho} | \alpha \rangle d^2\alpha = \int e^{\xi\alpha^* - \xi^*\alpha} Q(\alpha) d^2\alpha, \end{aligned} \quad (2.57)$$

where the Q-function

$$Q(\alpha) = \frac{1}{\pi} \langle \alpha | \hat{\rho} | \alpha \rangle \quad (2.58)$$

has been defined. If we insert  $\hat{\rho} = |\psi\rangle\langle\psi|$  according to (1.15) the Q-function is  $Q(\alpha) = |\langle\psi|\alpha\rangle|^2/\pi \geq 0$  in any case. This is an important result and corresponds with Sect. 2.2.

Similar to (2.46) and (2.51), the Q-function is expressed as a Fourier transform of the corresponding characteristic function:

$$Q(\alpha) = \frac{1}{\pi^2} \int \chi_A(\xi) e^{\xi^* \alpha - \xi \alpha^*} d^2 \xi. \quad (2.59)$$

If  $\chi_A(\xi)$  of (2.56) is inserted into (2.59) and if (2.28) is used, we get, after some manipulation, a correlation between  $Q(\alpha)$  and  $P(\alpha)$ :

$$Q(\alpha) = \frac{1}{\pi} \int P(\beta) e^{-|\alpha-\beta|^2} d^2 \beta. \quad (2.60)$$

Using (2.28),  $\chi_A(\xi)$  can be expressed by  $\chi_N(\xi)$  and we get

$$\chi_A(\xi) = \text{Tr}[\hat{\rho} e^{-\xi^* \hat{a}} e^{\xi \hat{a}^+}] = e^{-|\xi|^2} \text{Tr}[\hat{\rho} e^{\xi \hat{a}^+} e^{-\xi^* \hat{a}}] = e^{-|\xi|^2} \chi_N(\xi). \quad (2.61)$$

For  $\hat{\rho} = |\alpha\rangle\langle\alpha| \Rightarrow |\chi_A(\xi)| = e^{-|\xi|^2} \leq 1$ . If we merge (2.50) and (2.61), we get a relation between the three characteristic functions:

$$\chi_N(\xi) e^{-|\xi|^2} = \chi_S(\xi) e^{-|\xi|^2/2} = \chi_A(\xi). \quad (2.62)$$

### 2.3.5 Quasi-Distribution Functions of Coherent States

The density operator of a coherent state reads  $\hat{\rho} = |\beta\rangle\langle\beta|$ . The Q-function is therefore  $Q(\alpha) = |\langle\alpha|\beta\rangle|^2/\pi = e^{-|\alpha-\beta|^2}/\pi$  (compare to Sect. 2.3.1).

From (2.43) it follows directly that  $P(\alpha)$  is a Delta-function:  $P(\alpha) = \delta^2(\alpha - \beta) \equiv \delta[\Re(\alpha - \beta)]\delta[\Im(\alpha - \beta)]$ .

The Wigner function  $W(\alpha)$  is directly identified from (2.52):  $W(\alpha) = (2/\pi)e^{-2|\alpha-\beta|^2}$ . We recognize that the mean square deviation of the Q-function is twice as big as that of the Wigner function.

### 2.3.6 Q-Function of the Harmonic Oscillator

The density operator of a QMHO is  $\hat{\rho} = |n\rangle\langle n|$ . According to (2.58) and (2.31) the Q-function reads as

$$Q(\alpha) = \frac{1}{\pi} |\langle n|\alpha\rangle|^2 = \frac{1}{\pi} \frac{|\alpha|^{2n}}{n!} e^{-|\alpha|^2} = \frac{1}{\pi} P_n. \quad (2.63)$$

The eigenvalue of  $\hat{a}$  with regard to coherent states  $|\alpha\rangle$  is  $\alpha$ , or briefly:  $\hat{a}|\alpha\rangle = \alpha|\alpha\rangle$ . According to (2.21) we have  $\alpha = (\lambda x + ip/\lambda)/\sqrt{2\hbar}$  with  $\lambda = \sqrt{M\Omega}$ . Using (2.17)  $|\alpha|^2$  can be expressed through ( $p = \hbar k$ )

$$|\alpha|^2 = h(x, k) = \frac{1}{2} \left( \frac{k^2}{\alpha'^2} + x^2 \alpha'^2 \right), \quad (2.64)$$

where  $\alpha' = \lambda/\sqrt{\hbar}$ . Finally we get for the Q-function

$$\pi Q(\alpha) \equiv \pi Q(x, k, n) = \frac{1}{n!} [h(x, k)]^n e^{-h(x, k)}. \quad (2.65)$$

This function is plotted in Figs. 2.7 to 2.10. As can be seen from these drawings, the Q-function is positive everywhere and no oscillations appear as in the Wigner function (Figs. 2.3 to 2.5). The ground state of the Q-function

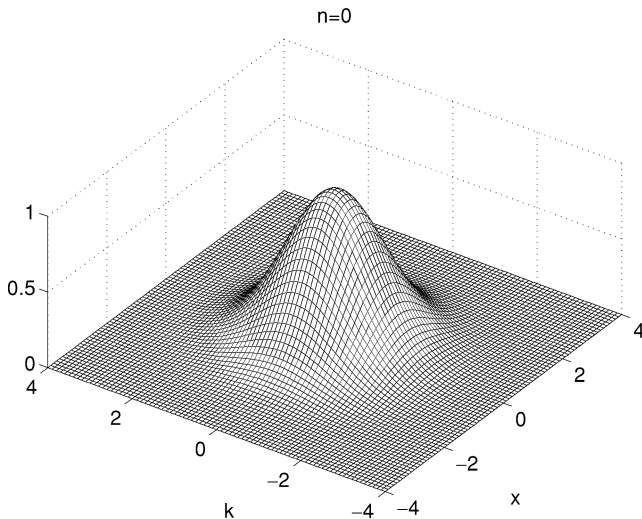


**Fig. 2.7.** Q-function of QMHO (2.65): ground state  $n = 0$  ( $\alpha' = 1$ )

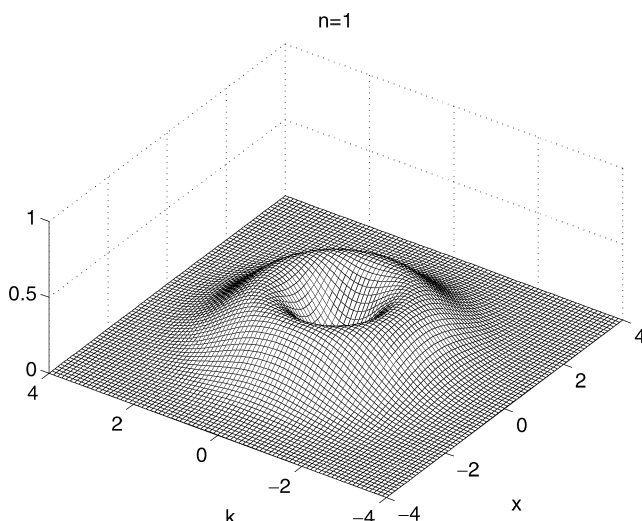


**Fig. 2.8.** Q-function of QMHO: first state  $n = 1$

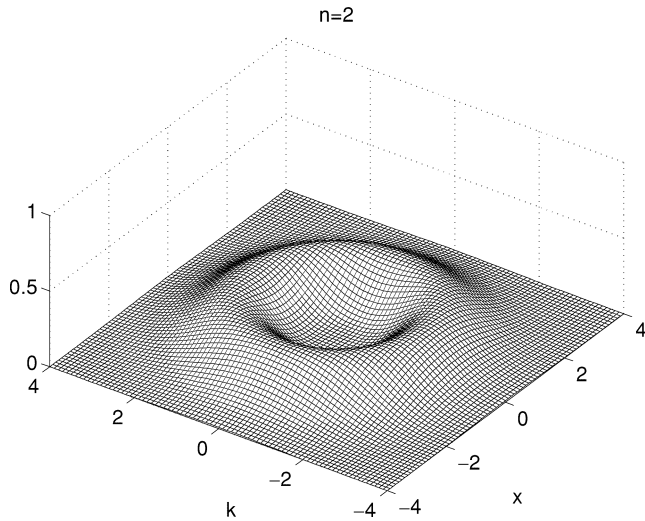


**Fig. 2.9.** Q-function of QMHO: second state  $n = 2$

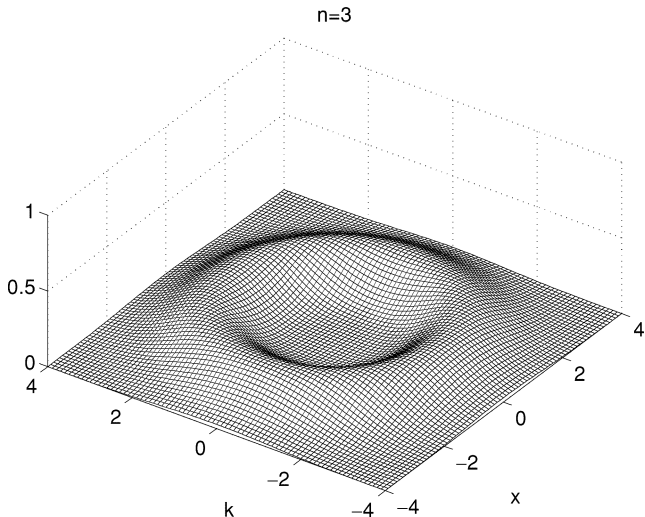


**Fig. 2.10.** Q-function of QMHO: third state  $n = 3$

(Fig. 2.7) is twice as broad as the ground state of the Wigner function (Fig. 2.2).

### 2.3.7 Distribution Functions of a Radiation Field

In this section we are dealing with quantum mechanical distribution functions of a radiation field of temperature  $T$  [4]. The radiation field is in thermal

equilibrium with its environment. Physically it can be described by a canonical ensemble of harmonic oscillators, where the mean photon number of these oscillators, is  $n_{th} = (e^\beta - 1)^{-1}$  and  $\beta = \hbar\Omega/(k_B T)$  (compare to Sect. 1.2.2 and (1.21)). If  $T \rightarrow 0$  (which means  $\beta \rightarrow \infty$ ), then  $n_{th} \rightarrow 0$  and no photons are excited. If  $T \rightarrow \infty$  (which means  $\beta \rightarrow 0$ ), then the mean number of excited photons goes to  $\infty$ .

We envisage a radiation field built up by a large amount of single radiation sources. The single sources are made up of an incoherent superposition of coherent states. Looking at the density operator  $\hat{\rho}$  of (2.43), we recognize that  $\hat{\rho}$  is exactly an incoherent mixture of coherent states, where  $P(\alpha)$  is the corresponding distribution function. At first, we consider two sources 1 and 2. Each single source consists of coherent states like

$$|\alpha_1\rangle = \hat{D}(\alpha_1)|0\rangle, \quad |\alpha_2\rangle = \hat{D}(\alpha_2)|0\rangle, \quad (2.66)$$

where (2.30) has been used. For later purposes, we try to find the common state of these two coherent states. To this end, we build up (using (2.28))

$$\hat{D}(\alpha_1)\hat{D}(\alpha_2) = \hat{D}(\alpha_1 + \alpha_2)e^{(\alpha_1\alpha_2^* + \alpha_1^*\alpha_2)/2}, \quad (2.67)$$

where the exponent is a pure phase factor. The new coherent state can be written as

$$|\alpha_1 + \alpha_2\rangle = \hat{D}(\alpha_1 + \alpha_2)|0\rangle. \quad (2.68)$$

*Remark:* A superposition of two coherent states like  $|\alpha_1\rangle + |\alpha_2\rangle$  (Schrödinger-cat-like state) can be established, e.g., in an interferometer where phase relations are taken into account via an interference term. This is not realized in a thermal radiation field.

We have already mentioned that each single source can be described by an incoherent superposition of coherent states. For the first source, we can therefore write an appropriate density operator

$$\hat{\rho}_1 = \int P_1(\alpha_1)|\alpha_1\rangle\langle\alpha_1|d^2\alpha_1. \quad (2.69)$$

Acting on its own, the second source would produce the field

$$\hat{\rho}_2 = \int P_2(\alpha_2)|\alpha_2\rangle\langle\alpha_2|d^2\alpha_2 = \int P_2(\alpha_2)\hat{D}(\alpha_2)|0\rangle\langle 0|\hat{D}^{-1}(\alpha_2)d^2\alpha_2. \quad (2.70)$$

The second source acting after the first field generates the field

$$\begin{aligned} \hat{\rho} &= \int P_2(\alpha_2)\hat{D}(\alpha_2)\hat{\rho}_1\hat{D}^{-1}(\alpha_2)d^2\alpha_2 \\ &= \iint P_2(\alpha_2)P_1(\alpha_1)|\alpha_1 + \alpha_2\rangle\langle\alpha_1 + \alpha_2|d^2\alpha_1 d^2\alpha_2 \\ &= \iiint \delta^2(\alpha - \alpha_1 - \alpha_2)|\alpha\rangle\langle\alpha|d^2\alpha P_1(\alpha_1)P_2(\alpha_2)d^2\alpha_1 d^2\alpha_2 \\ &= \int P(\alpha)|\alpha\rangle\langle\alpha|d^2\alpha, \end{aligned} \quad (2.71)$$

where the joint distribution function  $P(\alpha)$  is defined by

$$\begin{aligned} P(\alpha) &= \iint \delta^2(\alpha - \alpha_1 - \alpha_2) P_1(\alpha_1) P_2(\alpha_2) d^2\alpha_1 d^2\alpha_2 \\ &= \int P_1(\alpha - \alpha') P_2(\alpha') d^2\alpha' = P_1 * P_2. \end{aligned} \quad (2.72)$$

We see that the distribution function for the superposition of two fields is the convolution of the distribution functions for each field. If we have three sources, the distribution function is  $P(\alpha) = P_1 * [P_2 * P_3]$  and so on. If there are  $N$  statistically independent sources, we have

$$P(\alpha) = \int \dots \int \delta^2(\alpha - \sum_{j=1}^N \alpha_j) \prod_{j=1}^N p(\alpha_j) d^2\alpha_j. \quad (2.73)$$

Here,  $N$  identical P-functions  $p(\alpha_j)$  have been used. In (2.45) we became acquainted with the characteristic function of normal ordered operators. We establish a characteristic function  $\chi(\lambda)$  of an P-function  $p(\alpha)$  by the following expression

$$\chi(\lambda) = \int e^{i\bar{\lambda}\alpha} p(\alpha) d^2\alpha, \quad (2.74)$$

where  $\lambda = \lambda_r + i\lambda_i$ ,  $\alpha = \alpha_r + i\alpha_i$  and  $\bar{\lambda}\alpha \equiv (\lambda\alpha^* + \lambda^*\alpha)/2 = \lambda_r\alpha_r + \lambda_i\alpha_i$  is defined as a real quantity. If  $P(\alpha)$  is inserted in (2.74) instead of  $p(\alpha)$ , the convolution theorem can be used and we get the characteristic function of  $N$  incoherent superimposed sources:

$$X(\lambda) = \int e^{i\bar{\lambda}\alpha} P(\alpha) d^2\alpha = [\chi(\lambda)]^N. \quad (2.75)$$

Let us consider  $\chi(\lambda)$  more precisely. We expand  $e^{i\bar{\lambda}\alpha}$  into a series and obtain

$$\chi(\lambda) = \int \left[ 1 + i\bar{\lambda}\alpha + \frac{(i\bar{\lambda}\alpha)^2}{2} + \dots \right] p(\alpha) d^2\alpha. \quad (2.76)$$

If the individual sources are stationary, their weight function  $p(\alpha)$  depends only on  $|\alpha|$ . We assume that the radiation field should be “unphased” which means that for mean values the relation  $\langle \alpha \rangle = \int \alpha p(\alpha) d^2\alpha = 0$  is valid. Assuming an “unphased” field, we calculate  $\langle (\bar{\lambda}\alpha)^2 \rangle = \langle (\lambda_r\alpha_r)^2 \rangle + \langle (\lambda_i\alpha_i)^2 \rangle \approx |\lambda|^2 \langle |\alpha|^2 \rangle / 2$ . The mean value

$$\langle |\alpha|^2 \rangle = \int |\alpha|^2 p(\alpha) d^2\alpha = \langle n \rangle \quad (2.77)$$

is the mean photon number of one source. The transform  $\chi(\lambda)$  may then be approximated for small values of  $|\lambda|$  by

$$\chi(\lambda) \approx 1 - \frac{1}{4} |\lambda|^2 \langle n \rangle. \quad (2.78)$$

The transform for the superposed field may be approximated by

$$X(\lambda) \approx \exp \left\{ -\frac{1}{4} |\lambda|^2 n_{th} \right\}, \quad (2.79)$$

where

$$n_{th} = N \langle n \rangle \gg 1 \quad (2.80)$$

is just the average of the total number of quanta present in the mode. The inverse Fourier transform becomes (see (2.46) and the definition of the expression  $\overline{\lambda\alpha}$ )

$$P(\alpha) \approx \frac{1}{(2\pi)^2} \int e^{-i\overline{\lambda\alpha}} X(\lambda) d^2\lambda = \frac{1}{\pi n_{th}} \exp \left\{ -\frac{|\alpha|^2}{n_{th}} \right\}, \quad (2.81)$$

where the integration has to be performed over real and imaginary parts separately. This is the P-function of the thermal radiation field.  $P(\alpha)$  can only be accurately interpreted as a probability distribution for  $n_{th} \gg 1$ . The Gaussian distribution  $P(\alpha)$  for the excitation of a mode has extremely wide applicability. The random or chaotic sort of excitation it describes is presumably characteristic of most of the familiar types of non-coherent macroscopic light sources.

If  $n_{th} = (e^\beta - 1)^{-1}$  is used,  $P(\alpha)$  takes the form

$$P(\alpha) = \frac{1}{\pi} (e^\beta - 1) \exp \{-(e^\beta - 1)|\alpha|^2\}. \quad (2.82)$$

To reach the classical analogue ( $|\alpha|^2 \gg 1$ ) of this distribution, namely

$$P_{cl}(\alpha) = \frac{1}{\pi} \beta \exp \{ -\beta |\alpha|^2 \}, \quad (2.83)$$

only for  $\beta \ll 1$  in (2.82) (low frequency modes) the modes are sufficiently excited, to be accurately described by classical theory. For higher frequencies, the two distributions differ greatly in nature even though both are Gaussian. For higher frequencies (or  $\beta$ )  $P(\alpha)$  approaches zero much faster than  $P_{cl}(\alpha)$ . This difference epitomizes the ultraviolet catastrophe of the classical radiation theory.

The density operator of the system is (see (2.43))

$$\hat{\rho}_{th} = \frac{1}{\pi n_{th}} \int e^{-|\alpha|^2/n_{th}} |\alpha\rangle \langle \alpha| d^2\alpha. \quad (2.84)$$

After integration, using the definition of coherent states (2.30) and inserting  $n_{th} = (e^\beta - 1)^{-1}$ , we finally get

$$\hat{\rho}_{th} = (1 - e^{-\beta}) \sum_{n=0}^{\infty} e^{-n\beta} |n\rangle \langle n| \quad (2.85)$$

and this equation corresponds exactly to (1.19).

The Q-function is determined from (2.58) and gives

$$Q(\alpha) = \frac{1}{\pi} \langle \alpha | \hat{\rho}_{th} | \alpha \rangle = \frac{1}{\pi} (1 - e^{-\beta}) \exp\{-(1 - e^{-\beta})|\alpha|^2\}. \quad (2.86)$$

If  $T \rightarrow 0 \Rightarrow Q(\alpha) = e^{-|\alpha|^2}/\pi = P_0/\pi$ . If  $T \rightarrow \infty \Rightarrow Q(\alpha) \rightarrow 0$ .

To obtain the Wigner function, we find at first the characteristic function  $\chi_A(\xi)$  of anti-normal ordered operators identified, e.g., in (2.57) using  $Q(\alpha)$  of (2.86). The result is  $\chi_A(\xi) = \exp\{-|\xi|^2/(1 - e^{-\beta})\}$ . From (2.62) we have the relation  $\chi_S(\xi) = e^{|\xi|^2/2} \chi_A(\xi) = \exp\{-|\xi|^2[(e^\beta - 1)^{-1} + 1/2]\}$ . Inserting into (2.51) we achieve

$$W(\alpha) = \frac{2}{\pi} \tanh\left(\frac{\beta}{2}\right) \exp\left\{-2|\alpha|^2 \tanh\left(\frac{\beta}{2}\right)\right\}. \quad (2.87)$$

$W(\alpha)$  as well as  $Q(\alpha)$  and  $P(\alpha)$  are Gaussian functions. If we consider the case  $T \rightarrow 0 \Rightarrow W(\alpha) = (2/\pi)e^{-2|\alpha|^2} = (2/\pi)P_0^2$  we find that the mean square deviation of the Wigner function is one half of that of the Q-function.

## 2.4 Uncertainty Relations and Squeezed States

In this section, we investigate some uncertainty relations of the coherent and squeezed states and in this regard encounter the time-dependent wave function.

### 2.4.1 Uncertainty of the Coherent States

So far we have not focussed on time-dependent effects of coherent states. According to (2.30), coherent states are composed of Fock states. Solving the time-dependent Schrödinger equation (1.5) and using the potential (1.6), we obtain a wave function

$$\psi(x, t) = \sum_{n=0}^{\infty} c_n u_n(x) \exp\{-iE_n t/\hbar\}, \quad (2.88)$$

where  $u_n(x)$  is given in (1.10) and  $E_n = \hbar\Omega(n+1/2)$  are the energy eigenvalues of the QMHO. Treating coherent states, the coefficients  $c_n$  can be ruled

out via the condition  $\sum_{n=0}^{\infty} c_n u_n(x) = \psi_{\alpha}(x)$ , where  $\psi_{\alpha}(x)$  is taken from (2.39).

It is by far much easier to maintain the formalism of creation and annihilation operators taking time-dependence into account. An extension to (2.21) is given by [1]

$$\hat{x}(t) = \frac{1}{\lambda} \sqrt{\frac{\hbar}{2}} [\hat{a} e^{i\Omega t} + \hat{a}^+ e^{-i\Omega t}], \quad \hat{p}(t) = \frac{\lambda}{i} \sqrt{\frac{\hbar}{2}} [\hat{a} e^{i\Omega t} - \hat{a}^+ e^{-i\Omega t}]. \quad (2.89)$$

It is now easy to carry out expectation values  $x_{\alpha\alpha}$  and  $p_{\alpha\alpha}$  of the operators  $\hat{x}(t)$  and  $\hat{p}(t)$  in terms of coherent states:

$$x_{\alpha\alpha} = \langle \alpha | \hat{x}(t) | \alpha \rangle = x_0 \cos(\Omega t), \quad x_0 = \frac{\alpha}{\lambda} \sqrt{2\hbar} \quad (2.90)$$

and

$$p_{\alpha\alpha} = \langle \alpha | \hat{p}(t) | \alpha \rangle = p_0 \sin(\Omega t), \quad p_0 = \alpha \lambda \sqrt{2\hbar} \quad (2.91)$$

where  $\alpha$  has been taken to be real. These equations resemble the solutions of the classical harmonic oscillator. Similarly, the expectation values  $x_{\alpha\alpha}^2$  and  $p_{\alpha\alpha}^2$  can be calculated and we get

$$x_{\alpha\alpha}^2 = \langle \alpha | \hat{x}^2(t) | \alpha \rangle = \frac{\hbar}{2\lambda^2} [1 + 4\alpha^2 \cos^2(\Omega t)] \quad (2.92)$$

and

$$p_{\alpha\alpha}^2 = \langle \alpha | \hat{p}^2(t) | \alpha \rangle = \frac{\lambda^2 \hbar}{2} [1 + 4\alpha^2 \sin^2(\Omega t)]. \quad (2.93)$$

The mean square deviations can be evaluated directly and are not time-dependent:

$$(\delta x)^2 = x_{\alpha\alpha}^2 - (x_{\alpha\alpha})^2 = \frac{\hbar}{2\lambda^2}, \quad (\delta p)^2 = p_{\alpha\alpha}^2 - (p_{\alpha\alpha})^2 = \frac{\lambda^2 \hbar}{2}. \quad (2.94)$$

These relations have already been obtained in (2.37) and (2.40). This is a typical result for coherent states. Heisenberg's uncertainty relation reads

$$(\delta x)(\delta p) = \hbar/2. \quad (2.95)$$

It should be mentioned that in quantum electrodynamics, the momentum operator  $\hat{p}(t)$  and the position operator  $\hat{x}(t)$  are associated with the electric and the magnetic field operator, respectively.

The relative uncertainty of position and of momentum is equal:

$$(\delta x/x_0)^2 = (\delta p/p_0)^2 = \frac{1}{4|\alpha|^2} = \frac{1}{4\langle n \rangle}, \quad (2.96)$$

where (2.32) has been inserted. The larger the mean photon number  $\langle n \rangle$ , the smaller the relative uncertainties.

Because of the time-dependence of the mean value  $x_{\alpha\alpha}$  of the position operator in (2.90), a time-dependent wave function  $\psi_\alpha(x, t)$  can be constructed similarly to (2.39):

$$\begin{aligned}\psi_\alpha(x) &= \left[ \frac{\lambda^2}{\pi\hbar} \right]^{1/4} \exp \left\{ -\frac{\lambda^2}{2\hbar}[x - x_0]^2 \right\} \\ \Rightarrow \psi_\alpha(x, t) &= \left[ \frac{\lambda^2}{\pi\hbar} \right]^{1/4} \exp \left\{ -\frac{\lambda^2}{2\hbar}[x - x_0 \cos(\Omega t)]^2 \right\}. \quad (2.97)\end{aligned}$$

### 2.4.2 Uncertainty of Squeezed States

In the preceding sections we created a coherent state of a mechanical, harmonic oscillator from its ground state by displacing the quadratic potential. The width of the wave packet was identical to the ground state wave packet of the oscillator. Coherent states are minimum-uncertainty states (see (2.95)) with equal noise in both quadratures  $\hat{x}(t)$  and  $\hat{p}(t)$  (see (2.96)). A general class of minimum-uncertainty states is known as squeezed states. In general, a squeezed state may have less noise in one quadrature than a coherent state. To satisfy the requirements of a minimum-uncertainty state, the noise in the other quadrature is greater than that of a coherent state.

We may define squeezed states by the following considerations. The annihilation operator  $\hat{a}$  and the creation operator  $\hat{a}^+$  meet the eigenvalue equations  $\hat{a}|\alpha\rangle = \alpha|\alpha\rangle$  and  $\langle\alpha|\hat{a}^+ = \alpha^*\langle\alpha|$ , respectively. Now examine the operator

$$\hat{b} = \mu\hat{a} + \nu\hat{a}^+, \quad \hat{b}^+ = \mu^*\hat{a}^+ + \nu^*\hat{a}, \quad \hat{b}|\beta\rangle = \beta|\beta\rangle, \quad \langle\beta|\hat{b}^+ = \beta^*\langle\beta|, \quad (2.98)$$

where  $\beta$  is the eigenvalue of the operator  $\hat{b}$  with regard to the eigenvectors  $|\beta\rangle$ , which are called squeezed states. Alternatively,  $\hat{b}$  can be obtained by a unitary transformation using  $\hat{S}(\epsilon)$  (called squeezing operator):  $\hat{b} = \hat{S}(\epsilon)\hat{a}\hat{S}^+(\epsilon)$ , where  $\hat{S}(\epsilon) = \exp\{[\epsilon^*\hat{a}^2 - \epsilon(\hat{a}^+)^2]/2\}$ ,  $\epsilon = re^{2i\Phi}$ ,  $\mu = \cosh r$ ,  $\nu = e^{2i\Phi} \sinh r$  and  $r = |\epsilon|$  is called the “squeeze factor”. Regarding a detailed discussion about squeezed states, we would like to refer to the appropriate literature [2, 3, 6–10, 12]. In Parts III and IV a somewhat analogous squeezing effect in neutron interferometry is discussed.

From the commutation relation  $[\hat{b}, \hat{b}^+] = \hat{I}$  a connection between  $\mu$  and  $\nu$  can be established:

$$|\mu|^2 - |\nu|^2 = 1. \quad (2.99)$$

Moreover, we can immediately determine the following relations:

$$\hat{a} = \mu^*\hat{b} - \nu\hat{b}^+, \quad \hat{a}^+ = \mu\hat{b}^+ - \nu^*\hat{b}. \quad (2.100)$$

Because  $\mu$ ,  $\nu$  and  $\beta$  are in general complex values, we express them by  $\mu = |\mu| \exp\{i\Phi_\mu\}$ ,  $\nu = |\nu| \exp\{i\Phi_\nu\}$  and  $\beta = |\beta| \exp\{i\Phi_\beta\}$ . Taking (2.89) and (2.100) into account, squeezed-state mean values can be specified:

$$\begin{aligned}x_{\beta\beta} &= \langle \beta | \hat{x}(t) | \beta \rangle = \frac{\sqrt{2\pi}}{\lambda} |\beta| [|\mu| \cos(\Omega t + \Phi_\mu - \Phi_\beta) - |\nu| \cos(\Omega t - \Phi_\nu + \Phi_\beta)], \\ p_{\beta\beta} &= \langle \beta | \hat{p}(t) | \beta \rangle = \lambda \sqrt{2\pi} |\beta| [|\mu| \sin(\Omega t + \Phi_\mu - \Phi_\beta) - |\nu| \sin(\Omega t - \Phi_\nu + \Phi_\beta)].\end{aligned}$$

If  $\nu = 0 \rightarrow \mu = 1, \beta = \alpha$ . For a real  $\alpha$  (2.90) and (2.91) follow and this is the case of coherent states. The corresponding uncertainties are

$$\begin{aligned}(\delta x)_\beta^2 &= \frac{1}{\lambda^2} \frac{\hbar}{2} [|\mu|^2 + |\nu|^2 - 2|\mu||\nu| \cos(\Omega t + \Phi_\mu - \Phi_\nu)], \\ (\delta p)_\beta^2 &= \lambda^2 \frac{\hbar}{2} [|\mu|^2 + |\nu|^2 + 2|\mu||\nu| \cos(\Omega t + \Phi_\mu - \Phi_\nu)].\end{aligned}\quad (2.101)$$

Compared to coherent states (2.94), the noise of squeezed states is time-dependent. Let us assume real values for  $\mu$ ,  $\nu$  and  $\beta$ . Then

$$(\delta x)_\beta (\delta p)_\beta = \frac{\hbar}{2} \sqrt{(\mu^2 + \nu^2)^2 - 4\mu^2\nu^2 \cos^2(\Omega t)} \geq \frac{\hbar}{2} \quad (2.102)$$

taking (2.99) into account. The equals sign is valid for  $\cos(\Omega t) = 1$ . In this case

$$\begin{aligned}(\delta x)_{\beta, \min} &= \sqrt{\hbar/(2\lambda^2)}(\mu - \nu), \\ (\delta p)_{\beta, \max} &= \sqrt{\lambda^2 \hbar/2}(\mu + \nu).\end{aligned}\quad (2.103)$$

Finally, we would like to compute the mean photon number in the squeezed state. The photon number operator is  $\hat{N} = \hat{a}^\dagger \hat{a}$  and using (2.100) we obtain

$$\langle \beta | \hat{N} | \beta \rangle = -\mu^* \nu^* \beta^2 - \mu \nu (\beta^*)^2 + |\beta|^2 (|\mu|^2 + |\nu|^2) + |\nu|^2.\quad (2.104)$$

The photon number, even in the vacuum ( $\beta = 0$ ), for squeezed states is equal to  $|\nu|^2$ , whereas for coherent states no photons are present in the vacuum.

Part II

## Optical Interferometry

### 3 Interferometry Using Wave Packets

In this chapter, we investigate single-photon interference based on a wave packet description of the incoming beam. This is equivalent to quantum interference with individual photons, as shown below. The interference pattern is observed by sending particles, one by one, through an interferometer. Many particles are then collected at the detector. In the simplest of such experiments, the light intensity can be dimmed down far enough, so that only one photon at a time is inside the interferometer.

A single-photon interference experiment was performed by Grangier and co-workers [13]. Here a Mach–Zehnder interferometer is employed to observe real single-photon interferences [14, 15], where the photon source is a parametric down-conversion source. Thereby the intensities are very low. Nevertheless, the interference pattern of accumulated photons shows perfect interference fringes. This confirms that the quantum state is not just a statistical property of an ensemble of particles.

It must be emphasized that the conceptual questions arising for photon interference are the same as those arising for interference of massive particles like neutrons. In Parts III and IV neutron interferometry and spin interferometry using neutrons is discussed extensively.

In this second part of the book, we investigate optical interferometry. This technique relies heavily on one or many beam splitters (BS). So we have to understand how quantum states transform at a beam splitter, i.e., how the states of the incident fields transform into the states of the outgoing fields.

The description presented here is rigorously equivalent to a full quantum mechanical description of the electromagnetic field in the case where single photon states are considered. Simultaneously, this description also holds in the case of classical electrodynamics [2].

This chapter is organized as follows. We use wave functions (Gaussian wave packets in position and momentum space) for the beam description. Subsequently, a description of the action of a beam splitter is presented. Then the Mach–Zehnder interferometer (MZ) with one input beam is discussed, where we calculate space and momentum spectra, as well as intensities and visibility functions behind the interferometer. Then a combination of three MZs is analyzed. Afterwards the double-loop device is studied. Finally an MZ with two input and two output fields is examined.

### 3.1 Beam Splitter

The beam splitter (BS) and its quantum features is described in detail in the literature (see, e.g., [2, 8, 12]). Thereby both the classical treatment and the quantum mechanical description is carried out. In principle, this means a transition from wave amplitudes to operators. Another, but equivalent, approach rests on quantum states. Since the beam splitter combines two input modes into linear combinations, we can expect the output modes to be entangled. The beam splitter transforms two wave functions of the two input modes to two wave functions of the output mode. In Fig. 3.1 a BS together with incoming and outgoing beam paths is shown.

#### 3.1.1 Wave Packet

As mentioned above, we use the concept of a Gaussian wave packet in order to describe the wave function.

On the one hand, the formalism presented below can be seen as a pure classical wave packet description of dynamic electromagnetic fields. On the other hand, the full-scale quantum mechanical description of a multi mode electromagnetic field involves a linear Hilbert space  $\mathcal{H}$ , which is a tensor product of the Fock spaces corresponding to the single modes. This linear space  $\mathcal{H}$  is a product space of subspaces  $\mathcal{H}_i$  of frequencies  $\Omega_i$  ( $i = 1, \dots, n$ ) of the following form:  $\mathcal{H} = \mathcal{H}_1 \otimes \mathcal{H}_2 \otimes \dots \otimes \mathcal{H}_n$ . The corresponding

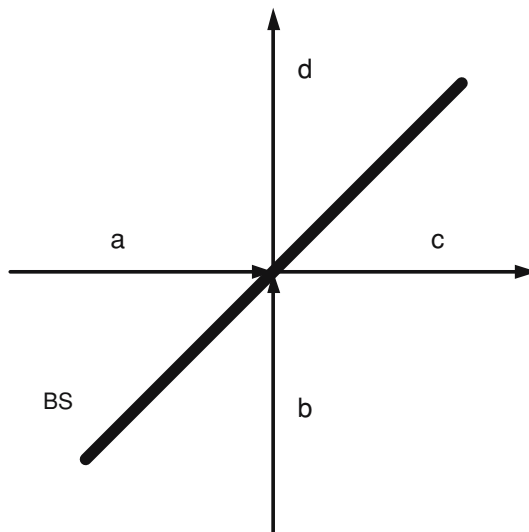


**Fig. 3.1.** Schematic sketch of a beam splitter (BS):  $a$  and  $b$  denote incoming beams,  $c$  and  $d$  are outgoing beams

state vector in  $\mathcal{H}$  reads  $|m_1\rangle|m_2\rangle\dots|m_n\rangle$ , where  $|m_i\rangle$  means  $m_i$  photons of frequency  $\Omega_i$ .

However, a well-defined subspace  $\mathcal{H}_I$  of the full space  $\mathcal{H}$ , is formed by a vector  $|\psi_I\rangle$ , which is a linear combination of vectors  $|\psi_i\rangle$  of the form

$$|\psi_I\rangle = \sum_{i=1}^n p_i |\psi_i\rangle$$

corresponding to one photon (index  $I$ ) in a chosen mode and vacuum in the rest. Thus  $\mathcal{H}_I$  contains convex combinations of vectors like  $|\psi_1\rangle = |1\rangle|0\rangle\dots|0\rangle$ ,  $|\psi_2\rangle = |0\rangle|1\rangle|0\rangle\dots|0\rangle$ , ...,  $|\psi_n\rangle = |0\rangle|0\rangle\dots|1\rangle$  and hence is built up of one-photon state vectors in each frequency  $\Omega_i$ . So we have  $\mathcal{H} \supset \mathcal{H}_I$ . The set of normalized vectors  $|\psi_i\rangle$  (norm equal to 1) in the subspace  $\mathcal{H}_I$  is all states corresponding to a “one-photon electromagnetic field” in  $\mathcal{H}$ . The coefficients  $p_i$  in the above-mentioned linear combinations can be seen as energy wave functions, since the squared moduli  $|p_i|^2$  of these coefficients are energy distributions of the corresponding wave functions.

If the input modes are denoted by  $a$  and  $b$  and the output modes by  $c$  and  $d$  (see Fig. 3.1), the corresponding full Hilbert spaces are  $\mathcal{H}_a \otimes \mathcal{H}_b$  and, after the beam splitter transformation,  $\mathcal{H}_c \otimes \mathcal{H}_d$ , respectively. The appropriate one-photon subspaces are given by the following expressions:

$$\begin{aligned} \mathcal{H}_a \otimes \mathcal{H}_b &\supset (\mathcal{H}_{I,a} \otimes \mathcal{H}_{0,b}) \oplus (\mathcal{H}_{0,a} \otimes \mathcal{H}_{I,b}), \\ \mathcal{H}_c \otimes \mathcal{H}_d &\supset (\mathcal{H}_{I,c} \otimes \mathcal{H}_{0,d}) \oplus (\mathcal{H}_{0,c} \otimes \mathcal{H}_{I,d}), \end{aligned}$$

where, for example,  $\mathcal{H}_{0,b}$  is the vacuum space in mode  $b$  and  $\mathcal{H}_{I,a}$  is the one-photon Hilbert space in mode  $a$ . Since a vector in the space  $(\mathcal{H}_{I,a} \otimes \mathcal{H}_{0,b}) \cong \mathcal{H}_{I,a}$  can be described by the wave function  $p_i \sim \alpha_a(k)$  in the continuous case (see (3.1) below), an arbitrary vector in  $(\mathcal{H}_{I,a} \otimes \mathcal{H}_{0,b}) \oplus (\mathcal{H}_{0,a} \otimes \mathcal{H}_{I,b})$  can be represented as

$$\begin{pmatrix} \alpha_a(k) \\ \alpha_b(k) \end{pmatrix}.$$

An analogous expression can be written for the output modes  $c$  and  $d$ .

To begin with, we are investigating one incoming beam, let us say a beam in path  $a$ . So we omit the beam in path  $b$  for the moment. Because of the considerations above, the basic approach for the momentum wave packet of this incoming beam in path  $a$  is given according to Sect. 2.1.1, (2.3) by

$$\alpha_a(k) = [2\pi(\delta k)^2]^{-1/4} \exp \left\{ -\frac{(k - k_0)^2}{4(\delta k)^2} \right\}, \quad (3.1)$$

where the normalization condition for the intensity  $I_a = \int \alpha_a^2(k) dk = 1$  holds. The wave number  $k = \Omega/c$  is associated with the wave length  $\lambda$  via the equation  $k = 2\pi/\lambda$ . The relation  $p = \hbar k$  connects the momentum  $p$  and wave number  $k$ . A mean wave number  $k_0 > 0$  is important for describing

an experimental wave length distribution. The corresponding wave function  $\psi_a(x)$  is given by Fourier transformation and reads as

$$\psi_a(x) = \left[ \frac{2(\delta k)^2}{\pi} \right]^{1/4} \exp\{-(\delta k)^2 x^2 + ik_0 x\}, \quad (3.2)$$

where  $(\delta k)^2$  is the mean square deviation of wave numbers. The suitable momentum and position spectra are calculated as

$$\alpha_a^2(k) = \sqrt{\frac{1}{2\pi(\delta k)^2}} \exp\left\{-\frac{(k - k_0)^2}{2(\delta k)^2}\right\} \quad (3.3)$$

and

$$|\psi_a(x)|^2 = \sqrt{\frac{2(\delta k)^2}{\pi}} \exp\{-2(\delta k)^2 x^2\}, \quad (3.4)$$

respectively. Again, the normalization condition for intensity can be written as  $I_a = \int |\psi_a(x)|^2 dx = 1$ . The momentum spectrum  $\alpha_a^2(k)$  is an experimental quantity. A Gaussian spectrum is definitely an idealization, but a very reasonable and even realistic one. The advantage of Gaussian shaped momentum and position spectra is mainly given by the mathematical simplicity of the formalism and by the easy interpretation of the results.

Let us make one more remark on time-dependence. So far, we have omitted time in our formalism. Because of the linear dispersion relation  $\Omega = ck$  between the frequency  $\Omega$  and the speed of light  $c$  in vacuum (or in glass fiber or whatsoever),  $x$  has to be replaced appropriately by  $(x - ct)$  when the wave function  $e^{ikx}$  is substituted for  $e^{ikx-i\Omega t}$ .

### 3.1.2 Action of a Beam Splitter

We restrict ourselves to 50 : 50 beam splitters, which means that 50% of the intensity is transmitted and 50% is reflected. Then the action of a beam splitter can be described by the so-called Hadamard transformation (see, e.g., [2, 9, 12, 16, 17]) usually denoted by  $\hat{H}$  (this should not be confused with the Hamiltonian):

$$\hat{H} = \frac{1}{\sqrt{2}} \begin{pmatrix} 1 & 1 \\ 1 & -1 \end{pmatrix}. \quad (3.5)$$

This is a particular but traditional beam splitter. It can be shown that when we restrict our considerations to single-photon wave functions, whereby a single photon, not only in each beam splitter input but in both modes, is required, the full-scale quantum-mechanical description of the beam splitter reduces to the following matrix equation:

$$\begin{pmatrix} \psi_d(x) \\ \psi_c(x) \end{pmatrix} = \hat{H} \begin{pmatrix} \psi_a(x) \\ \psi_b(x) \end{pmatrix}. \quad (3.6)$$

Here the functions  $\psi_{a,b,c,d}(x)$  are single-photon wave functions as introduced above. It is also well-known [2] that (3.6) holds also when the functions  $\psi_{a,b,c,d}(x)$  are seen as classical electromagnetic amplitudes.

In the case where we restrict our discussion to a beam splitter with only one input, i.e., if we set, e.g.,  $\psi_b(x) = 0$ , the result is:

$$\psi_c(x) = \psi_d(x) = \frac{\psi_a(x)}{\sqrt{2}}, \quad \alpha_c(k) = \alpha_d(k) = \frac{\alpha_a(k)}{\sqrt{2}}. \quad (3.7)$$

Directly, the following relations can be established:  $|\psi_c(x)|^2 = |\psi_d(x)|^2 = |\psi_a(x)|^2/2$ ,  $\alpha_c^2(k) = \alpha_d^2(k) = \alpha_a^2(k)/2$  and  $I_c = I_d = I_a/2 = 1/2$ .

### 3.2 Mach–Zehnder Interferometer (MZ)

In Fig. 3.2 a MZ is shown. One input  $a$  and two output beams  $g$  and  $h$  are considered. The MZ is made from glass fibers. The path length inside the MZ is  $l_i$  and acts like a phase shifter  $e^{-ikl_i}$ , where  $i = c, d$ . A particular phase shifter  $P_i = e^{-ik\Delta_i}$  is applied, where  $\Delta_i$  is the specific phase shift inside path  $i$ . Because absorption is always existent, transmission  $T_i = e^{-2a_i}$  ( $a_i$  is the

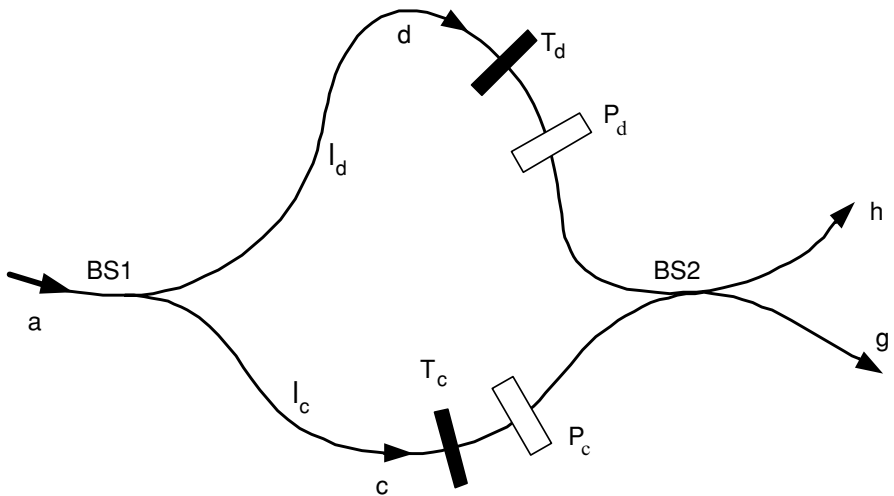


**Fig. 3.2.** Mach–Zehnder interferometer (MZ) made of glass fibers:  $a$  denotes the incoming beam,  $c$  and  $d$  are pathways inside the MZ,  $h$  and  $g$  are outgoing beams.  $BS1$  and  $BS2$  are two beam splitters.  $l_i$  is the length,  $P_i = e^{-ik\Delta_i}$  is the phase shift,  $T_i = e^{-2a_i}$  is the transmission ( $a_i$  is the absorption coefficient) in the  $i$ -th( $= c, d$ ) pathway

absorption coefficient) is included as a separate element. If we denote the total phase shift by

$$L_i = l_i + \Delta_i, \quad i = c, d, \quad (3.8)$$

a total phase shifter  $e^{-ikL_i}$  in path  $i$  can be specified.

*Remark:* In principle, pulse propagation in a dispersive medium (glass fiber) has to be taken into account [18, p. 182]. A dispersive medium is characterized by a frequency-dependent refractive index  $n(\nu)$ , absorption coefficient  $a(\nu) \approx \text{constant}$  and phase velocity  $v(\nu)$ , so that monochromatic waves of different frequencies  $\nu = (c/2\pi)k$  travel in the medium at different velocities. Since a pulse of light is the sum of many monochromatic waves, each of which is modified differently, the pulse is delayed and broadened (dispersed in time) and its shape is altered. The pulse delay is caused by the group velocity  $v_g$  of the wave packet in the medium and is characterized by the time  $\tau_d = l_i/v_g$ , and the dispersion coefficient  $D_\nu = (\lambda_0^3/c^2)[d^2n(\lambda_0)/d\lambda_0^2]$  (dimension  $[s/(m.\text{Hz})]$ ) is responsible for pulse-broadening. These effects can therefore be taken into account essentially by replacing the exponent of the expression  $\exp(-ikl_i)$  with  $(-ik\tau_d c)$  and by adding a quadratic term in  $k$ , namely  $(-\iota D_\nu c^2 k^2 l_i / 4\pi)$ , to the exponent. However, to simplify matters, we concentrate in the following on the calculation of momentum and position spectra as a matter of principle, and therefore do not consider these effects in detail.

### 3.2.1 Wave Functions of the MZ

Now the wave functions inside and behind the interferometer have to be determined. Directly before  $BS2$ , the wave functions have the full information of absorption and phase shift of the different paths inside the MZ. From (3.7), (3.2) and (3.1) we therefore conclude:

$$\psi_{c,d}(x) = \frac{1}{\sqrt{2}} \sqrt{T_{c,d}} \left[ \frac{2(\delta k)^2}{\pi} \right]^{1/4} \exp\{-(\delta k)^2(x - L_{c,d})^2 + \iota k_0(x - L_{c,d})\} \quad (3.9)$$

and

$$\alpha_{c,d}(k) = \frac{1}{\sqrt{2}} \sqrt{T_{c,d}} \alpha_a(k) \exp\{-\iota k L_{c,d}\}. \quad (3.10)$$

Behind the interferometer the Hadamard transformation (3.5) has to be applied:

$$\begin{pmatrix} \psi_h(x) \\ \psi_g(x) \end{pmatrix} = \hat{H} \begin{pmatrix} \psi_d(x) \\ \psi_c(x) \end{pmatrix}. \quad (3.11)$$

We get

$$\psi_{h,g}(x) = \frac{1}{\sqrt{2}} [\psi_d(x) \pm \psi_c(x)], \quad \alpha_{h,g}(k) = \frac{1}{\sqrt{2}} [\alpha_d(k) \pm \alpha_c(k)]. \quad (3.12)$$

### 3.2.2 Spectra, Intensities and Visibility of the MZ

Now we can identify the momentum and position spectra behind the MZ defined via the Wigner function in (2.9) and (2.8), respectively. The Wigner functions  $W_{h,g}(x, k)$  themselves can be determined using (3.12) and (2.2). We postpone the related calculations to Part III (neutron interferometry) and Sect. 7.2.

In any case, especially the momentum spectrum can be determined experimentally, measuring the energy-dependence of the beam in both directions  $h$  and  $g$  (Fig. 3.2). Because of (3.12) and (3.10), the momentum wave function is a complex quantity. Therefore,  $|\alpha_{h,g}(k)|^2$  has to be set up. The result of the calculation is

$$|\alpha_{h,g}(k)|^2 = \frac{1}{4} \alpha_a^2(k) \{T_d + T_c \pm 2\sqrt{T_d T_c} \cos[k(L_d - L_c)]\}, \quad (3.13)$$

where the “+” sign belongs to the  $h$  beam and the “−” sign belongs to the  $g$  beam. The momentum spectra  $|\alpha_{h,g}(k)|^2$  are proportional to the incoming energy distribution  $\alpha_a^2(k)$ , however, they are modulated through a cos-term and thus depend on the phase difference  $[k(L_d - L_c)]$ . The transmissions  $T_c$  and  $T_d$  are additional attenuators. Figures 3.3 and 3.4 show these spectra for a certain parameter set, specified in the drawings. For large phase shifts (Fig. 3.3) an oscillatory spectrum appears. Small phase shifts exhibit a Gaussian

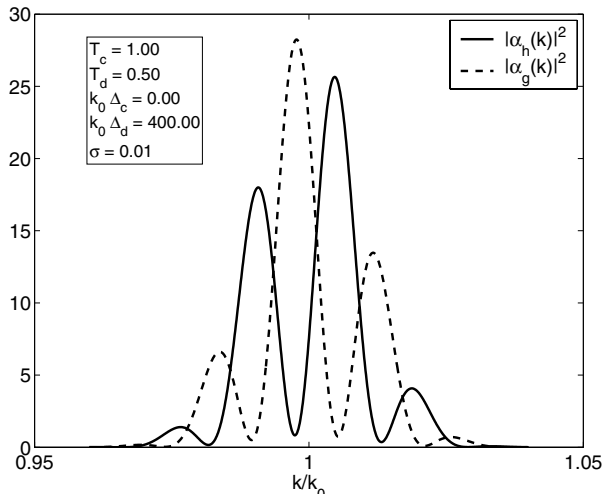


**Fig. 3.3.** Momentum spectra  $|\alpha_{h,g}(k)|^2$  of (3.13). Because of the transmission coefficient  $T_d = 0.5$  there are no zero points in the region around  $k/k_0 = 1$ . Due to the large phase shift  $(k/k_0)(L_d k_0 - L_c k_0)$ , the spectra exhibit a distinct oscillatory pattern.  $\sigma = (\delta k)/k_0$ . Further parameters:  $k_0 = 1$  and  $l_c = l_d$

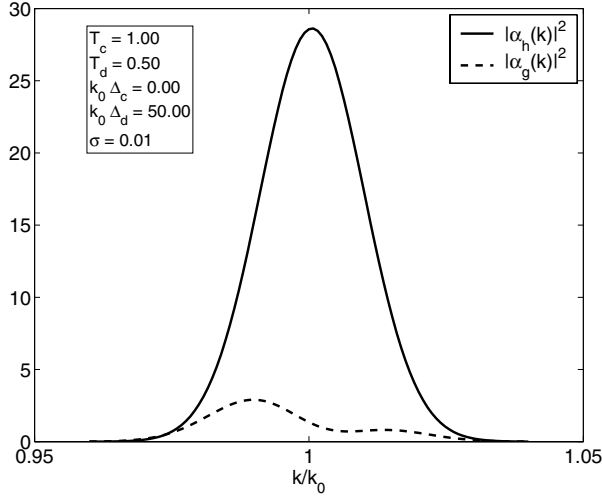


**Fig. 3.4.** Momentum spectra  $|\alpha_{h,g}(k)|^2$  of (3.13). Due to a relatively small phase shift  $(k/k_0)(L_d k_0 - L_c k_0)$  the  $h$ -spectrum exhibits an almost Gaussian pattern. Further parameters:  $k_0 = 1$  and  $l_c = l_d$

pattern of  $|\alpha_h(k)|^2$  (Fig. 3.4). If there is no absorption, the transmission terms are equal to 1 and we get

$$|\alpha_{h,g}(k)|^2 = \frac{1}{2} \alpha_a^2(k) \{1 \pm \cos[k(L_d - L_c)]\}. \quad (3.14)$$

The position spectra  $|\psi_{h,g}(x)|^2$  result from (3.12) and (3.9):

$$|\psi_{h,g}(x)|^2 = \frac{1}{4} \sqrt{\frac{2(\delta k)^2}{\pi}} \{T_d e^{-2(\delta k)^2(x-L_d)^2} + T_c e^{-2(\delta k)^2(x-L_c)^2} \\ \pm 2\sqrt{T_d T_c} e^{-(\delta k)^2[(x-L_d)^2 + (x-L_c)^2]} \cos[k_0(L_d - L_c)]\}. \quad (3.15)$$

These spectra consist of two Gaussian functions displaced by  $L_d$  and  $L_c$ , respectively. The cos-term is damped by an additional exponential factor that depends strongly on the distance between these two Gaussian functions. If the two wave packets are separated, the cos-term is practically zero (Fig. 3.5). If, on the other hand, the wave packets are close together, the interfering part of the position spectrum possibly causes dramatic modifications of the spectrum as depicted in Fig. 3.6.

The intensities  $I_{h,g}$  are defined via  $\int |\alpha_{h,g}(k)|^2 dk$  or  $\int |\psi_{h,g}(x)|^2 dx$ :

$$I_{h,g} = \frac{1}{4} \{T_d + T_c \pm 2\sqrt{T_d T_c} e^{-(\delta k)^2(L_d - L_c)^2/2} \cos[k_0(L_d - L_c)]\}. \quad (3.16)$$

In Fig. 3.7 this equation is drawn for the parameter set specified previously. The transmission coefficient  $T_d = 0.5$  causes attenuation of the interference

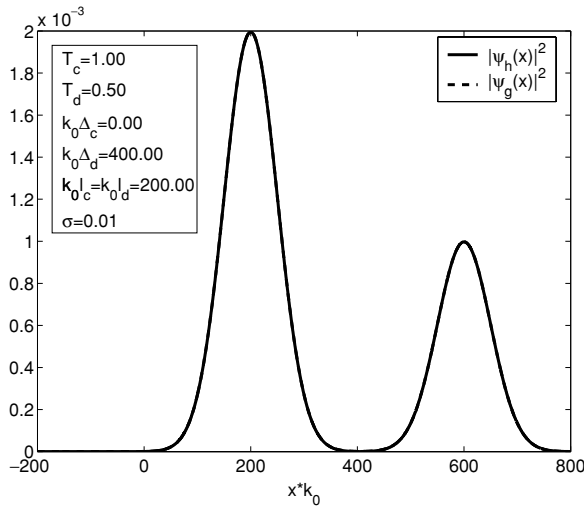


**Fig. 3.5.** Position spectra  $|\psi_{h,g}(x)|^2$  of (3.15). The two spectra cannot be distinguished from each other. They exhibit a double Gaussian peak separated by the related phase shift. Due to absorption ( $T_d = 0.5$ ) the right peak is smaller than the left one

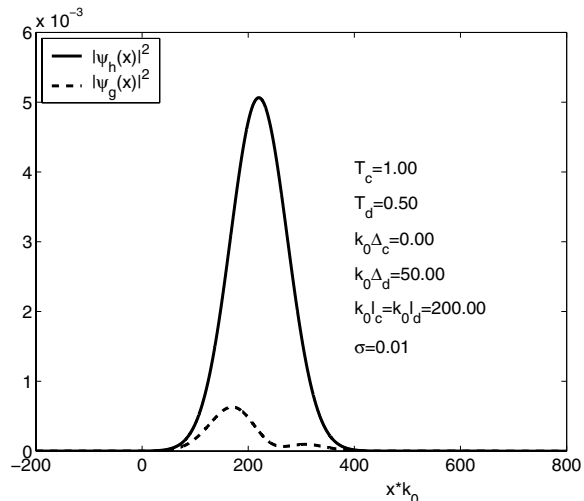


**Fig. 3.6.** Position spectra  $|\psi_{h,g}(x)|^2$  of (3.15). Because of the small phase shift the interference term, which has little attenuation, causes a strong change between the spectra

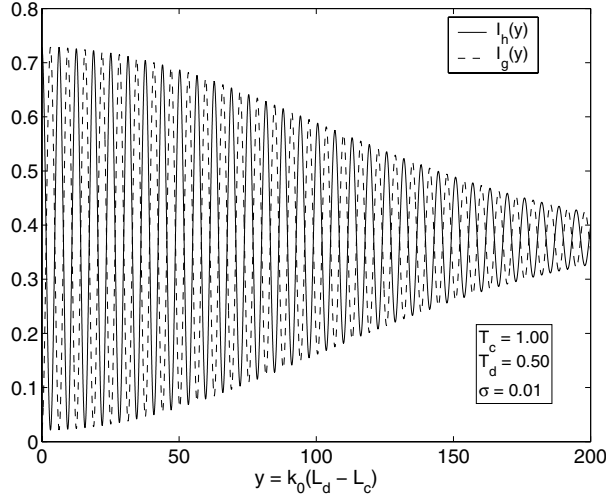


**Fig. 3.7.** Intensities  $I_{h,g}$  (see (3.16)):  $I_h$  and  $I_g$  have opposite phase, and for large values of  $y$  we obtain  $I_h = I_g \approx (T_d + T_c)/4 = 3/8 = 0.375$

pattern and, therefore, causes maxima smaller than 1 and minima larger than 0. If, for example,  $T_d = T_c = 1$  and  $L_d = L_c$ , we obtain  $I_h = 1$  and  $I_g = 0$ . The total intensity is available in the outgoing beam  $h$ .

Now we consider the visibility  $V$ . It is defined as

$$V = \frac{I_{max} - I_{min}}{I_{max} + I_{min}}. \quad (3.17)$$

It is enough to treat only beam  $h$ , for example. The cosine is 1 for  $k_0(L_d - L_c) = 2n\pi$  and this is a maximum; it is  $-1$  for  $k_0(L_d - L_c) = (2n + 1)\pi$  and this is a minimum. The result is

$$V = \frac{2\sqrt{T_d T_c} \{ e^{-(2n\pi\sigma)^2/2} + e^{-[(2n+1)\pi\sigma]^2/2} \}}{2(T_d + T_c) + 2\sqrt{T_d T_c} \{ e^{-(2n\pi\sigma)^2/2} - e^{-[(2n+1)\pi\sigma]^2/2} \}}, \quad (3.18)$$

where  $\sigma = (\delta k)/k_0$ . Usually the visibility is taken for  $\sigma \ll 1$  and low interference order, and then  $V$  can be simplified to

$$V = \frac{2\sqrt{T_d T_c}}{T_d + T_c}. \quad (3.19)$$

In the case of no absorption we get  $V = 1$ , as expected. On the other hand, absorption brings about a visibility smaller than 1 (see Fig. 3.8).

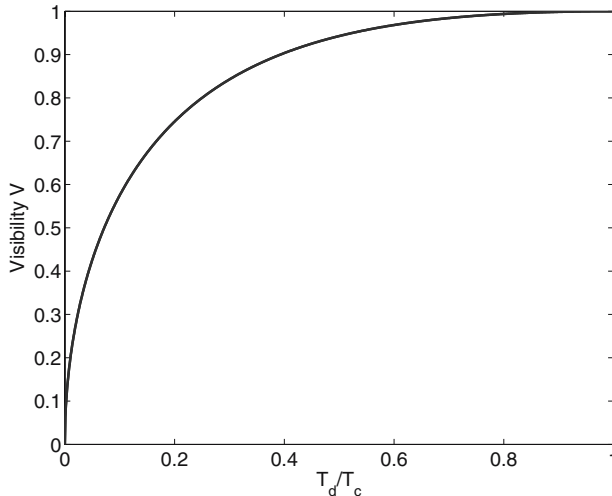


**Fig. 3.8.** Visibility (3.19) as a function of the ratio  $T_d/T_c$ . For  $T_d/T_c = 0.5$  we obtain  $V = 0.94$ , and this value is relevant for  $\sigma = \delta k/k_0 \ll 1$  and low interference order

### 3.3 Three Mach–Zehnder Interferometers

In Fig. 3.9 three MZs are drawn that form a network and are arranged like branches of a tree. Similarly to in (3.8) a total phase shift for each pathway can be defined:

$$L_\kappa = l_\kappa + \Delta_\kappa, \quad \kappa = c, d, h, g, i, j, m, n. \quad (3.20)$$

#### 3.3.1 Wave Functions of Three MZs

Here, only a short description of the calculation procedure is sketched and the results of the spectra are presented at the end of the next section. Using (3.9) and (3.10), the results from (3.12) can be used for the first MZ. Therefore, the wave functions  $\alpha_{h,g}(k)$  and  $\psi_{h,g}(x)$  are fixed. The wave functions  $\alpha_{i,j}(k)$  and  $\alpha_{m,n}(k)$  can be determined directly, using an MZ with only one input  $\alpha_h(k)$  and  $\alpha_g(k)$ , respectively. As a matter of course, the corresponding transmissions and phase shifts have to be included:

$$\alpha_{i,j}(k) = \frac{1}{\sqrt{2}} \sqrt{T_{i,j}} \alpha_h(k) e^{-ikL_{i,j}}, \quad \alpha_{m,n}(k) = \frac{1}{\sqrt{2}} \sqrt{T_{m,n}} \alpha_g(k) e^{-ikL_{m,n}}. \quad (3.21)$$

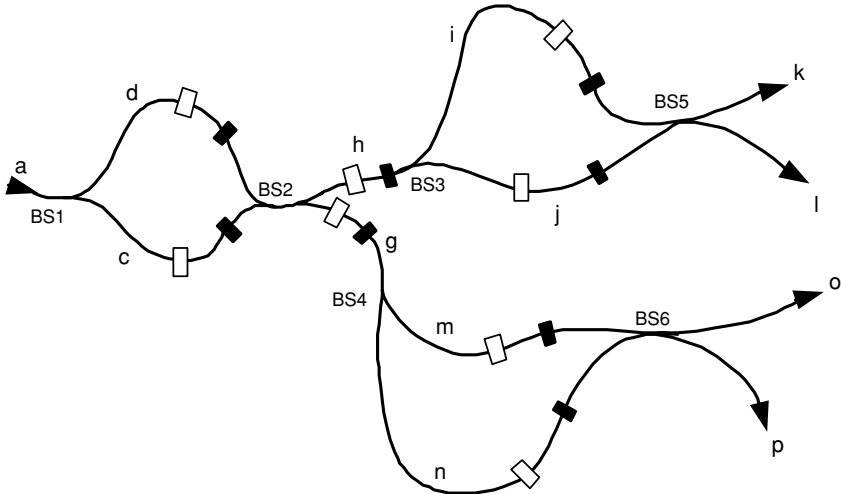


**Fig. 3.9.** Three Mach-Zehnder interferometers:  $a$  denotes the incoming beam,  $c, d, h, g, i, j, m, n$  are interior pathways,  $k, l, o, p$  are four outgoing beams.  $BS1$  to  $BS6$  are six beam splitters. In each pathway a phase shifter and an absorber is inserted.  $l_\kappa$  is the length,  $P_\kappa = e^{-ik\Delta_\kappa}$  is the phase shift,  $T_\kappa = e^{-2a_\kappa}$  is the transmission ( $a_\kappa$  is the absorption coefficient) in the  $k$ -th ( $= c, d, h, g, i, j, m, n$ ) pathway (compare to Fig. 3.2)

By means of Fourier transformation we get:

$$\psi_{i,j}(x) = \frac{1}{\sqrt{2\pi}} \int \alpha_{i,j}(k) e^{ikx} dk, \quad \psi_{m,n}(x) = \frac{1}{\sqrt{2\pi}} \int \alpha_{m,n}(k) e^{ikx} dk. \quad (3.22)$$

The last step is the Hadamard transformation at  $BS5$  and  $BS6$  and for the wave functions, with respect to the four outputs  $k, l, o, p$ , we get the following relations:

$$\begin{pmatrix} \psi_k(x) \\ \psi_l(x) \end{pmatrix} = \hat{H} \begin{pmatrix} \psi_i(x) \\ \psi_j(x) \end{pmatrix}, \quad \begin{pmatrix} \psi_o(x) \\ \psi_p(x) \end{pmatrix} = \hat{H} \begin{pmatrix} \psi_m(x) \\ \psi_n(x) \end{pmatrix}, \quad (3.23)$$

and

$$\begin{pmatrix} \alpha_k(k) \\ \alpha_l(k) \end{pmatrix} = \hat{H} \begin{pmatrix} \alpha_i(k) \\ \alpha_j(k) \end{pmatrix}, \quad \begin{pmatrix} \alpha_o(k) \\ \alpha_p(k) \end{pmatrix} = \hat{H} \begin{pmatrix} \alpha_m(k) \\ \alpha_n(k) \end{pmatrix}. \quad (3.24)$$

### 3.3.2 Spectra, Intensities and Visibility of Three MZs

Using these formulas, the position spectra  $|\psi_{k,l}(x)|^2$  and  $|\psi_{o,p}(x)|^2$ , as well as the momentum spectra  $|\alpha_{k,l}(k)|^2$  and  $|\alpha_{o,p}(k)|^2$  of the four output beams can

be computed. Integration over  $dx$  on the one hand, and over  $dk$  on the other hand, entails the intensities  $I_{k,l}$  and  $I_{o,p}$ . Thereby, the following abbreviations have been introduced:

$$\begin{aligned} \kappa_h &= \frac{1}{8} T_h \sqrt{\frac{2(\delta k)^2}{\pi}}, \quad \kappa_g = \frac{1}{8} T_g \sqrt{\frac{2(\delta k)^2}{\pi}} \\ \alpha &= k_0(L_j - L_i), \quad \beta = k_0(L_d - L_c), \quad \alpha' = k_0(L_n - L_m), \\ d_{i,j} &= k_0(x - L_d - L_h - L_{i,j}), \quad d_{m,n} = k_0(x - L_d - L_g - L_{m,n}), \\ c_{i,j} &= k_0(x - L_c - L_h - L_{i,j}), \quad c_{m,n} = k_0(x - L_c - L_g - L_{m,n}). \end{aligned} \quad (3.25)$$

The results are as follows:

$$\begin{aligned} |\psi_{k,l}(x)|^2 &= \frac{1}{2} \kappa_h \left\{ T_i \left[ T_d e^{-2\sigma^2 d_i^2} + T_c e^{-2\sigma^2 c_i^2} + 2\sqrt{T_d T_c} \cos(\beta) e^{-\sigma^2(c_i^2 + d_i^2)} \right] \right. \\ &\quad + T_j \left[ T_d e^{-2\sigma^2 d_j^2} + T_c e^{-2\sigma^2 c_j^2} + 2\sqrt{T_d T_c} \cos(\beta) e^{-\sigma^2(c_j^2 + d_j^2)} \right] \\ &\quad \pm 2\sqrt{T_i T_j} [\cos(\alpha)(T_d e^{-\sigma^2(d_i^2 + d_j^2)} + T_c e^{-\sigma^2(c_i^2 + c_j^2)}) \\ &\quad \left. + \sqrt{T_d T_c} (\cos(\alpha - \beta) e^{-\sigma^2(d_i^2 + c_j^2)} + \cos(\alpha + \beta) e^{-\sigma^2(c_i^2 + d_j^2)})] \right\}, \end{aligned} \quad (3.26)$$

$$\begin{aligned} |\psi_{o,p}(x)|^2 &= \frac{1}{2} \kappa_g \left\{ T_m \left[ T_d e^{-2\sigma^2 d_m^2} + T_c e^{-2\sigma^2 c_m^2} - 2\sqrt{T_d T_c} \cos(\beta) e^{-\sigma^2(c_m^2 + d_m^2)} \right] \right. \\ &\quad + T_n \left[ T_d e^{-2\sigma^2 d_n^2} + T_c e^{-2\sigma^2 c_n^2} - 2\sqrt{T_d T_c} \cos(\beta) e^{-\sigma^2(c_n^2 + d_n^2)} \right] \\ &\quad \pm 2\sqrt{T_m T_n} [\cos(\alpha') (T_d e^{-\sigma^2(d_m^2 + d_n^2)} + T_c e^{-\sigma^2(c_m^2 + c_n^2)}) \\ &\quad \left. - \sqrt{T_d T_c} (\cos(\alpha' - \beta) e^{-\sigma^2(d_m^2 + c_n^2)} + \cos(\alpha' + \beta) e^{-\sigma^2(c_m^2 + d_n^2)})] \right\}, \end{aligned} \quad (3.27)$$

$$\begin{aligned} I_{k,l} &= \frac{1}{16} T_h \left\{ (T_d + T_c) \left[ T_i + T_j \pm 2\sqrt{T_i T_j} e^{-\sigma^2 \alpha^2 / 2} \cos(\alpha) \right] \right. \\ &\quad + 2\sqrt{T_d T_c} \left[ (T_i + T_j) e^{-\sigma^2 \beta^2 / 2} \cos(\beta) \right. \\ &\quad \left. \left. \pm \sqrt{T_i T_j} (e^{-\sigma^2(\alpha - \beta)^2 / 2} \cos(\alpha - \beta) + e^{-\sigma^2(\alpha + \beta)^2 / 2} \cos(\alpha + \beta)) \right] \right\}, \end{aligned} \quad (3.28)$$

$$\begin{aligned}
I_{o,p} = \frac{1}{16} T_g \left\{ & (T_d + T_c) \left[ T_m + T_n \pm 2\sqrt{T_m T_n} e^{-\sigma^2 \alpha'^2/2} \cos(\alpha') \right] \right. \\
& - 2\sqrt{T_d T_c} \left[ (T_m + T_n) e^{-\sigma^2 \beta^2/2} \cos(\beta) \right. \\
& \left. \left. \pm \sqrt{T_m T_n} (e^{-\sigma^2 (\alpha' - \beta)^2/2} \cos(\alpha' - \beta) + e^{-\sigma^2 (\alpha' + \beta)^2/2} \cos(\alpha' + \beta)) \right] \right\}. 
\end{aligned} \tag{3.29}$$

A special case appears if  $\alpha = \alpha' = \beta = 0$  and if no absorption occurs. Then,  $I_k = 1$  and  $I_l = I_o = I_p = 0$ . That is to say, we have the possibility of directing direct the intensity into a chosen output beam (here selecting between four output beams) by manipulating phase shifters.

The momentum spectra read as follows:

$$|\alpha_{k,l}(k)|^2 = |\alpha_h(k)|^2 \frac{1}{4} T_h \{ T_i + T_j \pm 2\sqrt{T_i T_j} \cos[k(L_i - L_j)] \} \tag{3.30}$$

and

$$|\alpha_{o,p}(k)|^2 = |\alpha_g(k)|^2 \frac{1}{4} T_g \{ T_m + T_n \pm 2\sqrt{T_m T_n} \cos[k(L_m - L_n)] \}, \tag{3.31}$$

where  $|\alpha_{h,g}(k)|^2$  is taken from (3.13).

*Corollary:* The momentum spectrum of a chain of MZs is the product of the corresponding momentum spectra of the individual MZs.

Figures 3.10 to 3.13 show the momentum spectra according to (3.30) and (3.31) with respect to the three Mach-Zehnder interferometer system (see Fig. 3.9) for output ports  $k/l$  and  $o/p$ , respectively. Looking at Fig. 3.10 we observe that the solid line is similar to the solid line of Fig. 3.3. This is not surprising, because both parameter sets of the corresponding interferometers  $d/c$  and  $i/j$  are similar. However, the transmissions  $T_d$  and  $T_i$  cause some absorption and, therefore, the absolute values of the relevant spectra are different. The dashed line in Fig. 3.11 shows analogue resemblance with that of Fig. 3.3. Because of the symmetry, the  $l$ -output of Fig. 3.10 and the  $o$ -output of Fig. 3.11 are equal. Simulation just provides a lot of insight to interferometric procedures that cannot be understood easily otherwise.

Looking at Figs. 3.12 and 3.13, we recognize the similarity to Fig. 3.4 for the same reasons as discussed before.

The position spectra  $|\psi_{k,l}(x)|^2$  and  $|\psi_{o,p}(x)|^2$  of (3.26) and (3.27), respectively are drawn in Figs. 3.14 to 3.17. In Fig. 3.14 three peaks can be realized for  $|\psi_k(x)|^2$  and only two peaks for  $|\psi_l(x)|^2$ . The large peak in  $|\psi_k(x)|^2$  arises from superposition of two peaks at the same position  $k_0 x = 1000$ , whereas for  $|\psi_l(x)|^2$ , the two peaks annihilate each other at that position. In beams  $o$  and  $p$  it is the opposite way around, as can be seen from Fig. 3.15. The right and left side wings are the same in both figures and, therefore, the four functions  $|\psi_{k,l,o,p}(x)|^2$  are identical here. The position coordinates of these peaks are

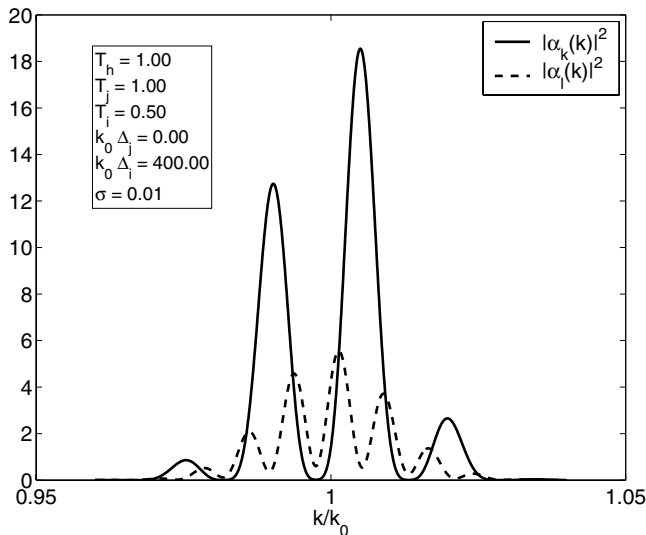


**Fig. 3.10.** Momentum spectra  $|\alpha_{k,l}(k)|^2$  of (3.30). The parameters of the first interferometer (pathways  $d$  and  $c$ ) are the same as in Fig. 3.3

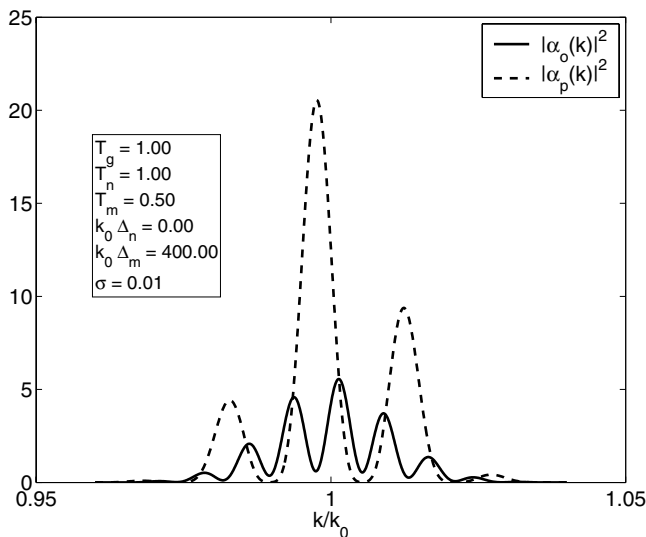


**Fig. 3.11.** Momentum spectra  $|\alpha_{o,p}(k)|^2$  of (3.31). The parameters of the first interferometer (pathways  $d$  and  $c$ ) are the same as in Fig. 3.3

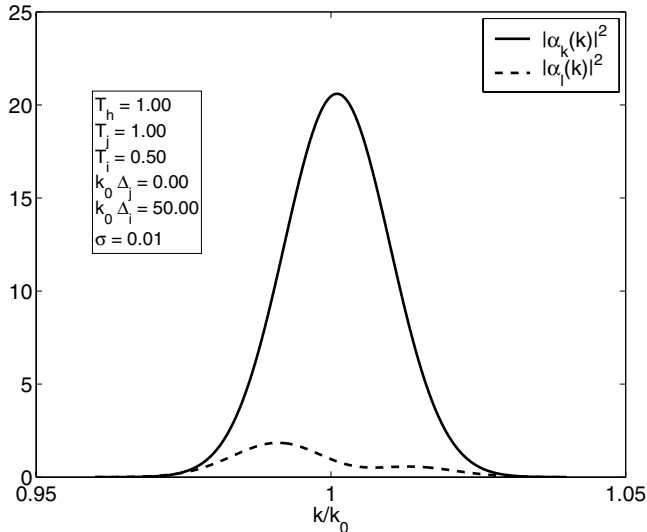


**Fig. 3.12.** Momentum spectra  $|\alpha_{k,l}(k)|^2$  of (3.30). The parameters of the first interferometer (pathways  $d$  and  $c$ ) are the same as in Fig. 3.4

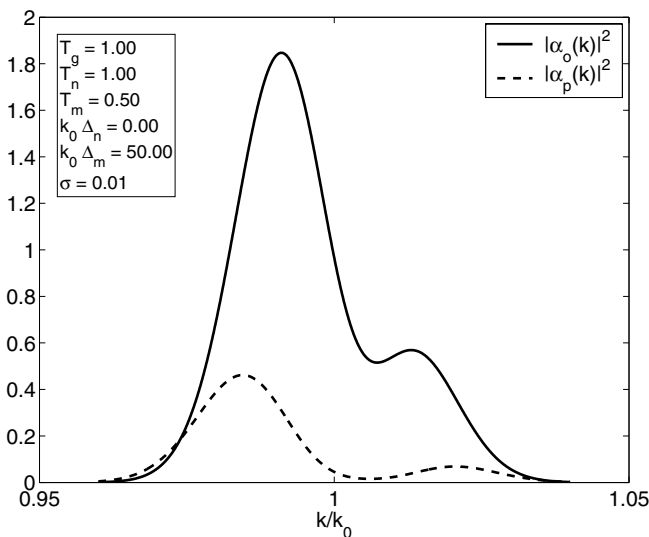


**Fig. 3.13.** Momentum spectra  $|\alpha_{o,p}(k)|^2$  of (3.31). The parameters of the first interferometer (pathways  $d$  and  $c$ ) are the same as in Fig. 3.4

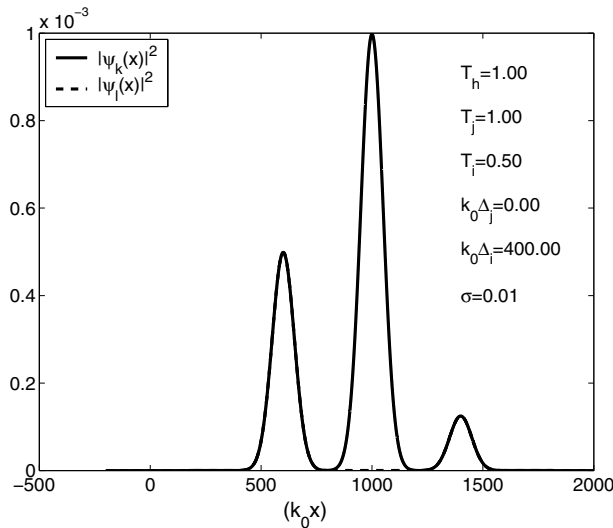


**Fig. 3.14.** Position spectra  $|\psi_{k,l}(x)|^2$  of (3.26). The parameters of the first interferometer (pathways  $d$  and  $c$ ) are the same as in Fig. 3.5. All lengths  $k_0 l_\alpha$  of the glass fiber segments are assumed to be equal to 200.00

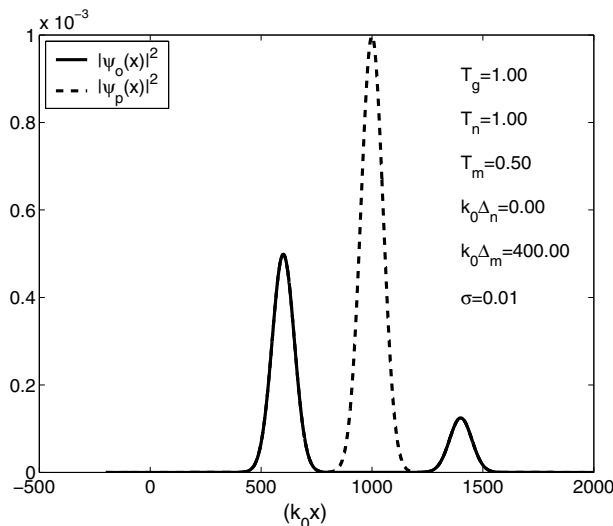


**Fig. 3.15.** Position spectra  $|\psi_{o,p}(x)|^2$  of (3.27). The parameters of the first interferometer (pathways  $d$  and  $c$ ) are the same as in Fig. 3.5

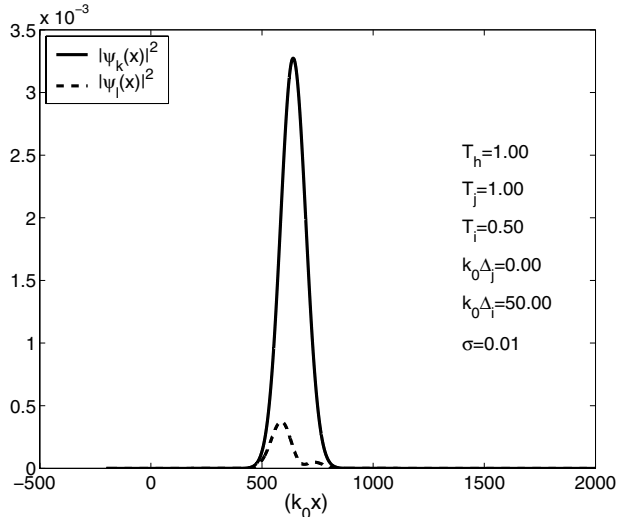


**Fig. 3.16.** Position spectra  $|\psi_{k,l}(x)|^2$  of (3.26). The parameters of the first interferometer (pathways  $d$  and  $c$ ) are the same as in Fig. 3.6

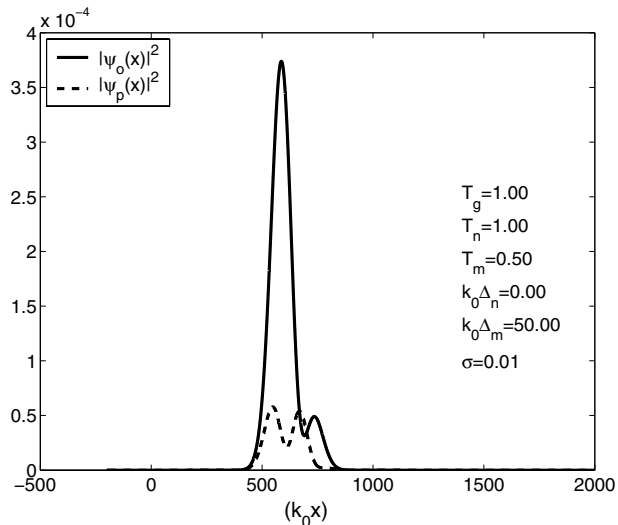


**Fig. 3.17.** Position spectra  $|\psi_{o,p}(x)|^2$  of (3.27). The parameters of the first interferometer (pathways  $d$  and  $c$ ) are the same as in Fig. 3.6

$k_0x = 600$  and  $k_0x = 1400$ , respectively, because of the lengths of the fiber segments on the one hand and of the maximum possible phase shifts on the other hand. For small phase shifts  $k_0\Delta_i = k_0\Delta_m = 50.00$  Figs. 3.16 and 3.17 exhibit peaks at position  $k_0x = 600$ . Almost all the intensity is concentrated in  $|\psi_k(x)|^2$  (notice the different scales in the figures). Small contributions are caused by interference between the corresponding wave functions. The spectra can be compared to those of Figs. 3.12 and 3.13. Basically one large Gaussian function  $|\alpha_k(k)|^2$  appears in Fig. 3.12.

To simplify matters, for the three MZ interferometer systems Fig. 3.9, the intensities  $I_{k,l}$  and  $I_{o,p}$  (see (3.28) and (3.29)) are drawn in Figs. 3.18 and 3.19, respectively, using transmission  $T = 1$  everywhere and using a parameter  $\sigma = 0.1$ , which is 10 times larger than in the previous pictures. As a consequence, the sum of the four intensities has to be one for any fixed value  $\beta$ :  $I_k + I_l + I_o + I_p = 1$ . As can be seen from the figures, the quantities  $I_k$  ( $I_o$ ) and  $I_l$  ( $I_p$ ) have opposite phase if  $\beta$  takes values around the fixed parameters  $k_0\Delta_i = 50$  and  $k_0\Delta_m = 50$ , respectively.

Finally, we consider the visibility in the  $k$  beam for  $\sigma \ll 1$  and  $\alpha = 0$ .  $\beta$  is varied and we get  $I_k \frac{\max}{\min} = \frac{1}{16} T_h (T_i + T_j + 2\sqrt{T_i T_j}) (T_d + T_c \pm 2\sqrt{T_d T_c})$ . The visibility is  $V = \frac{2\sqrt{T_d T_c}}{T_d + T_c}$  (as in (3.19)).

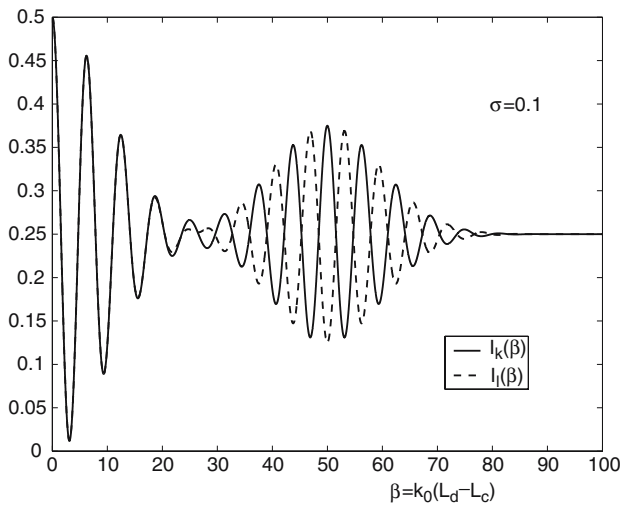


**Fig. 3.18.** Intensities  $I_{k,l}$  for the three MZ interferometer systems (Fig. 3.9) according to (3.28) as a function of the relative phase shift  $\beta = k_0(L_d - L_c)$  in the first MZ:  $\sigma = 0.1$ , transmission  $T = 1$  everywhere,  $k_0\Delta_i = 50$ . For  $\beta = 50$ , the intensities increase again and have opposite phase

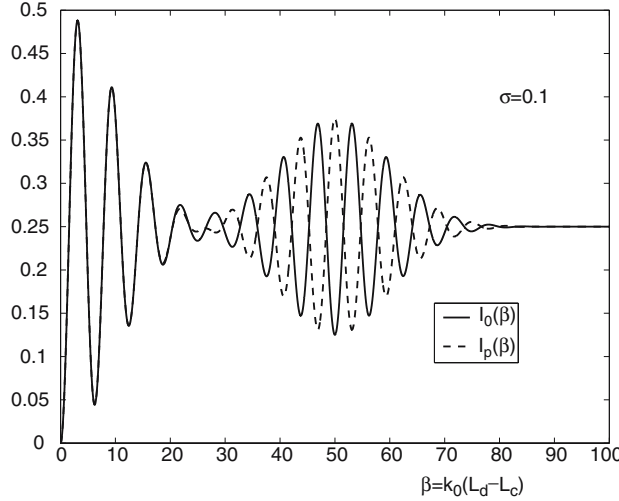


**Fig. 3.19.** Intensities  $I_{o,p}$  for the three MZ interferometer systems (Fig. 3.9) according to (3.29) as a function of the relative phase shift  $\beta = k_0(L_d - L_c)$  in the first MZ;  $\sigma = 0.1$ , transmission  $T = 1$  everywhere,  $k_0\Delta_m = 50$ . For  $\beta = 50$ , the intensities increase again and have opposite phase

### Comments on Phase Coding in Quantum Cryptography:

Two unbalanced Mach–Zehnder interferometers (one for Alice and one for Bob, the two communication parties) connected in series by a single optical fiber can be used to exchange a quantum key by the method of phase coding (an excellent overview on quantum cryptography, or quantum key distribution, can be found in [19]). The two Mach–Zehnder interferometers (input  $a$ , paths  $(c-d)$ ,  $h$ ,  $(i-j)$ , outputs  $(k, l)$ ) as seen in Fig. 3.9 constitute such a system. When monitoring counts as a function of time, Bob obtains three peaks (an example is given by the position spectra  $|\psi_{k,l}(x)|^2$  in Fig. 3.14). The left one corresponds to the cases where the photons chose the short paths both in Alice’s and in Bob’s interferometers, while the right one corresponds to photons taking the long paths in both interferometers. Finally, the central peak corresponds to photons choosing the short path in Alice’s interferometer and the long one in Bob’s, or vice versa. If these two processes are indistinguishable, they produce interference. A quantum key can be established by choosing the related phase shifts at Alice’s and Bob’s sides.

### 3.4 Double-Loop

In Fig. 3.20 a double-loop interferometer is depicted. Loop 1 consists of beam paths  $c$ ,  $d$  and  $f$ , whereas loop 2 is built up of beam paths  $f$ ,  $i$  and  $j$ . The

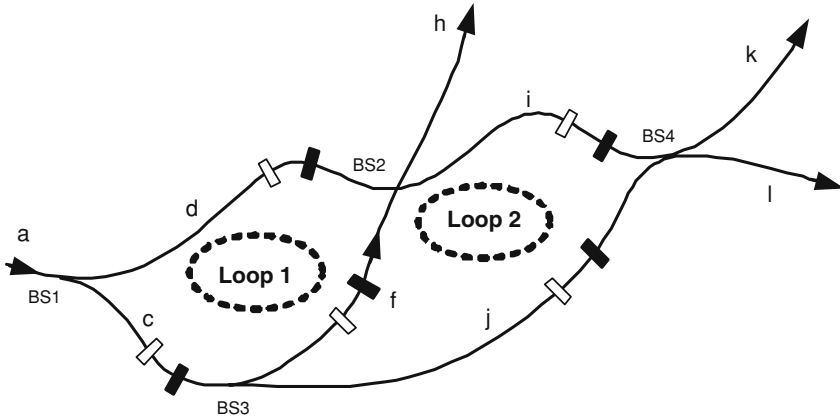


**Fig. 3.20.** Double loop interferometer: one input beam  $a$ , three output beams  $h, k, l$  and four beam splitters  $BS1-BS4$ . Beam path  $f$  belongs to both loops 1 and 2. The small white rectangles are phase shifters and the black ones are absorbers

outgoing beam  $h$  is only influenced by loop 1, while the output beams  $k$  and  $l$  are governed by both loops. So beam path  $f$  occupies a central position.

### 3.4.1 Wave Functions in a Double-Loop

The construction of the wave functions is carried out as in the preceding sections and for the suitable wave packets we get the following expressions:

$$\begin{aligned}\alpha_d(k) &= \frac{1}{\sqrt{2}}\alpha_a(k)\sqrt{T_d}e^{-ikL_d}, \quad \alpha_c(k) = \frac{1}{\sqrt{2}}\alpha_a(k)\sqrt{T_c}e^{-ikL_c}, \\ \alpha_f(k) &= \frac{1}{\sqrt{2}}\alpha_c(k)\sqrt{T_f}e^{-ikL_f}, \quad \alpha_j(k) = \frac{1}{\sqrt{2}}\alpha_c(k)\sqrt{T_j}e^{-ikL_j}, \\ \alpha_{h,i}(k) &= \frac{1}{\sqrt{2}}[\alpha_d(k) \pm \alpha_f(k)], \\ \alpha_{k,l}(k) &= \frac{1}{\sqrt{2}}[\sqrt{T_i}e^{-ikL_i}\alpha_i(k) \pm \alpha_j(k)].\end{aligned}\tag{3.32}$$

In the last two equations, the Hadamard transformation at the beam splitters  $BS2$  and  $BS4$  has been applied, respectively.

### 3.4.2 Spectra and Intensities in a Double-Loop

Equation (3.32) contains a chain of equations that have to be inserted and determined. A detailed discussion of the results presented in this section is given in the next section by means of a simple, but instructive, example.

We first consider beam  $h$  of Fig. 3.20. The results of the calculations are the following:

$$|\alpha_h(k)|^2 = \frac{1}{4} \alpha_a^2(k) \left\{ T_d + \frac{1}{2} T_c T_f + \sqrt{2T_d T_c T_f} \cos[k(L_d - L_c - L_f)] \right\}. \quad (3.33)$$

This spectrum depends only on parameters of the first loop, of course. The appropriate intensity is given by  $I_h = \int |\alpha_h(k)|^2 dk$  and we obtain

$$I_h = \frac{1}{4} \left\{ T_d + \frac{1}{2} T_c T_f + \sqrt{2T_d T_c T_f} e^{-(\delta k)^2 (L_d - L_c - L_f)^2 / 2} \right. \\ \left. \times \cos[k_0(L_d - L_c - L_f)] \right\}. \quad (3.34)$$

The position wave function  $\psi_h(x)$  of beam  $h$  is defined via the Fourier transformation of  $\alpha_h(k)$  and the result for the spectrum  $|\psi_h(x)|^2$  is

$$|\psi_h(x)|^2 = \sqrt{\frac{2(\delta k)^2}{\pi}} \left\{ \frac{1}{4} T_d e^{-2(\delta k)^2 (x - L_d)^2} + \frac{1}{8} T_c T_f e^{-2(\delta k)^2 (x - L_c - L_f)^2} \right. \\ \left. + \frac{1}{4} \sqrt{2T_d T_c T_f} e^{-(\delta k)^2 [(x - L_d)^2 + (x - L_c - L_f)^2]} \right. \\ \left. \times \cos[k_0(L_d - L_c - L_f)] \right\}. \quad (3.35)$$

The spectra and intensities in the outgoing beams  $k$  and  $l$  are the following.

Momentum spectra:

$$|\alpha_{k,l}(k)|^2 = \frac{1}{8} \alpha_a^2(k) \left\{ T_d T_i + \frac{1}{2} T_f T_i T_c + T_j T_c \right. \\ \mp T_c \sqrt{2T_f T_j T_i} \cos[k(L_f + L_i - L_j)] \\ - \sqrt{2T_d T_c T_i} [\sqrt{T_f T_i} \cos[k(L_d - L_c - L_f)] \\ \mp \sqrt{2T_j} \cos[k(L_d + L_i - L_c - L_f)]] \right\}. \quad (3.36)$$

Intensities:

$$I_{k,l} = \frac{1}{8} \left\{ T_d T_i + \frac{1}{2} T_f T_i T_c + T_j T_c \right. \\ \mp T_c \sqrt{2T_f T_j T_i} e^{-(\delta k)^2 (L_f + L_i - L_j)^2 / 2} \cos[k_0(L_f + L_i - L_j)] \\ - \sqrt{2T_d T_c T_i} [\sqrt{T_f T_i} e^{-(\delta k)^2 (L_d - L_c - L_f)^2 / 2} \cos[k_0(L_d - L_c - L_f)] \\ \mp \sqrt{2T_j} e^{-(\delta k)^2 (L_d + L_i - L_c - L_f)^2 / 2} \cos[k_0(L_d + L_i - L_c - L_f)]] \right\}. \quad (3.37)$$

Position spectra:

$$\begin{aligned}
 |\psi_{k,l}(x)|^2 = & \frac{1}{8} \sqrt{\frac{2(\delta k)^2}{\pi}} \{ T_d T_i e^{-2(\delta k)^2(x-L_d-L_i)^2} \\
 & + \frac{1}{2} T_c T_f T_i e^{-2(\delta k)^2(x-L_c-L_f-L_i)^2} + T_j T_c e^{-2(\delta k)^2(x-L_c-L_j)^2} \\
 & \mp T_c \sqrt{2T_f T_i T_j} e^{-(\delta k)^2[(x-L_c-L_f-L_i)^2+(x-L_c-L_j)^2]} \\
 & \times \cos[k_0(L_f + L_i - L_j)] \\
 & - \sqrt{2T_d T_c T_i} [\sqrt{T_f T_i} e^{-(\delta k)^2[(x-L_c-L_f-L_i)^2+(x-L_d-L_i)^2]} \\
 & \times \cos[k_0(L_d - L_c - L_f)] \\
 & \mp \sqrt{2T_j} e^{-(\delta k)^2[(x-L_d-L_i)^2+(x-L_c-L_j)^2]} \\
 & \times \cos[k_0(L_d + L_i - L_c - L_j)]] \}.
 \end{aligned}$$

An instructive example of a balanced double loop interferometer is presented in Figs. 3.21 and 3.22 where the spectra  $|\alpha_{h,k,l}(k)|^2$  of (3.33) and (3.36) are drawn, using a simple parameter set. In Fig. 3.21 all phase shifts are chosen to be zero. All spectra have a Gaussian shape. As can be immediately verified from (3.34) and (3.37), the intensities are as follows:  $I_h = (6\sqrt{2}+8)/(16\sqrt{2}) = 0.72855$ ,  $I_k = (9\sqrt{2}-8)/(16\sqrt{2}) = 0.20895$  and  $I_l = \sqrt{2}/(16\sqrt{2}) = 0.06250$ , where  $I_h + I_k + I_l = 1$ . The areas below the curves in Fig. 3.21 correspond to

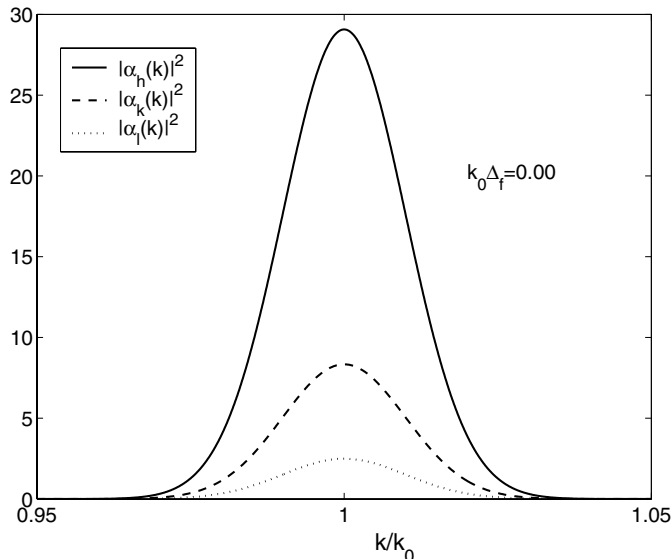


**Fig. 3.21.** Momentum spectra  $|\alpha_{h,k,l}(k)|^2$  according to (3.33) and (3.36) of a balanced double loop interferometer (compare to Fig. 3.23). All transmission coefficients  $T_\kappa = 1$ , fiber lengths  $l_i = l_f = l_c = \bar{l}$ ,  $l_d = l_j = 2\bar{l}$  and phase shifts  $\Delta_i = \Delta_j = \Delta_d = \Delta_c = \Delta_f = 0$ ,  $\sigma = 1/100$ ,  $k_0 = 1$

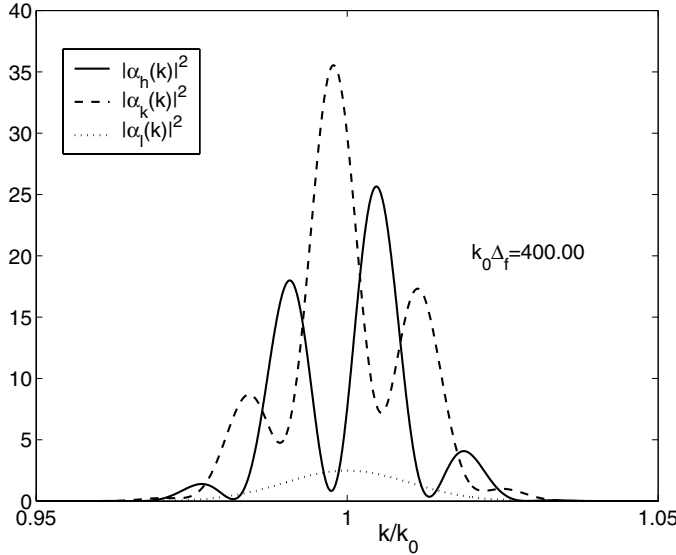


**Fig. 3.22.** Same functions and parameters as in Fig. 3.21, but  $k_0\Delta_f = 400$

the intensities given above. More than 70% of the intensity escapes through the output port  $h$ . If the phase shift  $k_0\Delta_f = 400$ , the spectra  $|\alpha_h(k)|^2$  and  $|\alpha_k(k)|^2$  have an oscillatory appearance, as can be seen from Fig. 3.22 and most of the intensity is found in output port  $k$ .

### 3.4.3 Simple Example of Visibility in a Double-Loop

We apply (3.37) to a simple double loop example (see Fig. 3.23). In order to find an interesting formula of the visibility in beam  $k$  we permit only one transmission coefficient  $T_f = e^{-2a_f}$  to be  $\leq 1$  (all other transmissions  $T$  should be = 1). A definite phase shifter  $P_j = e^{-ik\Delta_j}$  is taken and  $P_f = e^{-ik\Delta_f}$  is varied. All other phase shifts  $\Delta$  should be = 0. The lengths of the arms of the interferometer are as follows:  $l_c = l_f = l_i = \bar{l}$  and  $l_d = l_j = 2\bar{l}$ . So the interferometer in Fig. 3.23 is balanced. If again  $\sigma \ll 1$ , the intensity in beam  $k$  reads (see (3.37))

$$I_k = \frac{1}{8} \left\{ \frac{1}{2} T_f - \sqrt{2T_f} [\cos[k_0(\Delta_f - \Delta_j)] + \cos(k_0\Delta_f)] + 4 \cos^2 \left( \frac{k_0\Delta_j}{2} \right) \right\}. \quad (3.38)$$

This intensity has maxima at  $(k_0\Delta_f) = (k_0\Delta_j)/2 + (2n+1)\pi$  and minima at  $(k_0\Delta_f) = (k_0\Delta_j)/2 + 2n\pi$ . Then we have

$$I_{k_{\max}} = \frac{1}{16} \left\{ T_f \pm 4 \cos \left( \frac{k_0\Delta_j}{2} \right) \left[ \sqrt{2T_f} \pm 2 \cos \left( \frac{k_0\Delta_j}{2} \right) \right] \right\}. \quad (3.39)$$

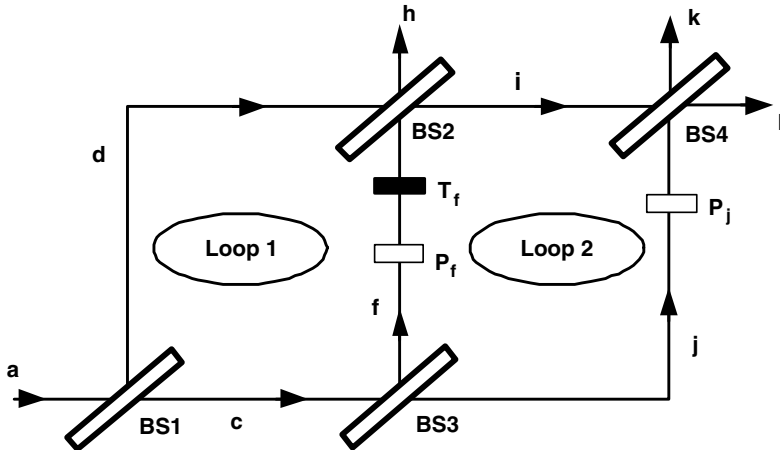


**Fig. 3.23.** A balanced double loop interferometer: one input beam  $a$ , three output beams  $h, k, l$  and four beam splitters  $BS1-BS4$ . Beam path  $f$  belongs to both loops 1 and 2. The two small white rectangles are phase shifters  $P_f = e^{-ik\Delta_f}$  and  $P_j = e^{-ik\Delta_j}$ , respectively, and the black rectangle is an absorber  $T_f = e^{-2a_f}$

According to the definition of the visibility in (3.17) we get

$$V = \frac{4 \cos(\frac{k_0 \Delta_j}{2}) \sqrt{2T_f}}{T_f + 8 \cos^2(\frac{k_0 \Delta_j}{2})}. \quad (3.40)$$

We have the interesting result:

$$V = 1 \rightarrow T_f = 8 \cos^2\left(\frac{k_0 \Delta_j}{2}\right). \quad (3.41)$$

If, for example, the transmission  $T_f$  in beam  $f$  is given, one can obtain  $V = 1$  in the output beam  $k$  by appropriately adjusting the phase shift  $\Delta_j$  in beam path  $j$  via (3.41). We will see later in Part III that a similar effect can be achieved in a double loop neutron interferometer. We refer, therefore, to Sect. 8.3.2 for a discussion of visibility aspects in a double loop interferometer.

### 3.5 Mach–Zehnder with Two Inputs

We discuss an MZ with two input ports  $a$  and  $b$  (see Fig. 3.24). Assuming two different Gaussian momentum distributions

$$\alpha_{a,b}(k) = \left[ \frac{1}{2(\delta k)_{a,b}^2 \pi} \right]^{1/4} \exp\left\{ -\frac{(k - k_0)^2}{4(\delta k)_{a,b}^2} \right\}, \quad (3.42)$$

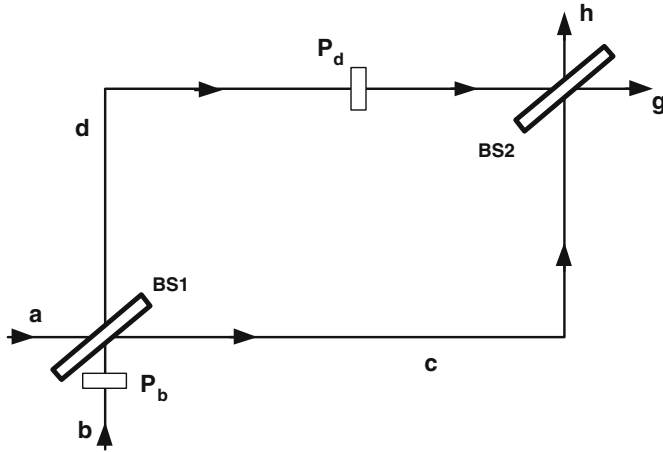


**Fig. 3.24.** Mach-Zehnder with two inputs beams  $a, b$ , two output beams  $h, g$  and two beam splitters  $BS1, BS2$ . The small white rectangles are the phase shifters  $P_b = e^{-ik\Delta_b}$  and  $P_d = e^{-ik\Delta_d}$

the normalization condition

$$\int [c_a^2 \alpha_a^2(k) + c_b^2 \alpha_b^2(k)] dk = 1, \rightarrow c_a^2 + c_b^2 = 1 \quad (3.43)$$

should be valid.  $(\delta k)_a^2$  and  $(\delta k)_b^2$  are the mean square deviations of the Gaussian distributions. The phase shift  $\Delta_b$  in beam  $b$  is varied.  $\Delta_d$  is an arbitrary, but fixed value.

### 3.5.1 Wave Functions, Spectra and Intensities

Directly in front of the beam splitter  $BS1$  the wave functions are:  
beam  $a$ :

$$\alpha_a(k), \psi_a(x) = \left[ \frac{2(\delta k)_a^2}{\pi} \right]^{1/4} e^{-(\delta k)_a^2 x^2 + ik_0 x}. \quad (3.44)$$

beam  $b$ :

$$\alpha_b(k) e^{-ik\Delta_b}, \psi_b(x) = \left[ \frac{2(\delta k)_b^2}{\pi} \right]^{1/4} e^{-(\delta k)_b^2 (x - \Delta_b)^2 + ik_0 (x - \Delta_b)}. \quad (3.45)$$

Applying the Hadamard transformation, the momentum wave functions directly in front of the beam splitter  $BS2$  are

$$\begin{aligned} \alpha_d(k) &= \frac{1}{\sqrt{2}} e^{-ik\Delta_d} [\alpha_a(k) + \alpha_b(k) e^{-ik\Delta_b}], \\ \alpha_c(k) &= \frac{1}{\sqrt{2}} [\alpha_a(k) - \alpha_b(k) e^{-ik\Delta_b}]. \end{aligned} \quad (3.46)$$

Behind the beam splitter  $BS2$  the wave packets are:

$$\begin{pmatrix} \alpha_h(k) \\ \alpha_g(k) \end{pmatrix} = \hat{H} \begin{pmatrix} \alpha_d(k) \\ \alpha_c(k) \end{pmatrix}. \quad (3.47)$$

Adding everything together, the spectra and intensities at the output read as follows.

Momentum spectra:

$$\begin{aligned} |\alpha_{h,g}(k)|^2 = & \frac{1}{2} \{ c_a^2 \alpha_a^2(k) [1 \pm \cos(k\Delta_d)] + c_b^2 \alpha_b^2(k) [1 \mp \cos(k\Delta_d)] \\ & \mp c_a c_b \alpha_a(k) \alpha_b(k) [\cos[k(\Delta_d - \Delta_b)] - \cos[k(\Delta_d + \Delta_b)]] \} \end{aligned} \quad (3.48)$$

Position spectra:

$$\begin{aligned} |\psi_{h,g}(x)|^2 = & \frac{1}{4} \left\{ \sqrt{\frac{2(\delta k)_a^2}{\pi}} c_a^2 [e^{-2(\delta k)_a^2(x-\Delta_d)^2} + e^{-2(\delta k)_a^2 x^2} \right. \\ & \pm 2 \cos(k_0 \Delta_d) e^{-(\delta k)_a^2[(x-\Delta_d)^2+x^2]}] \\ & + \sqrt{\frac{2(\delta k)_b^2}{\pi}} c_b^2 [e^{-2(\delta k)_b^2(x-\Delta_b-\Delta_d)^2} + e^{-2(\delta k)_b^2(x-\Delta_b)^2} \\ & \mp 2 \cos(k_0 \Delta_d) e^{-(\delta k)_b^2[(x-\Delta_b-\Delta_d)^2+(x-\Delta_b)^2]}] \\ & + 2 c_a c_b \sqrt{\frac{2(\delta k)_a (\delta k)_b}{\pi}} \left[ \cos(k_0 \Delta_b) (e^{-(\delta k)_a^2(x-\Delta_d)^2} - e^{-(\delta k)_b^2(x-\Delta_b-\Delta_d)^2} \right. \\ & \left. - e^{-(\delta k)_a^2 x^2} - e^{-(\delta k)_b^2(x-\Delta_b)^2}) \right. \\ & \pm \cos[k_0(\Delta_b + \Delta_d)] e^{-(\delta k)_a^2 x^2 - (\delta k)_b^2(x-\Delta_b-\Delta_d)^2} \\ & \left. \mp \cos[k_0(\Delta_b - \Delta_d)] e^{-(\delta k)_a^2(x-\Delta_d)^2 - (\delta k)_b^2(x-\Delta_b)^2} \right] \} \end{aligned} \quad (3.49)$$

Intensities:

$$\begin{aligned} I_{h,g} = & \frac{1}{2} \left\{ c_a^2 [1 \pm e^{-(\delta k)_a^2 \Delta_d^2/2} \cos(k_0 \Delta_d)] + c_b^2 [1 \mp e^{-(\delta k)_b^2 \Delta_d^2/2} \cos(k_0 \Delta_d)] \right. \\ & \mp c_a c_b \sqrt{\frac{2(\delta k)_a (\delta k)_b}{(\delta k)_a^2 + (\delta k)_b^2}} \left[ e^{-\frac{(\delta k)_a^2 (\delta k)_b^2}{(\delta k)_a^2 + (\delta k)_b^2} (\Delta_d - \Delta_b)^2} \cos[k_0(\Delta_d - \Delta_b)] \right. \\ & \left. - e^{-\frac{(\delta k)_a^2 (\delta k)_b^2}{(\delta k)_a^2 + (\delta k)_b^2} (\Delta_d + \Delta_b)^2} \cos[k_0(\Delta_d + \Delta_b)] \right] \} \end{aligned} \quad (3.50)$$

Figure 3.25 presents six examples (a to f) of the momentum spectra  $|\alpha_{h,g}(k)|^2$  of (3.48), and Fig. 3.26 six examples of the corresponding position spectra  $|\psi_{h,g}(x)|^2$  of (3.49). In Fig. 3.25a, the special case  $c_a = 1$  (i.e.,  $c_b = 0$ ), is shown

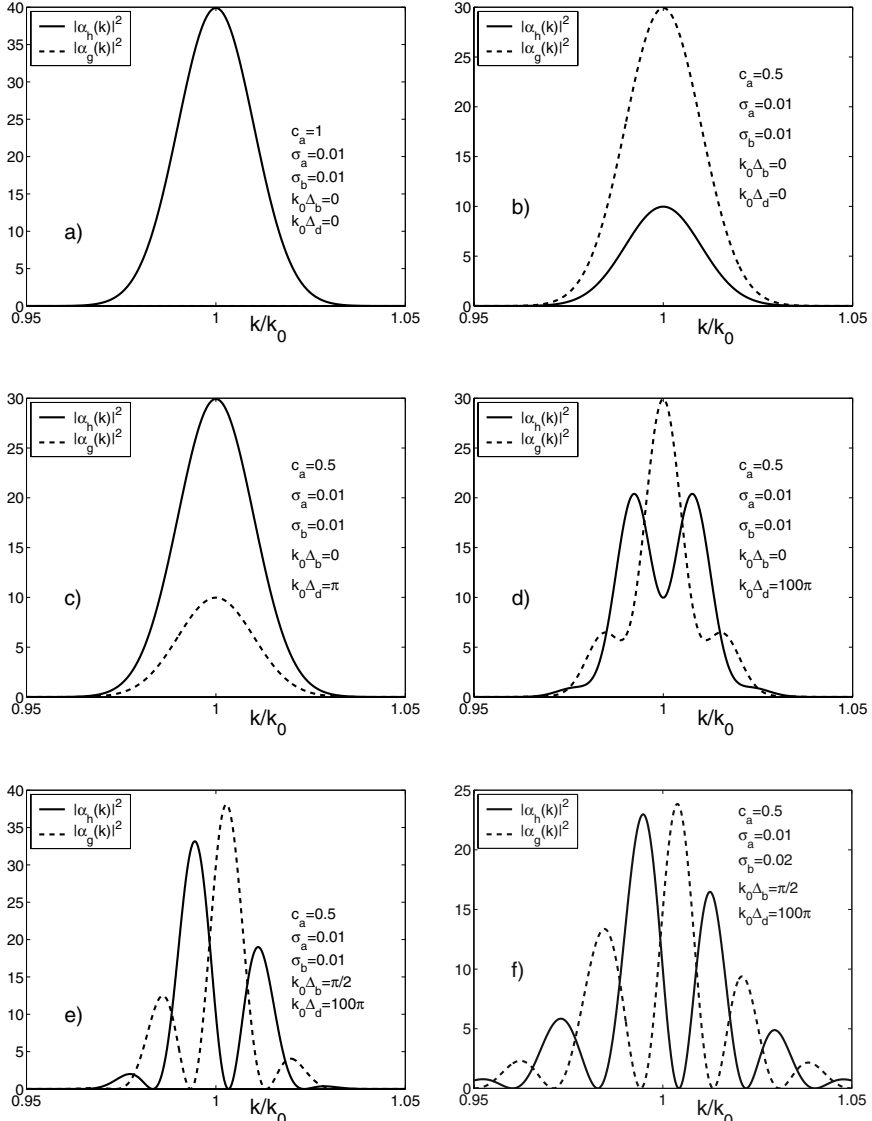


**Fig. 3.25.** Momentum spectra  $|\alpha_{h,g}(k)|^2$  of (3.48) for the Mach–Zehnder interferometer with two inputs (see Fig. 3.24). The subdiagrams a) to f) are explained in the text

which corresponds to an MZ interferometer with only one input, and no phase shift is included. Consequently,  $|\alpha_h(k)|^2$  is strictly a Gaussian function and  $|\alpha_g(k)|^2$  is zero. The corresponding position spectra  $|\psi_{h,g}(x)|^2$  are given in Fig. 3.26a. If  $c_a = 0.5$ , the spectrum  $|\alpha_h(k)|^2$  has a statistical weight of 1/4 and  $|\alpha_g(k)|^2$  a weight of 3/4. This case is graphically displayed in Figs. 3.25b and 3.26b, respectively. In Figs. 3.25c and 3.26c the phase shift  $k_0\Delta_d = \pi$  provokes an interchange between the spectra discussed before. A phase shift of  $k_0\Delta_d = 100\pi$  entails explicit oscillations in the momentum spectra  $|\alpha_{h,g}(k)|^2$  as seen in Fig. 3.25d. However, the position spectra  $|\psi_{h,g}(x)|^2$  of Fig. 3.26d are practically the same because of the almost complete attenuation of interference terms. Two peaks of largely different heights emerge. In Fig. 3.25e an additional phase shift  $k_0\Delta_b = \pi/2$  has been included. This action changes the momentum spectra  $|\alpha_{h,g}(k)|^2$  dramatically and the two peaks of the position spectra  $|\psi_{h,g}(x)|^2$  become almost equal in height. Finally, the mean square deviation of  $\alpha_b(k)$  has been changed from  $\sigma_b = 0.01$  to  $\sigma_b = 0.02$ . This has effect of broadening on the momentum spectra and a narrowing effect on the position spectra, as can be observed in Figs. 3.25f and 3.26f.

### 3.5.2 Discussion of MZ with Two Inputs

Since there is no absorption included in the model in Fig. 3.24, the intensities  $I_h$  and  $I_g$  sum up to 1. We discuss the visibility in beam  $h$ . Taking  $\sigma_a$  and  $\sigma_b$  to be  $\ll 1$ , the intensity  $I_h$  reads

$$I_h = \frac{1}{2} \{1 + (c_a^2 - c_b^2) \cos(k_0\Delta_d) - 2c_a c_b \sin(k_0\Delta_b) \sin(k_0\Delta_d)\}, \quad (3.51)$$

where  $k_0\Delta_d$  is a fixed parameter and  $k_0\Delta_b$  is a variable. The maxima and minima of this function are

$$(I_h)_{\frac{\max}{\min}} = \frac{1}{2} \{1 + (c_a^2 - c_b^2) \cos(k_0\Delta_d) \pm 2c_a c_b \sin(k_0\Delta_d)\}, \quad (3.52)$$

and the visibility is

$$V = \frac{2c_a c_b \sin(k_0\Delta_d)}{1 + (c_a^2 - c_b^2) \cos(k_0\Delta_d)}, \quad c_a^2 + c_b^2 = 1. \quad (3.53)$$

The visibility is equal to 1 under the following conditions:

$$V = 1 \rightarrow c_a = \sin(k_0\Delta_d/2), \quad c_b = \cos(k_0\Delta_d/2). \quad (3.54)$$

Hence the phase shift  $\Delta_d$  can be adjusted according to the amplitudes  $c_a$  and  $c_b$  of the incoming spectra in such a way that the visibility becomes 1 in beam  $h$ . If we take  $V = 1$  into consideration, the intensity  $I_h$  becomes

$$V = 1 \rightarrow I_h = 2c_a^2 c_b^2 [1 - \sin(k_0\Delta_b)]. \quad (3.55)$$

In the case where one input signal is very weak, the output signal  $I_h$  is proportional to this weak input signal if  $V = 1$ . This is an interferometric method for measuring weak signals.

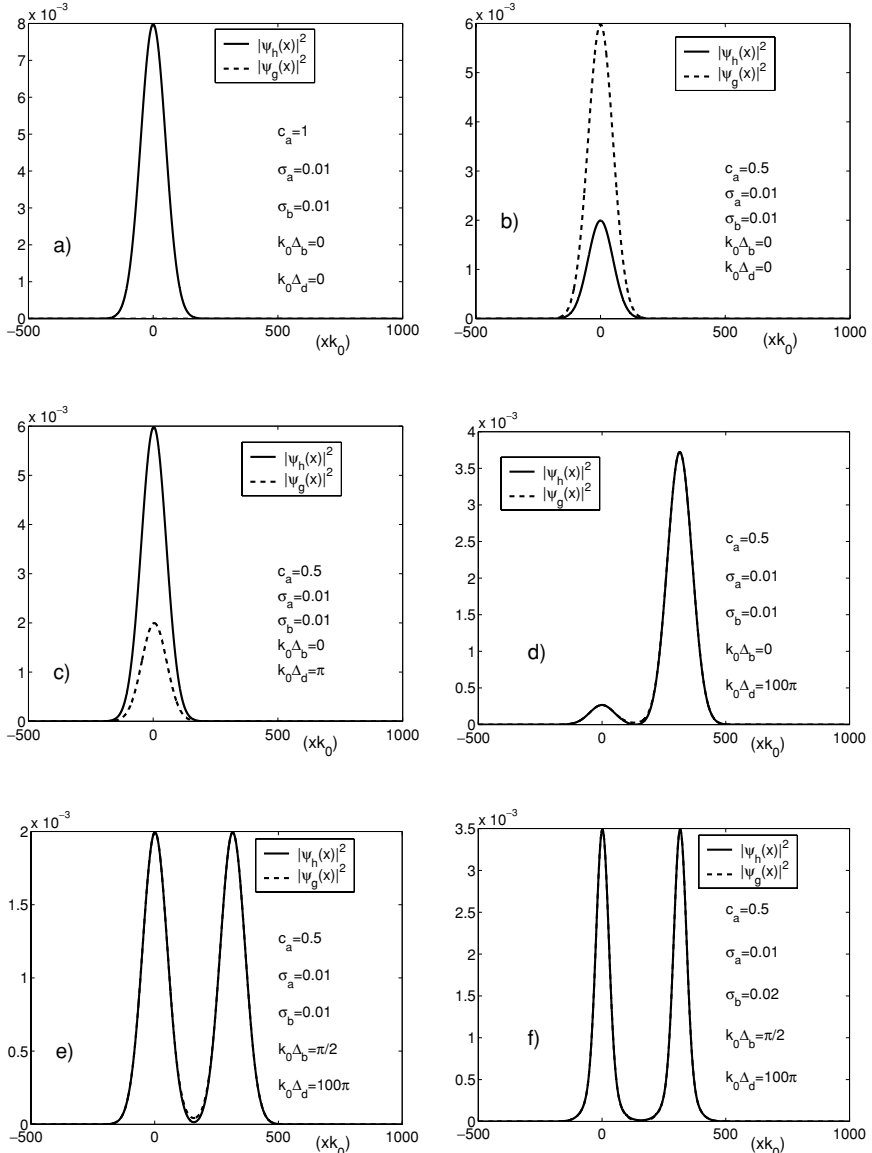


**Fig. 3.26.** Position spectra  $|\psi_{h,g}(x)|^2$  of (3.49) for the Mach–Zehnder interferometer with two inputs (see Fig. 3.24). The subdiagrams a) to f) are explained in the text

### 3.6 Comment on Two-Photon Interference

The considerations above apply to the input of single-photon states. However, a lot of literature is dedicated to interferometry using entangled states or two-photon interferometry (see, e.g., [9, 15, 16, 20–22]). In this case, pairs of signal and idler photons are produced by spontaneous parametric down-conversion and are sent into the two beams  $a$  and  $b$  mentioned above. “Postponed compensation” experiments suggest that the observed two-photon entangled state interference cannot be pictured in terms of the overlap of the two individual photon wave packets on a beam splitter. If the two photons do not arrive simultaneously, each has a 50% chance of going either way after the beam splitter, independently of the other photon. This results in coincidences. However, if the photons arrive simultaneously, they become indistinguishable and end up together randomly in either beam. In the experiment, the rate of co-incident photon detections at the beam splitter outputs can be monitored. The resulting coincidence rate is called Hong–Ou–Mandel coincidence [8, 21]. An analytical treatment of time-resolved two-photon quantum interference is also presented in the literature [23]. Different aspects of the phenomenon are elaborated using different representations of the single-photon wave packets, like the decomposition into single-frequency field modes or spatio-temporal modes matching the photonic wave packets. Both representations lead to equivalent results.

Here we do not discuss such interferometers, but refer only to the literature.

## Part III

### Neutron Interferometry

## 4 Introductory Remarks

Neutron interferometry is a part of neutron optics. Among the various areas of neutron optical research, neutron interferometry has provided some of the most challenging and spectacular developments [24]. In most cases, separated coherent beams, which are produced either by wavefront division (Young's type) or by amplitude division (Mach-Zehnder type), are used. These beams are subsequently coherently superposed, after passing through regions of space where the neutron wave function is modified in phase and amplitude by various interactions: nuclear, magnetic, electromagnetic, gravitational, or by geometry and topology. Here we are dealing with the coherence properties of neutron interferometry. Thereby the perfect crystal neutron interferometer plays a central role in our considerations.

The perfect crystal interferometer [24], which is considered here, provides widely separated coherent beams and has become a standard method for advanced optical investigations. The superposition of spin-up and spin-down states in the longitudinal direction provides the basis for Larmor and Ramsey interferometry. The well-known spin-echo systems [25] and zero-field spin-echo systems [26] are examples of such interferometers and are discussed in Part IV.

The operation of silicon perfect crystal neutron interferometers is based on division of amplitudes by dynamical Bragg diffraction for perfect crystals (see Chap. 5). In the standard version, a monolithic triple-plate system in the Laue transmission geometry is used (see Fig. 6.1). Its geometry is analogous to the well-known Mach-Zehnder interferometer of light optics. The most essential feature is that the reflecting planes are exactly arranged throughout the whole crystal with a precision comparable to the lattice parameter. The perfect silicon crystal interferometer is extremely useful for fundamental neutron physics studies and for studies of the basic quantum mechanical principles of nature.

This part of the book is organized as follows. After some preliminary remarks about the coherence length and neutron wave packets, we firstly focus on the dynamical theory of diffraction, which provides us with the basic principles of neutron diffraction in single crystals. Subsequently, the application of the theory to the Laue-type interferometer is carried out. In a

third step, the superposition of wave packets in the three-plate interferometer is discussed, where the Wigner function and the Q-function play an important role. Dephasing and decoherence are further issues to be considered. Fourthly, the four-plate neutron interferometer is treated, including a discussion about double-loop interferometry and correlation functions.

## 4.1 Coherence Length

Heisenberg's minimum uncertainty relation, as discussed briefly in Sect. 2.1.1, is given by

$$(\delta k)(\delta x) = \frac{1}{2}. \quad (4.1)$$

This relation defines the coherence length  $l_c \equiv (\delta x)$ , which can be expressed alternatively by using  $k = 2\pi/\lambda$ , where  $\lambda$  is the wave length:

$$l_c \equiv (\delta x) = \frac{1}{2(\delta k)} = \frac{1}{4\pi} \frac{\lambda^2}{(\delta \lambda)}. \quad (4.2)$$

The smaller the uncertainty  $(\delta k)$  of a wave packet, the larger the coherence length  $l_c$ . Because of the finite spectral width  $(\delta k)$  of a Gaussian wave number distribution  $\alpha(k)$  (2.3), a free neutron wave packet is localized in space (see (2.6)). This is in contrast to a plane wave  $e^{ikx-i\Omega t}$  with  $\Omega = \hbar k^2/(2M) = E/\hbar$ , which has a fixed wave number  $k$ , but is infinitely expanded in space (infinite coherence length for plane waves). In the following sections, we investigate interference phenomena. We shall see that the separation of wave packets is due to a finite coherence length.

## 4.2 Wigner Function, Wave Packets and Shannon Entropy

The time-dependent wave function  $\psi(x, t)$  of a wave packet and the corresponding Gaussian wave-number function  $\alpha(k)$  are derived in (2.5) and (2.3), respectively. The appropriate Wigner function  $W_{WP}(x, k, t)$  was evaluated in (2.7). In the phase-space picture, a general expression for  $W(x, k, t)$  can be given according to (2.2) and (2.11) in a two-fold manner:

$$\begin{aligned} W(x, k, t) &= \frac{1}{2\pi} \int \psi^* \left( x + \frac{x'}{2}, t \right) \psi \left( x - \frac{x'}{2}, t \right) e^{ikx'} dx' \\ &= \frac{1}{2\pi} \int \alpha^* \left( k + \frac{k'}{2} \right) \alpha \left( k - \frac{k'}{2} \right) e^{-ik'(x-vt)} dk'. \end{aligned} \quad (4.3)$$

Here  $v = \hbar k/M$  is the group velocity of the wave packet.  $\alpha(k)$  is time-independent, whereas  $\psi(x, t)$  depends on time. Now some important properties of the Wigner function (see Sect. 2.1.2) are recalled:

$$\int W(x, k, t) dx = |\alpha(k)|^2 , \quad \int W(x, k, t) dk = |\psi(x, t)|^2 , \\ \iint W(x, k, t) dk dx = 1. \quad (4.4)$$

Because of the normalization of the position distribution  $|\psi(x, t)|^2$  and the momentum distribution  $|\alpha(k)|^2$ , that is to say  $\int |\psi(x, t)|^2 dx = \int |\alpha(k)|^2 dk = 1$ , expectation values

$$\langle x^i \rangle = \int |\psi(x, t)|^2 x^i dx , \quad \langle k^i \rangle = \int |\alpha(k)|^2 k^i dk \quad (4.5)$$

can be evaluated. Taking wave packets ((2.6) and (2.3)) into account, the expectation values for  $i = 1, 2$  are:

$$\langle x \rangle = v_0 t , \quad \langle x^2 \rangle = (v_0 t)^2 + [\Delta x(t)]^2 , \quad \langle k \rangle = k_0 , \quad \langle k^2 \rangle = k_0^2 + (\delta k)^2 . \quad (4.6)$$

It is interesting to assess the mean square deviations using these results. We get:

$$\langle [\Delta x(t)]^2 \rangle \equiv \langle x^2 \rangle - \langle x \rangle^2 = [\Delta x(t)]^2 , \\ \langle (\Delta k)^2 \rangle \equiv \langle k^2 \rangle - \langle k \rangle^2 = (\delta k)^2 , \quad (4.7)$$

where  $[\Delta x(t)]^2 = [1 + (\gamma t)^2]/[4(\delta k)^2]$ . Hence Heisenberg's uncertainty relation reads as follows:

$$\langle [\Delta x(t)]^2 \rangle \langle (\Delta k)^2 \rangle = \frac{1}{4} [1 + (\gamma t)^2] \geq \frac{1}{4} . \quad (4.8)$$

Here  $\gamma = 2\hbar(\delta k)^2/M$ . If  $t = 0$ , Heisenberg's minimum uncertainty relation (4.1) is obtained.

Another uncertainty measure is sometimes taken into account. This is called the Shannon entropy [27]. However, for any probability distribution, we define a quantity called the Shannon entropy, which has many properties that agree with the intuitive notion of what a measure of information should be. Entropy then becomes the self-information of a random variable. Here we focus on continuous random variables, and the differential entropy  $H(X)$  of a continuous random variable  $X$  with a probability density function  $f(x)$  is defined as

$$H(X) = - \int_S f(x) \ln f(x) dx , \quad (4.9)$$

where  $S$  is the support set of the random variable.

Using the distribution functions mentioned above, we can define two types of Shannon entropy:

$$H_x = - \int |\psi(x, t)|^2 \ln[|\psi(x, t)|^2] dx, \quad H_k = - \int |\alpha(k)|^2 \ln[|\alpha(k)|^2] dk. \quad (4.10)$$

For wave packets we derive

$$(H_x)_{WP} = \ln \left\{ \frac{\sqrt{1 + (\gamma t)^2}}{2(\delta k)} \sqrt{2\pi e} \right\}, \quad (H_k)_{WP} = \ln \{(\delta k)\sqrt{2\pi e}\}. \quad (4.11)$$

If  $H \rightarrow -\infty$ , full information is available from the respective value,  $H \rightarrow +\infty$  means the opposite. The sum of the two entropies yields

$$(H_x)_{WP} + (H_k)_{WP} = \ln \{ \sqrt{\langle [\Delta x(t)]^2 \rangle \langle (\Delta k)^2 \rangle} 2\pi e \}. \quad (4.12)$$

If  $t = 0$ , the right-hand side of this equation is the constant  $\ln(\pi e) \simeq 2, 15$ .

## 5 The Dynamical Theory of Diffraction

Before discussing the neutron perfect silicon crystal interferometer, it is helpful to go into more details about the dynamical theory of diffraction of neutrons in single crystals, [24, 28]. Therefore, the main features of this theory are exhibited here.

Compared to the geometrical theory, the dynamical theory of diffraction accounts for the spatial periodicity of the interaction potential in perfect single crystals. Thereby the Schrödinger equation has to be solved taking this potential into account.

When neutron radiation is brought into a perfect crystal under near-Bragg orientation conditions, the dynamical theory of diffraction predicts a coherent splitting of the incident wave into four components, with two travelling wave components passing within the crystal in the Bragg direction and two components in the forward, or incident, direction. Each of these four components represents a permitted solution of the excitation dynamics of the three-dimensional lattice for the orientation of the incident ray. In general, each of the four components is to be described by different wave vectors, differing in both magnitude and direction. Ewald has shown in his historic investigation of the dynamical theory of x-ray diffraction (which characterizes neutron diffraction as well), that this splitting will result in a periodic beating of radiation density travelling in either the Bragg or forward direction at different depths in the crystal, this feature being described as a Pendellösung structure. Excellent reviews of the dynamical theory of x-ray diffraction have been given by James [29] and Batterman and Cole [30], where both the theory and experimental verification are treated in detail. Goldberger and Seiz [31] have discussed the applicability of the dynamical theory to the neutron case, and Sippel, Kleinstück and Schulze [32] have demonstrated in a neutron experiment the presence of a periodic modulation of integrated Bragg intensity from thin crystal slices, as predicted by the dynamical theory. The present Chap. 5 deals with the dynamical theory of diffraction for neutrons and the next Chap. 6 deals with the implications for the three-plate interferometer.

## 5.1 Interaction Potential

The stationary Schrödinger equation for neutrons in a single crystal reads

$$\left[ -\frac{\hbar^2}{2M} \Delta + V(\vec{r}) \right] \psi(\vec{r}) = E\psi(\vec{r}). \quad (5.1)$$

In terms of the Fermi pseudo-potential of the assembly of nuclei in the crystal, we have the expression

$$V(\vec{r}) = \frac{2\pi\hbar^2 b_c}{M} \sum_{i,j} \delta(\vec{r} - \vec{r}_{i,j}). \quad (5.2)$$

The following quantities are defined here:

$M$  ... Neutron mass

$b_c$  ... Coherent scattering length

$\vec{r}_{i,j} = \vec{R}_j + \vec{\rho}_i$  ... Vector of lattice position

$\vec{R}_j$  ... Vector from origin to elementary cell  $j$

$\vec{\rho}_i$  ... Vector from origin of elementary cell  $j$  to position of atom  $i$  in cell  $j$

$\vec{a}_i = m_i \vec{a}_1 + n_i \vec{a}_2 + p_i \vec{a}_3$

$\vec{a}_i$  ... Lattice vectors of an elementary cell

$m_i, n_i, p_i$  ... Rational numbers between 0 and 1

Now the Fourier transformation of the potential  $V(\vec{r})$  is carried out:

$$\begin{aligned} V(\vec{\kappa}) &= \frac{1}{V} \int V(\vec{r}) e^{-i\vec{\kappa}\cdot\vec{r}} d\vec{r} = \frac{2\pi\hbar^2 b_c}{MV} \sum_{i,j} e^{-i\vec{\kappa}\cdot\vec{r}_{i,j}} \\ &= \frac{2\pi\hbar^2 b_c}{MV} \sum_{\vec{R}_j} e^{-i\vec{\kappa}\cdot\vec{R}_j} \sum_{\vec{\rho}_i} e^{-i\vec{\kappa}\cdot\vec{\rho}_i} = \frac{2\pi\hbar^2 b_c}{MV} (LF)(SF). \end{aligned} \quad (5.3)$$

$V$  ... Volume of the crystal ( $V = N_c V_c$ )

$N_c$  ... Number of elementary cells

$V_c$  ... Volume of elementary cell

$V_c = \vec{a}_1(\vec{a}_2 \times \vec{a}_3) = \vec{a}_2(\vec{a}_3 \times \vec{a}_1) = \vec{a}_3(\vec{a}_1 \times \vec{a}_2)$

$LF$  ... Lattice factor

$SF$  ... Structure factor

We will now discuss the lattice factor  $LF$  and the structure factor  $SF$ .

### 5.1.1 Lattice Factor LF

The lattice factor  $LF$  is

$$LF = \sum_{\vec{R}_j} e^{-i\vec{\kappa}\cdot\vec{R}_j} = \begin{cases} N_c & \text{for } \vec{\kappa} = \vec{G} \\ 0 & \text{otherwise} \end{cases}. \quad (5.4)$$

*Proof:* We consider the geometrical theory of diffraction.  $\vec{k}_0$  is the incoming beam and  $\vec{k}$  the diffracted beam. The Bragg angle is denoted by  $\Theta_B$ . The Bragg equation reads (see Fig. 5.1)  $\vec{\kappa} = \vec{G}$ , where  $\vec{k} - \vec{k}_0 = \vec{\kappa}$  and  $\vec{G}$  is the reciprocal lattice vector.  $\vec{G}$  is perpendicular to the lattice plains, which have a distance  $d$  from each other. The absolute values of  $\vec{k}$  and  $\vec{k}_0$  are equal:  $|\vec{k}| = |\vec{k}_0| = k$ . We determine  $|\vec{G}|$  (see Fig. 5.1):

$$\begin{aligned} G &= |\vec{G}| = |\vec{k} - \vec{k}_0| = \sqrt{(\vec{k} - \vec{k}_0)^2} \\ &= k\sqrt{2 - 2 \cos(\vec{k}, \vec{k}_0)} = 2k \sin(\Theta_B). \end{aligned} \quad (5.5)$$

This is Bragg's equation in reciprocal space. Likewise, we obtain the Bragg equation (for first diffraction order) in real space:  $2d \sin(\Theta_B) = \lambda$ , where  $\lambda$  is the optical retardation caused by two parallel lattice planes of distance  $d$ . Because  $k = 2\pi/\lambda$ , we obtain  $G = 2\pi/d$ .

Now the reciprocal lattice vector  $\vec{G}$  is investigated in more detail, using the Miller indices  $h'$ ,  $k'$  and  $l'$ , which are integers [33]:

$$\vec{G} = h' \vec{g}_1 + k' \vec{g}_2 + l' \vec{g}_3, \quad (5.6)$$

where

$$\vec{g}_1 = \frac{2\pi}{V_c} (\vec{a}_1 \times \vec{a}_2), \quad \vec{g}_2 = \frac{2\pi}{V_c} (\vec{a}_2 \times \vec{a}_3), \quad \vec{g}_3 = \frac{2\pi}{V_c} (\vec{a}_3 \times \vec{a}_1). \quad (5.7)$$

For ortho-rhombical systems, e.g., we obtain  $1/d^2 = (h'/a_3)^2 + (k'/a_1)^2 + (l'/a_2)^2$ . The vectors  $\vec{g}_i$  and  $\vec{a}_i$  form a reciprocal system, that is to say we

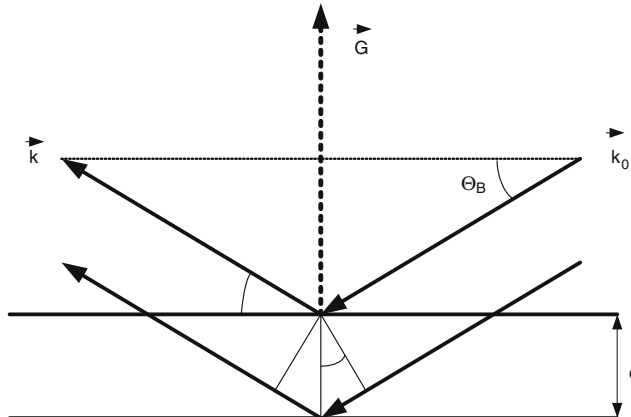


**Fig. 5.1.** Visualization of the Bragg equation  $2d \sin(\Theta_B) = n\lambda$

have  $(\vec{g}_1 \vec{a}_3)/(2\pi) = 1$ ,  $(\vec{g}_2 \vec{a}_1)/(2\pi) = 1$  and  $(\vec{g}_3 \vec{a}_2)/(2\pi) = 1$ . The other scalar products are zero. The volume of an elementary cell of the reciprocal lattice can be calculated using (5.7) and we obtain:  $\vec{g}_1(\vec{g}_2 \times \vec{g}_3) = (2\pi)^3/V_c$ .

Now the lattice factor  $LF$  can be evaluated for  $\vec{\kappa} = \vec{G}$ : If  $\vec{R}_j = m' \vec{a}_1 + n' \vec{a}_2 + p' \vec{a}_3$ , where  $m', n', p'$  are integers, the exponent in  $LF$  reads  $\vec{R}_j \cdot \vec{G} = 2\pi(h'p' + k'm' + l'p') = 2\pi n$ . Because  $n$  is an integer as well, we obtain  $e^{-i2\pi n} = 1$  and  $LF = N_c$ .

In the case where  $\vec{\kappa} \neq \vec{G}$ , e.g.,  $\vec{\kappa} = z \vec{g}_1$ , where  $z$  is real but not integer, the lattice factor  $LF$  becomes

$$LF = \sum_{m', n', p'} e^{-i(m' \vec{a}_1 + n' \vec{a}_2 + p' \vec{a}_3) \cdot z \vec{g}_1} = \sum_{p'=0}^{N_c \gg 1} e^{-i2\pi z p'} \rightarrow 0. \quad \square$$

### 5.1.2 Structure Factor SF

The second summation in (5.3) is easily evaluated. Because the definition of  $\vec{\rho}_i = m_i \vec{a}_1 + n_i \vec{a}_2 + p_i \vec{a}_3$ , (5.6) and  $\vec{\kappa} = \vec{G}$ , the result is

$$SF = \sum_{\vec{\rho}_i} e^{-i\vec{\kappa} \cdot \vec{\rho}_i} = \sum_{(m_i, n_i, p_i)} e^{-i2\pi(m_i k' + n_i l' + p_i h')} . \quad (5.8)$$

As a simple example, we consider a body-centered cubic crystal system, where  $\vec{\rho}_1 = (0, 0, 0)$  and  $\vec{\rho}_2 = (1/2, 1/2, 1/2)$ . The structure factor reads

$$SF = \sum_{i=1}^2 e^{-i\vec{G} \cdot \vec{\rho}_i} = 1 + e^{-i\pi(k' + l' + h')} = \begin{cases} 0 & \text{for } (h' + k' + l') \text{ odd} \\ 2 & \text{for } (h' + k' + l') \text{ even} \end{cases} .$$

In the following, we consider, for example, the  $(2, 2, 0)$ -reflexion of the face-centered cubic lattice of a silicon single crystal (diamond lattice). Then the structure factor yields a value of  $SF = 8$ .

We return to (5.3), taking (5.4) into account:

$$V(\vec{\kappa}) = V(\vec{G}) = V(h', k', l') = \frac{2\pi\hbar^2 b_c}{MV_c} SF. \quad (5.9)$$

If  $N_S$  is the number of scattering centers (or atoms) per elementary cell, then  $N = N_S/V_c$  is the number of scattering centers per unit volume. Calculating  $V(0)$ , the structure factor is always equal to  $N_S$  and we obtain

$$V(0) = \frac{2\pi\hbar^2 b_c}{M} N, \quad \frac{V(\vec{G})}{V(0)} = \frac{SF}{V_c N}. \quad (5.10)$$

Example: silicon,  $(2, 2, 0)$ -reflexion  $\rightarrow a = 5,43 \cdot 10^{-8} \text{ cm}$ ,  $V_c = a^3$ ,  $N = 5,04 \cdot 10^{22} \text{ cm}^{-3}$ ,  $b_c = 0,415 \cdot 10^{-12} \text{ cm}$ ,  $M = 1,675 \cdot 10^{-27} \text{ kg}$ ,  $SF = 8$ ,

$\rightarrow V(\vec{G})/V(0) = 1$  and  $1/a^3 = N/8 \rightarrow V(2, 2, 0) = V(0) = 16\pi\hbar^2 b_c/(a^3 M) = 5,395.10^{-8} eV$ . If thermal neutrons are considered, the energy is about  $E \approx 0,025 eV$ , and the ratio between the potential and the energy can be calculated. The outcome is

$$\frac{V(\vec{G})}{E} = \frac{V(0)}{E} \approx 2.10^{-6} \ll 1. \quad (5.11)$$

This result is important for the dynamical theory of diffraction in connection with the so-called two-beam approximation (see below). The inverse Fourier transformation of (5.3) yields

$$V(\vec{r}) = \sum_{\vec{G}} V(\vec{G}) e^{i\vec{G}\vec{r}}, \quad (5.12)$$

and this equation describes the periodicity of the potential in the crystal lattice.

In deriving the dynamical theory of diffraction (see below), we neglect the absorption of neutrons, because absorption is very small in silicon.

## 5.2 Basic Equations

The solution of the stationary Schrödinger equation (5.1) is given by the so-called Bloch-ansatz

$$\psi(\vec{r}) = e^{i\vec{K}\vec{r}} u(\vec{r}), \quad (5.13)$$

where the exponential factor comprises the vector  $\vec{K}$ , which is a wave vector inside the crystal, and  $u(\vec{r})$  is the amplitude of this wave. Analogously to the potential equation (5.12) an ansatz is made for  $u(\vec{r})$ :

$$u(\vec{r}) = \sum_{\vec{G}} u(\vec{G}) e^{i\vec{G}\vec{r}}. \quad (5.14)$$

The amplitude  $u(\vec{G})$ , which is defined in the reciprocal space, has to be identified. The wave function  $\psi(\vec{r})$  now reads

$$\psi(\vec{r}) = \sum_{\vec{G}} u(\vec{G}) e^{i(\vec{G} + \vec{K})\vec{r}}. \quad (5.15)$$

If (5.15) and (5.12) are inserted into (5.1), we obtain the basic equations of the dynamical theory of diffraction:

$$\left[ \frac{\hbar^2}{2M} (\vec{K} + \vec{G})^2 - E \right] u(\vec{G}) = - \sum_{\vec{G}'} V(\vec{G} - \vec{G}') u(\vec{G}'). \quad (5.16)$$

There is a finite number of equivalent waves in the crystal whose wave vectors differ by  $\vec{G}$ , respectively. This system of equations cannot be solved generally. However, we expect the respective amplitudes  $u(\vec{G})$  to be especially large, if the wave vector  $(\vec{K} + \vec{G})$  of the reflected beam is near a reciprocal lattice point.

### 5.3 One-Beam Approximation

If only a single lattice vector  $\vec{G} = 0$  is effective, one speaks of one-beam approximation or beam refraction (Fig. 5.2). The appropriate wave vector in the crystal is denoted by  $\vec{K}_0$ . From (5.16) we obtain

$$\left[ \frac{\hbar^2}{2M} K_0^2 - E \right] u(0) = -V(0)u(0) \rightarrow K_0^2 = k^2 \left[ 1 - \frac{V(0)}{E} \right], \quad (5.17)$$

where the energy of the incoming neutrons is  $E = \hbar^2 k^2 / (2M)$ . Because of (5.11)  $K_0$  can be written approximately

$$K_0 \approx k \left[ 1 - \frac{V(0)}{2E} \right]. \quad (5.18)$$

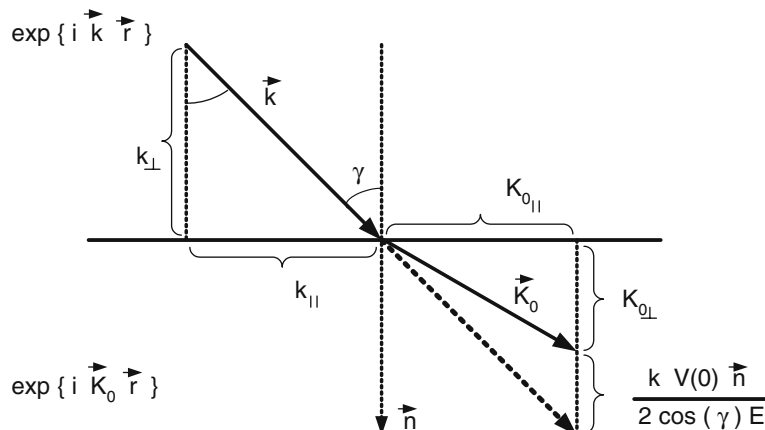


**Fig. 5.2.** Beam refraction (see text). A plane wave of wave number  $k$  impinges on a surface of a single crystal and the refracted wave has wave number  $K_0$  inside the crystal

$V(0)$  can be understood as a mean potential of the crystal. Using (5.10) the index of refraction  $n$  reads

$$n = \frac{K_0}{k} \approx 1 - \lambda^2 \frac{Nb_c}{2\pi}. \quad (5.19)$$

The index of refraction of neutrons in silicon is only a little bit smaller than 1 (refraction from the perpendicular). In Fig. 5.2 the incoming plane wave  $e^{i\vec{k}\cdot\vec{r}}$  has a wave vector  $\vec{k}$ . The wave vector  $\vec{K}_0$  of the refracted plane wave  $e^{i\vec{K}_0\cdot\vec{r}}$  has changed both in direction and in magnitude. Thereby the continuity of the tangential components  $k_{\parallel} = K_{0\parallel}$  has to be taken into account. The unit vector  $\vec{n}$  is perpendicular to the crystal surface.  $\gamma$  is the angle between  $\vec{n}$  and  $\vec{k}$  and we have  $\cos(\gamma) = k_{\perp}/k$ . From the geometrical proportions and (5.17) we identify:

$$\begin{aligned} K_0^2 &= K_{0\perp}^2 + K_{0\parallel}^2 = K_{0\perp}^2 + k_{\parallel}^2 = k_{\perp}^2 + k_{\parallel}^2 - k^2 \frac{V(0)}{E} \\ \rightarrow K_{0\perp} &= \sqrt{k_{\perp}^2 - k^2 \frac{V(0)}{E}} \approx k_{\perp} \left[ 1 - \frac{1}{2 \cos^2(\gamma)} \frac{V(0)}{E} \right] \rightarrow \vec{K}_0 = \vec{K}_{0\perp} + \vec{K}_{0\parallel} \\ &= \vec{n} k_{\perp} \left[ 1 - \frac{1}{2 \cos^2(\gamma)} \frac{V(0)}{E} \right] + \vec{k}_{\parallel} = \vec{k} - \frac{k V(0)}{2 \cos(\gamma) E} \vec{n}. \end{aligned} \quad (5.20)$$

This equation is visualized in Fig. 5.2. Hence, the one-beam approximation describes the transition of a beam from vacuum into the crystal (refraction).

## 5.4 Two-Beam Approximation

In this case, two lattice points ( $\vec{G} = 0$  and one single  $\vec{G} \neq 0$ ) have to be regarded. This approximation is justified only if all the other lattice points are far away from Bragg refraction. We shall see that the refracted intensity decreases very quickly in the neighborhood of a lattice point. Hence, from the basic relations (5.16) it can be concluded that two equations have to be solved simultaneously:

$$\begin{aligned} \vec{G} = 0 : \quad &\left[ \frac{\hbar^2}{2M} (\vec{K})^2 - E \right] u(0) = -V(0)u(0) - V(-\vec{G})u(\vec{G}), \\ \vec{G} \neq 0 : \quad &\left[ \frac{\hbar^2}{2M} (\vec{K} + \vec{G})^2 - E \right] u(\vec{G}) = -V(\vec{G})u(0) - V(0)u(\vec{G}). \end{aligned} \quad (5.21)$$

If we consider the one-beam approximation (5.17), the squared value  $(\vec{K}_0)^2 \equiv K_0^2$  of the wave vector  $\vec{K}_0$  in the mean crystal potential  $V(0)$  is, because of

(5.11), almost equal to  $k^2$ . It can be expected that  $(\vec{K})^2$  and  $(\vec{K} + \vec{G})^2$  are very close to  $k^2$  as well. Therefore, the following ansatz is made:

$$(\vec{K})^2 \approx k^2(1 + 2\epsilon), \quad (\vec{K} + \vec{G})^2 \approx k^2(1 + 2\epsilon_G). \quad (5.22)$$

$\epsilon$  and  $\epsilon_G$  are called excitation errors of  $\vec{K}$  and  $\vec{K} + \vec{G}$ , respectively.  $|\epsilon|$  and  $|\epsilon_G|$  are, therefore, in the range of  $V(0)/E \ll 1$ . The vectors themselves can be written according to (5.20) as

$$\vec{K} = \vec{k} + \frac{k}{\cos(\gamma)}\epsilon \vec{n} \quad (5.23)$$

for the forward beam ( $\vec{k} \cdot \vec{n} = k \cos(\gamma) = k_\perp$ ) and

$$\vec{K}_G = \vec{K} + \vec{G} = \vec{k} + \vec{G} + \frac{k}{\cos(\gamma)}\epsilon \vec{n} \quad (5.24)$$

for the diffracted beam. In both expressions only  $\epsilon$  can be found and  $\epsilon$  and  $\epsilon_G$  are not independent of each other. Because of (5.22) we get

$$(\vec{K} + \vec{G})^2 = (\vec{K})^2 + (\vec{G})^2 + 2\vec{K}\vec{G} \rightarrow 2\epsilon_G = 2\epsilon + \frac{(\vec{G})^2}{k^2} + \frac{2\vec{K}\vec{G}}{k^2}.$$

Using (5.23), we finally obtain

$$2\epsilon_G = 2\epsilon \frac{1}{b} + \alpha, \quad \frac{1}{b} = \left[ 1 + \frac{\vec{G} \cdot \vec{n}}{k \cos(\gamma)} \right], \quad \alpha = \frac{1}{k^2}[(\vec{G})^2 + 2\vec{k} \cdot \vec{G}]. \quad (5.25)$$

$b$  characterizes geometrical proportions (Laue diffraction or Bragg diffraction) and  $\alpha$  describes the deviation from the exact Bragg angle  $\Theta_B$  (see below).

Two cases can be distinguished (see Fig. 5.3):

Laue case: In this case, the beam  $\vec{k}_G$  is diffracted behind the crystal. We consider henceforth symmetrical diffraction. In the Laue case, the reflection planes are perpendicular to the crystal surface ( $\gamma = \Theta_B$ ).  $\vec{G} \cdot \vec{n} = 0$  is valid and  $b = 1$  according to (5.25). In the dynamical theory of diffraction, the exact Bragg equation reads (see (5.24))

$$\vec{K}_G - \vec{K} = \vec{G}, \quad (5.26)$$

where all these vectors belong to the interior of the crystal. Because  $\vec{k}$  and  $\vec{k}_G$  are outside beams,  $\approx \vec{G}$  has been written in Fig. 5.3. Note that (5.5) has been derived using the geometrical theory of diffraction.

Bragg case: The reflection planes are parallel to the crystal surface ( $\gamma = \pi/2 - \Theta_B$ ). We have:  $\vec{G} \cdot \vec{n} = -G = -2k \cos(\gamma) \rightarrow b = -1$ , taking (5.5) into account.

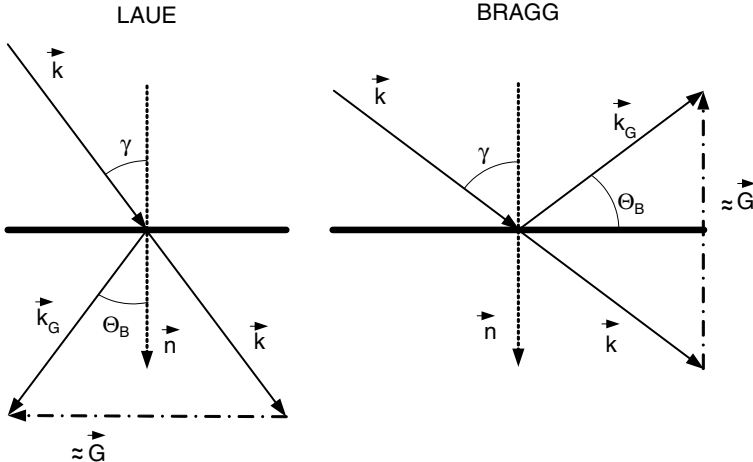


**Fig. 5.3.** Left: symmetrical Laue diffraction ( $b = 1$ ). Right: symmetrical Bragg diffraction ( $b = -1$ ). The horizontal line illustrates the crystal. The  $k$ -vectors are outside the crystal. The reflection planes are normal to the crystal surface in the Laue case, and parallel to the crystal surface in the Bragg case (see text)

The quantity  $\alpha$  in (5.25) describes the deviation from the exact Bragg angle  $\Theta_B$ . This can be shown as follows: let  $\Theta = \Theta_B + \delta\Theta_B$ , where  $\delta\Theta_B$  is a very small angle. That means that  $\vec{k}$  should fulfill Bragg's equation almost exactly. Then the expression  $\vec{k} \cdot \vec{G}$  in (5.25) reads:  $\vec{k} \cdot \vec{G} = kG \cos(\pi/2 + \Theta) = -kG \sin(\Theta) \approx -kG[\sin(\Theta_B) + \cos(\Theta_B)\delta\Theta_B]$ . Using (5.5),  $\alpha$  can be written as  $\alpha = (G^2 + 2\vec{k} \cdot \vec{G})/k^2 \approx -2 \sin(2\Theta_B)\delta\Theta_B$ . If  $\alpha = 0$ , the exact Bragg condition is fulfilled.

Later in this book we consider the Laue-type neutron interferometer. Hence our main attention is directed to the Laue case of diffraction. Setting  $b = 1$ , the excitation errors are

$$\epsilon_G = \epsilon + \alpha/2. \quad (5.27)$$

Returning to the basic equations of the two-beam approximation, we insert (5.22) into (5.21) and obtain the homogenous equation system

$$\begin{aligned} \left[2\epsilon + \frac{V(0)}{E}\right] u(0) + \frac{V(-\vec{G})}{E} u(\vec{G}) &= 0, \\ \frac{V(\vec{G})}{E} u(0) + \left[2\epsilon_G + \frac{V(0)}{E}\right] u(\vec{G}) &= 0, \end{aligned} \quad (5.28)$$

which has only non-trivial solutions if the determinant is equal to zero. Because  $V(-\vec{G})V(\vec{G}) = |V(\vec{G})|^2$  and using (5.27), we have

$$\left[2\epsilon + \frac{V(0)}{E}\right] \left[2\epsilon + \alpha + \frac{V(0)}{E}\right] - \frac{|V(\vec{G})|^2}{E^2} = 0, \quad (5.29)$$

and the two solutions are:

$$\epsilon_{1,2} = \frac{1}{4} \left[ -\alpha - 2\frac{V(0)}{E} \pm \sqrt{\alpha^2 + 4\frac{|V(\vec{G})|^2}{E^2}} \right]. \quad (5.30)$$

Note that  $V(\vec{G}) = V(0)$  for the silicon-(2, 2, 0) reflection. Because of the two values  $\epsilon_{1,2}$ , two wave fields in the forward direction  $u_{1,2}(0)$  and two wave fields in the diffracted direction  $u_{1,2}(\vec{G})$  appear in the crystal:

$$\frac{u_{1,2}(\vec{G})}{u_{1,2}(0)} = X_{1,2} = -\frac{2\epsilon_{1,2} + V(0)/E}{V(-\vec{G})/E}. \quad (5.31)$$

From (5.23) two wave vectors

$$\overrightarrow{K_{1,2}} = \overrightarrow{k} + \frac{k}{\cos(\gamma)} \epsilon_{1,2} \overrightarrow{n} \quad (5.32)$$

appear in the crystal and, therefore, two wave functions  $\psi_{1,2}(\vec{r})$  arise, which are superpositions of the forward and diffracted directions themselves (see (5.15)). These wave functions are solutions of the Schrödinger equation.

The most interesting are the wave functions that are outside in the forward (0) and diffracted ( $\vec{G}$ ) directions, respectively. These are superpositions of two wave fields:

$$\begin{aligned} \psi_0(\vec{r}) &= u_1(0)e^{i\vec{K}_1 \cdot \vec{r}} + u_2(0)e^{i\vec{K}_2 \cdot \vec{r}}, \\ \psi_G(\vec{r}) &= u_1(\vec{G})e^{i(\vec{K}_1 + \vec{G}) \cdot \vec{r}} + u_2(\vec{G})e^{i(\vec{K}_2 + \vec{G}) \cdot \vec{r}}. \end{aligned} \quad (5.33)$$

In the next section we determine these wave functions for the coplanar crystal plate including the Laue-case.

## 5.5 Solutions for Plane Plate in Laue Position

Now we have to bear in mind boundary conditions. Combining (5.33) and (5.32), we recognize that the scalar product  $(\overrightarrow{n} \cdot \overrightarrow{r})$  defines these conditions. Putting the coordinate origin on the crystal surface (see also Fig. 5.5) and the  $z$ -axis parallel to  $\overrightarrow{n} = \overrightarrow{e}_z$ ,  $(\overrightarrow{n} \cdot \overrightarrow{r}) = 0$  provides the boundary condition of the front side of the plate and  $(\overrightarrow{n} \cdot \overrightarrow{r}) = D$  yields the boundary condition on the back side. Here  $D$  denotes the thickness of the crystal plate.

The incoming plane wave is written as

$$\psi_e = u_0 e^{i \vec{k} \cdot \vec{r}}. \quad (5.34)$$

The continuity condition of the wave function  $\psi_e$  and the wave function  $\psi_0(\vec{r})$  at the front side ( $\vec{n} \cdot \vec{r} = 0$ ) of the crystal yields

$$u_0 = u_1(0) + u_2(0). \quad (5.35)$$

Because there is no reflected wave at the front side in the Laue case, the second equation of (5.33) together with (5.31) provides

$$0 = X_1 u_1(0) + X_2 u_2(0). \quad (5.36)$$

These equations give

$$u_1(0) = \frac{X_2}{X_2 - X_1} u_0, \quad u_2(0) = -\frac{X_1}{X_2 - X_1} u_0. \quad (5.37)$$

The forward and diffracted beam behind the crystal can be calculated easily from (5.33) using ( $\vec{n} \cdot \vec{r} = D$ ):

$$\begin{aligned} \frac{\psi_0(D)}{\psi_e} &= \frac{X_2 e^{i k \epsilon_1 D / \cos(\gamma)} - X_1 e^{i k \epsilon_2 D / \cos(\gamma)}}{X_2 - X_1} = v_0, \\ \frac{\psi_G(D)}{\psi_e} &= \frac{X_1 X_2 [e^{i k \epsilon_1 D / \cos(\gamma)} - e^{i k \epsilon_2 D / \cos(\gamma)}]}{X_2 - X_1} e^{i \vec{G} \cdot \vec{r}} = v_G e^{i \vec{G} \cdot \vec{r}}. \end{aligned} \quad (5.38)$$

$v_0$  and  $v_G$  are complex crystal functions and important quantities for obtaining proper amplitudes for the plane waves behind the crystals of an interferometer (see below).

### 5.5.1 Intensities of Laue Position

The squared absolute values  $|\psi_0(D)/\psi_e|^2$  and  $|\psi_G(D)/\psi_e|^2$  are of interest because they are the ratios of intensity, which are diffracted behind the crystal. Before these quantities are identified, two new parameters  $A$  and  $y$  are introduced:

$$A = \frac{k}{2 \cos(\gamma)} \frac{|V(\vec{G})|}{E} D, \quad y = \frac{1}{2} \frac{E}{|V(\vec{G})|} \alpha. \quad (5.39)$$

The parameter  $A$  is proportional to the crystal thickness  $D$  and  $y$  depends on  $\alpha$ , the deviation from the exact Bragg angle  $\Theta_B$ . The exponents in (5.38) become

$$\frac{k \epsilon_{1,2} D}{\cos(\gamma)} = A(-y \pm \sqrt{y^2 + 1}) - \frac{k D}{2 \cos(\gamma)} \frac{V(0)}{E}. \quad (5.40)$$

The quantities  $X_{1,2}$  are defined via (5.31) and the expressions for the intensities are as follows:

$$\left| \frac{\psi_G(D)}{\psi_e} \right|^2 = \frac{\sin^2(A\sqrt{1+y^2})}{1+y^2}, \quad \left| \frac{\psi_0(D)}{\psi_e} \right|^2 = 1 - \frac{\sin^2(A\sqrt{1+y^2})}{1+y^2}. \quad (5.41)$$

In Fig. 5.4 the function  $\sin^2(A\sqrt{1+y^2})/(1+y^2)$  is drawn for the parameter  $A = 7\pi/2$ . The sum of the intensities in (5.41) yields one. This equation is the most important outcome of the dynamical theory of diffraction. It is called “pendular solution” or “Pendellösung”, simply because the intensity oscillates between the forward and diffracted directions, depending on the crystal thickness  $D$ , respectively  $A$ . Therefore, the “Pendellösung period”  $\delta_0$  is defined by

$$\delta_0 = \frac{\pi D}{A}. \quad (5.42)$$

For the silicon (2, 2, 0)-reflection and a wave length of  $\lambda = 2\text{\AA}$ , the “Pendellösung period” becomes  $\delta_0 = 0,614 \cdot 10^{-2}\text{cm}$ . On the other hand, the intensity oscillates as a function of the deviation  $y$  from the Bragg angle and these oscillations become narrower the thicker the crystal.  $y$  can be expressed using  $\delta_0$  by

$$y = \frac{k\delta_0}{4\pi \cos(\gamma)} \alpha. \quad (5.43)$$

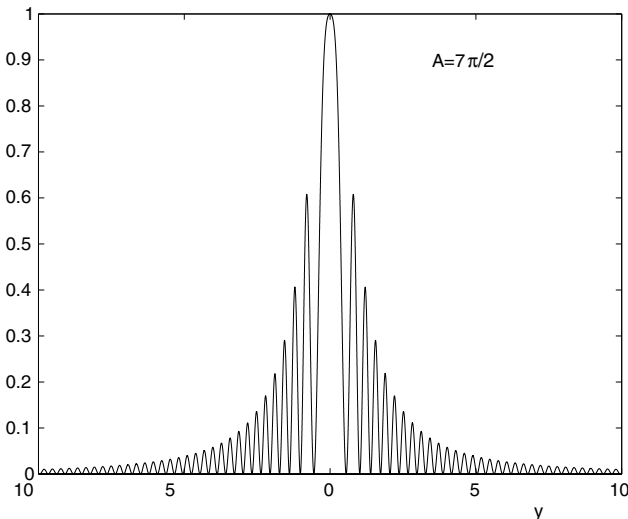


**Fig. 5.4.** The function  $\frac{\sin^2(A\sqrt{1+y^2})}{(1+y^2)}$

### 5.5.2 Wave Functions for Different Incident Directions

In this section we calculate wave functions and phase relations, taking into account different incident directions of the incoming beam. Such considerations are important in specifying waves, which appear in the neutron interferometer described below.

We emanate from (5.23) and (5.24), writing an analogue equation for  $\vec{K}_G$ , namely

$$\vec{K}_G = \vec{K} + \vec{G} = \vec{k}_G + \frac{k}{\cos(\gamma)} \epsilon_G \vec{n}, \quad (5.44)$$

where the direction  $\vec{k}_G$  of the diffracted beam behind the crystal appears (provided that symmetric diffraction takes place). Using (5.27) and (5.43),  $\vec{k}_G - \vec{k}$  reads as

$$\vec{k}_G - \vec{k} = \vec{G} - p \vec{n}, \quad p = 2\pi \frac{y}{\delta_0}. \quad (5.45)$$

This equation sheds light on the difference between the geometrical and dynamical theory of diffraction. We refer to Sect. 5.1.1 and Fig. 5.1, where the geometrical theory of diffraction leads to the relation  $\vec{k}_G - \vec{k} \approx \vec{G}$ , which turns out to be only an approximation (we apply our notation here). The vectors  $\vec{k}_G$  and  $\vec{k}$  belong to the outside region, whereas  $\vec{G}$  is the reciprocal lattice vector of the crystal. According to the exact Bragg equation (5.26),  $\vec{G}$  is the difference of the quantities  $\vec{K}_G$  and  $\vec{K}$ , which belong to the inside of the crystal. Therefore, the geometrical theory has been corrected and improved by the dynamical theory of diffraction by the correction term  $p \vec{n}$ . Only if  $p = 0$ , or equivalently  $y = 0$ , are both Bragg equations identical. Nevertheless, the geometrical theory of diffraction does not take into account the thickness of a crystal and hence the “Pendellösung” according to (5.41) is in any case a characteristic of the dynamical theory.

Henceforth, we simplify our calculations taking into account the special silicon  $(2, 2, 0)$ -reflection, where  $V(\vec{G}) = V(0)$  (see Sect. 5.1.2). In addition, we introduce the quantity

$$P(y) = -\frac{p}{2} - \frac{k}{2 \cos(\gamma)} \frac{V(0)}{E} = -\frac{\pi}{\delta_0} (1 + y), \quad (5.46)$$

which will be used below. Particularly with regard to the description of the Laue-type interferometer, we introduce general distances  $(\vec{n} \cdot \vec{r})$ . We remember that this quantity was equal to the crystal thickness  $D$  specifying the back of the crystal plate. Going back to (5.33) and (5.38) and taking into account (5.45), the wave functions  $\psi_0$  and  $\psi_G$  are written in the following generalized manner:

$$\begin{aligned} \psi_e &= u_0 e^{i \vec{k} \cdot \vec{r}}, \\ \psi_0 &= v_0(y) \psi_e, \end{aligned} \quad (5.47)$$

$$\begin{aligned}\psi_G &= v_G(y) e^{i\vec{G} \cdot \vec{r}} \psi_e = v_G(y) u_0 e^{i(\vec{k} + \vec{G}) \cdot \vec{r}} = v_G(y) u_0 e^{i(\vec{k}_G + \vec{p} \cdot \vec{n}) \cdot \vec{r}} \\ &= v_G(y) u_0 e^{ipz_b} e^{i\vec{k}_G \cdot \vec{r}} \equiv v_G(y) e^{i\vec{G} \cdot \vec{r} - ip(\vec{n} \cdot \vec{r} - z_b)} \psi_e,\end{aligned}\quad (5.48)$$

where in a first step  $(\vec{n} \cdot \vec{r}) = z_b$  (see Fig. 5.5) has been inserted. On the back of the crystal,  $z_b$  is exactly equal to the crystal thickness  $D$ . Introducing  $z_b$  permits us to define any position of a crystal plate, which will be of importance in the interferometer discussed below. In the last step of the above equation, we have rewritten the exponent in order to include arbitrary distances  $(\vec{n} \cdot \vec{r})$ . The amplitudes  $v_0(y)$  and  $v_G(y)$  now depend on the parameter  $y$ :

$$\begin{aligned}v_0(y) &= e^{iP(y)D} \{ \cos(A\sqrt{1+y^2}) + \frac{i}{\sqrt{1+y^2}} \sin(A\sqrt{1+y^2}) \}, \\ v_G(y) &= -e^{iP(y)D} \frac{i}{\sqrt{1+y^2}} \sin(A\sqrt{1+y^2}),\end{aligned}\quad (5.49)$$

In (5.48) the phase factor  $e^{ipz_b}$  defines the position of the crystal plate, and this is important for a focusing requirement of the interferometer (see below).

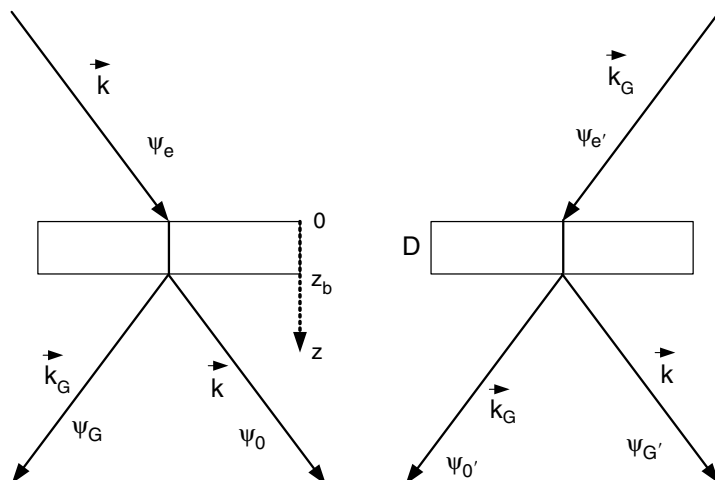


**Fig. 5.5.** Diffraction in Laue-position. Left picture: incoming wave function  $\psi_e$  impinges from the left side. Right picture: incoming wave function  $\psi_{e'}$  arrives from the right side. This means that the reciprocal lattice vector points to the opposite direction (see text).  $D$  denotes the thickness of the crystal. The coordinate origin on the crystal surface is marked by the level 0. The quantity  $z_b$  denotes the back of the crystal

The wave function  $\psi_e$  in (5.34) describes the incoming plane wave of a Laue-type diffraction (see Fig. 5.5, left picture), whereas the wave  $\psi_{e'} = u_0 e^{i\vec{k}_G \cdot \vec{r}}$  characterizes an incoming wave in the diffracted direction. This wave can be used as an incoming wave for a second crystal plate (see Fig. 5.5, right side). Indeed, we have to keep in mind that, because of the reversed diffraction process, the reciprocal lattice vector ( $\vec{G}$ ) has to be replaced by ( $-\vec{G}$ ). Basically, ( $y$ ) has to be replaced by ( $-y$ ). Altogether we obtain:

$$\begin{aligned}\psi_{e'} &= u_0 e^{i\vec{k}_G \cdot \vec{r}}, \\ \psi_{0'} &= v_0(-y)\psi_{e'}, \\ \psi_{G'} &= v_G(-y)e^{-ipz_b}u_0 e^{i\vec{k} \cdot \vec{r}} \equiv v_G(-y)e^{-i\vec{G} \cdot \vec{r} + ip(\vec{n} \cdot \vec{r} - z_b)}\psi_{e'}.\end{aligned}\quad (5.50)$$

## 6 Laue Interferometer

The wave functions defined in (5.47) to (5.50) are in an appropriate shape to be applied to a Mach–Zehnder-like neutron interferometer (Fig. 6.1). The silicon perfect crystal interferometer [24] provides widely separated coherent beams and has become a standard method for advanced neutron optical investigations. Its operation is based on division of amplitudes by dynamical Bragg reflection from perfect crystals. In the standard version, a monolithic triple-plate system in the Laue transmission geometry is used, which provides a wide beam separation ( $\geq 5$  cm) and a non-dispersive response to the incident neutron beam. The perfect silicon crystal interferometer is extremely useful for fundamental neutron physics studies.

For most applications, the standard triple Laue case interferometer is generally the best configuration (Fig. 6.1). It follows from symmetry considerations that the amplitude and the phase of the wave function in the forward (0) direction behind the empty interferometer is composed of equal parts coming from both beams traversing paths I and II. The wave on path I arrives in the  $\psi_0$ -beam after having made a transmission ( $t$ ) in the first crystal (splitter  $S$ ), a reflection ( $r$ ) in the second crystal (mirror  $M$ ) and another reflection ( $r$ ) in the third crystal (analyzer  $A$ ). On path II the sequence is ( $rrt$ ). From symmetry, it follows that these two waves are equal in phase and amplitude, as will be shown below. However, if a phase shifter is put into one of the arms of the interferometer, phase differences between the two paths can be generated, as will be discussed in the next section.

### 6.1 Wave Functions and Focusing Condition

A full analysis of the perfect silicon crystal neutron interferometer requires a detailed description of the coherent wave fields that propagate through the device. The starting point for this analysis is the plane wave dynamical diffraction theory for a symmetric Laue geometry crystal slab, as developed in the previous section. Repeated sequential application of the transmission and reflection functions (5.49) for each of the crystals of the interferometer leads to formulas describing the 0-beam and  $G$ -beam wave fields and the

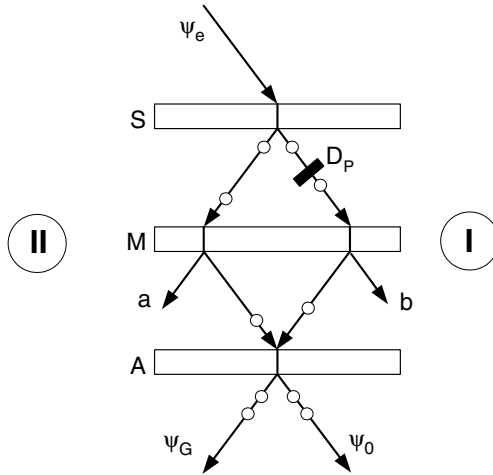


**Fig. 6.1.** Laue neutron interferometer: beam splitter  $S$ , mirror  $M$ , analyzer  $A$ , thickness of the phase shifter  $D_P$ , incident wave  $\psi_e$ . In the forward and diffracted directions, the waves  $\psi_0$  and  $\psi_G$  are superpositions of the two beam paths I and II (see text). Beams  $a$  and  $b$  leave the interferometer behind the mirror. The small circles illustrate wave packets that are shifted against each other if a phase shifter is put into one arm of the interferometer

intensities leaving the interferometer. Taking into account (5.47) to (5.50) the calculation is as follows.

Beam path I:

$$\text{Behind beam splitter } S: \quad \psi_0^{I,S} = v_0(y)\psi_e$$

$$\text{Behind beam mirror } M: \quad \psi_G^{I,M} = v_G(y)e^{i\vec{G}\vec{r}} - i\mu(\vec{n}\vec{r} - z_b^M)\psi_0^{I,S}$$

$$\begin{aligned} \text{Behind beam analyzer } A: \quad \psi_0^I &= v_G(-y)e^{-i\vec{G}\vec{r}} + i\mu(\vec{n}\vec{r} - z_b^A)\psi_G^{I,M} \\ \psi_G^I &= v_0(-y)\psi_G^{I,M} \end{aligned}$$

Putting them all together, the wave functions of beam path I read:

$$\begin{aligned} \psi_0^I &= v_0(y)v_G(y)v_G(-y)e^{-i\mu(z_b^A - z_b^M)}\psi_e \\ \psi_G^I &= v_0(y)v_G(y)v_0(-y)e^{i\mu z_b^M}\psi_{e'} \end{aligned}$$

Beam path II:

$$\text{Behind beam splitter } S: \psi_G^{\text{II},S} = v_G(y) e^{i\vec{G}\cdot\vec{r} - ip(\vec{n}\cdot\vec{r} - z_b^S)} \psi_e$$

$$\text{Behind beam mirror } M: \psi_0^{\text{II},M} = v_G(-y) e^{-i\vec{G}\cdot\vec{r} + ip(\vec{n}\cdot\vec{r} - z_b^M)} \psi_G^{\text{II},S}$$

$$\text{Behind beam analyzer } A: \psi_0^{\text{II}} = v_0(y) \psi_0^{\text{II},M}$$

$$\psi_G^{\text{II}} = v_G(y) e^{i\vec{G}\cdot\vec{r} - ip(\vec{n}\cdot\vec{r} - z_b^A)} \psi_0^{\text{II},M}$$

Putting them all together, the wave functions of beam path II read:

$$\psi_0^{\text{II}} = v_G(y) v_G(-y) v_0(y) e^{-ip(z_b^M - z_b^S)} \psi_e$$

$$\psi_G^{\text{II}} = v_G(y) v_G(-y) v_G(y) e^{-ip(-z_b^A + z_b^M - z_b^S)} \psi_{e'}$$

Hence, the focusing condition for an ideally perfect interferometer reads as follows:

$$z_b^A - z_b^M = z_b^M - z_b^S. \quad (6.1)$$

The three plates of the interferometer have to be equal and they have to be equispaced. Hence, in the forward direction, the two wave functions are equal:

$$\psi_0^{\text{I}} = \psi_0^{\text{II}}. \quad (6.2)$$

Both wave functions are reflected twice and transmitted once (rrt). They have equal amplitudes and phases. This is the most important result concerning the perfect Laue interferometer. The total wave function  $\psi_0$  is a superposition

$$\psi_0 = \psi_0^{\text{I}} + \psi_0^{\text{II}} = 2\psi_0^{\text{I}} = 2v_0(y) v_G(y) v_G(-y) e^{-ip(z_b^A - z_b^M)} \psi_e. \quad (6.3)$$

Because of the different amplitudes of the diffracted beams  $\psi_G^{\text{I}}$  and  $\psi_G^{\text{II}}$ , their phases disagree as well. The superposition reads

$$\psi_G = \psi_G^{\text{I}} + \psi_G^{\text{II}} = [v_0(y) v_G(y) v_0(-y) + v_G(y) v_G(-y) v_G(y)] e^{ipz_b^M} \psi_{e'}. \quad (6.4)$$

If the equations (5.49) are inserted, we obtain

$$\frac{\psi_G^{\text{I}}}{\psi_G^{\text{II}}} = -\frac{1 - \frac{\sin^2(A\sqrt{1+y^2})}{1+y^2}}{\frac{\sin^2(A\sqrt{1+y^2})}{1+y^2}} = -\frac{1 - |v_G(y)|^2}{|v_G(y)|^2}, \quad (6.5)$$

where a phase difference of  $\pi$  between the two beams can be observed ( $-1 = e^{i\pi}$ ).

## 6.2 Intensities and Phase Shift

Finally, the intensities should be computed. Because  $|v_G(y)v_G(-y)|^2 = |v_G(y)|^4$  and  $|v_0(y)v_0(-y)|^2 = |v_0(y)|^4$ , the intensities in the forward beam  $|\psi_0/\psi_e|^2$  and in the diffracted beam  $|\psi_G/\psi_e|^2$  are

$$\left| \frac{\psi_0}{\psi_e} \right|^2 = 4[|v_G(y)|^2]^2[1 - |v_G(y)|^2] \quad (6.6)$$

and

$$\left| \frac{\psi_G}{\psi_e} \right|^2 = |v_G(y)|^2[1 - 2|v_G(y)|^2]^2. \quad (6.7)$$

The sum is

$$\left| \frac{\psi_0}{\psi_e} \right|^2 + \left| \frac{\psi_G}{\psi_e} \right|^2 = |v_G(y)|^2. \quad (6.8)$$

Now we take into account the wave functions  $a$  and  $b$ , leaving the interferometer behind the mirror crystal ( $M$ ) (Fig. 6.1). They can be calculated following the considerations about reflection (r) and transmission (t). Beam  $a$  is reflected once and transmitted once, and beam  $b$  is transmitted twice. Hence,

$$\begin{aligned} \left| \frac{a}{\psi_e} \right|^2 &= |v_G(y)|^2[1 - |v_G(y)|^2], \quad \left| \frac{b}{\psi_e} \right|^2 = [1 - |v_G(y)|^2]^2, \\ \left| \frac{a}{\psi_e} \right|^2 + \left| \frac{b}{\psi_e} \right|^2 &= 1 - |v_G(y)|^2. \end{aligned} \quad (6.9)$$

$$|\psi_0|^2 + |\psi_G|^2 + |a|^2 + |b|^2 = |\psi_e|^2. \quad (6.10)$$

Hence, all outgoing intensities sum up to the ingoing intensity  $|\psi_e|^2$ .

Because of  $\psi_0^I = \psi_0^{II}$ , in an empty interferometer the forward beam (0) is particularly suitable for investigation when a phase shifter is put into one arm of the device. The coherent superposition of the two wave functions, taking a phase shift into account, is considered in the following sections. From the point of view of using the change of wave vector due to the optical potential provided by the collection of nuclei in a slab of matter (phase shifter) of thickness  $D_P$  in one of the sub-beams of the interferometer, we find that the phase shift is [24]

$$\chi = (n - 1)kD_P = -\lambda Nb_c D_P, \quad (6.11)$$

where we have used (5.19) for the index of refraction  $n$ . Thus, the intensity  $I_0(\chi)$  in the 0-beam is given by

$$I_0(\chi) = \left| \psi_0^I e^{-i\chi} + \psi_0^{II} \right|^2 = \frac{1}{2} |\psi_0|^2 [1 + \cos(\chi)]. \quad (6.12)$$

The intensity oscillates as a function of phase shift  $\chi$ , where maximum intensity and complete extinction alternate. However, in the following sections, we shall consider wave number packets, where the cosine in the intensity formula above is damped, due to the broadness of the packet.

It should be mentioned that

$$I_0(\chi) + I_G(\chi) = |\psi_0|^2 + |\psi_G|^2 \quad (6.13)$$

is a constant and, therefore,  $I_G(\chi)$  is oscillating in opposite phase to  $I_0(\chi)$ .

## 7 Three Plate Interferometry in Phase-Space

For many years it has been known from classical optics that the coherence properties manifest themselves in a spatial intensity variation for phase shifts smaller than the coherence length and in a spectral variation for large phase shifts [9]. These phenomena become more apparent for less monochromatic beams and can even cause squeezing effects [34].

It is generally known that coupling in phase-space is very effectively described in terms of the Wigner function [5, 35], which represents a quasi-probability distribution routinely used in quantum optics [2,6]. The formalism of Wigner function representation was introduced to visualize the behavior of various quantum systems that exhibit typical quantum optical phenomena. Although it cannot be interpreted as a probability function because of its partially negative values (see Part I), it is useful for the interpretation of various quantum effects. Neutron optics deals with massive particles, but can be formulated in quantum-optical terms also including the Wigner function formalism [24]. When the spatial phase shift, applied inside the interferometer to one coherent beam, becomes larger than the coherence length, spatially separated coherent Schrödinger-cat-like states are produced, which exhibit typical non-classical features and are notoriously fragile against any dissipations and fluctuations existing in any experimental arrangement, as will be discussed in later sections.

### 7.1 Superposition of Wave Packets

In Sect. 2.1, the Wigner function has been defined and its properties have been discussed. An especially simple expression of the Wigner function is derived for the wave packet in Sect. 2.1.1 and is specified in (2.7). Here we apply the Wigner formalism to neutron interferometry. The interference pattern behind the interferometer is given by the coherent superposition of wave functions, representing paths in arms I and II of the interferometer (Fig. 6.1). We have a phase shifter in path I as displayed in (6.12). Its action introduces a phase factor

$$e^{-i\chi} \equiv e^{ik_0\Delta_0}, \quad \Delta_0 = \frac{2\pi}{k_0} \frac{D_P}{D_{\lambda_0}}, \quad D_{\lambda_0} = \frac{k_0}{Nb_c}, \quad (7.1)$$

where, instead of  $\lambda$ , the mean wave length  $\lambda_0 = 2\pi/k_0$  of the wave packet has been inserted.  $\Delta_0$  denotes the order of the oscillations of intensity caused by the phase shifter of thickness  $D_P$ . The parameter  $D_{\lambda_0}$  is called  $\lambda_0$ -thickness. Behind the third plate of the interferometer, it is sufficient to consider only the outgoing neutron beam that is parallel to the incident beam in front of the apparatus (forward beam). The other (diffracted) beam exhibits a complementary intensity pattern and does not require separate examination. The superposition ( $s$ ) of the wave functions in the forward direction reads

$$\psi_s(x, t, \Delta_0) = \psi(x, t) + \psi(x + \Delta_0, t). \quad (7.2)$$

$\psi(x, t)$  is the wave function of the wave packet defined in (2.5).

The difference to the former considerations are apparent: for the superposition in (6.12) the plane wave theory has been applied, where the incident beam  $\psi_e = u_0 e^{i\vec{k} \cdot \vec{r}}$  (see (5.34)) entails a superposition of plane waves of certain amplitudes behind the interferometer. Hence, the modulation in intensity as a function of phase shift  $\chi$  is complete. However, in (7.2) wave packets are used and an appropriate damped intensity behavior can be expected, as shown below. Instead of  $\psi_e$ , a wave packet such as (2.5) impinges on the interferometer, giving rise to a superposition of wave packets behind the interferometer. The absolute power is determined primarily by the crystal functions  $v_0(y)$  and  $v_G(y)$  of (5.49) and integration over  $y$ , taking a certain beam divergence into account. Here we do not attach great importance to absolute intensities. Therefore the relation (7.2) is sufficient to describe the interference phenomena that we are interested in.

Fourier transformation of  $\psi_s(x, t, \Delta_0)$  leads to a superposition of Gaussian wave packets in  $k$ -space:

$$\alpha_s(k, \Delta_0) = \frac{1}{\sqrt{2\pi}} \int \psi_s(x, t, \Delta_0) e^{-i(kx - \Omega t)} dx = \alpha(k)[1 + e^{ik\Delta_0}]. \quad (7.3)$$

Here  $\Omega = \hbar k^2/(2M)$  and  $\alpha(k)$  is given in (2.3).

## 7.2 Wigner Function of Superposition

According to (4.3), the Wigner function of the superposition state (7.2) reads

$$W_s(x, k, t, \Delta_0) = \frac{1}{2\pi} \int \psi_s^* \left( x + \frac{x'}{2}, t, \Delta_0 \right) \psi_s \left( x - \frac{x'}{2}, t, \Delta_0 \right) e^{ikx'} dx'. \quad (7.4)$$

The calculation leads to the following expression [36, 37]:

$$\begin{aligned} W_s(x, k, t, \Delta_0) &= W_{WP}(x, k, t) + W_{WP}(x + \Delta_0, k, t) \\ &\quad + 2 \cos(k\Delta_0) W_{WP}(x + \frac{\Delta_0}{2}, k, t). \end{aligned} \quad (7.5)$$

This formula is described in detail and graphically displayed in the figures below. First of all,  $W_{WP}(x, k, t)$  is identical to the Wigner function of the wave packet defined in (2.7). The Wigner function of superposition is simply the sum of the Wigner functions of two wave packets shifted against each other by the phase shift  $\Delta_0$  plus an oscillating part (interference term). Time  $t$  simply “distorts” the function  $W_{WP}(x, k, t)$ , depending on the velocity of the single plane waves in the wave packet. It does not alter the phase shift and phase relations, and we shall omit the time parameter subsequently. However, we bear in mind that a matter wave packet spreads as it propagates. The explicit expression of  $W_s(x, k, \Delta_0)$  now reads

$$W_s(x, k, \Delta_0) = \frac{1}{\pi} e^{-\frac{(k/k_0 - 1)^2}{2\sigma^2}} \{ e^{-2\sigma^2(xk_0)^2} + e^{-2\sigma^2(xk_0 + \Delta_0 k_0)^2} \\ + 2 \cos(k\Delta_0) e^{-2\sigma^2(xk_0 + \Delta_0 k_0/2)^2} \}, \quad (7.6)$$

where  $\sigma = \delta k/k_0$ . The variables  $k/k_0$  and  $xk_0$  are dimensionless. Figures 7.1 to 7.4 display this function. Thus, the Wigner function of the coherent Schrödinger-cat-like states (7.2) becomes the sum of the Wigner function

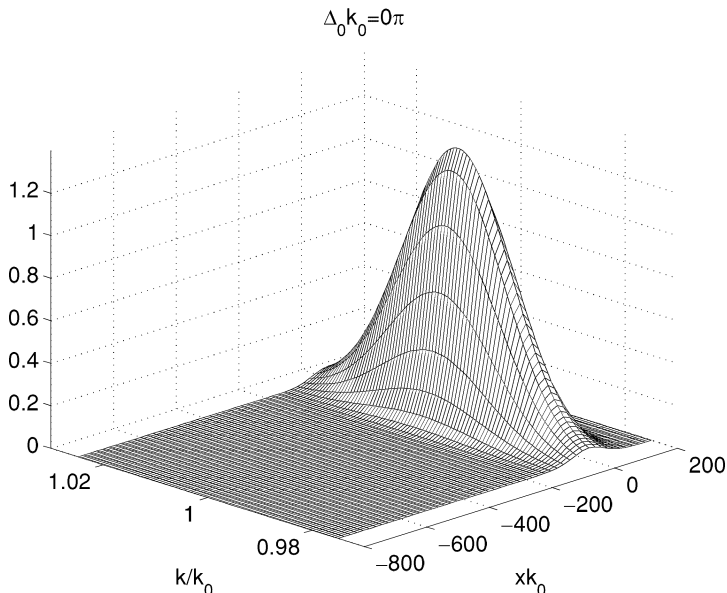


**Fig. 7.1.** Wigner function  $W_s(x, k, \Delta_0)$  (7.6) for superposition of two wave packets:  $\sigma = 1/100$ , interference order  $m_0 = \Delta_0 k_0/(2\pi) = 0$

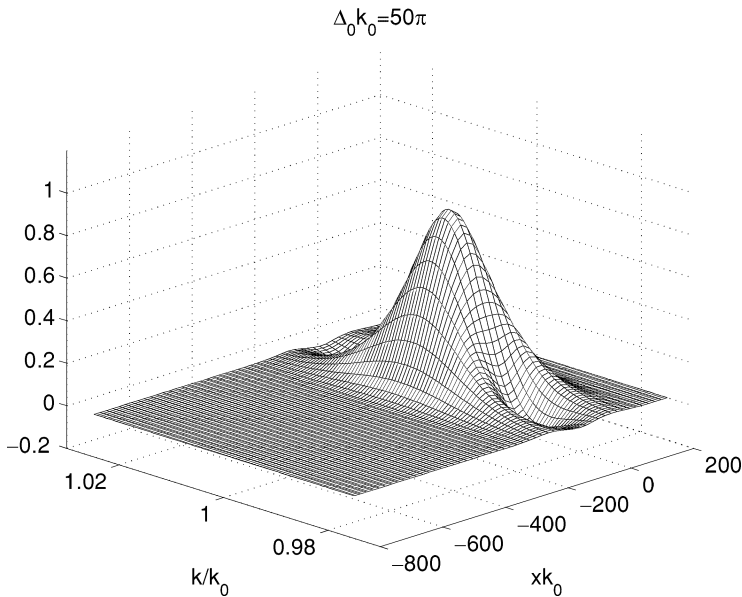


**Fig. 7.2.** Wigner function  $W_s(x, k, \Delta_0)$  (7.6) for superposition of two wave packets:  $\sigma = 1/100$ , interference order  $m_0 = \Delta_0 k_0 / (2\pi) = 25$

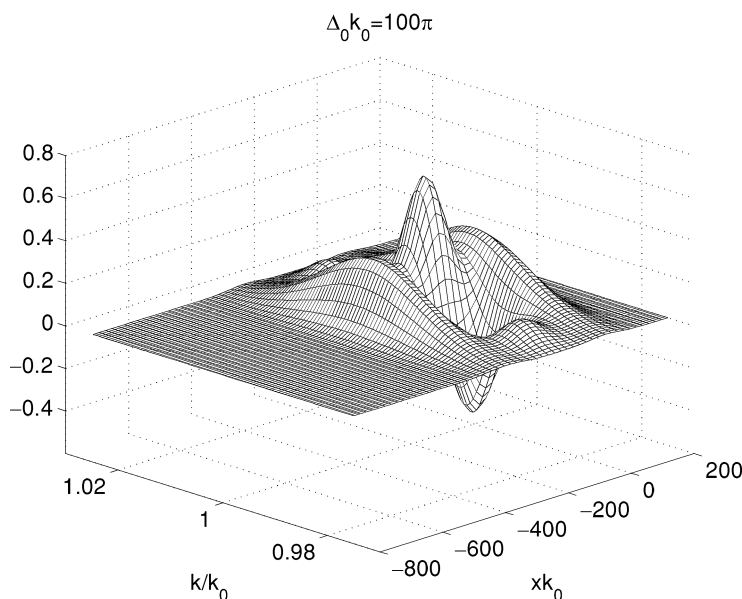


**Fig. 7.3.** Wigner function  $W_s(x, k, \Delta_0)$  (7.6) for superposition of two wave packets:  $\sigma = 1/100$ , interference order  $m_0 = \Delta_0 k_0 / (2\pi) = 50$

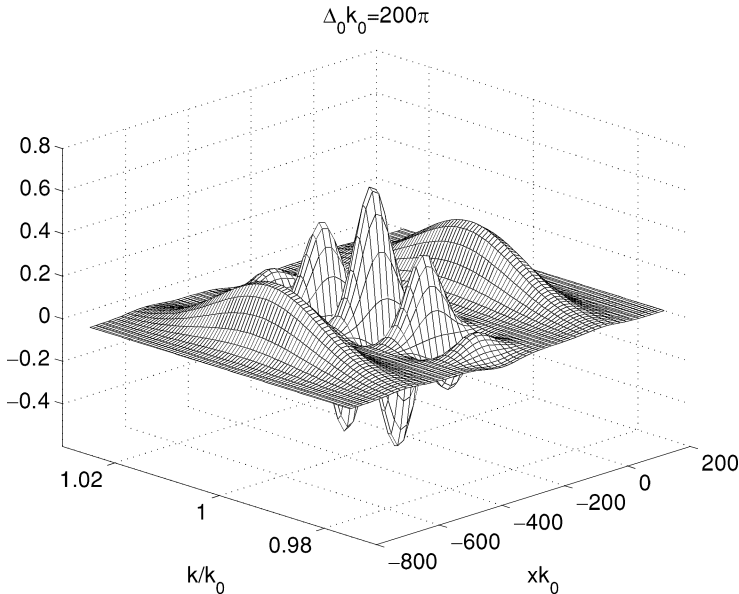


**Fig. 7.4.** Wigner function  $W_s(x, k, \Delta_0)$  (7.6) for superposition of two wave packets:  $\sigma = 1/100$ , interference order  $m_0 = \Delta_0 k_0 / (2\pi) = 100$

of the two spatially shifted wave packets and a cross term oscillating more rapidly in the case of increasing phase shifts  $\Delta_0 k_0$ . Schrödinger-cat-like neutron states not only exist in split beam interference experiments, but in spin-echo systems as well (see below). Both situations can be described properly by the Wigner function formalism. It is important to note that integration over the momentum variable gives the spatial distribution  $|\psi_s(x, \Delta_0)|^2$ , and integration over the spatial variable gives the momentum distribution  $|\alpha_s(k, \Delta_0)|^2$  (see Sect. 2.1 and the next section). This opens the possibility of quantum state tomography, because both quantities can be measured. It permits an interferometric measurement of the Wigner function, which is equivalent to knowledge of the state wave function [38, 39].

Coming back to the figures above, for higher interference order  $m_0 = \Delta_0 k_0 / (2\pi)$ , the negative parts of the Wigner function are clearly identified. One can observe how the wave packets become separated with increasing interference order, and the oscillating part in between becomes more and more pronounced. Attention should be paid to Fig. 7.2, where  $m_0 = 25$  is applied. The wave packets begin to separate, and it can be seen that the mean square deviation of momentum is considerably smaller (squeezed Wigner function) than in the case  $m_0 = 0$  (Fig. 7.1). We shall come back to this later.

### 7.3 Momentum and Position Spectra

As mentioned above, the momentum spectrum  $|\alpha_s(k, \Delta_0)|^2$  is an integral of the Wigner function over the spatial variable and we get:

$$|\alpha_s(k, \Delta_0)|^2 = \int W_s(x, k, \Delta_0) dx = 2\alpha^2(k) \left\{ 1 + \cos \left[ \frac{k}{k_0} (\Delta_0 k_0) \right] \right\}, \quad (7.7)$$

where

$$\alpha^2(k) = \frac{1}{\sqrt{2\pi\sigma^2 k_0^2}} e^{-\frac{(k/k_0 - 1)^2}{2\sigma^2}}. \quad (7.8)$$

The detailed structure of the wave packets in momentum space is presented in Figs. 7.5 to 7.8. Figure 7.5 displays the momentum spectrum as a function of interference order  $m_0$  between  $0 \leq m_0 = \Delta_0 k_0 / (2\pi) \leq 1$ . For  $m_0 = 0$ , the original Gaussian spectrum  $\alpha^2(k)$  is visible ( $k_0 = 1$  has been inserted). For  $m_0 = 1/2$  (or  $\Delta_0 k_0 = \pi$ ), the spectrum  $|\alpha_s(k, \Delta_0)|^2$  is almost zero. As mentioned before, we consider the forward beam of Fig. 6.1. Hence, (for  $m_0 = 1/2$ ) the intensity can be found in the diffracted beam (not shown here). This is a result of the dynamical theory of diffraction in a single crystal neutron interferometer (see (6.5) and (6.13)), where the forward and diffracted beams have opposite phase. Figure 7.6 exhibits a considerably smaller mean square deviation of momentum in comparison with Fig. 7.5. The momentum

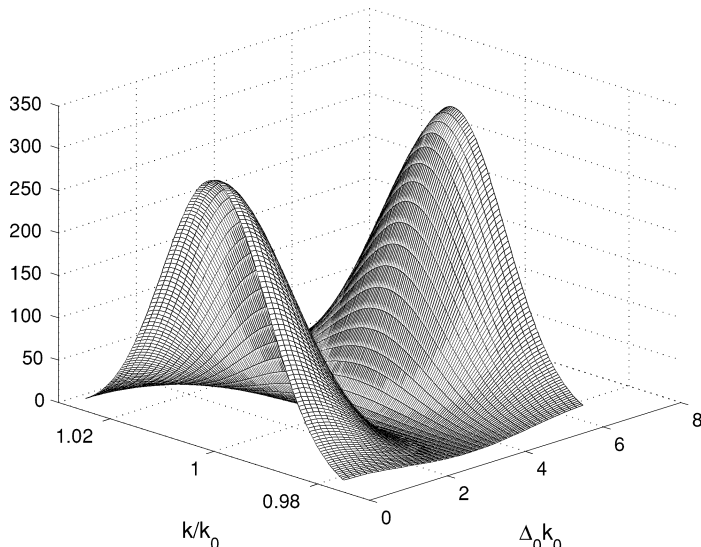


**Fig. 7.5.** Momentum spectrum  $|\alpha_s(k, \Delta_0)|^2$  (7.7) for superposition of two wave packets:  $\sigma = 1/100$ , interference order  $0 \leq m_0 = \Delta_0 k_0 / (2\pi) \leq 1$

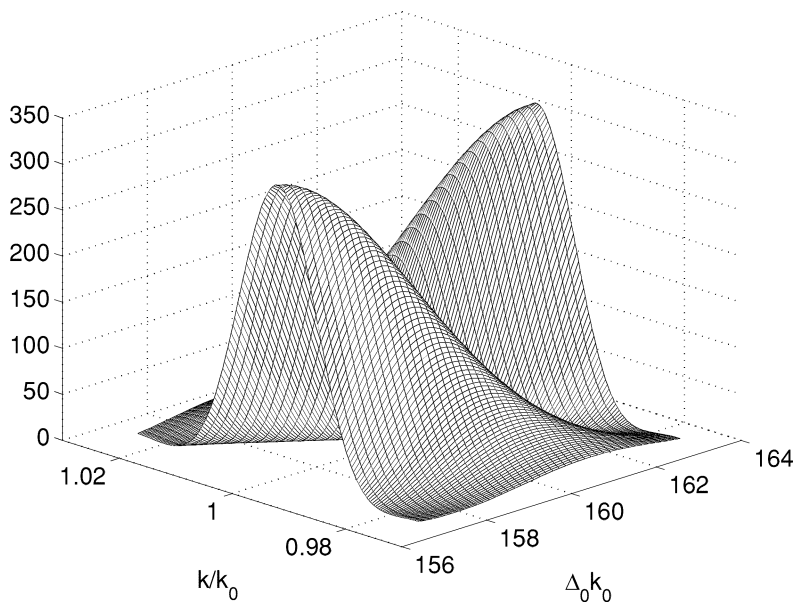


**Fig. 7.6.** Momentum spectrum  $|\alpha_s(k, \Delta_0)|^2$  (7.7) for superposition of two wave packets:  $\sigma = 1/100$ , interference order  $25 \leq m_0 = \Delta_0 k_0 / (2\pi) \leq 26$

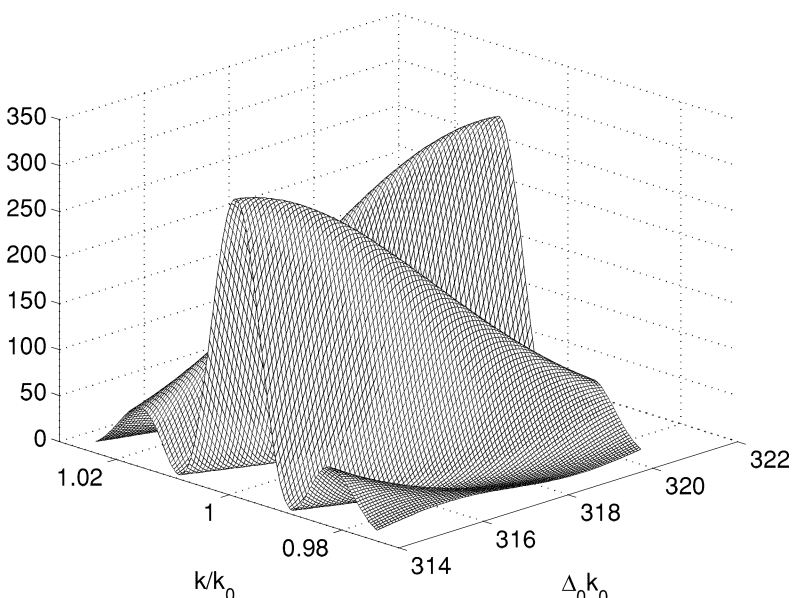


**Fig. 7.7.** Momentum spectrum  $|\alpha_s(k, \Delta_0)|^2$  (7.7) for superposition of two wave packets:  $\sigma = 1/100$ , interference order  $50 \leq m_0 = \Delta_0 k_0 / (2\pi) \leq 51$

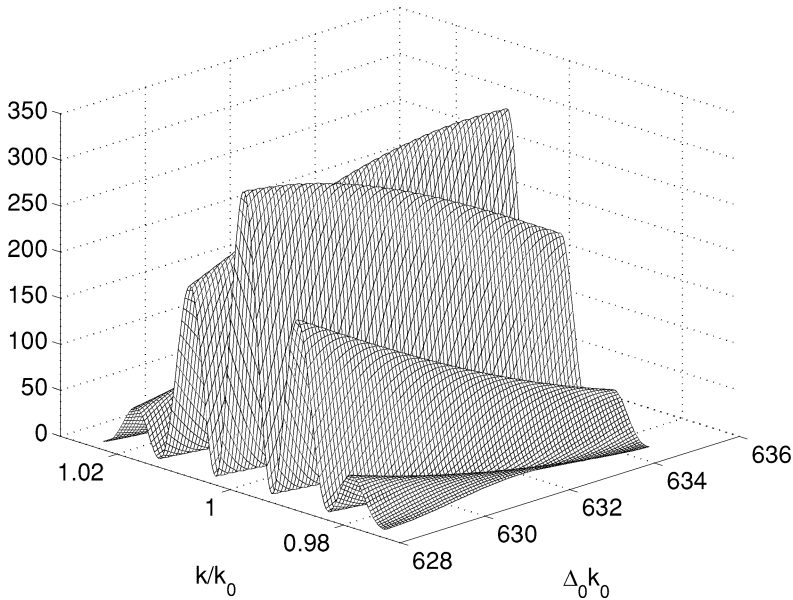


**Fig. 7.8.** Momentum spectrum  $|\alpha_s(k, \Delta_0)|^2$  (7.7) for superposition of two wave packets:  $\sigma = 1/100$ , interference order  $100 \leq m_0 = \Delta_0 k_0 / (2\pi) \leq 101$

spectrum has been squeezed for  $m_0 = 25$ . Figures 7.7 and 7.8 reveal more and more the cosine-structure because of the higher interference order.

The position spectrum can be evaluated as mentioned before:

$$|\psi_s(x, \Delta_0)|^2 = \int W_s(x, k, \Delta_0) dk = \sqrt{\frac{2\sigma^2 k_0^2}{\pi}} \left\{ e^{-2\sigma^2(xk_0)^2} + e^{-2\sigma^2(xk_0 + \Delta_0 k_0)^2} + 2 \cos(\Delta_0 k_0) e^{-2\sigma^2(xk_0 + \Delta_0 k_0/2)^2} e^{-\sigma^2(\Delta_0 k_0)^2/2} \right\}. \quad (7.9)$$

This function is drawn in Figs. 7.9 to 7.12. The space distribution of the non-shifted wave packets is reflected in Fig. 7.9 ( $m_0 = 0$ ). In the case of  $m_0 = 1/2$ , the intensity is turned to the diffracted beam, as already discussed in Fig. 7.5. For higher interference order (Figs. 7.11 and 7.12), the wave packets have been completely separated, as can be seen very clearly. Even though the wave packets have been entirely disconnected in space, their momentum spectra exhibit a pronounced structure, as can be seen in Figs. 7.7 and 7.8. The Wigner functions Figs. 7.3 and 7.4 accentuate both properties simultaneously.

## 7.4 Squeezing of Momentum Spectrum

Having figured out the momentum spectrum  $|\alpha_s(k, \Delta_0)|^2$  and the position spectrum  $|\psi_s(x, \Delta_0)|^2$  of the superposition state behind the interferometer in

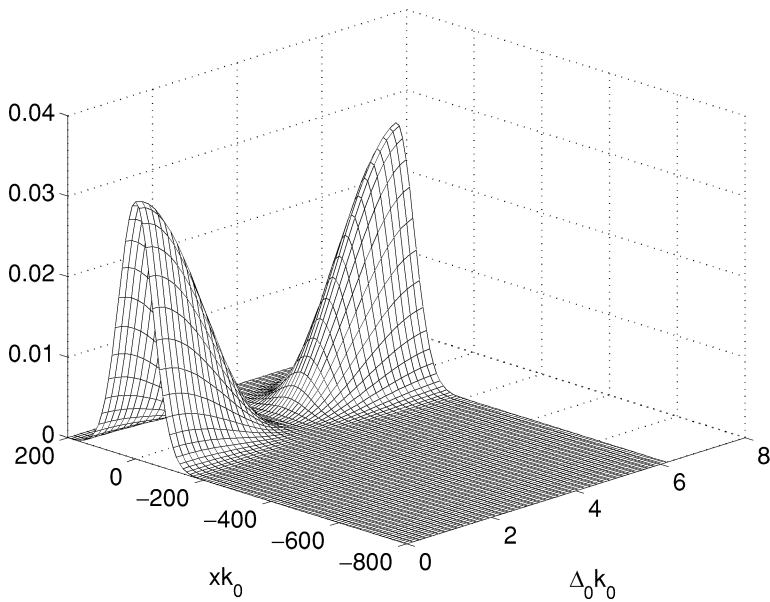


**Fig. 7.9.** Position spectrum  $|\psi_s(x, \Delta_0)|^2$  (7.9) for superposition of two wave packets:  $\sigma = 1/100$ , interference order  $0 \leq m_0 = \Delta_0 k_0 / (2\pi) \leq 1$

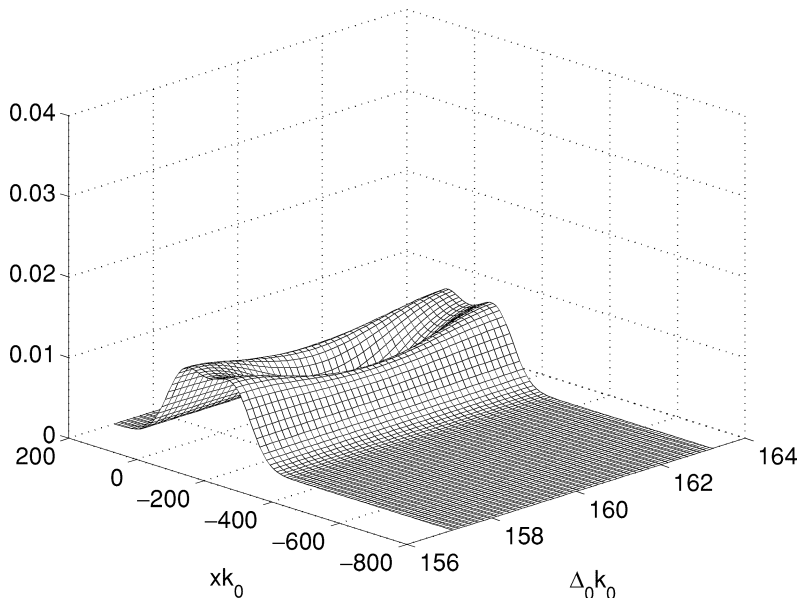


**Fig. 7.10.** Position spectrum  $|\psi_s(x, \Delta_0)|^2$  (7.9) for superposition of two wave packets:  $\sigma = 1/100$ , interference order  $25 \leq m_0 = \Delta_0 k_0 / (2\pi) \leq 26$

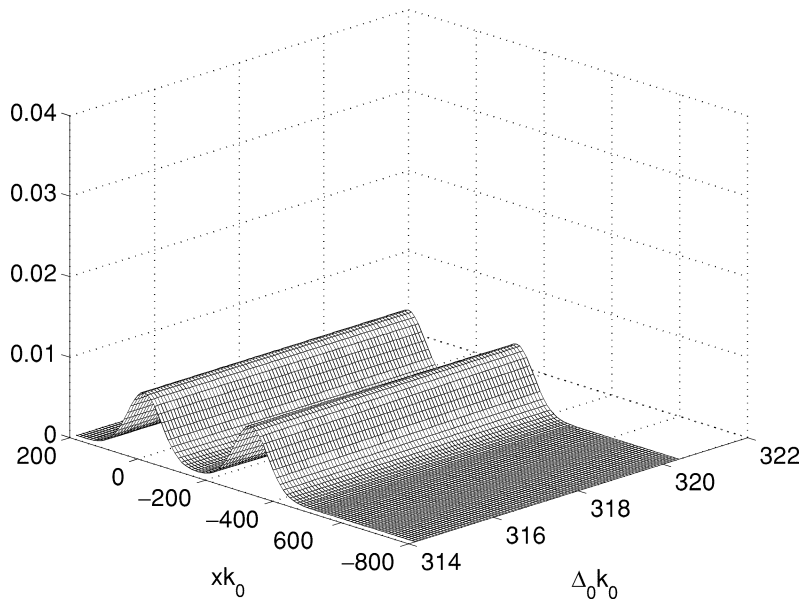


**Fig. 7.11.** Position spectrum  $|\psi_s(x, \Delta_0)|^2$  (7.9) for superposition of two wave packets:  $\sigma = 1/100$ , interference order  $50 \leq m_0 = \Delta_0 k_0 / (2\pi) \leq 51$

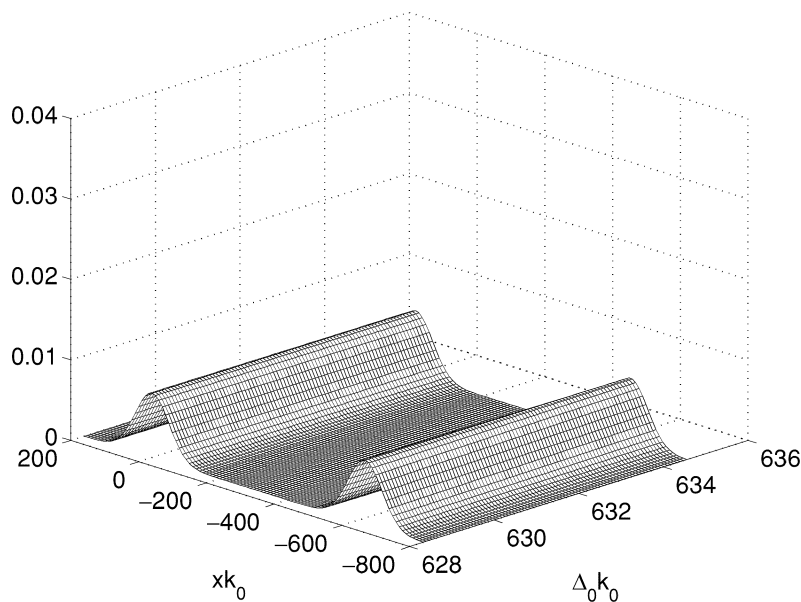


**Fig. 7.12.** Position spectrum  $|\psi_s(x, \Delta_0)|^2$  (7.9) for superposition of two wave packets:  $\sigma = 1/100$ , interference order  $100 \leq m_0 = \Delta_0 k_0 / (2\pi) \leq 101$

(7.7) and (7.9), the intensity can be determined by

$$\begin{aligned} I_s(X) &= \int |\psi_s(x, \Delta_0)|^2 dx = \int |\alpha_s(k, \Delta_0)|^2 dk \\ &= 2[1 + e^{-X^2/2} \cos(X/\sigma)]. \end{aligned} \quad (7.10)$$

The new variable  $X = (\Delta_0 k_0)\sigma$  has been introduced, and  $I_s(X)$  is drawn in Fig. 7.13, top. As has already been mentioned in Sect. 6.2, the intensity oscillations are damped due to the broadness  $\sigma = \delta k/k_0$  of the wave packet. The exponential factor  $V = e^{-X^2/2}$  is exactly the visibility function defined in (3.17). For  $\sigma = 1/100$  and  $X \geq 3$ , the intensity oscillations are almost completely damped out. This region is equivalent to  $(\Delta_0 k_0) \geq 300$ , and Fig. 7.11 exhibits already complete separation of the wave packets. However, the momentum spectrum (7.7) reveals a pronounced cosine-structure. This proves again that the two beams are coherently interconnected in phase space although they are completely disconnected in position space.

The new quantum states, created behind the interferometer, can be analyzed with regard to their uncertainty properties. In the case of  $X = 0$ ,

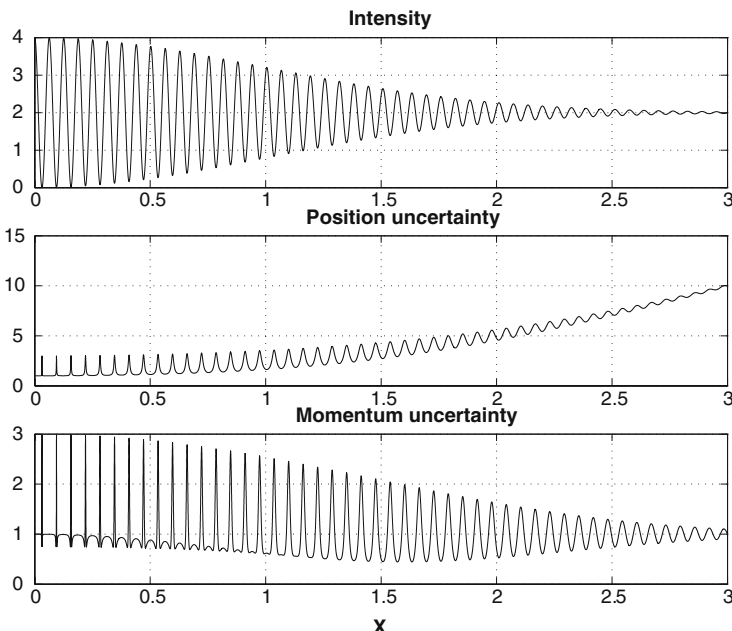


**Fig. 7.13.** Top: intensity  $I_s(X)$  (7.10). Mid: position uncertainty  $\langle(\Delta x)^2\rangle_s/(\delta x)^2$  (7.11). Bottom: momentum uncertainty  $\langle(\Delta k)^2\rangle_s/(\delta k)^2$  (7.12);  $\sigma = 1/100$ . For  $X = \pi/2$  (or  $\Delta_0 k_0 = \pi/(2\sigma) = 100\pi/2$  or  $m_0 = 1/(4\sigma) = 25$ ) the momentum uncertainty has a minimum and the momentum spectrum is squeezed (see Fig. 7.6)

the dynamical conjugate variables  $x$  and  $k$  minimize the uncertainty product with identical uncertainties  $(\delta x)^2 = (\delta k)^2 = 1/2$  (in dimensionless units). Using  $|\psi_s(x, \Delta_0)|^2$  and  $|\alpha_s(k, \Delta_0)|^2$  as distribution functions, we obtain for Gaussian packets (for  $\sigma \ll 1$ ) according to (4.5) and (4.7):

$$\frac{\langle(\Delta x)^2\rangle_s}{(\delta x)^2} = 1 + \frac{X^2}{[I_s(X)/2]} \quad (7.11)$$

and

$$\frac{\langle(\Delta k)^2\rangle_s}{(\delta k)^2} = 1 - X^2 \frac{e^{-X^2} + [I_s(X)/2] - 1}{\{[I_s(X)]^2/4\}}. \quad (7.12)$$

These relations are shown in Fig. 7.13, indicating that for  $\langle(\Delta k)^2\rangle_s$  a value below the coherent state value  $(\delta k)^2$  can be achieved, which in quantum optics terminology means state squeezing [2, 6, 40]. One emphasizes that a single coherent state does not exhibit squeezing, but a state created by superposition of two coherent states can exhibit a considerable amount of squeezing. Thus, highly non-classical states are made by the power of the quantum mechanical superposition principle. The degree of squeezing can be further enhanced by multi-plate interferometry (see the next sections). Properly formed squeezed input states can be used in a Mach–Zehnder interferometer to produce optical entangled states [41]. It should be mentioned that the general uncertainty relation  $\langle(\Delta x)\rangle_s \langle(\Delta k)\rangle_s \geq 1/2$  remains valid for squeezed states as well.

## 7.5 Q-Function

In Sects. 2.2, 2.3.4 and 2.3.6 we examined the Q-function from a theoretical point of view. We have discussed the Q-function of various quantum states (Fock states, coherent states, harmonic oscillator). Unlike the Wigner function, the Q-function has the nice property of being positive everywhere in phase-space. Hence we are led to the question: why not use the Q-function rather than the Wigner function? We recall that the Wigner function emphasizes the interference nature and hence the Wigner function is useful when we want to study interference phenomena. However, it is instructive to investigate and introduce the Q-function in neutron interferometry, by comparing it with the Wigner function.

### 7.5.1 Q-Function of a Wave Packet

First we study the Q-function of a wave packet. Going back to (2.19), the Q-function is a Wigner function washed out by two Gaussian functions

$$f(k) = \frac{1}{\sqrt{2\pi(\delta k)^2}} \exp\left\{-\frac{k^2}{2(\delta k)^2}\right\}, \quad g(x) = \sqrt{\frac{2(\delta k)^2}{\pi}} \exp\{-2(\delta k)^2 x^2\}. \quad (7.13)$$

$g(x)$ , e.g., is exactly the ground-state position distribution  $\psi_0^2(x)$  of a coherent state, where  $(\delta k)(\delta x) = 1/2$  (see 2.37). The Q-function then reads

$$Q(x, k) = \iint f(k - k') g(x - x') W(x', k') dk' dx'. \quad (7.14)$$

Using the Wigner function of a wave packet (2.7) (setting  $t = 0$ ), we obtain

$$Q_{WP}(x, k) = \frac{1}{2\pi} \exp \left\{ -\frac{(k - k_0)^2}{4(\delta k)^2} - (\delta k)^2 x^2 \right\} = \sqrt{\frac{W_{WP}(x, k)}{4\pi}}. \quad (7.15)$$

The appropriate distribution functions of momentum  $\varphi(k)$  and of position  $\gamma(x)$  are:

$$\begin{aligned} \varphi(k) &= \int Q_{WP}(x, k) dx = \frac{1}{2\pi} \sqrt{\frac{\pi}{(\delta k)^2}} \exp \left\{ -\frac{(k - k_0)^2}{4(\delta k)^2} \right\}, \\ \gamma(x) &= \int Q_{WP}(x, k) dk = \frac{1}{2\pi} \sqrt{4\pi(\delta k)^2} \exp \left\{ -(\delta k)^2 x^2 \right\}. \end{aligned} \quad (7.16)$$

The Q-function is normalized to 1:

$$\iint Q_{WP}(x, k) dk dx = \int \varphi(k) dk = \int \gamma(x) dx = 1. \quad (7.17)$$

Using  $\varphi(k)$  and  $\gamma(x)$ , the mean values are:  $\langle k \rangle = k_0$ ,  $\langle k^2 \rangle = k_0^2 + 2(\delta k)^2$ ,  $\langle x \rangle = 0$  and  $\langle x^2 \rangle = 1/[2(\delta k)^2]$ . The uncertainties and the uncertainty relation are:

$$\langle (\Delta k)^2 \rangle_Q = (\delta k)^2, \quad \langle (\Delta x)^2 \rangle_Q = \frac{1}{(\delta k)^2}, \quad \langle (\Delta k)^2 \rangle_Q \langle (\Delta x)^2 \rangle_Q = 1. \quad (7.18)$$

This relation is noteworthy, because the minimum uncertainty relation of a wave packet regarding the Wigner function (4.8) exhibits a value of  $1/4$  instead of 1 here. This is traced back precisely to the fact that the Q-function is washed out by Gaussian functions, as seen in (7.14).

The Shannon entropy can be established according to (4.9) and (4.10) using  $\varphi(k)$  and  $\gamma(x)$ , and we get

$$(H_x + H_k)_{WP,Q} - (H_x + H_k)_{WP,Wigner} = \ln(2) > 0, \quad (7.19)$$

indicating that the Q-function has less information content with respect to the Shannon entropy than the Wigner function.

### 7.5.2 Q-Function of Superposition

In analogy to (7.14), the Q-function of superposition reads

$$Q_s(x, k, \Delta_0) = \iint f(k - k') g(x - x') W_s(x', k', \Delta_0) dk' dx'. \quad (7.20)$$

Inserting (7.6), we achieve

$$Q_s(x, k, \Delta_0) = \frac{1}{2\pi} e^{-\frac{(k/k_0 - 1)^2}{4\sigma^2}} \left\{ e^{-\sigma^2(xk_0)^2} + e^{-\sigma^2(xk_0 + \Delta_0 k_0)^2} \right. \\ \left. + 2 \cos \left[ \frac{\Delta_0}{2}(k + k_0) \right] e^{-\sigma^2(xk_0 + \Delta_0 k_0/2)^2} e^{-\sigma^2(\Delta_0 k_0/2)^2} \right\}. \quad (7.21)$$

This function is drawn in Figs. 7.14 and 7.15. In comparison to Figs. 7.1 and 7.4, where the Wigner function is plotted, the Q-function is firstly two times broader and two times lower, and secondly there are no oscillations in between the cat-states. In addition, the Q-function is positive everywhere, of course. The momentum and position spectra of the Q-function can be obtained by integrating  $Q_s(x, k, \Delta_0)$  over the position and momentum variables, respectively, and it turns out that these spectra are different from  $|\alpha_s(k, \Delta_0)|^2$  and  $|\psi_s(x, \Delta_0)|^2$ , which are derived from the Wigner function ((7.7) and (7.9)). It is left to the reader to determine out these relations. Finally, it should be mentioned that the normalization

$$\iint Q_s(x, k, \Delta_0) dk dx = I_s(X) \quad (7.22)$$

is valid (see (7.10)).

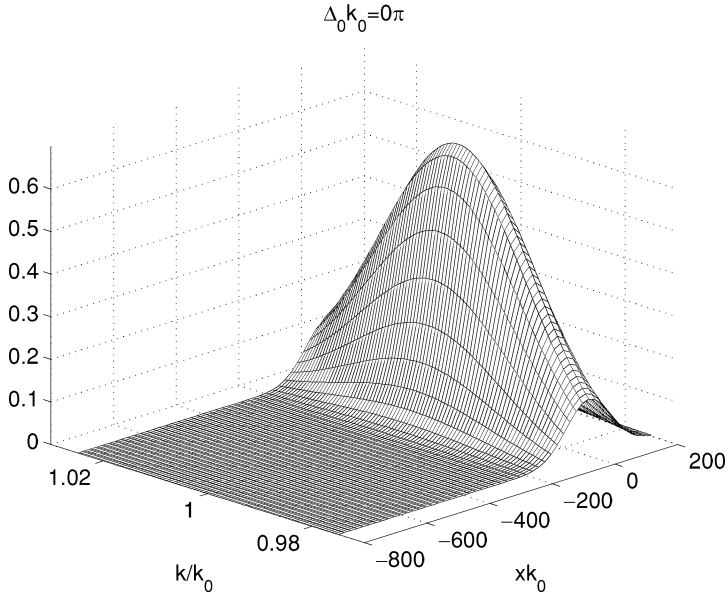


**Fig. 7.14.** Q-function  $Q_s(x, k, \Delta_0)$  (7.21) for superposition of two wave packets:  $\sigma = 1/100$ , interference order  $m_0 = \Delta_0 k_0 / (2\pi) = 0$

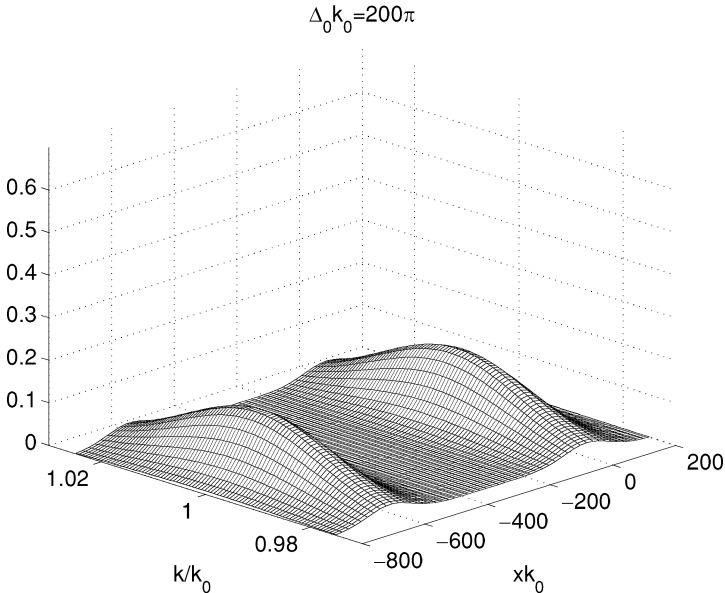


**Fig. 7.15.** Q-function  $Q_s(x, k, \Delta_0)$  (7.21) for superposition of two wave packets:  $\sigma = 1/100$ , interference order  $m_0 = \Delta_0 k_0 / (2\pi) = 100$

Comment: The Wigner functions Figs. 7.1 to 7.4 are more sensitive to the quantum nature of these states than the Q-functions Figs. 7.14 and 7.15, as we have seen already for the number states in Sects. 2.1.4 and 2.3.6. More importantly, the Wigner function can display the “totality” of interference effects associated with a quantum state [42].

## 7.6 Dephasing in Wigner Formalism

Dephasing or decoherence is an interesting phenomenon, related to the long-standing issues of irreversibility. There is a widespread consensus about the meaning of decoherence, viewed as a loss of quantum mechanical coherence of a physical system in interaction with other systems (“environment”). However, a quantitative definition of dephasing or decoherence is subtle [43–45].

We have shown that coupling in phase-space persists even in cases where the spatial wave functions originating from both coherent beam paths of an interferometer do no longer overlap. In this case, the interference fringes disappear, but an intensity modulation in the momentum distribution can be observed (Figs. 7.8, 7.12 and 7.13, top picture). The Wigner function is

especially suitable for demonstrating the appropriate interrelations in phase-space, as shown in Fig. 7.4, where the region of interference demonstrates the non-classical features of this quasi-distribution. However, exactly this region is fragile against any dissipations and fluctuations. This fragility increases with increasing spatial separation of the wave packets and is caused by unavoidable imperfections and uncertainties down to the atomic level and to zero-point fluctuations.

Here, we will describe the influence of several dissipative and uncertainty effects and their influence on dephasing, which is an inherent step towards a measuring process [46, 47]. The dissipative and uncertainty effects describe a stochastic disturbance of the system due to a coupling of the quantum system to the environment. Here we are dealing with stationary situations that exist in the case of a stationary neutron source and a time-independent phase shift.

### 7.6.1 Influence of Inhomogeneities of the Phase Shifter

Any physical system has intrinsic fluctuations and inhomogeneities around certain mean values. The roughness of the surfaces causes variations of the thickness. Density fluctuations inside a phase shifter arise due to thermodynamical reasons and residual stresses. Thus, imperfections exist even at zero temperature, and even a magnetic field used as phase shifter exhibits intrinsic photon numbers and, therefore, fluctuations (see Part IV). Here, we are dealing with fluctuations and inhomogeneities with dimensions larger than the coherence lengths of the neutron beam. In this case, averaging the different beam paths through the phase shifter accounts for these effects.

The phase shifter may have variations of its thickness  $\delta D_P$  around its mean value  $D_{P0}$ , and may have density variations  $\delta N$  around  $N_0$ , which influences the phase shift  $\Delta_0 = 2\pi D_P N b_c / (k_0^2)$  (7.1). In the case of Gaussian distribution functions

$$G(D_P - D_{P0}) = \frac{1}{\sqrt{2\pi}(\delta D_P)} \exp \left\{ -\frac{(D_P - D_{P0})^2}{2(\delta D_P)^2} \right\}, \quad (7.23)$$

$$G(N - N_0) = \frac{1}{\sqrt{2\pi}(\delta N)} \exp \left\{ -\frac{(N - N_0)^2}{2(\delta N)^2} \right\}, \quad (7.24)$$

and the constraints  $\delta D_P/D_{P0} \ll 1$  and  $\delta N/N_0 \ll 1$ , one obtains for the averaged Wigner function  $\overline{W_s}(x, k, \overline{\Delta_0})$  the expression

$$\overline{W_s}(x, k, \overline{\Delta_0}) = \iint G(D_P - D_{P0})G(N - N_0)W_s(x, k, \Delta_0)dD_PdN, \quad (7.25)$$

which means that a mixed state Wigner function is settled up (see (2.1) and (1.15)). Inserting (7.6), the result is:

$$\begin{aligned} \overline{W_s}(x, k, \overline{\Delta_0}) = & \frac{1}{\pi} e^{-\frac{(k/k_0-1)^2}{2\sigma^2}} \left\{ e^{-2\sigma^2(xk_0)^2} + \frac{1}{\sqrt{1+\epsilon}} e^{-2\sigma^2(xk_0+\overline{\Delta_0}k_0)^2/(1+\epsilon)} \right. \\ & + 2 \cos \left[ \frac{(k/k_0)(xk_0\epsilon/2 - \overline{\Delta_0}k_0)}{1+\epsilon/4} \right] \\ & \times \frac{1}{\sqrt{1+\epsilon/4}} e^{-2\sigma^2(xk_0+\overline{\Delta_0}k_0/2)^2/(1+\epsilon/4)} \\ & \left. \times \exp \left[ -\frac{(k/k_0)^2\epsilon/4}{2\sigma^2(1+\epsilon/4)} \right] \right\}, \end{aligned} \quad (7.26)$$

whereas the quantities  $\epsilon$  and  $\overline{\Delta_0}$  have the following meanings:

$$\epsilon = 4(\sigma \overline{\Delta_0} k_0)^2 \left[ \left( \frac{\delta D_P}{D_{P0}} \right)^2 + \left( \frac{\delta N}{N_0} \right)^2 \right], \quad \overline{\Delta_0} = 2\pi D_{P0} N_0 b_c / (k_0^2). \quad (7.27)$$

Figures 7.16, 7.17 and 7.18 can be compared to Figs. 7.1, 7.3 and 7.4. One notices that the cross term of the Wigner function is much more strongly influenced by the damping factor (last exponential factor in (7.26)) than the Wigner functions of the individual separated packets. This behavior can be

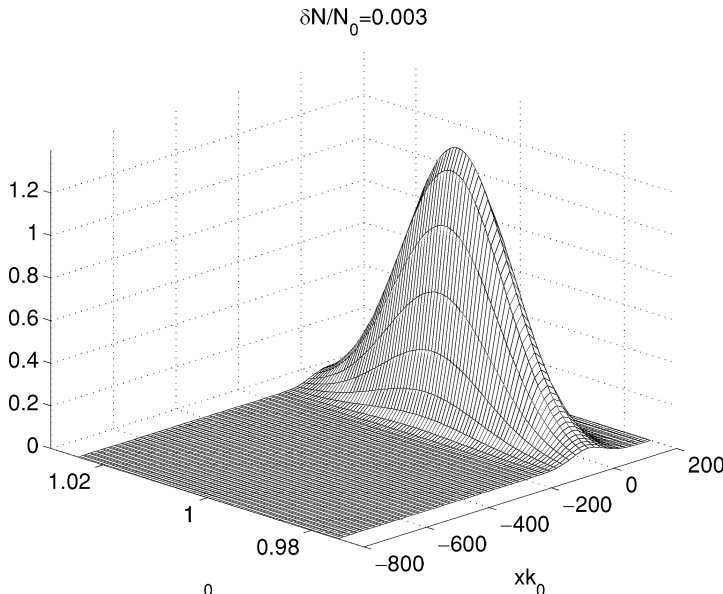


**Fig. 7.16.** Wigner function  $\overline{W_s}(x, k, \overline{\Delta_0})$  (7.26) for superposition of two wave packets:  $\sigma = 1/100$ ,  $\delta N/N_0 = 0.003$ , interference order  $\overline{m}_0 = \overline{\Delta_0}k_0/(2\pi) = 0$

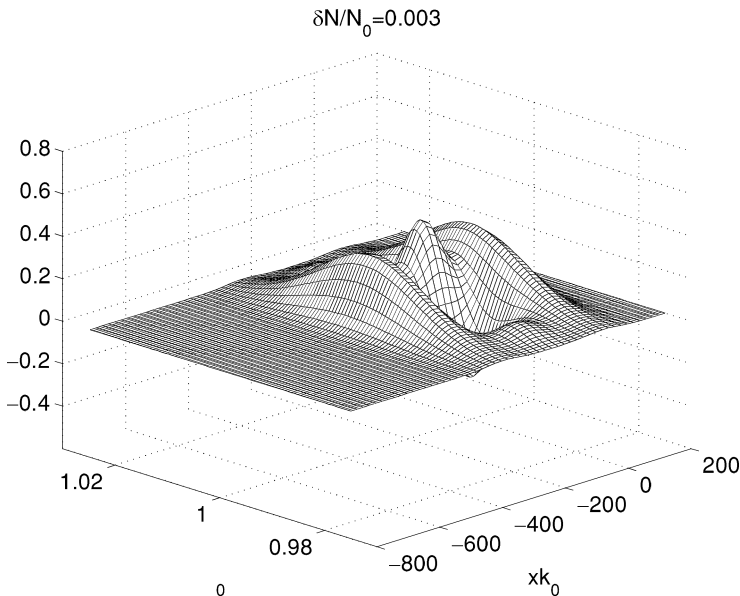


**Fig. 7.17.** Wigner function  $\overline{W}_s(x, k, \overline{\Delta_0})$  (7.26) for superposition of two wave packets:  $\sigma = 1/100$ ,  $\delta N/N_0 = 0.003$ , interference order  $\overline{m_0} = \overline{\Delta_0}k_0/(2\pi) = 50$

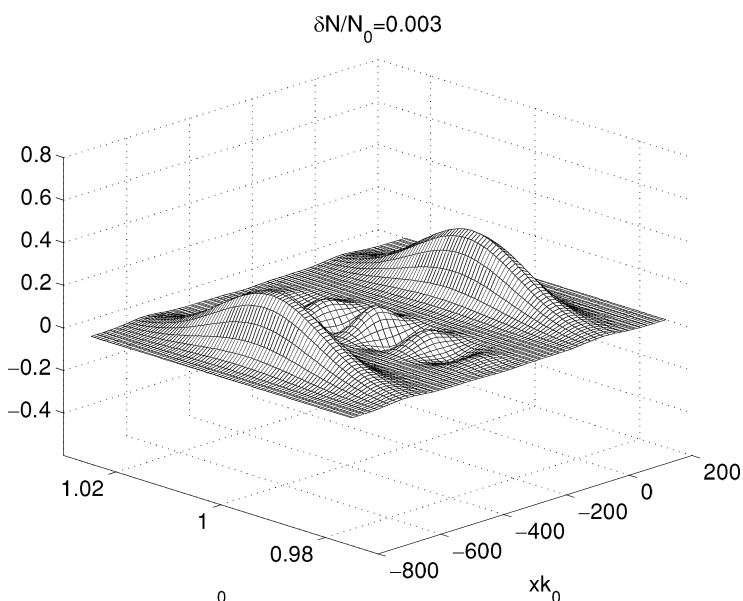


**Fig. 7.18.** Wigner function  $\overline{W}_s(x, k, \overline{\Delta_0})$  (7.26) for superposition of two wave packets:  $\sigma = 1/100$ ,  $\delta N/N_0 = 0.003$ , interference order  $\overline{m_0} = \overline{\Delta_0}k_0/(2\pi) = 100$

seen in the figures for the density fluctuation  $\delta N/N_0 = 0.003$ . The damping factor of the interference pattern shows that the dephasing effect depends quadratically on the mean spatial displacement  $\overline{\Delta_0}$  of the packets (parameter  $\epsilon$ ). According to (4.2), the coherence length is  $l_c = 1/(2\sigma k_0) = 50\text{\AA}$  (the mean wave number  $k_0$  has been assumed to be  $k_0 = 1\text{\AA}^{-1}$  and  $\sigma = 1/100$ ). In Figs. 7.17 and 7.18  $\overline{\Delta_0} = 100\pi\text{\AA} > l_c$  and  $200\pi\text{\AA} > l_c$ , respectively. This demonstrates the sensitivity of the interference region on fluctuations for the spatial displacement parameter  $\overline{\Delta_0}$  larger than the coherence length  $l_c$ .

It can be seen that fluctuations wash out the cross term in any case, which demonstrates that the coherent separation of Schrödinger-cat-like states becomes progressively more difficult with increasing separation, because even small fluctuations have to be avoided.

### 7.6.2 Fluctuations of the Beam Parameter

The beam is described by a wave packet, and the characteristic parameters  $k_0$  and  $\delta k$  have to be considered as fluctuating quantities as well. Such fluctuations originate from unavoidable variations of the experimental setup due to temperature variations, vibrations, etc. Assuming Gaussian fluctuations of  $k_0$  around a mean value  $\overline{k_0}$  with a variance  $\delta k_0$ , it can be shown that this is equivalent to a Gaussian increase of the momentum width  $\delta k$ :

$$(\delta k')^2 = (\delta k)^2 + (\delta k_0)^2, \quad (7.28)$$

and, therefore, (7.26) can still be used. Fluctuations of the spectral width  $\delta k$ , which we denote by  $\Delta(\delta k)$ , may be caused by fluctuations of the collimation width or vibrations of the monochromator, etc. Computer calculations [47] show that this effect on the Wigner function is rather small, because such fluctuations compensate, to a large extent, the usual beam fluctuations  $\delta k$ .

### 7.6.3 Decoherence in Neutron Interferometry

A quantum-mechanical process such as a beam superposition in a neutron interferometer is not an isolated process. The system interacts with its environment. The results show that the off-diagonal terms of the density matrix, which are related to the interference terms, become rapidly dephased at a rate governed by the separation of the coherent states. It has been shown in the last section that the influence of particle density inhomogeneities and of a phase shifter's surface in an interferometer result in a coherence loss of the beams' superposition. Now we are going to demonstrate that this loss of coherence can more generally be interpreted by a diffusion process in ordinary space [48].

To gain some insight into the physics described by dephasing, the one-dimensional Fokker–Planck equation for the distribution function  $P(x, t)$  is a useful starting point [49]:

$$\frac{\partial}{\partial t} P(x, t) = \left[ -\frac{\partial}{\partial x} A(x) + \frac{1}{2} \frac{\partial^2}{\partial x^2} D(x) \right] P(x, t). \quad (7.29)$$

The motion of the mean is governed by  $A(x)$ . This term is called “drift term”.  $D(x)$  acts as a “source of fluctuations”. If  $A = 0$  and  $D$  is constant (diffusion constant), the diffusion equation results:

$$\frac{\partial}{\partial t} P(x, t) = \frac{1}{2} D \frac{\partial^2}{\partial x^2} P(x, t). \quad (7.30)$$

The solution to this equation is well-known:

$$P(x, t) = \int P_1(x, t|x_0, 0) P(x_0, 0) dx_0. \quad (7.31)$$

Here  $P_1(x, t|x_0, 0)$  is the conditional probability (Green’s function)

$$P_1(x, t|x_0, 0) = \frac{1}{\sqrt{2\pi Dt}} \exp \left\{ -\frac{(x - x_0)^2}{2Dt} \right\}, \quad (7.32)$$

which is a function of the space variable  $x$  and time  $t$  (Brownian motion). In (7.31)  $P(x_0, 0)$  denotes the initial condition. Both functions  $P_1$  and  $P$  are solutions of the diffusion equation (7.30).

In the case of neutron interferometry, the superposition of wave packets  $\psi_s$  is produced by means of a phase shift  $\Delta_0$  in one of the arms of the interferometer, as shown in (7.1) and (7.2). The Wigner function  $W_s(x, k, \Delta_0)$  of superposition is given in (7.6). If this function is used as an initial condition  $P(x_0, 0)$  (see (7.31)), the following expression can be established:

$$\overline{W_s}(x, k, \overline{\Delta_0}) = \int P_1(\overline{\Delta_0}, t|\Delta_0, 0) W_s(x, k, \Delta_0) d\Delta_0, \quad (7.33)$$

with the resulting conditional probability in this case being:

$$P_1(\overline{\Delta_0}, t|\Delta_0, 0) = \frac{1}{\sqrt{2\pi Dt}} \exp \left\{ -\frac{(\Delta_0 - \overline{\Delta_0})^2}{2Dt} \right\}. \quad (7.34)$$

$\overline{W_s}(x, k, \overline{\Delta_0})$  is the mean of  $W_s(x, k, \Delta_0)$  related to a mean phase shifting value  $\overline{\Delta_0}$ , as given in (7.26). However, here the parameter  $\epsilon$  contains the diffusion constant  $D$  and time  $t$ , which is the mean transmission time of the beam through the phase shifter:

$$\epsilon = 4(\delta k)^2 Dt. \quad (7.35)$$

Considering (7.34) the exponent contains the mean phase shifting  $\overline{\Delta_0}$ , and this quantity comprises, according to (7.27), parameters like the mean particle number  $N_0$  or the mean thickness  $D_{P0}$  of the phase shifter. Hence, the exponent in (7.34) can be identified, e.g., with density fluctuations  $\delta N/N_0$ , and we obtain an equivalence such as

$$\frac{(\Delta_0/\overline{\Delta_0} - 1)^2}{2Dt/\overline{\Delta_0}^2} \equiv \frac{(N/N_0 - 1)^2}{2(\delta N/N_0)^2}. \quad (7.36)$$

Changing integration in (7.33) from  $\Delta_0$  to  $N$ , the denominators in (7.36) have to be equal and one reaches

$$\epsilon = 4(\delta k)^2 Dt = 4(\delta k)^2 \overline{\Delta_0}^2 (\delta N/N_0)^2. \quad (7.37)$$

If we compare this to (7.27), we recognize the correspondence with the second part of the expression with respect to the parameter  $\epsilon$ . The same considerations can be made with the fluctuations of the thickness of the phase shifter. Therefore we are led to the following differential equation of decoherence:

$$\frac{\partial}{\partial t} \overline{W_s}(x, k, \overline{\Delta_0}, t) = \frac{1}{2} \frac{\partial^2}{\partial \overline{\Delta_0}^2} \overline{W_s}(x, k, \overline{\Delta_0}, t), \quad (7.38)$$

where the parameter  $t$  has additionally been disclosed for clarity. This equation can immediately be proved by insertion. Equation (7.38) is a diffusion equation of the Wigner function [43], and in this case “diffusion” appears as a process in ordinary space. The damping of oscillations in the Wigner function  $\overline{W_s}$  of (7.26) is a general consequence of the non-unitary dynamics, caused in this case by density inhomogeneities and surface roughness of a phase shifter in an interferometer.

It can be concluded that decoherence in neutron interferometry can be formally interpreted very simply by a “diffusion” process. However, it must be emphasized that an interpretation of these dynamics as a result of random kicks (as in classical theory) would mistakenly intermingle classical and quantum concepts.

## 8 Four-Plate Interferometry in Phase-Space

We now discuss the case where an additional interferometer loop is used to revive coherence properties, which appear to be hidden behind the first interferometer loop. Such systems engender some interest, because there exist coupled interferometer loops that are partly fed with coherent beams, instead of incoherent beams as in the case of standard interferometers. The wave functions and the intensities can be calculated by extending the methods applied to the triple-plate interferometer to a multi-plate system [50]. In certain cases, the total interfering intensity can be higher than in the standard triple-Laue case interferometer. Multi-plate interferometers have again demonstrated the linear superposition principle of quantum mechanics and have stimulated discussion about coherent beam mixing and non-sharp particle or wave property determination [24].

Here we concentrate on double-loop systems. The system is described and the coherence properties are expressed via Wigner and distribution functions. Squeezing effects are discussed and correlations, as well as visibility aspects, are investigated.

### 8.1 Double-Loop System

In Fig. 8.1 a double-loop system is shown, which is an extension of a standard three-plate neutron interferometer (Fig. 6.1), and where a second loop is added and separate phase shifters  $\Delta$  (see (7.1)) can be inserted in each loop. Three path ways I, II and III can be distinguished and, therefore, three total phase shifts:

$$\begin{aligned}\Delta_I &= \Delta_{1A} + \Delta_{1B} + \Delta_{2B}, \\ \Delta_{II} &= \Delta_{1A} + \Delta_{2AB} + \Delta_{3B}, \\ \Delta_{III} &= \Delta_{2A} + \Delta_{3A} + \Delta_{3B}.\end{aligned}\tag{8.1}$$

$\chi_A$  and  $\chi_B$  are total phase shifts in loops  $A$  and loop  $B$ , respectively, and we obtain:

$$\begin{aligned}\chi_A &= k_0(\Delta_{II} - \Delta_{III}), \\ \chi_B &= k_0(\Delta_I - \Delta_{II}), \\ \chi_{AB} &= k_0(\Delta_I - \Delta_{III}) = \chi_A + \chi_B.\end{aligned}\tag{8.2}$$

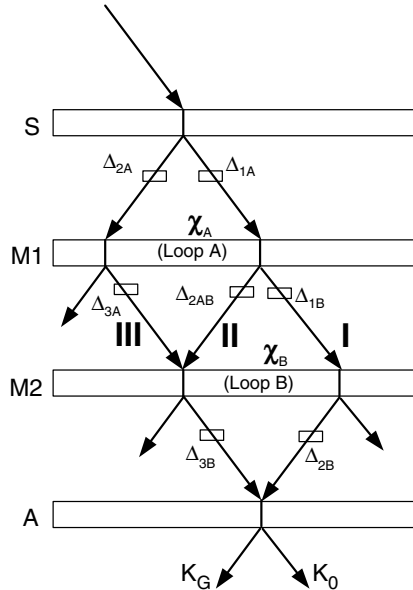


**Fig. 8.1.** Double-loop interferometer. Two loops  $A$  and  $B$ , beam splitter  $S$ , two mirrors  $M1$  and  $M2$ , analyzer  $A$ ;  $K_0$  and  $K_G$  denote intensities in the forward and diffracted directions, respectively;  $\chi_A$  is the total phase shift of loop  $A$ ,  $\chi_B$  of loop  $B$ ; three beam paths I, II and III;  $\Delta$  indicates a phase shifter (see text)

The appropriate interference order parameters are  $m_I = k_0\Delta_I/(2\pi)$ ,  $m_{II} = k_0\Delta_{II}/(2\pi)$  and  $m_{III} = k_0\Delta_{III}/(2\pi)$ .

### 8.1.1 Superposition of Three Waves

Behind the interferometer, only the intensity  $K_0$  shows a maximum theoretical contrast of 100% because three wave functions of equal amplitude superimpose [50]. These three wave functions are transmitted twice and refracted twice each, as can be seen immediately from Fig. 8.1. Hence, behind the interferometer in the forward direction the wave function can be written as:

$$\psi_0(x, \Delta_I, \Delta_{II}, \Delta_{III}) = \psi(x + \Delta_I) + \psi(x + \Delta_{II}) + \psi(x + \Delta_{III}). \quad (8.3)$$

The wave packet in  $k$ -space is (compare to (7.3))

$$\alpha_0(k) = \alpha(k)[e^{ik\Delta_I} + e^{ik\Delta_{II}} + e^{ik\Delta_{III}}]. \quad (8.4)$$

$\alpha(k)$  is given in (2.3).

### 8.1.2 Wigner Function of the Double-Loop System

Now it is convenient to determine the Wigner function by means of (4.3), where (8.4) is inserted. We obtain [51]

$$\begin{aligned} W_0(x, k, t, \Delta_I, \Delta_{II}, \Delta_{III}) = & W_I + W_{II} + W_{III} + 2 \left\{ W_{I,II} \cos \left[ \left( \frac{k}{k_0} \chi_B \right) \right] \right. \\ & + W_{I,III} \cos \left[ \left( \frac{k}{k_0} \chi_{AB} \right) \right] \\ & \left. + W_{II,III} \cos \left[ \left( \frac{k}{k_0} \chi_A \right) \right] \right\}, \end{aligned} \quad (8.5)$$

with the following abbreviations:

$$\begin{aligned} W_i &= W_{WP}(x + \Delta_i, k, t), \\ W_{i,j} &= W_{WP} \left( x + \frac{\Delta_i + \Delta_j}{2}, k, t \right), \quad i, j = I, II, III. \end{aligned} \quad (8.6)$$

$W_{WP}(x, k, t)$  is the Wigner function of a wave packet (2.7).

Figures 8.2 and 8.3 present the Wigner function of superposition (8.5) (for  $t = 0$ ) of three wave packets. It consists of three single Wigner functions due to the three partial beams and of three interference terms. As can be seen, the Wigner function of Fig. 8.2 exhibits a property of maximum squeezing, which will be demonstrated explicitly in the next section. The spectral width of wave numbers ( $k/k_0$ -axis) is minimal, using the specified parameters. Figure 8.2 can be compared with Fig. 7.2. It can be observed that the Wigner function in a double-loop arrangement is more squeezed than in a single-loop system.

### 8.1.3 Momentum Distribution and Squeezing

The momentum distribution function and the intensity can be expressed through the Wigner function. The calculation of the momentum distribution  $|\alpha_0(k, \Delta_I, \Delta_{II}, \Delta_{III})|^2$  is easily performed by integrating  $W_0$  (8.5) over the space coordinate  $x$ . One obtains:

$$\begin{aligned} |\alpha_0(k, \Delta_I, \Delta_{II}, \Delta_{III})|^2 &= \int W_0(x, k, t, \Delta_I, \Delta_{II}, \Delta_{III}) dx \\ &= \alpha^2(k) \left\{ 3 + 2 \left[ \cos \left( \frac{k}{k_0} \chi_B \right) + \cos \left( \frac{k}{k_0} \chi_{AB} \right) \right. \right. \\ &\quad \left. \left. + \cos \left( \frac{k}{k_0} \chi_A \right) \right] \right\}. \end{aligned} \quad (8.7)$$

$$\Delta_I k_0 = 0\pi, \Delta_{II} k_0 = 50\pi, \Delta_{III} k_0 = 100\pi$$

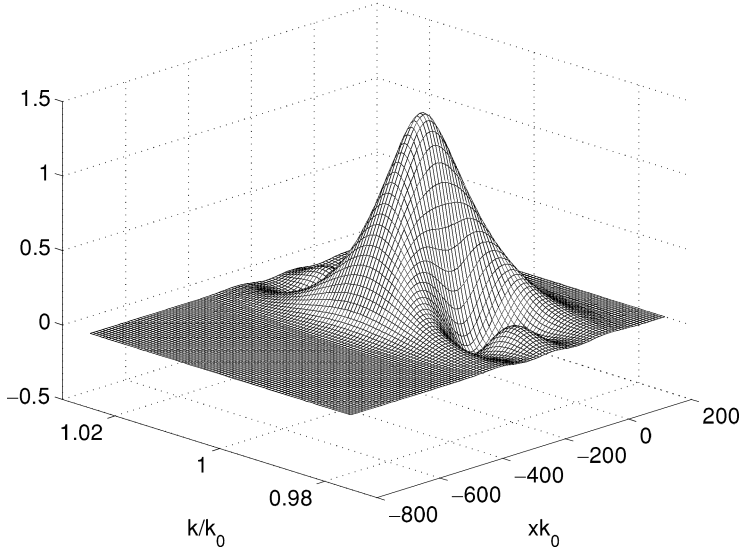


**Fig. 8.2.** Wigner function  $W_0$  in a double-loop interferometer according to (8.5). Maximum squeezing appears for  $\chi \equiv \chi_A = \chi_B = 50\pi$  or  $\chi = \pi/(2\sigma)$ , where  $\sigma = 1/100$  (see text);  $m_I = 0, m_{II} = 25, m_{III} = 50$

$$\Delta_I k_0 = 0\pi, \Delta_{II} k_0 = 100\pi, \Delta_{III} k_0 = 200\pi$$

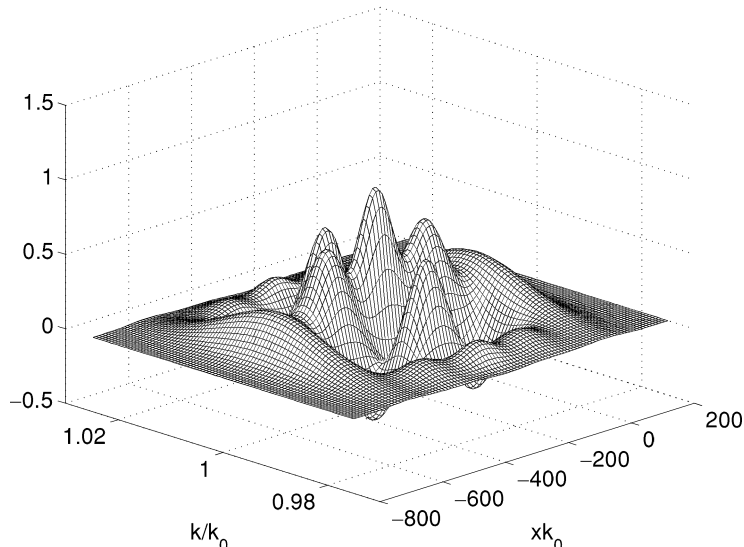


**Fig. 8.3.** Wigner function  $W_0$  in a double-loop interferometer according to (8.5).  $\chi_A = \chi_B = 100\pi, m_I = 0, m_{II} = 50, m_{III} = 100$

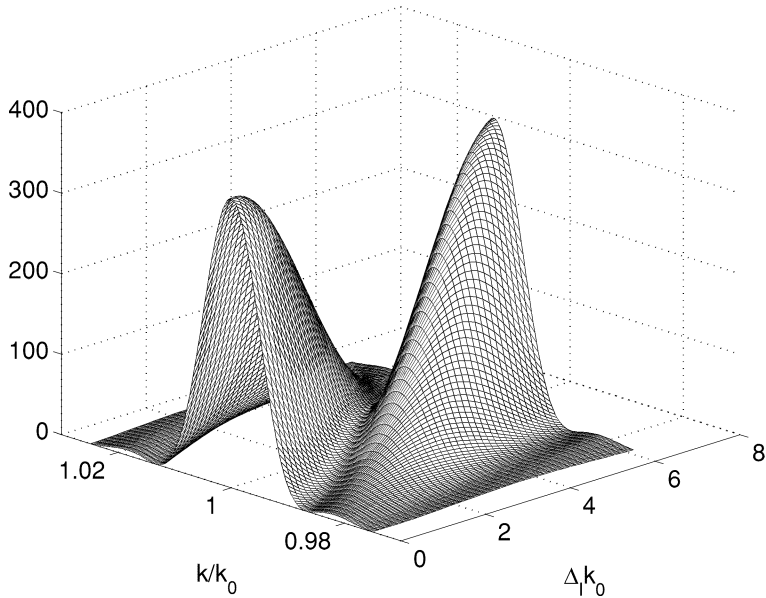


**Fig. 8.4.** Momentum distribution  $|\alpha_0(k, \Delta_I, \Delta_{II}, \Delta_{III})|^2$  in a double-loop interferometer according to (8.7). Maximum squeezing appears for  $\chi \equiv \chi_A = \chi_B = 50\pi$  or  $\chi = \pi/(2\sigma)$ , where  $\sigma = 1/100$ ;  $\Delta_{II}k_0 = 50\pi$ ,  $\Delta_{III}k_0 = 100\pi$  (or  $m_{II} = 25$ ,  $m_{III} = 50$ )

This function is drawn in Fig. 8.4. This figure should be compared to Fig. 7.6, where the squeezed spectrum for the three-plate interferometer has been visualized. In Fig. 8.4 the mean square deviation of momentum is considerably smaller than that in Fig. 7.6.

The intensity is obtained by

$$\begin{aligned} I_0(\Delta_I, \Delta_{II}, \Delta_{III}) &= \int |\alpha_0(k, \Delta_I, \Delta_{II}, \Delta_{III})|^2 dk \\ &= 3 + 2[e^{-(\sigma\chi_B)^2/2} \cos(\chi_B) + e^{-(\sigma\chi_{AB})^2/2} \cos(\chi_{AB}) \\ &\quad + e^{-(\sigma\chi_A)^2/2} \cos(\chi_A)]. \end{aligned} \quad (8.8)$$

This function is displayed in Fig. 8.5, top, for parameters  $\chi \equiv \chi_A = \chi_B$  and thus, according to (8.2),  $\chi_{AB} = 2\chi$ . The scale is  $X = \sigma\chi$ . The momentum uncertainty is determined according to (4.5) and (4.7) and we finally obtain:

$$\frac{\langle (\Delta k)^2 \rangle_0}{(\delta k)^2} = 1 - \frac{4}{I_0^2} \left( \frac{I_0}{2} A + B + 2C \right), \quad (8.9)$$

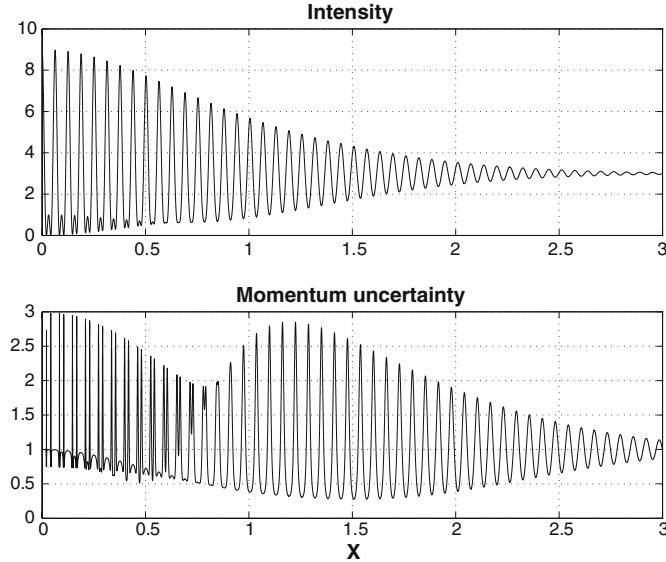


**Fig. 8.5.** Top: intensity  $I_0(X)$  (8.8); bottom: momentum uncertainty  $\langle(\Delta k)^2\rangle_0/(\delta k)^2$  (8.9);  $\sigma = 1/100$ . For  $X = \sigma\chi = \pi/2$  ( $\chi = \chi_A = \chi_B$ ) the momentum uncertainty has a minimum and the momentum spectrum is squeezed (see Fig. 8.4)

where

$$\begin{aligned}
 A &= E_A C_A + E_{AB} C_{AB} + E_B C_B, \\
 B &= (E_A S_A)^2 + (E_{AB} S_{AB})^2 + (E_B S_B)^2, \\
 C &= E_A E_{AB} S_A S_{AB} + E_A E_B S_A S_B + E_{AB} E_B S_{AB} S_B, \\
 E_A &= e^{-(\sigma\chi_A)^2/2}, E_{AB} = e^{-(\sigma\chi_{AB})^2/2}, E_B = e^{-(\sigma\chi_B)^2/2}, \\
 C_A &= (\sigma\chi_A)^2 \cos(\chi_A), C_{AB} = (\sigma\chi_{AB})^2 \cos(\chi_{AB}), C_B = (\sigma\chi_B)^2 \cos(\chi_B), \\
 S_A &= (\sigma\chi_A) \sin(\chi_A), S_{AB} = (\sigma\chi_{AB}) \sin(\chi_{AB}), S_B = (\sigma\chi_B) \sin(\chi_B).
 \end{aligned} \tag{8.10}$$

The squeezing of the Wigner function in Fig. 8.2 or of the momentum distribution in Fig. 8.4 above manifests itself in the mean square deviation expression of (8.9). In Fig. 8.5, bottom, this expression is visualized for the special case  $\chi = \chi_A = \chi_B = X/\sigma$  and  $\sigma = 1/100$ . A minimum of about 0.28 at  $X = \pi/2$  can be observed, which is actually further below the coherent state value of a single minimum wave packet (value 1.00) than that of a three-plate interferometer (minimum = 0.48, Fig. 7.13, bottom).

## 8.2 Correlations in a Double-Loop Interferometer

In a double-loop neutron interferometer two and three beams are superposed behind the first and second loops, respectively. Various correlations between the wave functions, therefore, can be defined. While the momentum distribution can be measured by means of post-selection [24], the space distribution is directly accessible via the visibility, which is expressed by an appropriate correlation function. It is shown that the space distribution behind the first loop can be represented by the visibility, which can be determined by measuring intensities behind the second loop [52].

### 8.2.1 First Loop

In the forward direction behind the first loop, the wave function  $\psi_1$  is a superposition of two beams of equal amplitudes, which have both been transmitted once and reflected twice by Bragg reflection on the silicon single-crystal plates of the interferometer (Fig. 8.6). Behind the second loop (after the fourth plate in the forward direction), three beams of equal amplitude are combined (see Sect. 8.1.1), each of which has been transmitted twice and reflected twice. The resulting wave function is denoted by  $\psi_2$ . A phase shift  $\Delta_1$  is introduced in one arm of the first loop. The superposition

$$\psi_1(x) = c_1[\psi(x) + \psi(x + \Delta_1)] \quad (8.11)$$

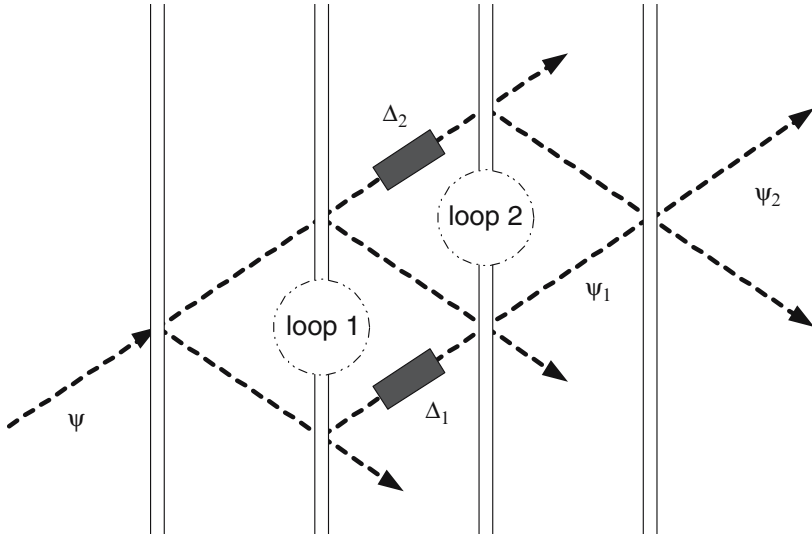


**Fig. 8.6.** The double-loop neutron interferometer:  $\Delta_1$  and  $\Delta_2$  are two phase shifters,  $\psi$  denotes the incoming wave function,  $\psi_1$  and  $\psi_2$  are superpositions of two and three beams, respectively

of the two individual wave packets of equal amplitude behind the first loop ( $c_1$  is a real constant and is defined by the dynamical theory of diffraction (see Chap. 5)) leads to the intensity (7.10)

$$I_1 = \int |\psi_1(x)|^2 dx \propto 2\{1 + e^{-[\sigma(\Delta_1 k_0)]^2/2} \cos(\Delta_1 k_0)\}. \quad (8.12)$$

The visibility is defined by (3.17) and leads to

$$V_1(\Delta_1) = e^{-[\sigma(\Delta_1 k_0)]^2/2}. \quad (8.13)$$

Alternatively, the correlation  $\Gamma_1(\Delta_1)$  between the two beams leads to

$$\begin{aligned} \Gamma_1(\Delta_1) &= \int \psi^*(x)\psi(x + \Delta_1)dx = \int \alpha(k)^2 \exp(ik\Delta_1)dk \\ &= V_1(\Delta_1) \exp(i\Delta_1 k_0), \end{aligned} \quad (8.14)$$

where  $|\Gamma_1(\Delta_1)| = V_1(\Delta_1)$ .  $\Gamma_1(\Delta_1)$  is an auto-correlation function, which is the Fourier-transform of the momentum distribution  $\alpha(k)^2$ . From the definition of the wave packet, one obtains the space distribution (see (2.6))  $|\psi(x)|^2 = c \exp\{-2[\sigma(xk_0)]^2\}$ , where  $c = (\sigma)\sqrt{2/\pi k_0}$ . From (8.13) it follows that the space distribution is proportional to the visibility:  $|\psi(\Delta_1/2)|^2 \propto V_1(\Delta_1)$  when  $x$  is substituted with  $\Delta_1/2$ . One can infer the space distribution of an individual wave packet from the visibility, which can be measured by means of intensities behind the first loop of the interferometer. It will be shown in the next section that, to a certain degree, an analogous relation is valid behind the second loop.

Both the momentum distribution  $|\alpha_1(k)|^2$  and the space distribution  $|\psi_1(x)|^2$  can directly be determined from the definition of the corresponding wave packets ((7.7) and (7.9)):

$$|\alpha_1(k)|^2 = 2c_1^2 \alpha(k)^2 \left\{ 1 + \cos\left[\frac{k}{k_0}(\Delta_1 k_0)\right] \right\}, \quad (8.15)$$

$$\begin{aligned} |\psi_1(x)|^2 &= c.c_1^2 \{ \exp[-2\sigma^2(xk_0)^2] + \exp[-2\sigma^2(xk_0 - \Delta_1 k_0)^2] \\ &\quad + 2 \cos(\Delta_1 k_0) \exp[-2\sigma^2(xk_0)^2] \exp[-2\sigma^2(xk_0 - \Delta_1 k_0)^2] \}. \end{aligned} \quad (8.16)$$

### 8.2.2 Second Loop

The superposition  $\psi_2(x) = c_2[\psi(x) + \psi(x + \Delta_1) + \psi(x + \Delta_2)]$  of three wave packets of equal amplitude ( $c_2$  is a real constant) behind the second loop entails the intensity (8.8)

$$\begin{aligned} I_2 &\propto A_1 + 2\{\exp[-\sigma^2(\Delta_2 k_0)^2/2] \cos(\Delta_2 k_0) \\ &\quad + \exp[-\sigma^2(\Delta_2 k_0 - \Delta_1 k_0)^2/2] \cos[(\Delta_2 - \Delta_1)k_0]\}, \end{aligned} \quad (8.17)$$

where a second phase shift  $\Delta_2$  and  $A_1 = 3 + 2 \exp[-\sigma^2(\Delta_1 k_0)^2/2] \cos(\Delta_1 k_0)$  have been defined. If the wave packets are separated, i.e., if  $\sigma(\Delta_1 k_0) > 5$  or  $A_1 \approx 3$ , the visibility can be written as

$$\begin{aligned} V_2(\Delta_1, \Delta_2) \\ = (2/A_1)\{\exp[-\sigma^2(\Delta_2 k_0)^2/2] + \exp[-\sigma^2(\Delta_2 k_0 - \Delta_1 k_0)^2/2]\}. \end{aligned} \quad (8.18)$$

Now a cross-correlation, which combines the superposition state behind the first loop with the corresponding state including  $\Delta_2$  in the second loop (see Fig. 8.6) has to be set up:

$$\Gamma_2(\Delta_1, \Delta_2) = \frac{1}{c_1} \int \psi_1^*(x) \psi(x + \Delta_2) dx = \Gamma_1(\Delta_2) + \Gamma_1(\Delta_2 - \Delta_1). \quad (8.19)$$

The modulus of this cross-correlation is given by

$$\begin{aligned} |\Gamma_2(\Delta_1, \Delta_2)| \\ = \sqrt{e^{-X_2^2} + e^{-(X_2 - X_1)^2} + 2 \cos(X_1/\sigma) e^{-X_2^2/2 - (X_2 - X_1)^2/2}}, \end{aligned} \quad (8.20)$$

where  $X_1 = \sigma(\Delta_1 k_0)$  and  $X_2 = \sigma(\Delta_2 k_0)$  and  $\sigma = (\delta k)/k_0$ . The function  $|\Gamma_2(\Delta_1, \Delta_2)|$  is shown in Fig. 8.7. For small values of  $X_1$  and  $X_2$ , the interference behavior in space between the two beams  $\psi_1(x)$  and  $\psi(x + \Delta_2)$

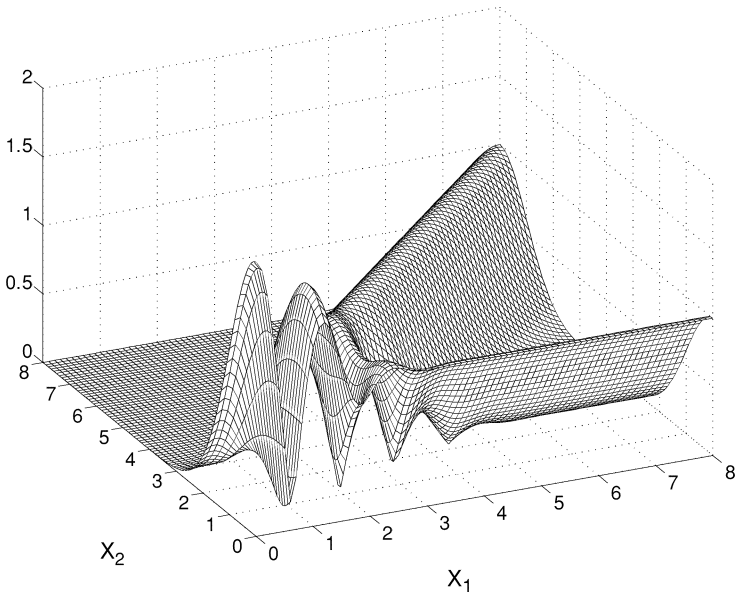


**Fig. 8.7.** The correlation  $|\Gamma_2(\Delta_1, \Delta_2)|$ :  $\sigma = 0.2$ ,  $X_1 = \sigma(\Delta_1 k_0)$ ,  $X_2 = \sigma(\Delta_2 k_0)$ . For  $X_1 > 5$  the wave packets are separated and  $|\Gamma_2(\Delta_1, \Delta_2)|$  becomes proportional to the space distribution function  $|\psi_1|^2$  behind the first loop

is visible. If  $X_1 > 5$  is achieved, the oscillations are damped out and it can be observed clearly that the function is split up into two parts. This split is interpreted as separation of the wave packets due to a large phase shift  $\Delta_1$ . In this region, the relation  $|\Gamma_2(\Delta_1, \Delta_2)| \propto V_2(\Delta_1, \Delta_2)$  is valid. If, similarly to in Sect. 8.2.1, the variable  $x$  is replaced by  $\Delta_2/2$  and  $\Delta_1$  by  $\Delta_1/2$ , the space distribution for separated wave packets behind the first loop can be seen to be proportional to the visibility:  $|\psi_1(x \rightarrow \Delta_2/2, \Delta_1 \rightarrow \Delta_1/2)|^2 \propto V_2(\Delta_1, \Delta_2)$ . The important message of these considerations is that one can deduce the space distribution behind the first loop of the interferometer (two-wave superposition) from the measured visibility behind the second loop (three-wave superposition).

### 8.3 Intensity and Visibility in a Double-Loop System

We are now able to determine the mean intensity levels of the forward and diffracted beams behind an empty four-plate interferometer of this type. Various phase shifters and absorbers can be put into the arms of a double-loop neutron interferometer. Below, it is shown that the intensities in the forward and diffracted direction can be made equal, using certain absorbers. In this case, the interferometer can be regarded as a 50/50 beam splitter. Furthermore, in this section, the visibilities of single and double-loop interferometers are compared to each other, by varying the transmission in the first loop using different absorbers. It will be shown that the visibility becomes exactly 1, using a phase shifter in the second loop. In this case, the phase shifter in the second loop must be strongly correlated to the transmission coefficient of the absorber in the first loop [53].

Here, again, we concentrate on coherence effects in a double-loop interferometer [24, 50]. Figure 8.8 describes an extension of a standard three-plate neutron interferometer, where a second loop is added by using a second mirror crystal  $M2$ , and where various phase shifters  $\Delta$  and absorbers  $\alpha$  can be inserted in each loop. Both loops are coupled via beam (d) and, therefore, most attention will be given to the action of an absorbing phase shift in this beam. We focus on two phase shifters  $\Delta_d$  and  $\Delta_f$  and two absorbers  $\alpha_d$  and  $\alpha_f$  in beams (d) and (f), respectively, because phase shifters or absorbers in beam (b) are of no additional significance. The main aim is to find an interaction where small signals transmitted through phase shifter  $\Delta_d$  can be detected with high precision. In this respect, it is a search for homodyne-like detection of weak neutron signals by the constraint that a symmetric beam splitter does not exist in the case of diffraction from a crystal. The new system consists of a coupled double-loop perfect crystal system and provides a symmetric beam splitting or can serve as a basis of homodyne neutron detection in a sense similar to that known for photon beams [12].

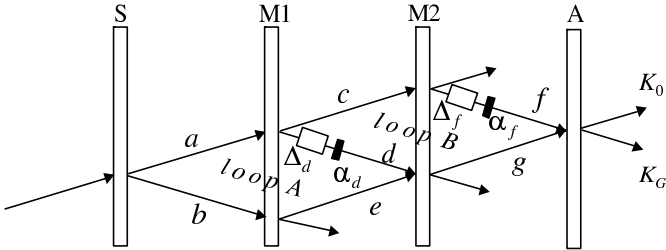


**Fig. 8.8.** Double-loop neutron interferometer similar to Fig. 8.1, but here we account additionally for two absorbers:  $\Delta_d$  and  $\Delta_f$  are two phase shifters,  $\alpha_d$  and  $\alpha_f$  are two absorbers with transmissions  $T_d = e^{-2\alpha_d}$  and  $T_f = e^{-2\alpha_f}$ , respectively.  $K_0$  and  $K_G$  denote the intensity in the forward and diffracted direction. There are three beam paths:  $(acf)$  (path I),  $(adg)$  (path II) and  $(beg)$  (path III). The first loop ( $A$ ) is formed by the beams  $(adeb)$ , the second loop ( $B$ ) by the beams  $(cfgd)$ . Beam  $(g)$  is a superposition of beam  $(ad)$  and beam  $(be)$

### 8.3.1 Intensity Aspects

From the dynamical theory of diffraction (Chap. 5), the wave function behind the analyzer crystal in the forward direction, which is a superposition of three waves due to the three pathways (see Fig. 8.8), reads as (see Sect. 5.5.2 and (5.49))

$$\psi_0^{(acf)+(adg)+(beg)} = \psi_e e^{i\gamma} v_0^2(y) v_G(y) v_G(-y) [e^{ik\Delta_f - \alpha_f} + e^{ik\Delta_d - \alpha_d} + 1]. \quad (8.21)$$

$e^{i\gamma}$  is a phase factor that is of no relevance in the following. The three terms in (8.21) form a superposition of three wave functions that belong to the three pathways  $(acf)$ ,  $(adg)$  and  $(beg)$ . They have different phase shifts and absorptions. The crystal functions defined above are equal for each of the three wave functions, because each beam is transmitted (function  $v_0^2(y)$ ) and diffracted (functions  $v_G(y)$  and  $v_G(-y)$ ) twice, respectively.

The wave function in the diffracted direction behind the analyzer crystal reads

$$\begin{aligned} \psi_G^{(acf)+(adg)+(beg)} &= \psi_{e'} e^{i\delta} v_0(y) v_G(y) [v_0(y) v_0(-y) e^{ik\Delta_f - \alpha_f} \\ &\quad + v_G v_G(-y) (e^{ik\Delta_d - \alpha_d} + 1)]. \end{aligned} \quad (8.22)$$

$e^{i\delta}$  is again a phase factor of no relevance. From the last two equations, it can be recognized that the three wave functions that are superimposed in the forward direction (0) have the same number of reflections and transmissions, but those in the diffracted direction  $G$  do not. Therefore, an unsymmetrical intensity behavior can be expected in the diffracted direction, as shown below.

In order to compute the intensities  $K_0$  and  $K_G$  behind the analyzer crystal, the squared moduli of the wave functions, i.e.,  $|\psi_0^{(acf)+(adg)+(beg)}|^2$  and

$|\psi_G^{(acf)+(adg)+(beg)}|^2$ , have to be taken into account. Because of the thickness of about 0.5 cm of the crystal plates in Fig. 8.8, the quantity  $A = \pi D/\Delta_0 \gg 1$  in (5.39) causes very rapid oscillations of the terms  $\sin^{2n}(x)$  that appear in these expressions. Therefore, the mean values of these trigonometric functions can be used. One gets:  $\overline{\sin^2(x)} = 1/2$ ,  $\overline{\sin^4(x)} = 3/8$ ,  $\overline{\sin^6(x)} = 5/16$  and  $\overline{\sin^8(x)} = 35/128$  [28, 50]. Moreover, integration over the variable  $y$  must be performed because of the beam divergence, which has to be taken into account. Finally a normalized Gaussian spectral distribution  $\alpha^2(k)$  (7.8) of incoming wave numbers  $k$  is assumed. The intensities can now be calculated (setting  $u_0 = 1$ , see (5.47) to (5.50)) as follows (the limits of integration are always  $-\infty$  and  $+\infty$ ):

$$\begin{aligned} K_0 &= \int \alpha^2(k) \left[ \int \overline{|\psi_0^{(acf)+(adg)+(beg)}|^2} dy \right] dk = \frac{79\pi}{2048} \left\{ 1 + e^{-2\alpha_d} + e^{-2\alpha_f} \right. \\ &\quad + 2e^{-\alpha_d} e^{-(\delta k)^2(\Delta_d)^2/2} \cos(\Delta_d k_0) + 2e^{-\alpha_f} e^{-(\delta k)^2(\Delta_f)^2/2} \cos(\Delta_f k_0) \\ &\quad \left. + 2e^{-(\alpha_d+\alpha_f)} e^{-(\delta k)^2(\Delta_d-\Delta_f)^2/2} \cos[(\Delta_d - \Delta_f)k_0] \right\}, \end{aligned} \quad (8.23)$$

$$\begin{aligned} K_G &= \int \alpha^2(k) \left[ \int \overline{|\psi_G^{(acf)+(adg)+(beg)}|^2} dy \right] dk = \frac{\pi}{2048} \left\{ 65(1 + e^{-2\alpha_d}) \right. \\ &\quad + 417e^{-2\alpha_f} + 130e^{-\alpha_d} e^{-(\delta k)^2(\Delta_d)^2/2} \cos(\Delta_d k_0) \\ &\quad - 158e^{-\alpha_f} e^{-(\delta k)^2(\Delta_f)^2/2} \cos(\Delta_f k_0) \\ &\quad \left. - 158e^{-(\alpha_d+\alpha_f)} e^{-(\delta k)^2(\Delta_d-\Delta_f)^2/2} \cos[(\Delta_d - \Delta_f)k_0] \right\}. \end{aligned} \quad (8.24)$$

Figure 8.9 plots  $K_0$  and  $K_G$  for  $\Delta_d = 0$  and  $\alpha_d = \alpha_f = 0$  as a function of  $\Delta_f$ . If  $\Delta_f = 0$ ,  $K_0 = 711\pi/2048$  and  $K_G = 361\pi/2048$ . These results can be found elsewhere [50]. One can recognize that the mean intensities of the two beams are, in general, different (just like in single-loop interferometry, (6.13)). The question arises as to whether these intensity levels can be made equal by using special parameter values. The answer is yes. If one takes the mean values of  $K_0$  and  $K_G$  to be equal, i.e.,  $\overline{[K_0 - K_G]}_{\Delta_f} = 0$ , one gets a condition for  $\alpha_f$ :

$$\alpha_f = -\frac{1}{2} \ln \left\{ \frac{7}{169} [1 + e^{-2\alpha_d} + 2e^{-\alpha_d} e^{-(\delta k)^2(\Delta_d)^2} \cos(\Delta_d k_0)] \right\} \geq 0. \quad (8.25)$$

Any absorption  $\alpha$  has to be  $\geq 0$ , because the transmission  $T = e^{-2\alpha}$  of a beam obeys the relation  $0 \leq T \leq 1$ . In the case of  $\alpha_d = 0$  and  $\Delta_d = 0$ , the absorption  $\alpha_f$  becomes  $-(1/2) \ln(28/169) = 0.8988$ . Figure 8.10 demonstrates this example. In this case, the double loop interferometer may be regarded as a 50/50 beam splitter by using an absorption element in a suitable arm of the device. This is not possible using a single-loop interferometer.

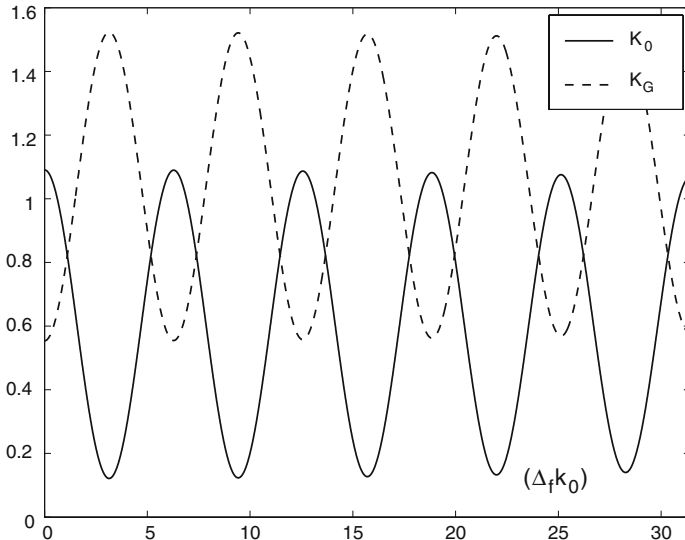


**Fig. 8.9.** Intensities  $K_0$  and  $K_G$  of (8.23) and (8.24) behind the double-loop interferometer (see Fig. 8.8) for  $\alpha_d = \alpha_f = 0$ ,  $\Delta_d = 0$  and  $(\delta k)/k_0 = 1/100$ . The level of oscillations of  $K_0$  is below that of  $K_G$

### 8.3.2 Visibility Aspects of Single and Double-Loops

The visibility is defined as (3.17)

$$V = \frac{I_{max} - I_{min}}{I_{max} + I_{min}}. \quad (8.26)$$

We distinguish two kinds of absorption processes: stochastic (sto) and deterministic (det) absorption [54]. In an interferometer, stochastic absorption is realized by inserting an absorbing material in one arm of a beam (Fig. 8.8). Deterministic absorption can be achieved by a chopper, which blocks the beam path periodically or by partial reduction of the beam cross-section. In the following, we investigate the visibility in a single and double-loop interferometer at low interference order (the coherence function is approximately one).

a) *Single-Loop Interferometer (Index 1)* : If one phase shifter  $\Delta_d$  and one absorber  $\alpha_d$  are put in beam path ( $d$ ), the intensity  $I_g$  of beam  $g$  in the forward direction behind the first loop  $A$  (Fig. 8.8) can be written as

$$I_g \propto |1 + e^{ik_0(\Delta_d - \alpha_d)}|^2 = 1 + T_d + 2\sqrt{T_d} \cos(\Delta_d k_0), \quad (8.27)$$

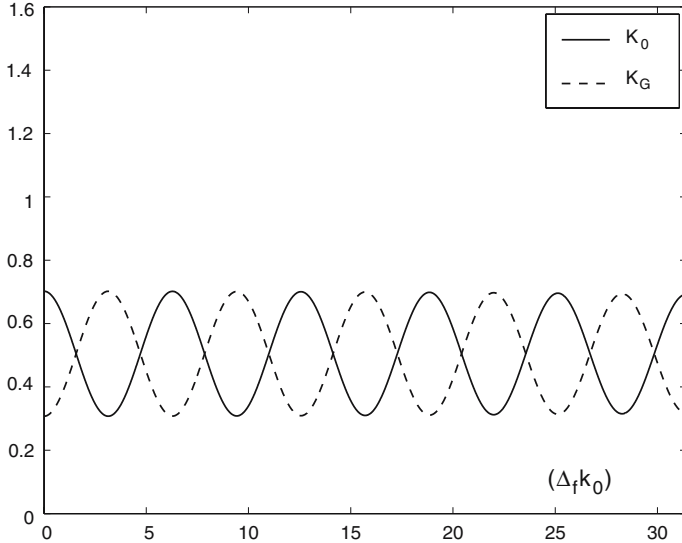


**Fig. 8.10.** Calculated intensity oscillations of  $K_0$  and  $K_G$  of (8.23) and (8.24) considering the following parameters:  $\alpha_d = 0$ ,  $\alpha_f = -(1/2) \ln(28/169) = 0.8988$ ,  $\Delta_d = 0$  and  $(\delta k)/k_0 = 1/100$ . The intensity levels are equal due to  $\alpha_f$

where  $T_d = e^{-2\alpha_d}$  is the transmission probability of beam ( $d$ ) and  $\Delta_d k_0$  is the phase difference between the two beam paths. The visibility is, therefore,

$$V_{sto1} = \frac{2\sqrt{T_d}}{1 + T_d}. \quad (8.28)$$

For deterministic absorption we get

$$I_g \propto |1 + e^{ik_0\Delta_d}|^2 T_d + (1 - T_d) = 1 + T_d + 2T_d \cos(\Delta_d k_0), \quad (8.29)$$

$$V_{det1} = \frac{2T_d}{1 + T_d}. \quad (8.30)$$

The difference between stochastic and deterministic absorption in a single-loop neutron interferometer is drawn in Fig. 8.11 and has been discussed in [54].

b) *Double-Loop Interferometer (Index 2)* : If  $\Delta_d$  and  $\alpha_d$  are placed in path ( $d$ ) and no phase shifter or absorber in beam path ( $f$ ) (see Fig. 8.8), the intensity is given as (see (8.23)):

$$K_0 \propto |2 + e^{ik_0\Delta_d - \alpha_d}|^2 = T_d + 4[1 + \sqrt{T_d} \cos(\Delta_d k_0)], \quad (8.31)$$

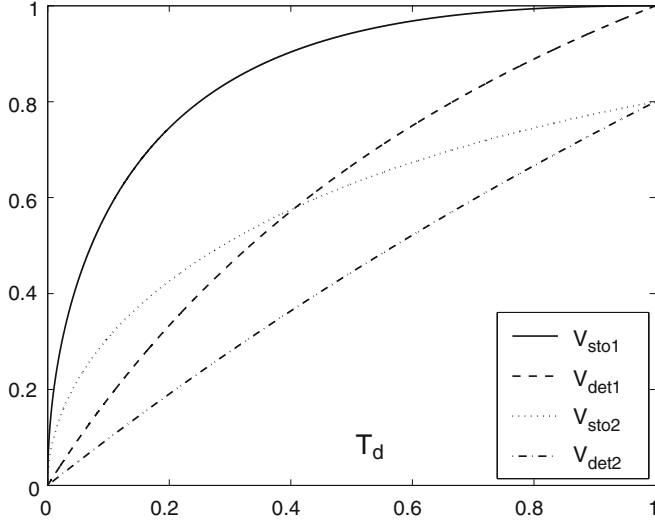


**Fig. 8.11.** Visibilities of single and double-loop interferometers. The visibilities  $V_{sto1}$  for stochastic (8.28) absorption and  $V_{det1}$  for deterministic (8.30) absorption in a single-loop interferometer are shown as a function of transmission probability  $T_d$  in beam path ( $d$ ). In the double-loop interferometer no phase shifter  $\Delta_f$  and no absorber  $\alpha_f$  in beam path ( $f$ ). In this case, the visibilities  $V_{sto2}$  and  $V_{det2}$  of (8.32) and (8.34) are smaller than in a single-loop device

$$V_{sto2} = \frac{4\sqrt{T_d}}{4 + T_d} < 1. \quad (8.32)$$

The deterministic case may be expressed as

$$K_0 \propto |2 + e^{ik_0\Delta_d}|^2 T_d + 4(1 - T_d) = T_d + 4[1 + T_d \cos(\Delta_d k_0)], \quad (8.33)$$

$$V_{det2} = \frac{4T_d}{4 + T_d} < 1. \quad (8.34)$$

In general,  $V_{sto1} > V_{sto2}$  and  $V_{det1} > V_{det2}$  for  $0 \leq T_d \leq 1$  (Fig. 8.11).

An interesting case arises, if a phase shifter  $\Delta_f$  (and no absorption  $\alpha_f$ ) is inserted in beam path ( $f$ ). The intensity then becomes

$$\begin{aligned} K_0 &\propto |e^{ik_0\Delta_d - \alpha_d} + 1 + e^{ik_0\Delta_f}|^2 \\ &= T_d + 2\sqrt{T_d}[\cos(\Delta_d k_0) + \cos(\Delta_d k_0 - \Delta_f k_0)] + 4\cos^2(\Delta_f k_0/2). \end{aligned} \quad (8.35)$$

If  $\Delta_f = 0$ , then (8.35) reduces to (8.31). If  $\Delta_f k_0 = (2n+1)\pi$ , then  $e^{i\Delta_f k_0} = -1$  and  $K_0 \propto T_d$ . If  $2n\pi \leq \Delta_f k_0 \leq (2n+1)\pi$ , maxima of  $K_0$  are at  $\Delta_d k_0 = \Delta_f k_0/2 + 2n\pi$  and minima at  $\Delta_d k_0 = \Delta_f k_0/2 + (2n+1)\pi$ . These maxima

and minima are interchanged in the range  $(2n + 1)\pi \leq \Delta_f k_0 \leq (2n + 2)\pi$ , and it is not necessary to consider this case separately. One gets:

$$K_{0,\frac{max}{min}} \propto T_d \pm 4 \cos(\Delta_f k_0/2) [\sqrt{T_d} \pm \cos(\Delta_f k_0/2)], \quad (8.36)$$

where the upper sign belongs to the maximum and the lower sign to the minimum intensity. The visibility is

$$V_{sto2\Delta_f} = \frac{4\sqrt{T_d} \cos(\Delta_f k_0/2)}{4 \cos^2(\Delta_f k_0/2) + T_d}. \quad (8.37)$$

If  $\Delta_f k_0 = 0$ , then  $V_{sto2\Delta_f} = V_{sto2}$ . If  $\Delta_f k_0 = 2\pi/3$ , then  $V_{sto2\Delta_f} = V_{sto1}$ . In particular, we emphasize the fact that the maximum of the function  $V_{sto2\Delta_f}$  is at  $T_d = 4 \cos^2(\Delta_f k_0/2)$ , where  $V_{sto2\Delta_f} = 1$ . For a given transmission  $T_d$  in beam path ( $d$ ), a phase shift  $\Delta_f k_0 = 2 \arccos(\sqrt{T_d}/2)$  in path ( $f$ ) should be chosen in order to achieve a visibility of one (Figs. 8.12 and 8.13)! Setting  $T_d = 1$ , the relation  $V_{sto2\Delta_f}$  of (8.37) reduces to a formula that has already been discussed in [55] (see Fig. 8.13).

An analogous equation can be derived for the deterministic case, which reads

$$V_{det2\Delta_f} = \frac{4 T_d \cos(\Delta_f k_0/2)}{4 \cos^2(\Delta_f k_0/2) + T_d} < 1, \quad \text{for } T_d < 1. \quad (8.38)$$

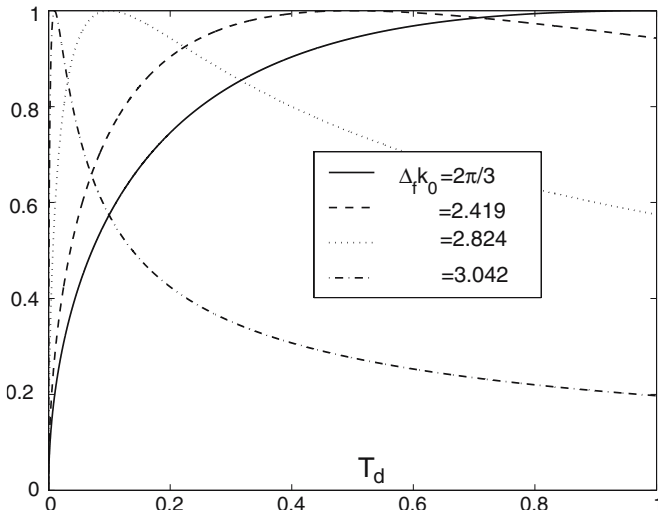


**Fig. 8.12.** Visibility  $V_{sto2\Delta_f}$  (8.37) in a double-loop interferometer as a function of transmission probability  $T_d$  in beam path ( $d$ ). A phase shift  $\Delta_f k_0$  is applied in beam path ( $f$ ). The visibility attains the value 1 for  $T_d = 4 \cos^2(\Delta_f k_0/2)$

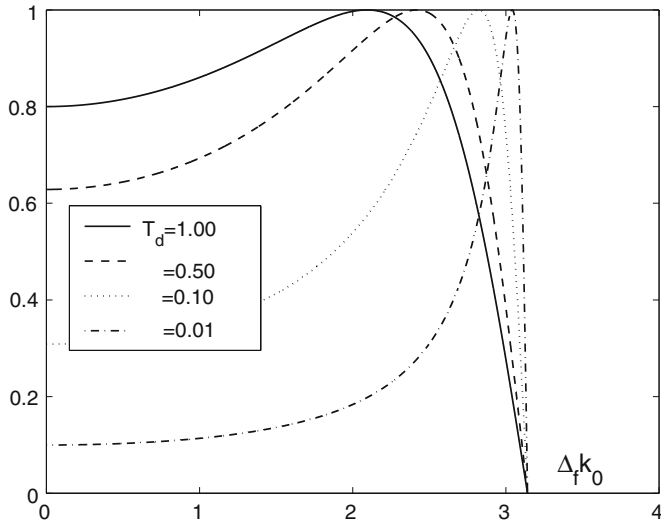


**Fig. 8.13.** Visibility  $V_{sto2\Delta_f}$  (8.37) in a double-loop interferometer as a function of phase shift  $\Delta_f k_0$  in beam path ( $f$ ). A transmission probability  $T_d$  is applied in beam path ( $d$ ). The visibility attains the value 1 for  $T_d = 4 \cos^2(\Delta_f k_0/2)$ , where the four parameters  $T_d$  correspond to the four parameters  $\Delta_f k_0$  in Fig. 8.12 via this equation

In the case of deterministic visibility, the value of 1 cannot be achieved for  $T_d < 1$ .

In order to compare intensities and to assess possibilities for measurements, Fig. 8.14 a,b,c presents values of  $K_0$  and  $K_G$  as functions of the phase shift  $\Delta_d k_0$  in beam path ( $d$ ). From these figures it can be concluded that in spite of strong absorption, small signals can be measured with visibility 1 and with sufficient intensity by adequately adjusting the phase shifter in the second loop of the interferometer. However, as shown below, the procedure described specifies an ideal situation and there is a limit for measuring weak signals using such a technique.

It should be noted that, to describe real experimental situations, an additive term  $I_{incoh}$  must be introduced in (8.35) to represent the incoherent part of the intensity (background intensity). The main reason for the incoherent effects is non-interference because of crystal imperfection (the crystal lattice planes are not absolutely parallel throughout the interferometer), as well as lattice vibrations and small temperature gradients. The term  $I_{incoh}$  leads to a new visibility  $V'_{sto2\Delta_f}$ :

$$V'_{sto2\Delta_f} = \frac{4 \sqrt{T_d} \cos(\Delta_f k_0/2)}{4 \cos^2(\Delta_f k_0/2) + T_d + I_{incoh}}. \quad (8.39)$$

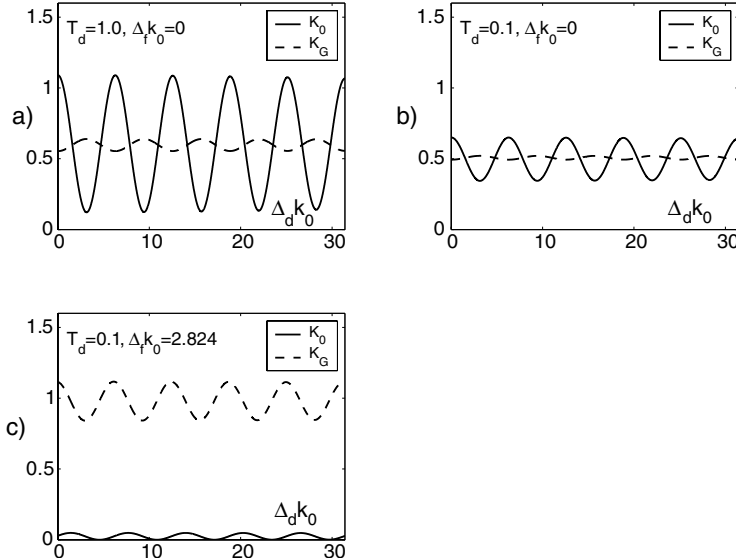


**Fig. 8.14.** Intensities  $K_0$  and  $K_G$  behind the double-loop interferometer (see Fig. 8.8) as a function of the phase shift  $\Delta_d k_0$  in beam path ( $d$ ). a) No absorption in beam ( $d$ ) ( $T_d = 1$ ) and no phase shift in beam ( $f$ ) ( $\Delta_f k_0 = 0$ ). Figure 8.14a can be compared to Fig. 8.9. Note that in Fig. 8.14a the intensities  $K_0$  and  $K_G$  are plotted as a function of  $\Delta_d k_0$ . b) Absorption in beam ( $d$ ) (transmission  $T_d = 0.1$ ) and no phase shift in beam ( $f$ ). The intensities have been attenuated accordingly. c)  $\Delta_f k_0 = 2.824$  has been chosen. This value corresponds to  $T_d = 0.1$  (see Figs. 8.12 and 8.13).  $K_0$  shows a visibility of 1 because of  $I_{min} = 0$

This expression is always less than one for  $I_{incoh} > 0$ . In order to measure weak signals (see Fig. 8.14c), the background intensity has to be as small as possible. This could be a serious constraint for considering real experimental conditions using neutrons. It should be mentioned that the background intensity has no influence on (8.25) concerning the 50/50 beam splitter system. Note also that an additional empty phase, which is a signature of an interferometer, does not affect the aforementioned considerations about the intensity and visibility.

Finally, as shown in Chap. 3, Sect. 3.4 (Part II), we would like to point out that similar results have been attained in double Mach–Zehnder interferometry where photonic beams in fiber glass are used. Because a visibility near 1 is of great advantage for measuring largely attenuated beams, our approach outlines a general method for investigating weak signals in double-loop interferometric devices.

**Two Comments on the Two-Loop System:**

1. By a simultaneous measurement of the correlation function (see Sect. 8.2) and of the modulated momentum distribution behind the interferometer, the Wigner function of various quantum states can be reconstructed. A first attempt of neutron quantum state reconstruction has been realized elsewhere [56].
2. It should be mentioned that by using a two-loop neutron interferometer, so-called geometrical phases can be investigated. Since Pancharatnam's [57] discovery in the fifties, a large amount of research work has been put into the exploration of geometrical phases. In particular, Berry [58] showed that a geometrical phase arises for the adiabatic evolution of a quantum mechanical state. In addition, neutron interferometry has been established as a particularly suitable tool for studying basic principles of quantum mechanics [24, 59, 60], providing explicit demonstrations [61] and facilitating further studies [62, 63] of geometric phenomena in double-loop systems where phase shifters and absorbers are applied.

## Part IV

### Spin Interferometry

## 9 Spin-Echo System

The neutron spin-echo technique has become a standard tool for condensed matter research [25, 64]. In most cases the semi-classical description by Larmor precession using the well-known Bloch equation is sufficient [65]. In this case, the rotation angle depends on the time  $t = l/v$  that the neutron spends in a perpendicular precession field of length  $l$  and, therefore, on the velocity  $v$  of the neutron.

In this chapter we will show how beam polarization and its rotation within a region of a constant magnetic field results from the interference of spin-up and spin-down states. It is known that Larmor precession exists due to the coherent superposition of a spin-up and a spin-down state with slightly different momenta (see (9.10) below),

$$\Delta k = \frac{|\mu|BM}{\hbar^2 k}, \quad (9.1)$$

caused by the Zeeman energy splitting (see (9.11))

$$\Delta E = \hbar\omega_L = 2|\mu|B, \quad (9.2)$$

where  $\mu = -1,913\mu_N$  denotes the magnetic moment of the neutron,  $\mu_N = 5,051.10^{-27} J/T$  the nuclear magneton and  $B$  the strength of the precession field.  $M$  denotes the mass of the neutron and  $\omega_L$  the Larmor frequency. This Zeeman shift is orders of magnitudes smaller than the momentum width of the beam and can, therefore, be neglected in most cases. A description based on the Bloch equation can be used, which relates the precession angle

$$\varphi = \omega_L t = \frac{2|\mu|Bl}{\hbar v} \quad (9.3)$$

to the velocity  $v$  of the neutron and the distance  $l$  the neutron travelling inside the precession field.

More generally, the Larmor precession has to be seen as an interference phenomenon in the longitudinal direction of the spin-up and the spin-down components of the initial wave packet [66–68]. This leads to a spatial separation of the wave packets and to non-classical states in neutron precession experiments [69]. A quantum optical description will show how wave packets, separated in ordinary space, become coupled in momentum space. The close

connection to split beam interference experiments is striking and should be mentioned [24]. The quantum optical description is even more appropriate for the description of resonance spin-echo systems [26]. Neutron-photon interaction within the resonance spin-rotator will be treated in the last chapter of this book.

## 9.1 Basic Description and Formulation

The procedure of a spin-echo interferometer is sketched in Fig. 9.1.

a)  $\pi/2$ -Flip : The neutron beam, initially polarized parallel to the magnetic guide field direction (say  $z$ ), which stretches over the whole interferometer, impinges on a flat flipper coil placed perpendicular to the beam. Inside this coil (of magnetic field strength  $B_f$ ), the spin of each neutron will be turned to  $90^\circ$  with respect to the guide field. This  $\pi/2$ -flip thus initiates Larmor precessions, which act as clocks keeping track of the time elapsed since the neutron hit the  $\pi/2$ -flipper.

b) Larmor Precessions : Inside a first magnetic field of strength  $B$ , the Larmor precession angle  $\varphi$  of (9.3) is proportional to the time the neutron spends traversing the field, i.e., it is a record of the individual neutron velocity  $v$ . The quantity  $l$  is the length of the first magnetic field  $B$  between the  $\pi/2$ -flipper and the  $\pi$ -flipper (= the field reversal in Fig. 9.1).

c)  $\pi$ -Flip (Field Reversal) : One of the two components of the neutron spin in the plane of the precession (say the  $(x-y)$  plane) is inverted, the other one is left unchanged, by a  $180^\circ$  turn around a properly chosen axis. This has the effect that the spin angle  $\varphi$  is transformed into  $-\varphi$  with respect to this axis.

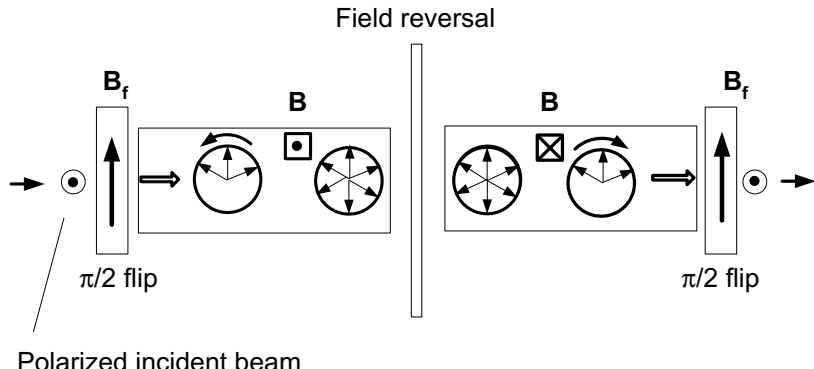


**Fig. 9.1.** Sketch of the spin-echo interferometer (spectrometer) [25], see text

d) *Larmor Precession* : Larmor precession in a second field region ( $B'$  of length  $l'$ ) will add another angle  $\varphi'$  to the apparent precession angle  $-\varphi$  up to the second  $\pi/2$ -flipper. At a possible sample between the field reversal and the second magnetic field  $B'$  (the sample is not shown here) the velocity of the neutron could have changed from  $v$  to  $v'$ . Therefore, we can write:

$$-\varphi + \varphi' = -\frac{2|\mu|}{\hbar} \left( \frac{Bl}{v} - \frac{B'l'}{v'} \right). \quad (9.4)$$

If  $B' = B$ ,  $l' = l$  and  $v' = v$  (no sample) (this case is drawn in Fig. 9.1), the difference of angles  $-\varphi + \varphi' = 0$ .

e)  $\pi/2$ -Flip : The  $90^\circ$  flip turns one (say  $x$ ) component of the precessing polarization parallel to the guide field direction (say  $z$ ). Hence, the initial state has been recovered (spin-echo).

The basic idea of spin-echo is that in a static magnetic field, the Larmor precession of the neutron polarization results from the beating of two waves of different  $k$  vectors (Zeeman splitting) and equal frequencies (constant total energy). The beat pattern is static, i.e., the spin direction at a fixed point in the magnetic field does not change with time. At high precession numbers, the polarization becomes equally distributed in the plane perpendicular to the magnetic field due to the velocity distribution of the neutrons. This effect can be retrieved by reversing the spin rotation in a second magnetic field (Fig. 9.1). We describe the process of spin rotation in the magnetic field quantum-mechanically using wave packets. The results will be discussed below under the aspect of the Wigner function taking into account intrinsic fluctuations of the magnetic field. This point of view is relevant, because coherence effects are strongly influenced thereby.

### 9.1.1 Wave Functions and Polarization

First we consider a monochromatic beam of particles. The beam is polarized in the positive  $x$ -direction and can be described by the following wave vector [1]:

$$|\psi_i\rangle = f|+\rangle_x = f\frac{1}{\sqrt{2}}(|+\rangle_z + |-\rangle_z), \quad f = e^{ikx - i\omega t}, \quad (9.5)$$

where we have used the  $z$ -direction as the quantization axis. The spin states are

$$|+\rangle_z = \begin{pmatrix} 1 \\ 0 \end{pmatrix}, \quad |-\rangle_z = \begin{pmatrix} 0 \\ 1 \end{pmatrix}. \quad (9.6)$$

We recall that

$$\begin{aligned} |\pm\rangle_x &= \frac{1}{\sqrt{2}}(|+\rangle_z \pm |-\rangle_z), \quad |\pm\rangle_y = \frac{1}{\sqrt{2}}(|+\rangle_z \pm i|-\rangle_z), \\ \vec{\sigma} &= (\hat{\sigma}_x, \hat{\sigma}_y, \hat{\sigma}_z), \quad \hat{\sigma}_x|\pm\rangle_x = \pm|\pm\rangle_x, \quad \hat{\sigma}_y|\pm\rangle_y = \pm|\pm\rangle_y, \quad \hat{\sigma}_z|\pm\rangle_z = \pm|\pm\rangle_z, \\ \hat{\sigma}_x &= \begin{pmatrix} 0 & 1 \\ 1 & 0 \end{pmatrix}, \quad \hat{\sigma}_y = \begin{pmatrix} 0 & -i \\ i & 0 \end{pmatrix}, \quad \hat{\sigma}_z = \begin{pmatrix} 1 & 0 \\ 0 & -1 \end{pmatrix}. \end{aligned} \quad (9.7)$$

$\hat{\sigma}_x, \hat{\sigma}_y, \hat{\sigma}_z$  are the Pauli matrices. The amplitude factor  $f$  describes a plane wave.  $E = \hbar\omega$  is the constant total energy.

The beam now enters a first static magnetic field of strength  $B$  that points to the  $z$ -direction. Inside this field, the single spin components of  $|\psi_i\rangle$  are now influenced by Zeeman splitting, and the wave vector is a superposition of spin components with different amplitude factors

$$|\psi\rangle = \frac{1}{\sqrt{2}}(f_+|+\rangle_z + f_-|-\rangle_z), \quad f_{\pm} = e^{\imath k_{\pm}x_1 - \imath\omega t}. \quad (9.8)$$

$x_1$  denotes a certain position of the particle in the first magnetic field  $B$ . The wave numbers  $k_{\pm}$  are derived from the equation

$$E = \hbar\omega = \frac{\hbar^2 k^2}{2M} = \frac{\hbar^2 k_{\pm}^2}{2M} \pm |\mu|B = E_{\pm} \pm |\mu|B. \quad (9.9)$$

Because (see (9.1))

$$\begin{aligned} \frac{\hbar^2}{2M}(k + k_{\pm})(k - k_{\pm}) &= \pm|\mu|B \rightarrow k_{\pm} = k \mp \Delta k, \\ \Delta k &\approx \frac{M|\mu|B}{\hbar^2 k} = \frac{\omega_L}{2v}, \quad \frac{\Delta k}{k} \approx \frac{|\mu|B}{2E} \ll 1, \end{aligned} \quad (9.10)$$

where  $v = \hbar k/M$  is the velocity of the neutron. The kinetic energies  $E_{\pm} = E \mp |\mu|B$  of the spin components differ from  $E$  by a very small amount:

$$\Delta E = E_- - E_+ = 2|\mu|B. \quad (9.11)$$

The components of the polarization vector  $\vec{P} = (P_x, P_y, P_z)$  can be determined by using the Pauli matrices and  $|\psi\rangle$ :

$$\begin{aligned} P_x &= \langle\psi|\hat{\sigma}_x|\psi\rangle = \frac{1}{2}(f_+f_-^* + f_+^*f_-) = \cos[2(\Delta k)x_1], \\ P_y &= \langle\psi|\hat{\sigma}_y|\psi\rangle = \imath\frac{1}{2}(f_+f_-^* - f_+^*f_-) = \sin[2(\Delta k)x_1], \\ P_z &= \langle\psi|\hat{\sigma}_z|\psi\rangle = 0. \end{aligned} \quad (9.12)$$

The polarization vector  $\vec{P}$  rotates in the magnetic field as a function of the position coordinate  $x_1$  and lies in the  $x$ - $y$  plane. If  $x_1 \equiv l$ , we get (9.3)

$$2(\Delta k)x_1 \equiv \omega_L \frac{l}{v} = \varphi. \quad (9.13)$$

### 9.1.2 Mean Intensity of the Wave Packet

In order to measure the intensities  $J_{\pm i}(k)$  of  $i$ -polarized particles ( $i = x, y, z$ ), the corresponding spin operator  $\hat{A}_{\pm i}$  has to be applied:

$$\hat{A}_{\pm i} = |\pm\rangle_i \langle \pm| = \frac{1}{2}(\hat{1} \pm \hat{\sigma}_i), \quad (9.14)$$

where the Pauli matrices (9.7) have been inserted. According to the concept of the expectation value (1.17), the mean value  $J_{\pm x}(k)$  of particles polarized, e.g., in the  $(+x)$ -direction is given by ( $\hat{\varrho} = |\psi\rangle\langle\psi|$ )

$$\begin{aligned} J_{\pm x}(k) &= \langle \hat{A}_{\pm x} \rangle = \text{Tr}(\hat{\varrho}\hat{A}_{\pm x}) = \langle \psi \left| \frac{1}{2}(\hat{1} \pm \hat{\sigma}_x) \right| \psi \rangle \\ &= \frac{1}{2}(1 \pm P_x) = \left| \frac{1}{2}(f_+ \pm f_-) \right|^2 = \frac{1}{2}\{1 \pm \cos[2(\Delta k)x_1]\}. \end{aligned} \quad (9.15)$$

In a similar manner we get

$$J_{\pm i}(k) = \frac{1}{2}(1 \pm P_i), \quad i = x, y, z. \quad (9.16)$$

The  $y$ -components can be constructed as follows:

$$J_{\pm y}(k) = \frac{1}{2}(1 \pm P_y) = \left| \frac{1}{2}(f_+ \mp if_-) \right|^2 = \frac{1}{2}\{1 \pm \sin[2(\Delta k)x_1]\}.$$

The  $z$ -components are constant, and we obtain

$$J_{\pm z}(k) = \frac{1}{2}.$$

$J_{\pm i}(k)$  depends on  $k$  via  $\Delta k$  (9.1). Instead of a monochromatic beam, we introduce the concept of a wave packet in order to take into account a slightly polychromatic beam, bearing in mind a Gaussian distribution  $\alpha^2(k)$  of wave numbers  $k$  (7.8). Multiplying this distribution with  $J_{\pm i}(k)$ , we are led to the related spectral intensity distribution

$$|\alpha_{\pm i}(k)|^2 = \alpha^2(k)J_{\pm i}(k). \quad (9.17)$$

We define the parameter  $\tau$  as

$$\tau = \frac{\Delta k_0}{k_0} \approx \frac{\Delta k}{k} \ll 1, \quad \Delta k_0 = \frac{|\mu|BM}{\hbar^2 k_0}, \quad (9.18)$$

assuming  $\sigma = \delta k/k_0 \ll 1$ . We consider the  $(+x)$ -direction of spins and hence, we obtain

$$|\alpha_{+x}(k)|^2 = \alpha^2(k) \frac{1}{2} \left\{ 1 + \cos \left[ 2\tau \frac{k}{k_0} (x_1 k_0) \right] \right\}. \quad (9.19)$$

The integrated intensity reads

$$I_{+x} = \int |\alpha_{+x}(k)|^2 dk = \frac{1}{2} \{ 1 + \cos[2\tau(x_1 k_0)] e^{-2(\sigma\tau)^2(x_1 k_0)^2} \}. \quad (9.20)$$

Let  $m_1$  be the number of spin rotations in the first magnetic field. Then  $m_1$  can be obtained via the relation  $2\tau(x_1 k_0) = 2\pi m_1$  or  $m_1 = \tau(x_1 k_0)/\pi$  and the above formulas can be expressed by this parameter.

### 9.1.3 Wigner Function and Spectra

In order to obtain the Wigner function  $W_{+x}$  of, say,  $(+x)$ -polarized neutrons we consider (4.3). What we need is an expression for  $\alpha_{+x}(k)$ . This is best achieved by inferring from (9.17) and (9.15):

$$\alpha_{+x}(k) = \frac{1}{2}\alpha(k)[f_+ + f_-]^*. \quad (9.21)$$

These considerations lead to the following Wigner function [70]:

$$W_{+x}(x, k, x_1, \sigma, \tau) = \frac{1}{4\pi} e^{-\frac{(k/k_0 - 1)^2}{2\sigma^2}} \left\{ e^{-2\sigma^2[xk_0 - (1-\tau)x_1k_0]^2} + e^{-2\sigma^2[xk_0 - (1+\tau)x_1k_0]^2} + 2 \cos\left(2\tau \frac{k}{k_0} x_1 k_0\right) e^{-2\sigma^2(xk_0 - x_1 k_0)^2} \right\}. \quad (9.22)$$

Here  $x_1$  means, as mentioned, a definite position of the particle in the first magnetic field  $B$  (Fig. 9.1). Figures 9.2 to 9.4 display three Wigner functions for a parameter  $\tau = 1.10^{-4}$  and for three different “positions”  $x_1 k_0$  of the

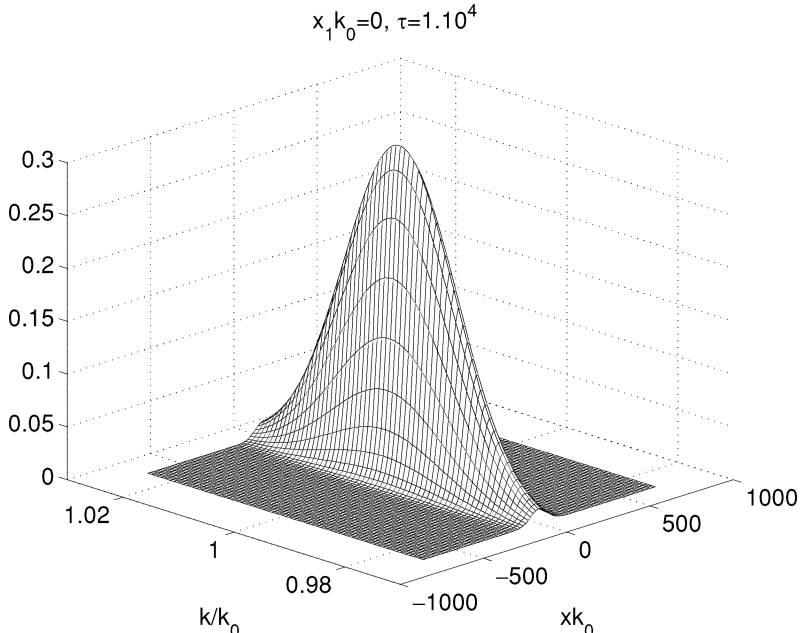


**Fig. 9.2.** Wigner function (9.22) at the beginning of the first magnetic field  $B$  (Fig. 9.1)

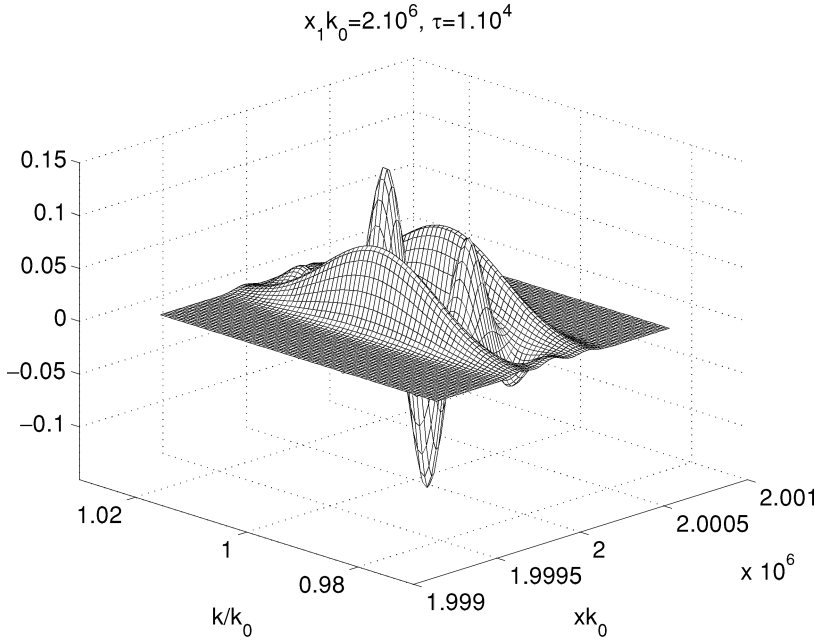


**Fig. 9.3.** Wigner function (9.22) in the first magnetic field  $B$  (Fig. 9.1). Number of rotations  $m_1 = \tau(x_1 k_0)/\pi = 200/\pi = 63,662$ . “Distance” of Schrödinger-cat-like states  $\Delta = 2\tau(x_1 k_0) = 400$

neutron in the first magnetic field  $B$ . If  $x_1 k_0$  increases, the Schrödinger-cat-like states begin to separate from each other. The difference  $\Delta$  between these states is given by

$$\Delta = 2\tau(x_1 k_0). \quad (9.23)$$

The position spectrum is obtained by means of

$$\begin{aligned} |\psi_{+x}(x)|^2 &= \int W_{+x}(x, k, x_1, \sigma, \tau) dk = \frac{1}{4} \sqrt{\frac{2\sigma^2 k_0^2}{\pi}} \{ e^{-2\sigma^2[xk_0 - (1-\tau)x_1 k_0]^2} \\ &\quad + e^{-2\sigma^2[xk_0 - (1+\tau)x_1 k_0]^2} \\ &\quad + 2 \cos(2\tau x_1 k_0) e^{-2\sigma^2[xk_0 - x_1 k_0]^2 - 2(\sigma\tau x_1 k_0)^2} \}, \end{aligned} \quad (9.24)$$

and the momentum spectrum  $|\alpha_{+x}(k)|^2$  is given by (9.19):

$$|\alpha_{+x}(k)|^2 = \int W_{+x}(x, k, x_1, \sigma, \tau) dx. \quad (9.25)$$

This function is plotted in Fig. 9.5 using the same parameters as for the Wigner function above.

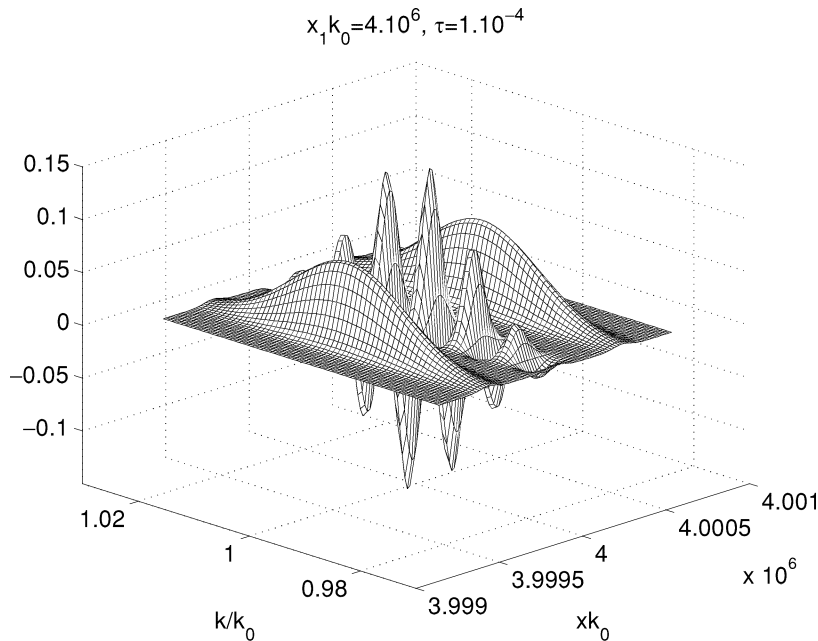


**Fig. 9.4.** Wigner function (9.22) in the first magnetic field  $B$  (Fig. 9.1). The number of rotations  $m_1 = \tau(x_1 k_0)/\pi = 400/\pi = 127,324$ . The “Distance” of Schrödinger-cat-like states  $\Delta = 2\tau(x_1 k_0) = 800$

So far we have considered  $(+x)$ -polarized neutrons in (9.21). On the other hand,  $(-x)$ - and  $(\pm y)$ -polarized neutrons can be accounted for as well, and we get for the corresponding distribution functions

$$\alpha_{-x}(k) = \frac{1}{2}\alpha(k)[f_+ - f_-]^*, \quad \alpha_{\pm y}(k) = \frac{1}{2}\alpha(k)[f_+ \mp i f_-]^*.$$

The results are similar and easily obtained and, therefore, we omit a detailed presentation of the calculation procedure.

#### 9.1.4 Squeezing of Spectra

Similarly as in Sect. 7.4, we can evaluate, e.g., the momentum uncertainty

$$\frac{\langle(\Delta K)^2\rangle}{(\delta k)^2} = 1 - X^2 \frac{e^{-X^2} + 2I_{+x} - 1}{4I_{+x}^2}, \quad (9.26)$$

where  $I_{+x} = [1 + \exp(-X^2/2) \cos(X/\sigma)]/2$  has been taken from (9.20) and  $X = 2\sigma\tau x_1 k_0$ . Equations (9.26) and (7.12) are comparable except for the different normalization of the intensities  $I_{+x}$  and  $I_s(X)$  (7.10), respectively. Therefore, Fig. 7.13 (bottom) can be used for visualization as well. This

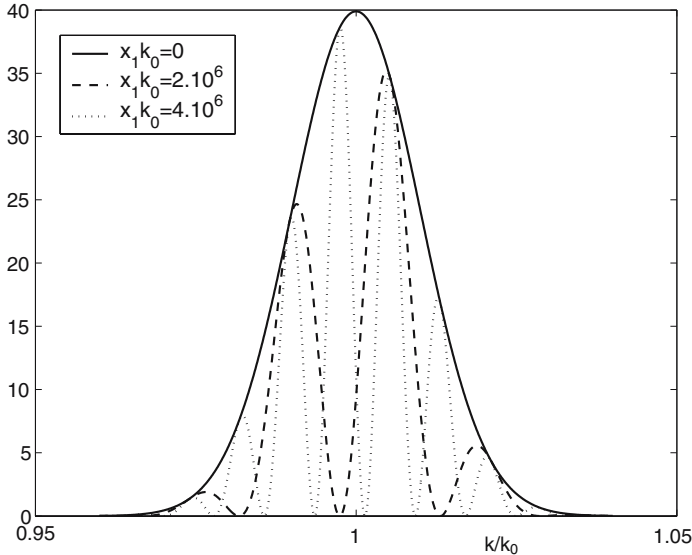


**Fig. 9.5.**  $|\alpha_{+x}(k)|^2$  from (9.19) for  $\tau = 10^{-4}$  and  $\sigma = 10^{-2}$ . The quantities  $x_1 k_0$  correspond to those of Figs. 9.2 to 9.4

proves that for  $X = \pi/2$ , or rather for a position coordinate  $x_1 = \pi/(4\sigma\tau k_0)$ , a squeezed momentum spectrum exists in the first magnetic field.

## 9.2 Dephasing and Spin-Echo After Two Magnetic Fields

We already pointed out in Sect. 7.6 that any physical system has intrinsic fluctuations and inhomogeneous properties around certain values. There we discussed density fluctuations and the surface roughness of a phase shifter in neutron interferometry. Here we take into account fluctuations  $\kappa = \delta B/B_0$  of the magnetic field, which are also assumed to be Gaussian:

$$G(B - B_0) = \frac{1}{\sqrt{2\pi}(\delta B)} \exp \left\{ -\frac{(B - B_0)^2}{2(\delta B)^2} \right\}, \quad (9.27)$$

where  $B_0$  is the mean value of  $B$ . Below, we shall average the Wigner function, as well as the intensity and the spectra, using this Gaussian function with respect to the fluctuations of the magnetic fields.

According to the spin-echo method, the beam enters a second magnetic field of the same strength but pointing to the opposite direction in comparison

to the first field (see Fig. 9.1). If, in addition, the second magnetic field also has the same length, all rotations of the individual particles can be turned back completely and the beam is again polarized in the  $x$ -direction upon exit from the second field. In order to calculate the related functions, we define the number of spin rotations  $m_1 = \tau x_1 k_0 / \pi$  and  $m_2 = \tau x_2 k_0 / \pi$  in the two magnetic fields, respectively. We notice that  $m_2$  has to be set = 0 in the first magnetic field ( $0 \leq m_1 \leq m_{1,max}$ ) and  $m_1 = m_{1,max}$  in the second magnetic field ( $0 \leq m_2 \leq m_{2,max}$ ).

The following abbreviations are used in the formulas below, where fluctuations  $\kappa$  are included:

$$\gamma' = |m_1 - m_2|, \quad \beta = 2\sigma\kappa\pi(m_1 + m_2), \quad \beta_1 = \sqrt{1 + \beta^2}, \quad \kappa = \delta B/B_0. \quad (9.28)$$

The averaged intensity  $\bar{I}_{+x}$ , the averaged momentum distribution  $|\bar{\alpha}_{+x}(k)|^2$  and the averaged Wigner function  $\bar{W}_{+x}(x, k, x_1, \sigma, \tau, \kappa)$  are finally obtained:

$$\bar{I}_{+x} = \frac{1}{2} \left\{ 1 + \frac{1}{\beta_1} \cos \left( \frac{2\pi\gamma'}{\beta_1^2} \right) \exp \left[ -\frac{1}{\beta_1^2} \left( 2\pi^2\sigma^2\gamma'^2 + \frac{\beta^2}{2\sigma^2} \right) \right] \right\}, \quad (9.29)$$

$$|\bar{\alpha}_{+x}(k)|^2 = \frac{1}{\sqrt{2\pi\sigma^2 k_0^2}} \frac{1}{2} \exp \left[ -\frac{1}{2\sigma^2} \left( \frac{k}{k_0} - 1 \right)^2 \right] \times \left\{ 1 + \cos \left( 2\pi \frac{k}{k_0} \gamma' \right) \exp \left[ -\beta^2 \frac{(k/k_0)^2}{2\sigma^2} \right] \right\}, \quad (9.30)$$

$$\bar{W}_{+x}(x, k, \gamma', \beta, \sigma, \tau) = \frac{1}{4\pi} \exp \left[ -\frac{1}{2\sigma^2} \left( \frac{k}{k_0} - 1 \right)^2 \right] \times \left\{ A_+ + A_- + 2A_0 \cos \left( 2\pi \frac{k}{k_0} \gamma' \right) \right\}, \quad (9.31)$$

$$A_{\pm} = \frac{1}{\beta_1} \exp \left\{ -\frac{2\sigma^2}{\beta_1^2} \left( \frac{\pi}{\tau} \right)^2 [m - \gamma'(1 \pm \tau)]^2 \right\}, \\ A_0 = \exp \left\{ -2\sigma^2 \left( \frac{\pi}{\tau} \right)^2 [m - \gamma']^2 - \beta^2 \frac{(k/k_0)^2}{2\sigma^2} \right\}, \quad (9.32)$$

where  $m = \tau x k_0 / \pi$  is connected to the position coordinate  $x$ . Equation (9.29) describes intensity oscillations of  $x$ -polarized neutrons. They are damped by an exponential factor that is proportional to the square of the number of rotations. For zero fluctuations of  $B$  ( $\beta = 0, \beta_1 = 1$ ), the initial intensity (9.20) can be restored if  $m_1 = m_2$  (or  $\gamma' = 0$ ). The momentum distribution (9.30) is proportional to the original Gaussian  $k$ -spectrum, which is modulated by a damped cosine term whose frequency depends on  $\gamma' = |m_1 - m_2|$ . The Wigner

function (9.31) is depicted in Figs. 9.6 and 9.7. If  $m_1 = m_2 = 0$ , (or  $\gamma' = 0$ ), a double Gaussian peak in space (variable  $m = \tau x k_0 / \pi$ ) and momentum (variable  $k/k_0$ ) appears. If, for example,  $m_1 = 127.324$  and  $m_2 = 0$ , i.e., at the end of the first magnetic field (we choose  $m_{1,max} = m_{2,max} = 127.324$ ), a typical

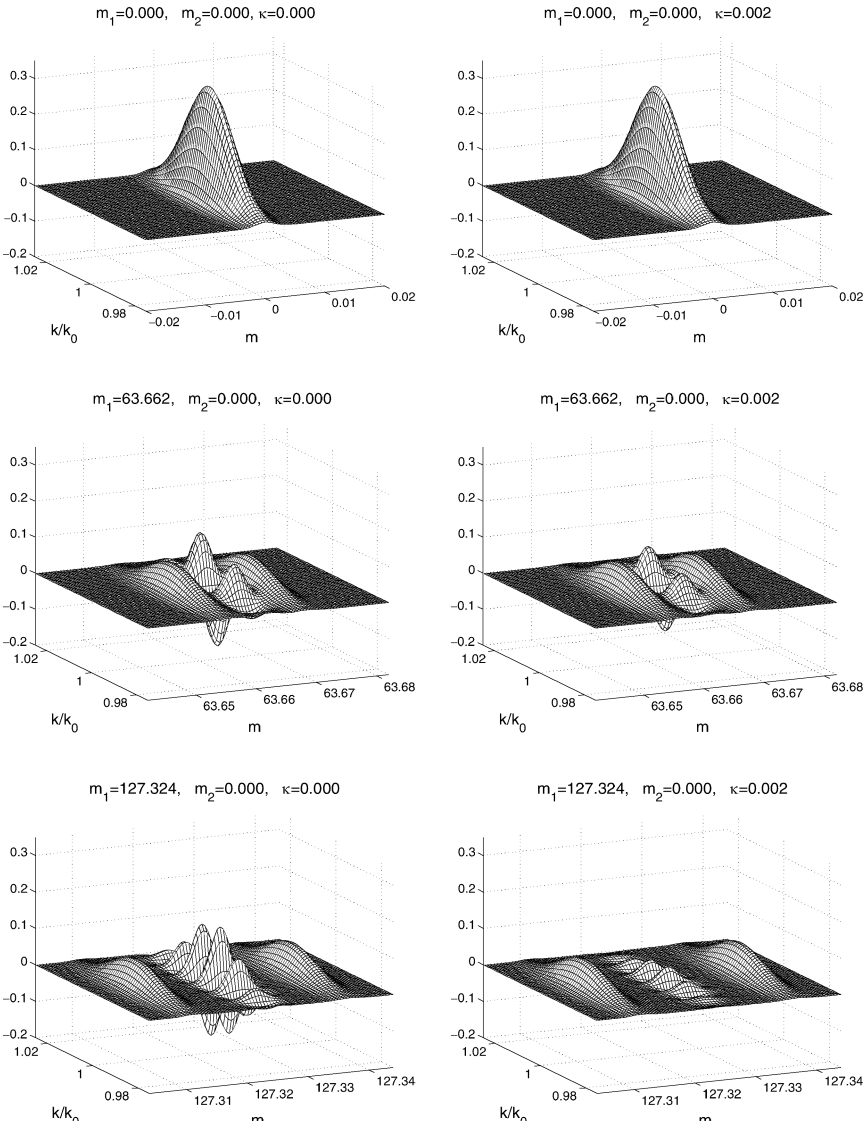


**Fig. 9.6.** Behavior of the Wigner function (9.31) without ( $\kappa = 0$ , left row) and with field fluctuations ( $\kappa = 0.002$ , right row), see text.  $\tau = 10^{-4}$ ,  $\sigma = 10^{-2}$

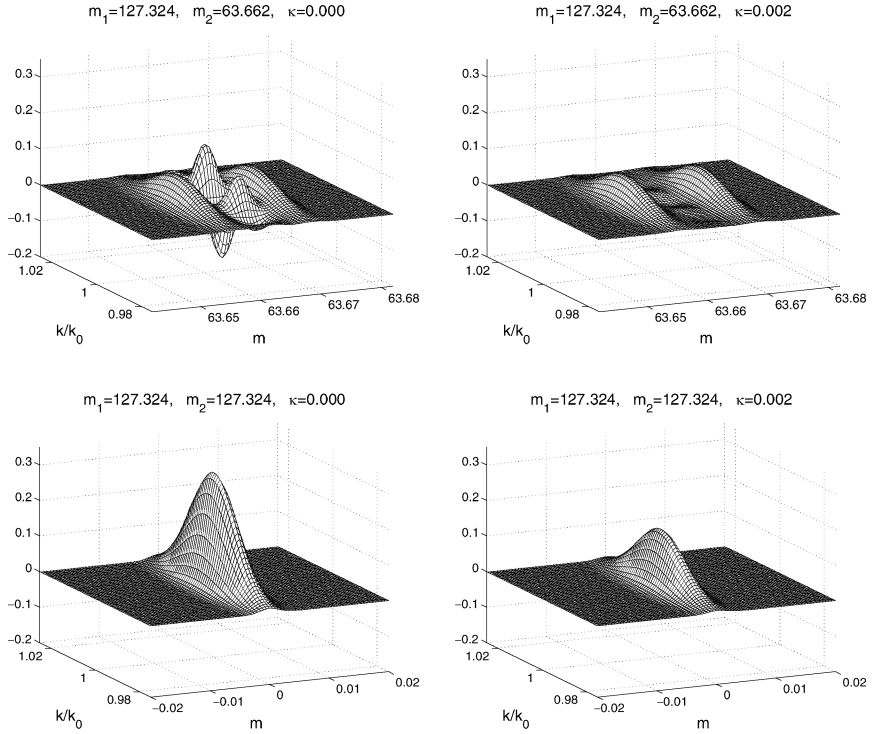


**Fig. 9.7.** Continuation of Fig. 9.6

Schrödinger-cat-like state is achieved (identical to Fig. 9.4). The oscillating term between the cat states is clearly visible. However, if  $\kappa = 0.002$ , these oscillations are considerably attenuated, as can be seen on the right-hand side of the picture. The initial state can again be obtained in a second magnetic field (Fig. 9.7). At the end of this second magnetic field, which has the same length and strength (Fig. 9.1), we have  $m_1 = m_2 = 127.324$ . If  $\kappa = 0.002$ , the cosine-term has been damped out completely and the initial double Gaussian peak has almost been halved. This demonstrates that the coherent separation of a Schrödinger-cat-like state becomes progressively more difficult with increasing spatial separation, which will result in an upper limit for separation when zero-point fluctuations are considered. The vanishing of the oscillating structure of the Wigner function indicates the transition from a superposed coherent state to a mixed state. This is equivalent to the disappearance of the off-diagonal terms of the density matrix (1.15).

The decoherence approach has many appealing aspects. It starts with the observation that quantum mechanical predictions are different for closed and

open systems. There are always influences from the environment that destroy the phase relations between the superposed states of a real quantum state. Therefore, this dephasing washes out the interference terms and results in a statistical mixture that describes the probabilities for the specific outcomes of an experiment [43–45]. The decoherence approach is seen as a rather pragmatic one and it cannot exactly discern between micro and macro-systems. Various calculations show that the influence of fluctuation is minimized for Gaussian (coherent) states, but increases strongly for non-classical states, like Schrödinger-cat-like states, as shown above [6,34]. The decoherence approach gives a realistic interpretation of the measurement process and provides a theory of dissipation (see also Sect. 7.6). The paper by W.H. Zurek [71] excellently reviews progress in the field, focusing on decoherence and the emergence of classicality and offering a preview of the future of this fundamental area.

### 9.3 Influence of Space-Dependent Inhomogeneities of Magnetic Fields

The process of averaging as a consequence of unknown fluctuations by using single Gaussian functions like (9.29) for a magnetic field, or (7.23) and (7.24) for thickness or density of a phase shifter, respectively, is definitely a relatively coarse, albeit simple, mathematical trick for describing mixed states in interferometry. In doing so, one is pretending that, e.g., every point in the magnetic field is totally correlated with every other point with respect to fluctuations, because no distinction has been made about the spatial distribution of the fluctuations. One can expect that this type of averaging yields the strongest possible damping of the interference term discussed above.

One step towards an improvement of the situation would be to take into account the two-dimensional Gaussian distribution functions  $G_2(B, B')$  of magnetic field fluctuations. Two-dimensional Gaussian functions have already been defined in Chap. 1, (1.4). Therefore, we write

$$G_2(B, B') = \frac{1}{2\pi(\delta B)^2\sqrt{1-\rho^2}} \exp \left\{ -\frac{1}{2(\delta B)^2(1-\rho^2)} [(B - B_0)^2 - 2\rho(B - B_0)(B' - B_0) + (B' - B_0)^2] \right\}, \quad (9.33)$$

correlating a magnetic field strength  $B$  (say at position  $x$ ) with another (slightly different) value  $B'$  (say at position  $x'$ ). The mean value  $B_0$  and the mean deviation  $(\delta B)$  of  $B$  and  $B'$  should be the same.  $-1 \leq \rho \leq 1$  is the correlation coefficient.  $\rho = 1$  means “correlated”,  $\rho = 0$  means “not correlated”,  $\rho = -1$  means “anti-correlated”.

Some properties of  $G_2(B, B')$  are:

- a)  $\iint G_2(B, B') dB dB' = 1$  ... normalization
- b)  $\int G_2(B, B') dB' = G(B - B_0)$  ... marginal distribution
- c)  $\int G_2(B, B') dB = G(B' - B_0)$  ... marginal distribution
- d)  $G_2(B, B', \rho = 0) = G(B - B_0)G(B' - B_0)$  ... independent variables
- e)  $\sigma_{12} = \iint (B - B_0)(B' - B_0)G_2(B, B') dB dB' = (\delta B)^2 \rho$  ... covariance
- f)  $G_2(B, B') = G(B - B_0) \frac{1}{\epsilon \sqrt{\pi}} \exp \left\{ -\frac{1}{\epsilon^2} [\rho(B - B_0) - (B' - B_0)]^2 \right\},$   
 $\epsilon = \sqrt{2}(\delta B)\sqrt{1 - \rho^2}, \quad \lim_{\epsilon \rightarrow 0} \frac{1}{\epsilon \sqrt{\pi}} \exp \left\{ -\frac{x^2}{\epsilon^2} \right\} = \delta(x), \quad \lim_{\rho \rightarrow 1} G_2(B, B')$   
 $= G(B - B_0)\delta(B - B'), \quad \lim_{\rho \rightarrow -1} G_2(B, B') = G(B - B_0)\delta[-(B + B') + 2B_0].$

The next step is to average the Wigner function  $W_{+x}$  (9.22) using  $G_2(B, B')$ . The outcome is denoted by  $\widetilde{W}_{+x}$ :

$$\widetilde{W}_{+x} = \iint G_2(B, B') W_{+x} dB dB'. \quad (9.34)$$

If we consider property f) above, it is obvious that  $B$  (which is contained in the parameter  $\tau$ , (9.18)) in (9.22) should be with  $(B + B')/2$ . In doing so, both  $B$  and  $B'$  are kept in mind for the process of averaging. After inserting  $W_{+x}$ , the integral can be carried out and we obtain after a somewhat longer, but elementary, calculation the following result:

$$\widetilde{W}_{+x} = \overline{W}_{+x} \left[ \beta^2 \Rightarrow \frac{\beta^2}{2}(1 + \rho) \right]. \quad (9.35)$$

Here  $\overline{W}_{+x}$  is the Wigner function (9.31), which is a result of averaging  $W_{+x}$  over a single Gaussian function  $G(B - B_0)$ . Thus, we can use  $\overline{W}_{+x}$  simply by replacing  $\beta^2$  with  $\beta^2(1 + \rho)/2$  in order to obtain  $\widetilde{W}_{+x}$ .

Some special cases can be distinguished:

1.  $\widetilde{W}_{+x}(\rho = 1) = \overline{W}_{+x}$  ... maximum damping (correlated).
2.  $\widetilde{W}_{+x}(\rho = -1) = W_{+x}$  ... no damping (anti-correlated), equivalent to  $\beta = 0$ .
3.  $\widetilde{W}_{+x}(\rho = 0) = \overline{W}_{+x}[\beta^2 \Rightarrow \beta^2/2] = \iint G(B - B_0)G(B' - B_0)W_{+x} dB dB'$   
... mean damping (not correlated).

This case is probably the most reasonable one, because uncorrelated field fluctuations are supposed to be realistic.

It should be mentioned that time-dependent fluctuations of the magnetic field can also be considered as giving rise to a particular characteristic damping behavior [72].

## 9.4 Experimental Verification

In an experiment described in [69], the generation of non-classical quantum states was investigated with a single homogeneous precession field with sufficiently low strength to resolve the wiggles by medium resolution time-of-flight spectroscopy. A polarized polychromatic neutron beam ( $\delta\lambda/\lambda_0 = 0.27$ ) with a mean wavelength  $\lambda_0 = 0.37$  nm non-adiabatically enters and leaves a magnetic field of mean strength  $B = 0.28$  Tm, which is orientated perpendicular to the polarization direction of the particles. The length of the field is  $L = 0.57$  m. This field causes a Zeeman splitting of the wave packet into two components with different momenta, which finally also leads to a separation in real space. According to (9.19), the momentum distribution of the neutrons that enter and leave the precession field with their polarization aligned along the  $(+x)$ -axis is given by ( $x_1 \equiv L$ )

$$|\Phi_{+x}(k)|^2 \propto |\Phi_0(k)|^2 \{1 + \cos[2L(\Delta k)]\},$$

where  $|\Phi_0(k)|^2$  is the incident momentum spectrum and  $\tau = 1.4 \times 10^{-6}$  according to (9.18) and the parameters given above. Treating the incident wavelength spectrum for reasons of simplicity as Gaussian, one obtains

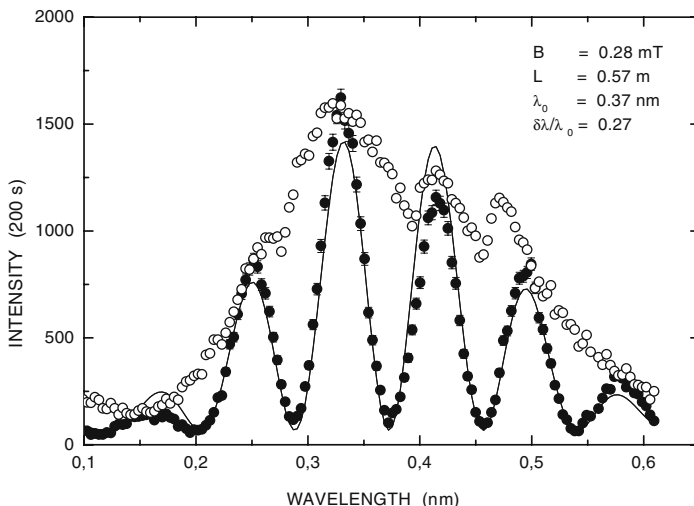


**Fig. 9.8.** Comparison of experimentally measured (full circles) and theoretically calculated ((9.36), full line) wavelength spectra [69]. The transmission spectrum  $|\Phi_0(\lambda)|^2$  (open circles) measured without any precession field is also shown

$$|\Phi_{+x}(\lambda)|^2 \propto \exp\left[-\frac{(\lambda - \lambda_0)^2}{2(\delta\lambda)^2}\right] \left\{ 1 + \cos\left[\frac{\gamma MBL}{\hbar}\lambda\right] \right\}. \quad (9.36)$$

Here  $\gamma = 2\mu/\hbar$  is the gyromagnetic ratio. It becomes apparent from Fig. 9.8 that, in spite of this simplifying assumption, there is a reasonably good agreement between the theoretically calculated and the measured wavelength spectra. In particular, the respective positions of the intensity maxima coincide. However, it is conclusive that their relative heights cannot be reproduced with similar accuracy. The spectrum measured without precession field is also indicated in Fig. 9.8. Notice that the plotted curve is not just a least-squares fit to the experimental data (except, of course, of the background intensity), but is calculated analytically according to (9.36) using the specific experimental parameters for  $\lambda_0$ ,  $(\delta\lambda)$ ,  $B$  and  $L$ .

# 10 Zero-Field Spin-Echo

## 10.1 Dynamical Spin-Flip

The crucial requirement of strong and homogeneous magnetic fields in spin-echo spectrometers can be circumvented by the so-called zero-field spin-echo method [26, 73]. In this case, the spin rotation is achieved by a neutron magnetic resonance system (Fig. 10.1). A rotating field  $B_1$  (frequency  $\omega$ ) is superposed to a static guide field  $B_0$ , such that the resulting magnetic field  $\vec{B}(t)$  can be written as

$$\vec{B}(t) = \begin{pmatrix} B_1 \cos(\omega t) \\ B_1 \sin(\omega t) \\ B_0 \end{pmatrix}. \quad (10.1)$$

The Pauli equation (see below) can be solved exactly for this potential using plane waves. For a beam initially polarized in the  $z$ -direction, the wave function behind the resonance system (dynamical  $\pi/2$ -spin-flip) can be calculated and conditions for a complete spin-reversal can be obtained.

Such a neutron magnetic resonance system (Rabi flipper) represents a time-dependent interaction, so that in addition to the spin rotation an energy exchange occurs according to the Zeeman energy (9.2)  $\Delta E_0 = \hbar\omega_L = 2|\mu|B_0$  as shown in the next section. In a zero-field spin-echo system, a  $\pi/2$  spin rotation is applied at the beginning, a  $\pi$ -rotation at the middle and an additional  $\pi/2$ -spin rotation at the end. The phases of the flipper fields are synchronized. Thus a spin-up  $|\uparrow\rangle \equiv |+\rangle_z$  and a spin-down state  $|\downarrow\rangle \equiv |-\rangle_z$  with a slightly different energy interfere with each other, which results in a Larmor rotation in the  $x/y$ -plane even in a zero magnetic field. The neutrons also accumulate a velocity-dependent phase (because  $t = l/v$ ) in the field-free region between the first  $\pi/2$  and the  $\pi$ -flipper (length  $L_1$ ) and the  $\pi$ -flipper and the second  $\pi/2$ -flipper (length  $L_2$ ). When the phases accumulated in the guide fields  $B_0$  are matching, the spin-echo condition is

$$\omega_r(t_1 - t_2) = \frac{2|\mu|B_0}{\hbar v}(L_1 - L_2) = 0 \rightarrow L_1 = L_2, \quad (10.2)$$

where  $\omega \equiv \omega_r = \omega_L$  is the resonance frequency of the rotating field  $B_1$ . Below it is shown that, using wave packets, a Schrödinger-cat-like state is obtained in the field-free region.

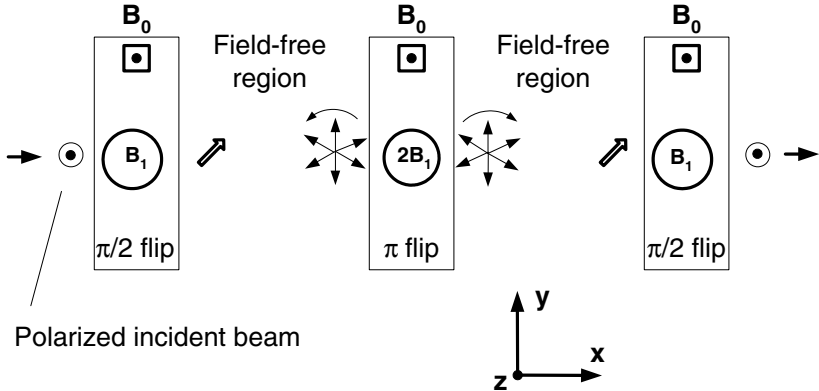


**Fig. 10.1.** Sketch of a zero-field spin-echo system: between three dynamical spin-flippers two field-free regions are seen, where spin rotation in the  $x/y$ -plane appears (see text)

In the following section, a detailed description of the interaction of neutrons with a rotating magnetic field is given and conditions for frequencies and amplitudes are derived for a dynamical spin-flip device (magnetic resonance) [1, 74].

### 10.1.1 Interaction of Neutrons with a Rotating Magnetic Field

Let us consider the Pauli matrices  $\hat{\sigma}_x$ ,  $\hat{\sigma}_y$  and  $\hat{\sigma}_z$  (9.7), which are components of the Pauli vector  $\vec{\sigma} = (\hat{\sigma}_x, \hat{\sigma}_y, \hat{\sigma}_z)$ . They have the following properties:  $\hat{\sigma}_x^2 = \hat{\sigma}_y^2 = \hat{\sigma}_z^2 = \hat{1}$ . The components  $P_i$  of the polarization vector  $\vec{P} = (P_x, P_y, P_z)$  of a free particle are defined via the Pauli matrices:

$$P_i = \langle \hat{\sigma}_i \rangle = \langle \chi | \hat{\sigma}_i | \chi \rangle / \langle \chi | \chi \rangle, \quad i = x, y, z. \quad (10.3)$$

The appropriate spin state  $|\chi\rangle$  can be written as [1]

$$|\chi\rangle \equiv |\theta, \phi\rangle = \cos\left(\frac{\theta}{2}\right) | \uparrow \rangle + e^{i\phi} \sin\left(\frac{\theta}{2}\right) | \downarrow \rangle, \quad (10.4)$$

where we have used the polar angles  $\theta$  and  $\phi$ . The polarization vector can immediately be identified:

$$\vec{P} = \begin{pmatrix} P_x \\ P_y \\ P_z \end{pmatrix} = \begin{pmatrix} \sin(\theta) \cos(\phi) \\ \sin(\theta) \sin(\phi) \\ \cos(\theta) \end{pmatrix}, \quad \vec{P}^2 = 1. \quad (10.5)$$

The initial polarization of the particle (in front of the first  $\pi/2$ -flip in Fig. 10.1) is given by  $\theta = 0$  and  $\vec{P} = (0, 0, 1)$ .

Now, the time-dependent Schrödinger equation (Pauli equation) of neutrons in a space and time-dependent magnetic field  $\vec{B}(\vec{r}, t)$  is considered (region of  $\pi/2$ -flip). Because of interaction of the spin-operators  $\hat{S}_i = (\hbar/2)\hat{\sigma}_i$  of the particles (with magnetic moment  $\mu\vec{S}$ ) with the magnetic field, this equation reads

$$\hat{H}\psi(\vec{r}, t) \equiv \left[ -\frac{\hbar^2}{2M}\Delta - \mu\vec{\sigma}\vec{B}(\vec{r}, t) \right] \psi(\vec{r}, t) = i\hbar\frac{\partial}{\partial t}\psi(\vec{r}, t). \quad (10.6)$$

We solve this equation firstly for a purely time-dependent field  $\vec{B}(t)$  (as shown in (10.1), which is switched on at time  $t = 0$  and switched off at time  $t = T$ ). The space-dependence is taken into account in a later section below. In the case of time-dependence of the magnetic field, one can expect that the process is inelastic (the total energy is no longer constant).

The particles move in the  $x$ -direction. Therefore, the Pauli equation can be written as follows:

$$i\hbar\frac{\partial}{\partial t}\psi(x, t) = \left[ -\frac{\hbar^2}{2M}\frac{\partial^2}{\partial x^2} - \mu\hat{\sigma}_x B_1 \cos(\omega t) - \mu\hat{\sigma}_y B_1 \sin(\omega t) - \mu\hat{\sigma}_z B_0 \right] \psi(x, t). \quad (10.7)$$

As always, a separation ansatz is made:

$$\psi(x, t) = \Phi(x)\chi(t) = \Phi(x) \begin{pmatrix} \chi_1(t) \\ \chi_2(t) \end{pmatrix}. \quad (10.8)$$

Because of the Pauli matrices, the wave function  $\psi(x, t)$  is a spinor. After inserting (10.8) into (10.7), we have

$$\begin{aligned} i\hbar\frac{1}{\chi(t)}\frac{\partial}{\partial t}\chi(t) + \{\mu B_1[\hat{\sigma}_x \cos(\omega t) + \hat{\sigma}_y \sin(\omega t)] + \mu B_0 \hat{\sigma}_z\} \\ = -\frac{\hbar^2}{2M}\frac{1}{\Phi(x)}\frac{\partial^2}{\partial x^2}\Phi(x) = C, \end{aligned} \quad (10.9)$$

where  $C$  is a constant. Solving the  $x$ -dependent part of the differential equation, we obtain

$$\begin{aligned} \left[ \frac{\partial^2}{\partial x^2} + \frac{2M}{\hbar^2}C \right]\Phi(x) = 0 \rightarrow \Phi(x) = A \exp\left[i\sqrt{\frac{2MC}{\hbar^2}}x\right] \\ + B \exp\left[-i\sqrt{\frac{2MC}{\hbar^2}}x\right]. \end{aligned}$$

Because of the space-independent magnetic field, no reflections appear and  $B$  can be chosen to be equal to zero. We have plane waves with  $A = 1/\sqrt{2\pi}$  and  $C \equiv (\hbar^2 k^2)/(2M) = E$ :

$$\Phi(x) = \frac{1}{\sqrt{2\pi}} \exp(\imath kx) \equiv \langle k|x \rangle. \quad (10.10)$$

The orthogonality of plane waves is given as

$$\langle x'|x \rangle = \int \Phi^*(x')\Phi(x)dk = \frac{1}{2\pi} \int \exp[\imath k(x - x')]dk = \delta(x - x'),$$

and  $\langle x|x \rangle = \delta(0)$  is not finite. The normalization is not finite until wave packets are used.

The time-dependent part of the differential equation (10.9) reads

$$\imath\hbar \frac{1}{\chi(t)} \frac{\partial}{\partial t} \chi(t) + \{\mu B_1 [\hat{\sigma}_x \cos(\omega t) + \hat{\sigma}_y \sin(\omega t)] + \mu B_0 \hat{\sigma}_z\} = E. \quad (10.11)$$

In order to obtain a homogeneous differential equation, we substitute  $\chi(t) = \xi(t) \exp\{-\imath Et/\hbar\}$ :

$$\imath\hbar \frac{\partial}{\partial t} \xi(t) + \{\mu B_1 [\hat{\sigma}_x \cos(\omega t) + \hat{\sigma}_y \sin(\omega t)] + \mu B_0 \hat{\sigma}_z\} \xi(t) = 0. \quad (10.12)$$

Now the following quantities are introduced:  $\hat{\sigma}_+ = \hat{\sigma}_x + \imath \hat{\sigma}_y$  and  $\hat{\sigma}_- = \hat{\sigma}_x - \imath \hat{\sigma}_y$ . The result is

$$\imath\hbar \frac{\partial}{\partial t} \xi(t) + \left[ \frac{\mu B_1}{2} (\hat{\sigma}_+ e^{-\imath\omega t} + \hat{\sigma}_- e^{\imath\omega t}) + \mu B_0 \hat{\sigma}_z \right] \xi(t) = 0. \quad (10.13)$$

A unitary transformation

$$\hat{U}(t) = \exp\{-\imath\omega t \hat{\sigma}_z/2\} \quad (10.14)$$

transforms  $\xi(t) = \hat{U}(t)\xi_r(t)$  to a rotating coordinate system, and the result is  $\xi_r(t)$ . If we denote  $\epsilon = \omega t/2$ , the unitary operator  $\hat{U}(t)$  can be calculated as follows:

$$\begin{aligned} \hat{U}(t) &= e^{-\imath\epsilon\hat{\sigma}_z} = \hat{1} - \imath\epsilon\hat{\sigma}_z + [(\imath\epsilon)^2/(2!)]\hat{\sigma}_z^2 - [(\imath\epsilon)^3/(3!)]\hat{\sigma}_z^3 + \dots \\ &= \hat{1} - \imath\epsilon\hat{\sigma}_z + [(\imath\epsilon)^2/(2!)]\hat{1} - [(\imath\epsilon)^3/(3!)]\hat{\sigma}_z + \dots \\ &= \begin{pmatrix} \exp\{-\imath\epsilon\} & 0 \\ 0 & \exp\{\imath\epsilon\} \end{pmatrix} \end{aligned} \quad (10.15)$$

using (9.7). The differential equation temporarily becomes a bit more complicated:

$$\begin{aligned} \frac{\hbar\omega}{2} \hat{\sigma}_z \hat{U}(t) \xi_r(t) + \imath\hbar \hat{U}(t) \frac{\partial}{\partial t} \xi_r(t) + \left\{ \frac{\mu B_1}{2} [\hat{\sigma}_+ e^{-\imath\omega t} \hat{U}(t) + \hat{\sigma}_- e^{\imath\omega t} \hat{U}(t)] \right. \\ \left. + \mu B_0 \hat{\sigma}_z \hat{U}(t) \right\} \xi_r(t) = 0. \end{aligned}$$

This equation is multiplied from the left-hand side with  $\hat{U}(t)^+$ , where  $\hat{U}(t)^+ \hat{U}(t) = \hat{1}$ . Thereby attention should be paid to

$$\hat{U}(t)^+ \hat{\sigma}_z \hat{U}(t) = \hat{\sigma}_z, \quad \hat{U}(t)^+ \hat{\sigma}_{\pm} \hat{U}(t) = e^{\pm i\omega t} \hat{\sigma}_{\pm}. \quad (10.16)$$

Finally, we get

$$i\hbar \frac{\partial}{\partial t} \xi_r(t) = - \left[ \frac{\hbar\omega}{2} \hat{\sigma}_z + \mu B_1 \hat{\sigma}_x + \mu B_0 \hat{\sigma}_z \right] \xi_r(t), \quad (10.17)$$

where  $(\hat{\sigma}_+ + \hat{\sigma}_-) = 2\hat{\sigma}_x$  has been inserted. The following abbreviations are now used:

$$\omega_0 = -\gamma B_0, \quad \omega_1 = -\gamma B_1, \quad \gamma = \frac{2\mu}{\hbar} = -\frac{2|\mu|}{\hbar}. \quad (10.18)$$

The quantity  $\gamma$  is called “gyromagnetic ratio”. The differential equation becomes

$$\frac{1}{\xi_r(t)} \frac{\partial}{\partial t} \xi_r(t) = -\frac{i}{2} [(\omega_0 - \omega) \hat{\sigma}_z + \omega_1 \hat{\sigma}_x], \quad (10.19)$$

and the solution is

$$\ln \xi_r(t) - \ln \xi_r(0) = -\frac{i}{2} [(\omega_0 - \omega) \hat{\sigma}_z + \omega_1 \hat{\sigma}_x] t. \quad (10.20)$$

We notice that  $\xi_r(0) = \xi(0)$ , where  $\xi(0)$  signifies the initial spinor for  $t = 0$ . For example,  $\xi(0) = |\uparrow\rangle = \begin{pmatrix} 1 \\ 0 \end{pmatrix}$  indicates an initial polarization in the  $z$ -direction. We, therefore, obtain

$$\xi_r(t) = \xi(0) \exp \left\{ -\frac{i}{2} [(\omega_0 - \omega) \hat{\sigma}_z + \omega_1 \hat{\sigma}_x] t \right\}$$

and after back-transformation

$$\xi(t) = \xi(0) \exp \left\{ -i \frac{\omega t}{2} \hat{\sigma}_z \right\} \exp \left\{ -\frac{i}{2} [(\omega_0 - \omega) \hat{\sigma}_z + \omega_1 \hat{\sigma}_x] t \right\}. \quad (10.21)$$

Defining a vector  $\vec{\alpha}(t) = [\omega_1 t, 0, (\omega_0 - \omega)t]$ , the solution can be written as

$$\xi(t) = \xi(0) \exp \left\{ -i \frac{\omega t}{2} \hat{\sigma}_z \right\} \exp \left\{ -i \vec{\sigma} \frac{\vec{\alpha}(t)}{2} \right\}. \quad (10.22)$$

For the time being, the problem has been solved theoretically. The point is to discuss the results. For this purpose, the second exponential has to be examined more precisely:

$$\exp \left\{ -i \vec{\sigma} \frac{\vec{\alpha}(t)}{2} \right\} = \hat{1} - i \vec{\sigma} \frac{\vec{\alpha}(t)}{2} + \frac{1}{2!} \left[ i \vec{\sigma} \frac{\vec{\alpha}(t)}{2} \right]^2 - \frac{1}{3!} \left[ i \vec{\sigma} \frac{\vec{\alpha}(t)}{2} \right]^3 + \dots$$

Discussing the single expressions sequentially, we obtain

$$\vec{\sigma} \frac{\vec{\alpha}(t)}{2} = \frac{1}{2} [\hat{\sigma}_x \omega_1 t + \hat{\sigma}_z (\omega_0 - \omega) t],$$

and, because  $\hat{\sigma}_x \hat{\sigma}_z + \hat{\sigma}_z \hat{\sigma}_x = 0$ ,

$$\left[ \vec{\sigma} \frac{\vec{\alpha}(t)}{2} \right]^2 = \left[ \frac{\omega_1 t}{2} \right]^2 \hat{1} + \left[ \frac{(\omega_0 - \omega) t}{2} \right]^2 \hat{1} = \left[ \frac{\vec{\alpha}(t)}{2} \right]^2 \hat{1}.$$

Altogether we obtain

$$\begin{aligned} \exp \left\{ -i \vec{\sigma} \frac{\vec{\alpha}(t)}{2} \right\} &= \hat{1} - i \vec{\sigma} \frac{\vec{\alpha}(t)}{2} - \frac{1}{2!} \left[ \frac{\vec{\alpha}(t)}{2} \right]^2 \hat{1} + \frac{1}{3!} i \vec{\sigma} \frac{\vec{\alpha}(t)}{2} \left[ \frac{\vec{\alpha}(t)}{2} \right]^2 \hat{1} + \dots \\ &= \hat{1} \cos \left[ \frac{\alpha(t)}{2} \right] - i \vec{\sigma} \vec{\alpha}_0 \sin \left[ \frac{\alpha(t)}{2} \right]. \end{aligned}$$

Here, the time-independent unit-vector  $\vec{\alpha}_0$  can be computed (see (10.18)) as follows:

$$\begin{aligned} \alpha(t) &= t \sqrt{\omega_1^2 + (\omega_0 - \omega)^2} = \gamma t \sqrt{B_1^2 + (B_0 + \frac{\omega}{\gamma})^2} = \gamma t B_{eff}, \\ \vec{\alpha}_0 &= \frac{\vec{\alpha}(t)}{\alpha(t)} = -\frac{1}{B_{eff}} \begin{pmatrix} B_1 \\ 0 \\ B_0 + \omega/\gamma \end{pmatrix} = -\frac{\vec{B}_{eff}}{B_{eff}}. \end{aligned} \quad (10.23)$$

In the rotating system, the neutron perceives the effective magnetic field  $\vec{B}_{eff}$ . If the rotating magnetic field has a resonance frequency  $\omega \equiv \omega_r = \omega_0 = -\gamma B_0$ , the action of the static field  $B_0$  has been compensated and  $\vec{B}_{eff}$  has an  $x$ -component only. This case leads to spin-flip and will be discussed below.

In summary, the total wave function  $\psi(x, t)$  of (10.8) can be expressed as ((10.10) and (10.22))

$$\begin{aligned} \psi(x, t) &= \Phi(x) \chi(t) = \frac{1}{\sqrt{2\pi}} \exp \left\{ ikx - i \frac{\omega t}{2} \hat{\sigma}_z - i \frac{\hbar k^2}{2M} t \right\} \\ &\times \left\{ \hat{1} \cos \left[ \frac{\alpha(t)}{2} \right] - i \vec{\sigma} \vec{\alpha}_0 \sin \left[ \frac{\alpha(t)}{2} \right] \right\} \xi(0). \end{aligned} \quad (10.24)$$

The unitary operator  $\hat{U}(t) = \exp\{-i\omega t \hat{\sigma}_z/2\}$  has already been evaluated in (10.15). According to (10.23), the quantity  $\vec{\sigma} \vec{\alpha}_0$  reads as follows:

$$\vec{\sigma} \vec{\alpha}_0 = -\vec{\sigma} \vec{B}_{eff}/B_{eff} = -[\hat{\sigma}_x B_1 + \hat{\sigma}_z (B_0 + \omega/\gamma)]/B_{eff}.$$

Moreover, we assume the incident beam to be polarized in the  $z$ -direction as indicated in Fig. 10.1, thus writing  $\xi(0) = \begin{pmatrix} 1 \\ 0 \end{pmatrix}$ . Putting everything together

and applying the Pauli matrices  $\hat{\sigma}_x$  and  $\hat{\sigma}_z$  (see (9.7)) and the identity matrix  $\hat{1}$ , we finally get

$$\begin{aligned}\psi(x, t) = & \frac{1}{\sqrt{2\pi}} \exp \left\{ i \left[ kx - \frac{E}{\hbar} t \right] \right\} \\ & \times \begin{pmatrix} e^{-i\omega t/2} \{ \cos[\frac{\alpha(t)}{2}] + i \frac{(B_0 + \omega/\gamma)}{B_{eff}} \sin[\frac{\alpha(t)}{2}] \} \\ ie^{i\omega t/2} \frac{B_1}{B_{eff}} \sin[\frac{\alpha(t)}{2}] \end{pmatrix}. \quad (10.25)\end{aligned}$$

$\alpha(t)$  and  $B_{eff}$  are defined in (10.23). Putting  $B_0 = B_1 = 0$ , we obtain  $\psi(x, t) = [1/(\sqrt{2\pi})] \exp\{ikx - i\frac{E}{\hbar}t\} \begin{pmatrix} 1 \\ 0 \end{pmatrix}$ , as required for a free particle of energy  $E = \hbar^2 k^2 / (2M)$  polarized in the  $z$ -direction. Equation (10.25) is our final result and the solution of the Pauli equation (10.7). It describes the wave function of a neutron with a wave number  $k$  that moves in the  $x$ -direction interacting with a time-dependent magnetic field  $\vec{B}(t)$  given in (10.1).

In the next sections we discuss the consequences arising from these results.

### 10.1.2 Time-Dependent Polarization

We would like to consider the  $z$ -component of the polarization. From (10.3), as well as accounting for normalization and using (10.25), the time-dependent polarization  $P_z(t)$  reads

$$P_z(t) = \frac{\langle \psi | \hat{\sigma}_z | \psi \rangle}{\langle \psi | \psi \rangle} = \cos^2 \left[ \frac{\alpha(t)}{2} \right] + \frac{(B_0 + \omega/\gamma)^2 - B_1^2}{(B_0 + \omega/\gamma)^2 + B_1^2} \sin^2 \left[ \frac{\alpha(t)}{2} \right]. \quad (10.26)$$

As has already been mentioned, resonance frequency (index  $rf$ ) appears, if  $B_0 = -\omega/\gamma$  and  $P_{z,rf}(t)$  becomes

$$P_{z,rf}(t) = \cos^2 \left[ \frac{\alpha(t)}{2} \right] - \sin^2 \left[ \frac{\alpha(t)}{2} \right] = \cos(\omega_1 t) \quad (10.27)$$

using (10.23) and (10.18). For  $t = 0$ , the initial polarization in the  $z$ -direction  $P_{z,rf}(0) = 1$  arises. Furthermore,  $P_{z,rf}[t = \pi/(2\omega_1)] = 0$ , which means that the polarization vector lies in the  $x/y$ -plane ( $\pi/2$ -flip). For  $P_{z,rf}[t \equiv T = \pi/\omega_1] = -1$  a  $\pi$ -flip occurs. The particle is polarized in the  $(-z)$ -direction.

### 10.1.3 Probability for $\pi$ -Flip

The probability  $W_{\pi\text{-}flip}(T)$  to have neutrons polarized in the  $(-z)$ -direction can be expressed by

$$W_{\pi\text{-}flip}(T) = \frac{1}{2} [1 - P_z(T)] = \frac{\sin^2 \left[ \frac{\gamma B_1 T}{2} \sqrt{1 + (\frac{B_0 + \omega/\gamma}{B_1})^2} \right]}{1 + \left( \frac{B_0 + \omega/\gamma}{B_1} \right)^2}. \quad (10.28)$$

For a complete  $\pi$ -flip, two conditions have to be fulfilled.

- 1) Condition for resonance frequency (as has already been mentioned):  
 $\omega \equiv \omega_r = -\gamma B_0$

$$\Rightarrow W_{\pi\text{-}flip,rf}(T) = \sin^2 \left[ \frac{\gamma T B_1}{2} \right].$$

- 2) Condition for amplitude resonance (index *ar*); from (10.23) we obtain for  $t = T$ :  $\alpha(t) = \gamma T B_1 = -\pi$

$$\Rightarrow W_{\pi\text{-}flip,rf,ar}(T) = 1, \quad T = \frac{\pi}{\omega_1}.$$

$T = L/v$  is the transmission time through the dynamical spin flipper, which can be converted into a flipper length  $L$ , depending on the velocity  $v$  of the particle.

The two conditions above have to be fulfilled in order to achieve a  $\pi$ -flip. Resonance frequency is generally necessary for a spin-flip process and amplitude resonance is sufficient to obtain a  $\pi$ -flip.

#### 10.1.4 Energy States of the System for Spin-Flip

In this section, we describe the energy states of the system undergoing a  $\pi$ -flip and a  $\pi/2$ -flip.

In the external region, the neutron is supposed to be initially polarized in the  $z$ -direction having an energy  $E$ . At time  $t = 0$ , a purely time-dependent magnetic field  $\vec{B}(t)$  (10.1) is switched on. The  $z$ -component of this field is constant and equal to  $B_0$ .  $B_0$  is sometimes called guiding field. A second, but time-dependent magnetic field  $\vec{B}_1$  of amplitude  $B_1$ , which rotates in the  $x/y$ -plane with frequency  $\omega$ , is superimposed to  $B_0$ . Spin-flippers generally have  $B_1 \ll B_0$ .

We analyze the process of spin-flip theoretically as follows. At the very beginning only  $B_0$  should be switched on and immediately afterwards the field  $\vec{B}_1$ . If initially only  $B_0$  is active,  $B_1 = 0$  and, from (10.23),  $B_{eff} = (B_0 + \omega/\gamma) = \alpha(t)/(\gamma t)$ . The wave function (10.25) becomes

$$\begin{aligned} \psi_0(x, t) &= \frac{1}{\sqrt{2\pi}} \exp \left\{ i \left[ kx - \frac{E}{\hbar} t \right] \right\} \begin{pmatrix} e^{-i\omega t/2} e^{i\alpha(t)/2} \\ 0 \end{pmatrix} \\ &= \frac{1}{\sqrt{2\pi}} \exp \left\{ i \left[ kx - \frac{E}{\hbar} t \right] \right\} \begin{pmatrix} e^{i\gamma t B_0 / 2} \\ 0 \end{pmatrix} \\ &= \frac{1}{\sqrt{2\pi}} \exp \left\{ i \left[ kx - \frac{(E + |\mu| B_0)}{\hbar} t \right] \right\} \begin{pmatrix} 1 \\ 0 \end{pmatrix}. \end{aligned} \quad (10.29)$$

In the last calculation step, the total energy  $E_0$  can be introduced as follows:

$$E_0 = \frac{\psi_0^*(x, t) i\hbar \frac{\partial}{\partial t} \psi_0(x, t)}{|\psi_0(x, t)|^2} = E + |\mu|B_0 > E. \quad (10.30)$$

Initially, the system has, therefore, gained an energy amount of  $(E_0 - E) = |\mu|B_0 > 0$ . The kinetic energy of the neutron has not changed and amounts to

$$E = \frac{\psi_0^*(x, t) \left(-\frac{\hbar^2}{2M}\right) \frac{\partial^2}{\partial x^2} \psi_0(x, t)}{|\psi_0|^2} = \frac{\hbar^2 k^2}{2M}.$$

The components of the polarization vector are:

$$P_{0,i} = \langle \psi_0 | \hat{\sigma}_i | \psi_0 \rangle / \langle \psi_0 | \psi_0 \rangle,$$

and we obtain  $\vec{P}_0 = (0, 0, 1)$ .

Now let us calculate the final energy after the  $\pi$ -flip at time  $t = T$ . The condition for resonance frequency gives  $\omega = -\gamma B_0 \equiv \omega_r$ , as well as  $B_{eff} = B_1$  and from the condition for amplitude resonance  $\alpha(t) = \gamma T B_1 = -\pi$  follows. Equation (10.25) yields

$$\begin{aligned} \psi_{\pi\text{-}flip}(x, t) &= \frac{1}{\sqrt{2\pi}} \exp \left\{ i \left[ kx - \frac{E}{\hbar} t \right] \right\} \begin{pmatrix} 0 \\ -ie^{-i\gamma B_0 t/2} \end{pmatrix} \\ &= -i \frac{1}{\sqrt{2\pi}} \exp \left\{ i \left[ kx - \frac{(E - |\mu|B_0)}{\hbar} t \right] \right\} \begin{pmatrix} 0 \\ 1 \end{pmatrix}. \end{aligned} \quad (10.31)$$

The total energy  $E_{\pi\text{-}flip}$  of the system after a  $\pi$ -flip reads as follows:

$$E_{\pi\text{-}flip} = E - |\mu|B_0 = E_0 - 2|\mu|B_0 = E_0 - \Delta E_0. \quad (10.32)$$

As was already indicated at the beginning of this chapter, an energy exchange between the neutron and the magnetic field takes place (inelastic process). When undergoing a  $\pi$ -spin flip, the particle removes an energy amount of  $\Delta E_0 = 2|\mu|B_0$  from the magnetic field. The process just described is called neutron-photon interaction. It should be noted that for usual spin flippers  $B_0 \approx 10kG$  and, therefore,  $\Delta E_0 \approx 0, 12 \cdot 10^{-6} eV$ , which is more than 5 orders of magnitude smaller than the energy  $E$  of thermal neutrons. For pure spin-flip applications, such a small energy exchange is of no consequence.

The components of the polarization vector are:

$$P_{\pi\text{-}flip,i} = \langle \psi_{\pi\text{-}flip} | \hat{\sigma}_i | \psi_{\pi\text{-}flip} \rangle / \langle \psi_{\pi\text{-}flip} | \psi_{\pi\text{-}flip} \rangle,$$

and we obtain  $\vec{P}_{\pi\text{-}flip} = (0, 0, -1)$ .

Finally, we would like to describe a  $\pi/2$ -spin flip. The condition for resonance frequency again reads  $\omega = -\gamma B_0 = \omega_L$  and  $B_{eff} = B_1$ . The condition for amplitude resonance reads  $t = T/2$  and  $\alpha(t) = \gamma(T/2)B_1 = -\pi/2$ . The wave function (10.25) reads:

$$\begin{aligned}\psi_{\pi/2\text{-}f\!l\!i\!p}(x, t) &= \frac{1}{2\sqrt{\pi}} \exp \left\{ i \left[ kx - \frac{E}{\hbar} t \right] \right\} \begin{pmatrix} e^{-it|\mu|B_0/\hbar} \\ -ie^{it|\mu|B_0/\hbar} \end{pmatrix} \\ &= \frac{1}{\sqrt{2}} [\psi_0(x, t) + \psi_{\pi\text{-}f\!l\!i\!p}(x, t)].\end{aligned}\quad (10.33)$$

The energy  $E_{\pi/2\text{-}f\!l\!i\!p}$  that the system carries after a  $\pi/2$ -flip can immediately be identified:

$$\begin{aligned}E_{\pi/2\text{-}f\!l\!i\!p} &= \frac{\psi_{\pi/2\text{-}f\!l\!i\!p}^*(x, t)i\hbar\frac{\partial}{\partial t}\psi_{\pi/2\text{-}f\!l\!i\!p}(x, t)}{|\psi_{\pi/2\text{-}f\!l\!i\!p}(x, t)|^2} \\ &= E = E_0 - |\mu|B_0 = E_0 - \frac{\Delta E_0}{2}.\end{aligned}\quad (10.34)$$

As expected, the energy loss ( $\Delta E_0/2$ ) of a  $\pi/2$ -flip is half the energy loss ( $\Delta E_0$ ) of a  $\pi$ -flip. It should be pointed out that spin-flips from the  $(-z)$ -direction to  $(+z)$ -direction entail energy gains of the same size, of course.

The components of the polarization vector are:

$$P_{\pi/2\text{-}f\!l\!i\!p, i} = \langle \psi_{\pi/2\text{-}f\!l\!i\!p} | \hat{\sigma}_i | \psi_{\pi/2\text{-}f\!l\!i\!p} \rangle / \langle \psi_{\pi/2\text{-}f\!l\!i\!p} | \psi_{\pi/2\text{-}f\!l\!i\!p} \rangle,$$

and we obtain for  $t = T/2$

$$\vec{P}_{\pi/2\text{-}f\!l\!i\!p} = \begin{pmatrix} \sin(\omega_L T/2) \\ -\cos(\omega_L T/2) \\ 0 \end{pmatrix}, \quad (10.35)$$

where  $\omega_L = 2|\mu|B_0/\hbar$  is the Larmor frequency. If the field  $\vec{B}(t)$  is switched off after a  $\pi/2$ -flip (see Fig. 10.1), the polarization vector has a certain position in the  $x/y$ - given by this equation (see also below).

### 10.1.5 Energy Characteristics of a Dynamical Spin-Flipper

We would like to determine the time-dependent energy characteristics  $E_{tot}(t)$  of the total energy during a complete  $\pi$ -flip. This is carried out by calculating the following expression:

$$E_{tot}(t) = \frac{\psi^*(x, t)i\hbar\frac{\partial}{\partial t}\psi(x, t)}{|\psi(x, t)|^2}. \quad (10.36)$$

Here  $\psi(x, t)$  has to be taken from (10.25). Taking into account the condition of frequency resonance  $\omega = -\gamma B_0$  and, therefore,  $\alpha(t) = \gamma t B_1 = \gamma t B_{eff}$ , the

wave function  $\psi(x, t)$  reads as follows:

$$\begin{aligned}\psi(x, t) = \frac{1}{\sqrt{2\pi}} e^{ikx} & \left\{ e^{-i(E+|\mu|B_0)t/\hbar} \cos\left(\frac{|\mu|B_1 t}{\hbar}\right) |\uparrow\rangle \right. \\ & \left. -ie^{-i(E-|\mu|B_0)t/\hbar} \sin\left(\frac{|\mu|B_1 t}{\hbar}\right) |\downarrow\rangle \right\},\end{aligned}\quad (10.37)$$

and the result is ( $\omega_1 = -\gamma B_1$ )

$$E_{tot}(t) = E_0 - \Delta E_0 \sin^2\left(\frac{\omega_1 t}{2}\right). \quad (10.38)$$

For  $t = 0$ , we obtain  $E_{tot}(0) = E_0$  (see (10.30)),  $E_{tot}(t = T/2 = \pi/(2\omega_1)) = E_0 - \Delta E_0/2 = E_{\pi/2\text{-flip}}$  (see (10.34)) and  $E_{tot}(t = T = \pi/\omega_1) = E_0 - \Delta E_0 = E_{\pi\text{-flip}}$  (see (10.32)).

Expressed independently of absolute values, the equation above can be written as:

$$\frac{E_{tot}(t) - E_{tot}(0)}{\Delta E_0} = -\sin^2\left(\frac{\omega_1 t}{2}\right). \quad (10.39)$$

This nonlinear energy characteristic during spin-flip is represented in Fig. 10.2.

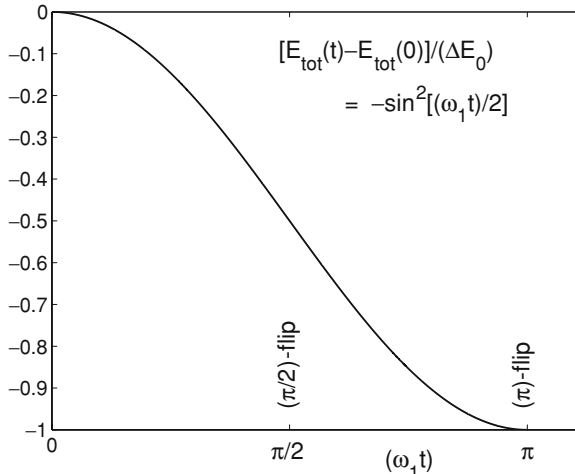


**Fig. 10.2.** Illustration of (10.39) in which the decrease of the total energy  $E_{tot}(t)$  during spin-flip causes the decline of the curve. The  $\pi/2$ -flip is characterized by  $t = T/2$ , where  $T = \pi/\omega_1$ , and a  $\pi$ -flip appears for  $t = T$

## 10.2 Wave Functions in the Case of Zero-Field Spin-Echo

We are now in a position to physically and mathematically describe the process of a dynamical spin-flip as indicated in Fig. 10.1 (first  $\pi/2$ -spin flip). To this end, we divide the area of the spin flipper into five regions as shown in Fig. 10.3. We shall treat each region separately.

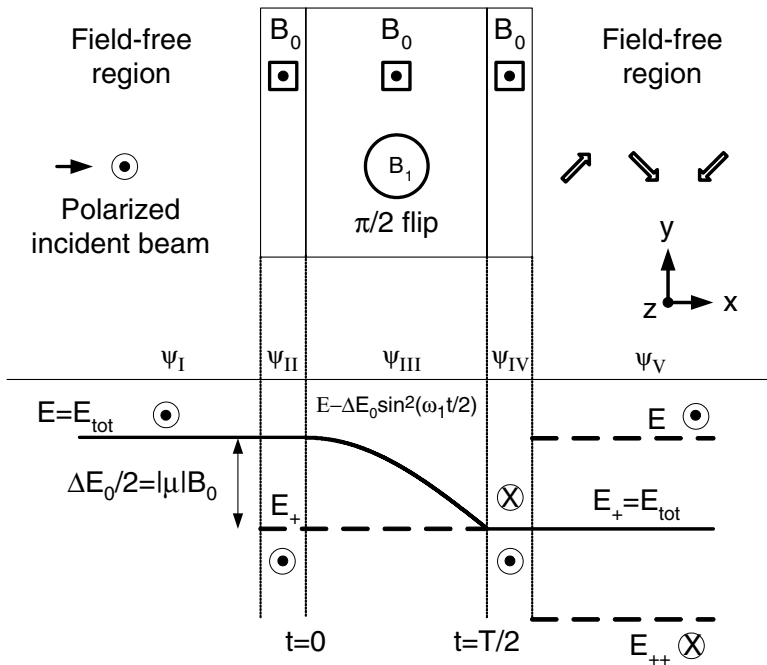


**Fig. 10.3.** Systematic illustration of conditions for a dynamical  $\pi/2$ -spin-flip. Five regions are shown. The corresponding wave functions  $\psi_I$  to  $\psi_V$  are calculated below. Region I is an external region without any magnetic field. In Region II a constant magnetic field  $B_0$ , is active. In Region III, in addition to  $B_0$ , a rotating magnetic field  $B_1$  is superposed. Region IV is again characterized by  $B_0$  alone and Region V is the field-free region behind the spin-flipper. The energy levels are drawn at the bottom (for an explanation see text)

*Region I :*

In this field-free region, a plane wave with spin-up orientation and total energy  $E_{tot} = E = \hbar^2 k^2 / (2M)$  impinges in the  $x$ -direction:

$$\psi_I(x, t) = \frac{1}{\sqrt{2\pi}} \exp \left\{ ikx - i \frac{E}{\hbar} t \right\} \begin{pmatrix} 1 \\ 0 \end{pmatrix} \quad (10.40)$$

*Region II :*

Here the neutron with spin-up state  $| \uparrow \rangle = \begin{pmatrix} 1 \\ 0 \end{pmatrix}$  enters a constant magnetic field  $B_0$ , which is oriented towards the same ( $+z$ )-direction. This is a purely space-dependent problem. We have to solve the Schrödinger equation

$$\left[ -\frac{\hbar^2}{2M} \frac{\partial^2}{\partial x^2} + |\mu| B_0 \right] \psi_{II}(x, t) = i\hbar \frac{\partial}{\partial t} \psi_{II}(x, t), \quad (10.41)$$

using the separation ansatz  $\psi_{II}(x, t) = \Phi(x)\chi(t)| \uparrow \rangle$  and we get

$$\frac{1}{\Phi(x)} \left[ -\frac{\hbar^2}{2M} \frac{\partial^2}{\partial x^2} \right] \Phi(x) + |\mu| B_0 = i\hbar \frac{\partial}{\partial t} \chi(t) = E. \quad (10.42)$$

In fact, in spin-echo devices, the relation  $E \gg |\mu| B_0$  is valid [26, 66, 67] and we can neglect reflected waves. The solutions are, therefore, (compare to (9.9) to (9.11)):

$$\begin{aligned} \Phi(x) &= \frac{1}{\sqrt{2\pi}} \exp\{ik_+ x\}, \quad k_+ = \sqrt{\frac{2M}{\hbar^2}(E - |\mu| B_0)} = k - \Delta k, \\ \Delta k &= \frac{M|\mu| B_0}{\hbar^2 k}, \quad E_+ = \frac{\hbar^2 k_+^2}{2M} = E - \Delta E_0/2, \quad \chi(t) = \exp \left\{ -i \frac{E}{\hbar} t \right\}. \end{aligned} \quad (10.43)$$

The total energy  $E_{tot} = E$  of the system remains constant. The kinetic energy of the neutron has been reduced from  $E$  to  $E_+$  (see Fig. 10.3). Hence, the wave function  $\psi_{II}(x, t)$  reads as follows:

$$\psi_{II}(x, t) = \frac{1}{\sqrt{2\pi}} \exp \left\{ ik_+ x - i \frac{E}{\hbar} t \right\} \begin{pmatrix} 1 \\ 0 \end{pmatrix}. \quad (10.44)$$

*Region III :*

In this region, a time-dependent magnetic field  $\vec{B}_1(t)$  rotating in the  $x/y$ -plane is superposed to  $B_0$ , as indicated in (10.1) and Fig. 10.3. The neutron should enter this field at time  $t = 0$ . Because  $B_1 \ll B_0$  for usual time-dependent spin flippers, reflected waves can be neglected. Moreover, it is assumed that the frequency resonance condition  $\omega = -\gamma B_0 = 2|\mu| B_0 / \hbar$  is

fulfilled (otherwise no spin flip is possible). At the beginning (index  $i$ ), the wave function reads

$$\psi_{\text{III},i}(x, t) = \frac{1}{\sqrt{2\pi}} \exp \left\{ i k_+ x - i \frac{E_+}{\hbar} t \right\} \begin{pmatrix} \exp\{-i\omega t/2\} \\ 0 \end{pmatrix} = \psi_{\text{II}}(x, t). \quad (10.45)$$

This expression can also be obtained from (10.29), simply by replacing  $k$  and  $E$  by  $k_+$  and  $E_+$ , respectively. Furthermore, we neglect slightly differing transmission times for both spin states during the  $\pi/2$ -flip. During spin-flip (between  $t = 0$  and  $t = T/2$ ) the wave function has the form (compare to (10.37))

$$\begin{aligned} \psi_{\text{III}}(x, t) = & \frac{1}{\sqrt{2\pi}} e^{ik_+ x - iE_+ t/\hbar} \left\{ e^{-i|\mu|B_0 t/\hbar} \cos \left( \frac{|\mu|B_1 t}{\hbar} \right) |\uparrow\rangle \right. \\ & \left. - ie^{i|\mu|B_0 t/\hbar} \sin \left( \frac{|\mu|B_1 t}{\hbar} \right) |\downarrow\rangle \right\}. \end{aligned} \quad (10.46)$$

The condition for amplitude resonance of a  $\pi/2$ -flip is  $t = T/2 = \pi/(2\omega_1)$ , with  $\omega_1 = -\gamma B_1 = 2|\mu|B_1/\hbar$ . Each of the trigonometric functions becomes equal to  $1/\sqrt{2}$ . At the end (index  $f$ ) of the  $\pi/2$ -flip we have

$$\psi_{\text{III},f}(x, t) = \frac{1}{\sqrt{2\pi}} \exp \left\{ i k_+ x - i \frac{E_+}{\hbar} t \right\} \frac{1}{\sqrt{2}} (e^{-i\omega_L T/4} |\uparrow\rangle - ie^{i\omega_L T/4} |\downarrow\rangle). \quad (10.47)$$

If the polarization is calculated we obtain

$$\vec{P}_{\text{III},f} = \frac{1}{\langle \psi_{\text{III},f} | \psi_{\text{III},f} \rangle} \begin{pmatrix} \langle \psi_{\text{III},f} | \hat{\sigma}_x | \psi_{\text{III},f} \rangle \\ \langle \psi_{\text{III},f} | \hat{\sigma}_y | \psi_{\text{III},f} \rangle \\ \langle \psi_{\text{III},f} | \hat{\sigma}_z | \psi_{\text{III},f} \rangle \end{pmatrix} = \begin{pmatrix} \sin(\omega_L T/2) \\ -\cos(\omega_L T/2) \\ 0 \end{pmatrix}, \quad (10.48)$$

and this result has already been obtained (10.35). The polarization vector lies in the  $x/y$ -plane and has a fixed rotation angle  $(\omega_L T/2) = \pi B_0/(2B_1)$ . The total energy can be determined directly and amounts to  $E_{\text{tot}} = E_+$  and it has so been reduced by a value of  $|\mu|B_0$ , as seen in Fig. 10.3.

*Region IV :*

The wave function here is  $\psi_{\text{IV}}(x, t) = \psi_{\text{III},f}(x, t)$ .

*Region V :*

Because of Zeeman-splitting, on exit from Region IV into Region V, the spin-up component  $|\uparrow\rangle$  of the wave function  $\psi_{\text{IV}}(x, t)$  receives a phase factor  $e^{i(\Delta k)x_V}$  and the spin-down component  $|\downarrow\rangle$  receives a phase factor  $e^{-i(\Delta k)x_V}$ . (From now on by  $x_V$  we denote a definite position in the

zero-field Region V.) This proves to be exactly the opposite procedure, compared to a wave function entering a constant magnetic field that is oriented perpendicular to the spin direction of the wave function as described in Sect. 9.1.1 and (9.8). If a new wave number  $k_{++}$  and an energy  $E_{++}$  is defined by

$$k_{++} = k - 2(\Delta k), \quad E_{++} = \frac{\hbar^2 k_{++}^2}{2M}, \quad (10.49)$$

and if we remember that  $k_+ = k - \Delta k$  (see (9.10)), the wave function in Region V reads

$$\psi_V(x_V, t) = \frac{1}{\sqrt{2\pi}} e^{-i\frac{E_+}{\hbar}t} \frac{1}{\sqrt{2}} (e^{-i\omega_L T/4 + ikx_V} |\uparrow\rangle - ie^{i\omega_L T/4 + ik_{++}x_V} |\downarrow\rangle). \quad (10.50)$$

The kinetic energy of the spin components are, therefore,  $E$  and  $E_{++}$ , respectively. However, the total energy remains constant and amounts to  $E_+$ . From these considerations it can be concluded that a spin rotation in the field-free Region V behind the  $\pi/2$ -spin flipper, as a function of the distance  $x_V$  in this region, can be anticipated. In Fig. 10.3 this process is indicated by rotating arrows.

### 10.3 Polarization and the Wigner Function

In order to determine the polarization vector in Region V, we have to build up

$$\vec{P}_V = \frac{1}{\langle \psi_V | \psi_V \rangle} \begin{pmatrix} \langle \psi_V | \hat{\sigma}_x | \psi_V \rangle \\ \langle \psi_V | \hat{\sigma}_y | \psi_V \rangle \\ \langle \psi_V | \hat{\sigma}_z | \psi_V \rangle \end{pmatrix} = \begin{pmatrix} \sin[\omega_L T/2 - 2(\Delta k)x_V] \\ -\cos[\omega_L T/2 - 2(\Delta k)x_V] \\ 0 \end{pmatrix}, \quad (10.51)$$

where  $x_V$  denotes a certain position in the free-field Region V. The polarization vector rotates in the  $x/y$ -plane as a function of the distance from the spin-flipper. Here we have a somewhat similar effect of spin rotation as in the problem of spin rotation in a constant magnetic field described in Sect. 9.1.1. However, here the rotation occurs in a region without any magnetic field due to the dynamical (inelastic) spin-flip from the  $z$ -axes down to the  $x/y$ -plane, where the spin components gain different Zeeman shifts on exit in the field-free Region V.

In order to compute the Wigner function in the field-free region, it is of advantage to reshape the corresponding wave  $\psi_V(x_V, t)$  (see (10.50)):

$$\psi_V(x_V, t) = \frac{1}{\sqrt{2\pi}} \frac{1}{\sqrt{2}} (g_+ |\uparrow\rangle + g_- |\downarrow\rangle), \quad (10.52)$$

and

$$\begin{aligned} g_+ &= \exp \left\{ -i \frac{E_+}{\hbar} t + i k x_V - i \omega_L T / 4 \right\}, \\ g_- &= \exp \left\{ -i \frac{E_+}{\hbar} t + i k x_V + i [\omega_L T / 4 - \pi / 2 - 2(\Delta k) x_V] \right\}. \end{aligned} \quad (10.53)$$

Equation (10.52) formally looks like (9.8). The calculation procedure in Sect. 9.1 can, therefore, be applied here without changes. Especially, the wave number distribution  $\alpha(k)$  (see (2.3)) is included in our concept, in order to take into account wave packets. For example, the spectral function

$$\alpha_{zf,+x}(k) = \frac{1}{2} \alpha(k) [g_+ + g_-]^* \quad (10.54)$$

can be constructed in accordance with (9.21). The index (*zf*) means “zero-field” and (+*x*) indicates that only the polarization in that direction is considered. Other polarization directions can be modelled in a similar manner as indicated in Sect. 9.1.

The time-independent Wigner function  $W_{zf,+x}(x, k)$  is built up in compliance with (4.3) and we get

$$W_{zf,+x}(x, k) = \frac{1}{2\pi} \int e^{-ik'x} \alpha_{zf,+x}^* \left( k + \frac{k'}{2} \right) \alpha_{zf,+x} \left( k - \frac{k'}{2} \right) dk'. \quad (10.55)$$

## 10.4 Spectra of Zero-Field Spin-Echo

From (10.54) the momentum spectrum  $|\alpha_{zf,+x}(k)|^2$  can be determined, keeping in mind that in (10.53) the expression  $2(\Delta k)x_V = 2(\Delta k/k)kx_V \approx 2\tau kx_V$ , where  $\tau = \Delta k_0/k_0$  and  $\Delta k_0 = |\mu|B_0M/(\hbar^2k_0)$  (compare to (9.18)). Taken all together, we obtain

$$|\alpha_{zf,+x}(k)|^2 = \frac{1}{2} \frac{1}{\sqrt{2\pi}(\sigma k_0)} e^{-\frac{(k/k_0-1)^2}{2\sigma^2}} \left\{ 1 + \cos \left[ 2\pi\bar{T} - 2\tau \frac{k}{k_0} (x_V k_0) \right] \right\}. \quad (10.56)$$

Here the parameter  $\bar{T} = (\omega_L T / 2 - \pi / 2) / (2\pi)$  contains the flip-time  $T$  and the Larmor frequency  $\omega_L$ . The intensity reads as

$$\begin{aligned} I_{zf,+x} &= \int |\alpha_{zf,+x}(k)|^2 dk \\ &= \frac{1}{2} \left\{ 1 + \cos[2\pi\bar{T} - 2\tau(x_V k_0)] e^{-2\sigma^2\tau^2(x_V k_0)^2} \right\}. \end{aligned} \quad (10.57)$$

These formulas are very similar to (9.19) and (9.20), except for the quantity  $2\pi\bar{T}$ , which denotes a constant phase in the cosine-term (and except for the different position coordinates  $x_1$  and  $x_V$ , of course).  $\bar{T}$  signifies a constant

phase shift due to the dynamical  $\pi/2$ -spin-flipper. This is immediately self-explanatory, because the rotating field of spin flipper causes spin rotation and, therefore, a phase shift. The Wigner function looks like

$$W_{zf,+x}(x, k) = \frac{1}{4\pi} e^{-\frac{(k/k_0 - 1)^2}{2\sigma^2}} \left\{ e^{-2\sigma^2[xk_0 - (1-\tau)x_V k_0]^2} + e^{-2\sigma^2[xk_0 - (1+\tau)x_V k_0]^2} + 2 \cos \left[ 2\pi\bar{T} - 2\tau \frac{k}{k_0} (x_V k_0) \right] e^{-2\sigma^2(xk_0 - x_V k_0)^2} \right\}. \quad (10.58)$$

This formula is similar to (9.22) as well, except for the constant phase shift  $2\pi\bar{T}$  present in the cosine-term. Thus, basically, there is no fundamental difference between these functions and Figs. 9.2 to 9.5 can be interpreted accordingly. If  $\bar{T} = n$ , and  $n = 0, 1, 2, \dots$ , there is even no difference between the formulas. We express the parameter  $\bar{T}$  as follows:

$$\bar{T} = \frac{1}{2\pi} \left( \frac{\omega_L T}{2} - \frac{\pi}{2} \right) = \frac{1}{4} \left( \frac{B_0}{B_1} - 1 \right) = \frac{1}{4}(p - 1), \quad (10.59)$$

where the parameter  $p = B_0/B_1$  specifies the ratio between the guiding magnetic field  $B_0$  and the amplitude  $B_1$  of the rotating magnetic field of the dynamical spin-flipper. Usually this ratio is much larger than 1 and hence  $p \gg 1$ . In Figs. 10.4 and 10.5, two Wigner functions are drawn using the

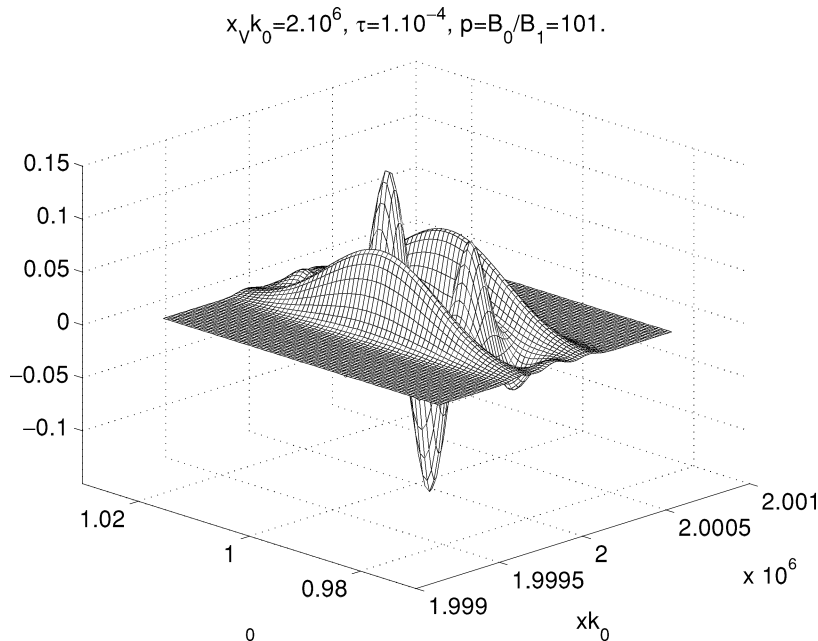


**Fig. 10.4.** The Wigner function (10.58) in the field-free region (Fig. 10.1) for  $\bar{T} = (p - 1)/4 = 25$

$$x_V k_0 = 2 \cdot 10^6, \tau = 1 \cdot 10^{-4}, p = B_0/B_1 = 103.$$

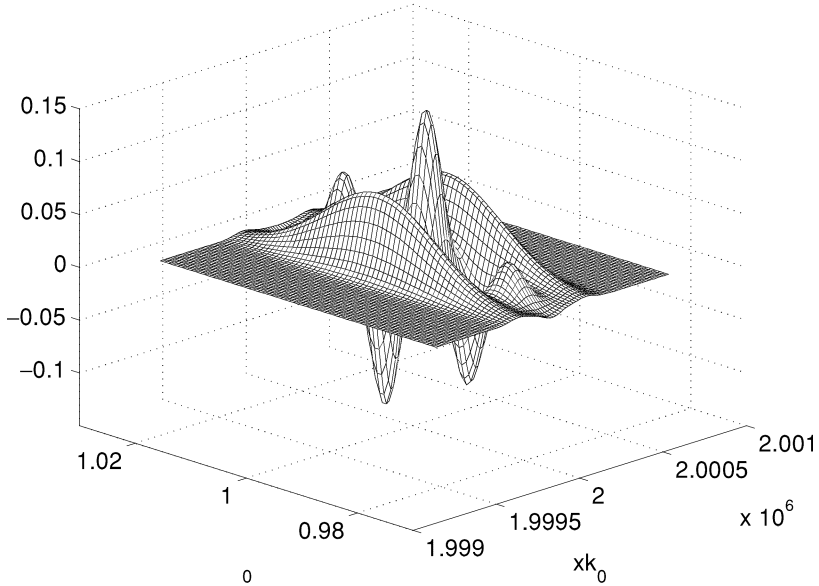


**Fig. 10.5.** The Wigner function (10.58) in the field-free region (Fig. 10.1) for  $\bar{T} = (p - 1)/4 = 25.5$

parameters  $\tau = (\Delta k_0)/k_0 = 1.10^{-4}$  (9.18),  $\sigma = (\delta k)/k_0 = 1.10^{-2}$  and the (dimensionless) position coordinate in the free-field region ( $x_V k_0$ ) =  $2 \cdot 10^6$ . Furthermore, the above-mentioned parameter  $p$  is 101 and 103, respectively. Because  $\bar{T} = 25$  is an integer, Fig. 10.4 looks like Fig. 9.3, but here the Wigner function exists in a field-free region, whereas Fig. 9.3 illustrates a Wigner function in a constant magnetic field. Figure 10.5 demonstrates the case where  $p = 103$  and  $\bar{T} = 25.5$ . As can be clearly seen, the oscillations between the Schrödinger-cat-states have opposite phase compared to Fig. 10.4. The other polarization directions can be obtained by using

$$\alpha_{zf,-x}(k) = \frac{1}{2}\alpha(k)[g_+ - g_-]^*, \quad \alpha_{zf,\pm y}(k) = \frac{1}{2}\alpha(k)[g_+ \mp ig_-]^*,$$

and, because of the strong similarity, we do not carry out the calculations.

## 11 Summary

Quantum interferometry is an area of quantum optics. In this book, an attempt has been made to describe quantum interferometric processes in phase space using quantum mechanical distribution functions of both light waves and matter waves.

After an introductory chapter of basic quantum theoretical concepts, we have discussed in Part I quantum mechanical distribution functions such as the Wigner function, the Q-function and the P-function based on a systematic approach using both wave packets and coherent states. Properties of those “quasi-distributions” are derived and examples presented. Squeezed states and uncertainty relations are mentioned at the end of Part I.

The outcome of these considerations is a phase-space formalism, which has been applied to optical interferometry in Part II. The concept of wave packets has been used in this case. Thereby, the beam splitter, the Mach–Zehnder interferometer, a system of three Mach–Zehnders, double loop systems and a Mach–Zehnder interferometer with two inputs have been discussed in detail. There the momentum and the position distribution functions play an important role in obtaining appropriate representations of the wave functions under consideration.

Part III is entirely devoted to neutron interferometry. After a chapter about the dynamical theory of diffraction of neutrons in single crystals, the Laue-type interferometer is introduced. The three and four-plate neutron interferometer has been analyzed using the phase-space formalism. The investigation of squeezing phenomena, as well as decoherence and visibility aspects, are further important items in Part III.

The last part, IV, deals with spin interferometry. Both the spin-echo and the zero-field spin echo system have been examined. The spin-echo system investigates the spin rotation of particles in constant magnetic fields where coherent superposition of spin-up and spin-down states with slightly different momenta entails a quantum state that can be visualized using the Wigner function. Fluctuations of the magnetic field lead to dephasing processes, depending on the distance the particle travelled in the field. The interaction of neutrons with a rotating magnetic field is discussed and the energy exchange between the particle and the field has been described. The quantum state in a successive field-free region has been determined by using quantum mechanical distribution functions.

## References

1. C. Cohen-Tannoudji, B. Diu, F. Laloe: *Quantum Mechanics, I and II* (John Wiley & Sons, New York London Sydney Toronto 1977)
2. W.P. Schleich: *Quantum Optics in Phase Space*, 1st edn. (Wiley-VCH, Berlin 2001)
3. R. Loudon: *The Quantum Theory of Light*, 3rd edn. (Oxford University Press, Oxford, New York 2000)
4. R.J. Glauber: Phys. Rev. **131**, 202–224 (1963)
5. M. Hillery, R.F. O’Connell, M.O. Scully, E.P. Wigner: Phys. Rep. **106**, 121–167 (1984)
6. D.F. Walls, G.J. Milburn: *Quantum Optics*, 2nd edn. (Springer, Berlin Heidelberg New York 1995)
7. M. Orszag: *Quantum Optics*, 1st edn. (Springer, Berlin Heidelberg New York 2000)
8. C.C. Gerry, P.L. Knight: *Introductory Quantum Optics*, 1st edn. (Cambridge University Press, Cambridge 2005)
9. L. Mandel, E. Wolf: *Optical Coherence and Quantum Optics*, 1st edn. (Cambridge University Press, Cambridge 1995)
10. M.O. Scully, M.S. Zubairy: *Quantum Optics* (Cambridge University Press, Cambridge 1997)
11. A. Zavatta, S. Viciani, M. Bellini: Science **306**, 660–662 (2004)
12. U. Leonhardt: *Measuring the Quantum State of Light*, 1st edn. (Cambridge University Press, Cambridge 1997)
13. P. Grangier, G. Roger, A. Aspect: Europhys. Lett. **1**, 173–179 (1986)
14. A. Zeilinger: Rev. Mod. Phys. **71**, 288–297 (2000)
15. A. Zeilinger, G. Weihs, T. Jennewein, M. Aspelmeyer: Nature **433**, 230–238 (2005)
16. D. Bouwmeester, A. Ekert, A. Zeilinger (Eds.): *The Physics of Quantum Information*, 1st edn. (Springer, Berlin Heidelberg New York 2000)
17. M.A. Nielsen, I.L. Chuang: *Quantum Computation and Quantum Information*, 1st edn. (Cambridge University Press, Cambridge 2000)
18. B.E.A. Saleh, M.C. Teich: *Fundamentals of Photonics* (John Wiley & Sons, New York 1991)
19. N. Gisin, G. Ribordy, W. Tittel, H. Zbinden: Rev. Mod. Phys. **74**, 145–195 (2002)
20. V. Giovannetti, S. Lloyd, L. Maccone: Science **306**, 1330–1336 (2004)
21. C.K. Hong, Z.Y. Ou, L. Mandel: Phys. Rev. Lett. **59**, 2044–2046 (1987)
22. T.B. Pittman, D.V. Strekalov, A. Migdall, M.H. Rubin, A.V. Sergienko, Y.H. Shih: Phys. Rev. Lett. **77**, 1917–1920 (1996)

23. T. Legero, T. Wilk, A. Kuhn, G. Rempe: *Appl. Phys.* **B77**, 797–802 (2003)
24. H. Rauch, S.A. Werner: *Neutron Interferometry – Lessons in Experimental Quantum Mechanics*, 1st edn. (Clarendon Press, Oxford 2000)
25. F. Mezei: *Z. Physik* **255**, 146 (1972)
26. R. Gähler, R. Golub: *Z. Physik* **B65**, 269 (1987)
27. T.M. Cover, J.A. Thomas: *Elements of Information Theory*, 1st edn. (John Wiley & Sons, New York 1991)
28. H. Rauch, D. Petrascheck: In: *Neutron Diffraction*, Top. Curr. Phys. Vol. 6, ed. by H. Dachs (Springer, Berlin Heidelberg New York 1978) pp. 303
29. R.W. James: In: *Solid State Physics*, Vol 15, ed. by F. Seitz and D. Turnbull (Academic Press, New York, 1963) pp. 53–220
30. B.W. Batterman, H. Cole: *Rev. Mod. Phys.* **36**, 681 (1964)
31. M.L. Goldberger, F. Seitz: *Phys. Rev.* **71**, 294 (1947)
32. D. Sippel, K. Kleinstück, G.E.R. Schulze: *Phys. Lett.* **14**, 174 (1965)
33. M. Born, E. Wolf: *Principles of Optics*, 7th edn. (Cambridge University Press, Cambridge 2001)
34. W. Schleich, M. Pernigo, Fam Le Kien: *Phys. Rev. A* **44**, 2172 (1991)
35. E.P. Wigner: *Phys. Rev.* **40**, 749 (1932)
36. M. Suda: *Quantum Semiclass. Opt.* **7**, 901–916 (1995)
37. P.B. Lerner, H. Rauch, M. Suda: *Phys. Rev. A* **51**, 3889–3895 (1995)
38. K. Vogel, H. Risken: *Phys. Rev. A* **40**, 2847 (1989)
39. M. Freyberger, S.H. Kienle, V.P. Yakovlev: *Phys. Rev. A* **56**, 195 (1997)
40. V. Buzek, P.L. Knight: *Opt. Comm.* **81**, 331 (1991)
41. M.G.A. Paris: *Phys. Rev. A* **59**, 1615 (1999)
42. G.S. Agarwal: *Found. Phys.* **25**, 219 (1995)
43. D. Giulini, E. Joos, C. Kiefer, J. Kupsch, I.-O. Stamatescu, H.D. Zeh: *Decoherence and the Appearance of a Classical World in Quantum Theory*, 1st edn (Springer, Berlin Heidelberg New York 1996)
44. M. Namiki, S. Pascazio, H. Nakazato: *Decoherence and Quantum Measurements*, 1st edn. (World Scientific, Singapore 1997)
45. W.H. Zurek: *Phys. Today* **44**, 36 (1991)
46. P. Facchi, A. Mariano, S. Pascazio, M. Suda: *J. Opt. B: Quantum Semiclass. Opt.* **5**, 290–298 (2003)
47. H. Rauch, M. Suda: *Appl. Phys.* **B60**, 181–186 (1995)
48. M. Suda: *Act. Phys. Slov.* **49**, 761–764 (1999)
49. H.J. Carmichael: *Statistical Methods in Quantum Optics I – Master Equations and Fokker–Planck Equations*, 1st edn. (Springer, Berlin Heidelberg New York 1999)
50. M. Heinrich, D. Petrascheck, H. Rauch: *Z. Physik* **B72**, 357 (1988)
51. M. Suda, H. Rauch: *Act. Phys. Slov.* **46**, 499–504 (1996)
52. M. Suda: *J. Opt. B: Quantum Semiclass. Opt.* **5**, 392–394 (2003)
53. M. Suda, H. Rauch, M. Peev: *J. Opt. B: Quantum Semiclass. Opt.* **6**, 345–350 (2004)
54. J. Summhammer, H. Rauch, D. Tuppinger: *Phys. Rev. A* **36**, 4447 (1987)
55. M. Zawisky, M. Baron, R. Loidl: *Phys. Rev. A* **66**, 063608 (2002)
56. M. Baron, H. Rauch, M. Suda: *J. Opt. B: Quantum Semiclass. Opt.* **5**, 241–244 (2003)
57. S. Pancharatnam: *Proc. Indian Acad. Sci. Phys.* **A44**, 247 (1956)
58. M.V. Berry: *Proc. R. Soc. Lond.* **A392**, 45 (1984)

59. Y. Hasegawa, R. Loidl, G. Badurek, M. Baron, H. Rauch: Nature **425**, 45 (2003)
60. H. Rauch, H. Lemmel, M. Baron, R. Loidl: Nature **417**, 630 (2002)
61. Y. Hasegawa, M. Zawisky, H. Rauch, A.I. Ioffe: Phys. Rev. **A53**, 2486 (1996)
62. R.A. Bertlmann, K. Durstberger, Y. Hasegawa, B.C. Hiesmayr: Phys. Rev. **A69**, 032112 (2004)
63. S. Filipp, Y. Hasegawa, R. Loidl, H. Rauch: e-print quant-ph/0412038
64. F. Mezei: In: *Neutron Spin Echo, Lecture Notes in Physics*, Vol. 128, ed. by F. Mezei (Springer, Berlin Heidelberg New York 1980) pp. 3
65. O. Halpern, T. Holstein: Phys. Rev. **59**, 960 (1941)
66. F. Mezei: Physica **B151**, 34 (1988)
67. R. Gähler, R. Golub, K. Habicht, T. Keller, J. Felber: Physica **229**, 1 (1996)
68. H. Rauch, M. Suda: Physica **B241–243**, 157 (1998)
69. G. Badurek, H. Rauch, M. Suda, H. Weinfurter: Optics Comm. **179**, 13 (2000)
70. H. Rauch, M. Suda: In: *Neutron Spin Echo Spectroscopy, Lecture Notes in Physics*, vol. 601, ed. by F. Mezei, C. Pappas, T. Gutherlet (Springer, Berlin Heidelberg New York 2003) p. 133–141
71. W.H. Zurek: Rev. Mod. Phys. **75**, 715–775 (2003)
72. M. Suda: Fortschr. Phys. **49**, 1103–1108 (2001)
73. R. Gähler, R. Golub: J. Phys. France **49**, 1195 (1988)
74. G. Badurek: Physics of Polarized Neutrons. Thesis, Technical University, Vienna (1982)

# Index

- absorption, 41, 42, 44–46, 50, 65, 79, 130–133, 135  
amplitude resonance, 164–166, 170  
analyzer, 91–93, 120, 129  
annihilation operator, 17, 22, 32, 33  
  
Baker–Campbell–Hausdorff, 13, 18, 23  
beam parameter, 115  
beam splitter, 37–41, 62, 67  
Bloch equation, 141  
Bloch-ansatz, 79  
Bragg angle, 77  
Bragg equation, 77  
Brownian motion, 116  
  
characteristic function, 13, 14, 22–25, 29, 31  
coherence length, 71, 72, 97, 115  
coherent states, 9, 19, 20, 22, 24, 25, 28, 31, 34, 108, 115  
conditional probability, 116  
correlation, 4, 9, 72, 119, 125–127, 137, 153  
creation operator, 17, 22, 33  
crystal function, 85, 98, 129  
  
decoherence, 72, 111, 117, 152, 153  
density fluctuation, 115, 149  
density operator, 5, 6, 9, 11, 22, 24, 25, 28, 30  
dephasing, 111, 112, 115, 116, 153  
deterministic, 131–135  
diffusion, 115–117  
dispersion coefficient, 42  
displacement operator, 18, 19, 23  
dissipation, 97, 112, 153  
double-loop, 56, 60, 119, 121, 125, 128  
dynamical theory, 75, 79, 86, 102, 129  
  
energy loss, 166  
expectation value, 5, 13, 19, 22, 24, 145  
fluctuations, 18, 21, 97, 112, 115–117, 143, 149, 150, 152–154  
Fock state, 15, 18, 21, 31, 108  
focusing condition, 91, 93  
Fokker–Planck, 116  
four-plate, 128, 175  
  
Gaussian, 3, 4, 10, 17, 19, 21, 22, 30, 31, 38, 43, 55, 61, 72, 98, 108, 112, 115, 145, 149, 151, 153, 154  
geometrical phase, 137  
geometrical theory, 75, 77, 82, 87  
glass fiber, 40, 42, 53  
Green’s function, 116  
  
Hadamard transformation, 40, 42, 48, 57, 62  
Hamiltonian, 5, 7, 14, 17, 40  
harmonic oscillator, 4, 7, 9, 14, 21, 25, 32, 33  
Hilbert space, 38, 39  
Hong–Ou–Mandel, 67  
Husimi function, 17  
  
index of refraction, 81, 94  
inhomogeneities, 4, 112, 115, 117, 153  
intensity, 46, 58, 60, 81, 86, 95, 97, 98, 107, 119, 121, 123, 126, 130, 131, 133, 144, 145, 172  
interference pattern, 37, 46, 97, 115  
  
kinetic energy, 165, 169, 171  
  
Larmor, 71, 141–143, 157, 166, 172  
lattice factor, 76, 78  
Laue diffraction, 82  
Laue interferometer, 91

- Mach-Zehnder, 37, 41, 47, 50, 61, 62, 71, 91, 108, 136
- magnetic field, 4, 32, 112, 141–147, 149, 150, 152–155, 157–160, 162–165, 168, 169, 171, 173
- mirror, 91–94, 120, 128
- mixed state, 5, 11, 113, 152, 153
- momentum spectrum, 50, 102, 104, 149, 172
- neutron interferometry, 33, 37, 43, 71, 97, 108, 115–117, 137, 149
- optical interferometry, 37
- oscillations, 26, 65, 86, 98, 107, 110, 117, 128, 130–132, 150, 152, 174
- P-function, 22, 29, 30
- Pauli equation, 157, 159, 163
- Pauli matrices, 144, 145, 158, 159, 163
- Pendellösung, 75, 86, 87
- phase shift, 41–44, 47, 55, 60, 61, 65, 94, 97–99, 112, 116, 120, 125, 127, 128, 134, 135, 173
- phase-space, 6, 9, 72, 97, 107, 108, 111, 112, 119
- photon number, 19, 21, 23, 28, 30, 32, 34, 112
- Poissonian distribution, 19, 20, 22
- polarization, 141, 143, 144, 155, 158, 159, 161, 163, 165, 166, 170–172, 174
- position spectrum, 44, 104, 147
- pure state, 5, 10
- Q-function, 16, 24, 25, 31, 108, 109
- quadratures, 33
- quantum cryptography, 56
- quantum state reconstruction, 137
- quasi-distribution, 17, 112
- radiation field, 7, 23, 27–30
- reciprocal lattice, 77, 78, 80, 87–89
- resonance frequency, 157, 162–166
- rotating field, 157, 173
- Schrödinger-cat-like states, 97, 99, 115, 153
- Shannon entropy, 72, 73, 109
- silicon, 71, 75, 78, 79, 81, 84, 86, 87, 91, 125
- single crystal, 76, 78, 80, 102
- spin interferometry, 4, 37
- spin-echo, 71, 101, 141–143, 149, 150, 157, 169
- spin-flip, 157, 158, 162, 164–168, 170, 171
- squeezed states, 31, 33, 34, 108
- squeezing, 33, 97, 108, 121, 123, 124
- stochastic, 112, 131–133
- structure factor, 76, 78
- superposition, 4, 5, 28, 50, 71, 72, 93, 94, 97–99, 104, 108, 109, 113, 115, 116, 119, 121, 125, 126, 128, 129, 141, 144
- surface roughness, 117, 149
- thermal neutrons, 79
- thermal state, 7, 23
- total energy, 143, 144, 159, 165–167, 169–171
- transmission, 41, 43, 44, 47, 48, 50, 55, 56, 59–61, 91, 116, 128–130, 133, 134, 136, 164
- two-photon interference, 67
- uncertainty relation, 10, 14, 18, 21, 32, 72, 73, 108, 109
- vacuum state, 18, 19
- visibility, 37, 43, 46, 48, 55, 60, 65, 107, 119, 125–128, 131, 134–136
- wave field, 84, 91
- wave packet, 10, 33, 38, 39, 42, 72, 97, 99, 107, 108, 121, 126, 141, 144, 155
- Wigner function, 9–11, 13, 14, 23, 25, 31, 43, 72, 98, 101, 108, 111, 116, 117, 121, 137, 143, 146, 149, 151, 152, 154, 171, 172
- Zeeman, 141, 143, 144, 155, 157, 170, 171
- zero-field spin-echo, 71, 157, 158, 168, 172